ABSTRACT

Title of Dissertation: PHOTOIMMUNOTHERAPY-BASED COMBINATION REGIMENS AND DRUG DELIVERY SYSTEMS FOR OVARIAN CANCER TREATMENT

Aaron Joseph Sorrin
Doctor of Philosophy, 2023

Dissertation directed by: Associate Professor, Huang Chiao Huang,
Fischell Department of Bioengineering

Ovarian cancer is among the deadliest gynecologic malignancies, accounting for over 13,000 deaths and nearly 20,000 new cases each year in the United States alone. The lethality of this disease results from several fundamental challenges, including diagnosis at advanced stages, development of resistance to standard-of-care chemotherapies, and extensive metastasis throughout the peritoneal cavity. Photodynamic therapy (PDT) is a promising treatment modality which enables spatiotemporally controlled cancer ablation upon light-activation of specialized drugs (photosensitizers). Clinical studies have demonstrated the feasibility and safety of PDT for women with peritoneally disseminated ovarian cancer, though treatment outcomes were limited by off-target toxicities and the heterogenous cellular uptake of photosensitizer. The use of antibody-conjugated photosensitizers (photoimmunoconjugates) has the potential to overcome these prior limitations, making the targeted version of PDT (photoimmunotherapy, PIT) a valuable tool for ovarian cancer treatment.

The overarching objective of this dissertation is to develop PIT-based strategies for ovarian cancer management through three complimentary goals: 1) overcome metastatic behaviors in ovarian cancer using PIT-based combination therapies; 2) bolster photosensitizer drug delivery using a clinically-relevant, fluid flow-based drug delivery approach; and 3) enhance cytotoxic effects of PIT through developing a new nanocomplex for photochemotherapy. This work establishes novel PIT-based combination treatments that incorporate clinically relevant therapies, including prostaglandin E2 receptor 4 (EP4) antagonism, poly(ADP-Ribose) polymerase (PARP) inhibition, and epidermal growth factor receptor (EGFR)-targeted antibodies. Results from this dissertation reveal pronounced combination effects of PIT and EP4 antagonism, leading to cooperative reductions in metastasis-related behaviors and cell signaling *in vitro*. The findings of this work further demonstrate that fluid flow enhances photoimmunoconjugate delivery, modulates subcellular photosensitizer localization, and enhances the phototoxicity to ovarian cancer cells in a pump system. Lastly, we developed 1) a targeted nanocomplex for combination of PIT and PARP inhibitors; and 2) a 3-dimentional (3D) ovarian tumor spheroid coculture model for the longitudinal quantification of treatment effects and the development of multidrug resistance.

PHOTOIMMUNOTHERAPY-BASED COMBINATION REGIMENS AND DRUG DELIVERY SYSTEMS FOR OVARIAN CANCER TREATMENT

by

Aaron Joseph Sorrin

Dissertation submitted to the Faculty of the Graduate School of the
University of Maryland, College Park, in partial fulfillment
of the requirements for the degree of
Doctor of Philosophy
2023

Advisory Committee:
Associate Professor, Huang Chiao Huang, Chair
Associate Professor, Steven Jay
Associate Professor, Kimberly Stroka
Associate Professor, Dana Roque
Professor, Doron Levy

Acknowledgements

First and foremost, I would like to acknowledge my primary research advisor, Dr. Huang Chiao (Joe) Huang. It's been my privilege to work alongside you over these past years, and so much of my personal and professional development have been a direct result of your mentorship. I would also like to acknowledge my other committee members: Dr. Jay, Dr. Stroka, Dr. Roque, and Dr. Levy, for accompanying and guiding me along this journey. In particular, thank you to Dr. Roque for being a clinical sounding board and impactful mentor throughout my graduate studies. And thank you also to Dr. Jocelyn Reader for your limitless kindness and support.

To my lab members, of the past and present, thank you. To Collin Inglut and Barry Liang, my very first graduate student mentors in the lab, I learned by your example how to work hard and think critically about my research. I always felt supported by you, both personally and professionally. To Shruti Vig, Ariel Ma, Sumiao Pang, Idrisa Rahman, John Quinlan, Rebecca Hays, and Kathryn McNaughton: it was always a joy to work with you all. I hope we stay in touch in the coming years as you all continue your graduate educations and beyond.

Thank you to Drs. Payal Srivastava and Carla Arnau Del Valle, I'm so grateful I had the chance to work alongside you both during my PhD. Your chemistry expertise and mentorship were instrumental in my development as a scientist. To the undergraduate students I worked directly with during my PhD – Julia Cicalo, Cindy Liu, Keri Zhou, Katie May, and Anika Dasgupta – it was a pleasure training you and learning from you. Much of the work in this dissertation was supported by your hard work, and I know you will continue doing amazing things and achieving great

heights. I also would like to acknowledge all the UMD Bioengineering department staff, in particular Bill Churma, who has provided limitless support throughout my time as a PhD student. Finally, I would like to acknowledge my family and friends who supported me through this journey. In particular, thank you to my dad, stepmom, and sister for your continuous support throughout this process.

Table of Contents

List of Tables

Chapter 2 Tables

Chapter 4 Tables

Chapter 5 Tables

List of Figures

Chapter 2 Figures

Chapter 3 Figures

Chapter 4 Figures

Chapter 5 Figures

List of Abbreviations

AA – arachidonic acid

ATP – adenosine triphosphate

BPD – benzoporphyrin derivative

CAF – cancer-associated fibroblast

cAMP – cyclic adenosine monophosphate

Cet – cetuximab

COX2 – cyclooxygenase-2

CREB – cyclic AMP response element-binding protein

EGF – epidermal growth factor

EGFR – epidermal growth factor receptor

EMA – European Medicines Agency

EP4 – prostaglandin E2 receptor 4

EPR – enhanced permeability and retention

ERK1/2 – extracellular signal-regulated kinases 1/2

FDA – United States Food and Drug Administration

FSS – fluid shear stress

GAPDH - glyceraldehyde-3-phosphate dehydrogenase

HIPEC – hyperthermic intraperitoneal chemotherapy

IC_{50} – half-maximal inhibition concentration

Lig3α – DNA ligase 3

MRP4 – multidrug resistance-associated protein 4

NAD^+ – nicotinamide adenine dinucleotide

NHS - N-hydroxysuccinimidyl ester

NP-Tal – talazoparib-loaded nanoparticle

PARP – poly(ADP-ribose) polymerase

PBS – phosphate buffered saline

PdI – polydispersity index

PDP – photodynamic priming

PDT – photodynamic therapy

PEG – polyethylene glycol

PGE2 – prostaglandin E2

PIC – photoimmunoconjugate

PIC-Nal – photoimmunoconjugate-nanoliposome

PIC-NP – photoimmunoconjugate-nanoparticle

PIC-NP-Tal – photoimmunoconjugate-functionalized talazoparib-loaded nanoparticle

PKA – protein kinase A

PLGA – poly(lactic-co-glycolic acid)

polβ – DNA polymerase beta

PS – photosensitizer

ROS – reactive oxygen species

TAM – tumor-associated macrophage

TME – tumor microenvironment

XRCC1 – X-ray repair cross-complementing protein 1

β-arr – β-Arrestin

Chapter 1: Introduction and Thesis Outline

Ovarian cancer is the deadliest gynecologic malignancy. It is typically diagnosed at advanced stages, after metastasis to the peritoneal cavity has already begun. While photodynamic therapy has been tested clinically for peritoneally-disseminated diseases like ovarian cancer, its efficacy was hindered by heterogenous photosensitizer uptake and lack of selectivity [1]. Photoimmunotherapy is a clinically-relevant technology with the potential to overcome these hurdles through the use of antibody-conjugated photosensitizers. The **main objective** of this thesis to develop photoimmunotherapy based strategies for the treatment of advanced ovarian carcinomatosis. This thesis achieves this goal through two broad aims: **1)** establish rationally-designed photoimmunotherapy-based combination therapies; and **2)** engineer drug delivery modalities to mediate uptake of targeted photosensitizer by ovarian cancer cells.

Chapter 2 delivers essential background with literature summaries on topics that are central to this thesis. The origins, scope, and standard-of-care therapeutic regimen for advanced ovarian cancer are first explored. Next, the underlying mechanisms of photodynamic therapy (PDT) are probed, along with its role in the modulation of the tumor microenvironment (TME). Particular emphasis is placed on the use of nanoengineering approaches for targeting of photochemical damage to cancer and cancer-associated cells. Next, the cancer-promoting role of EP4 is explained along with the current status of EP4 inhibitors in the clinic. Lastly, the biological functions of poly(ADP-ribose), PARP, and poly(ADP-ribose) polymerase

inhibitors are explored. The major impact of these inhibitors on the clinical treatment of ovarian cancer and other malignancies is further discussed.

Next, **chapter 3** explores the role of low-dose PDT (photodynamic priming, PDP) in combination with inhibitors of EP4 for mitigation of ovarian cancer migration and invasion. In this work, the photosensitizer benzoporphyrin derivative (BPD) is chemically coupled with the EGFR-targeted antibody, cetuximab (Cet). This construct (photoimmunoconjugate, PIC) is paired with well-established EP4 inhibitor, AH23848, and used to treat OVCAR-5 and CAOV3 advanced ovarian carcinomatosis cell lines. Methods for therapeutic effect evaluation include gap closure assay, transwell invasion assay, immunoblotting, and enzyme-linked immunosorbent assay (ELISA). Results reveal potent anti-migratory and anti-invasive effects of the combination of PDP (using either BPD or PIC) with EP4 inhibition. PIC-mediated PDP combined with EP4 inhibition also downregulated multiple tumor-promoting signaling pathways including phosphorylation of EGFR, extracellular signal-regulated kinases 1/2 (ERK1/2), and cyclic AMP response element-binding protein (CREB). Overall, this chapter supports the development of PDP-based combination therapies with EP4 inhibition with an emphasis on antibody-targeted photosensitizers.

In **chapter 4**, the role of flow as a delivery method is explored for multiple photosensitizer formulations (free, antibody conjugated, and liposomal). In the clinic, during the hyperthermic intraperitoneal chemotherapy (HIPEC) procedure, a pump system is used to circulate drugs in the peritoneal cavity for the treatment of peritoneally disseminating malignancies like ovarian cancer. However, the impact of flow-mediated delivery on the therapeutic efficacy of photodynamic therapy remains

understudied, which this chapter seeks to elucidate. A microfluidic chip is used in conjunction with a pump system to generate laminar flow of drugs across OVCAR8 and OVCAR3 ovarian cancer cells. The PDT-based agents evaluated include BPD, PIC, and PIC-conjugated liposomes (PIC-Nal). Metrics of efficacy include total drug delivery, subcellular drug delivery, and cell killing. Results demonstrate that fluid shear stresses at 0.5 and 1 dynes/cm^2 significantly enhance the total and subcellular delivery of PIC. Cell killing after treatment with all three photosensitizing agents was evaluated at multiple light doses following treatment at 0 vs. 1 dyne/cm^2. All three agents show enhanced cytotoxicity when delivered under flow compared to static conditions. Data is further validated using confocal microscopy to show cellular accumulation.

Next, **chapter 5** expands on this work by developing a targeted nanoparticle for codelivery of PARP inhibitor, talazoparib, with photosensitizer, BPD, for targeted photochemotherapy. First, talazoparib-loaded nanoparticles (NP-Tal) are engineered and surface decorated with PICs (PIC-NP-Tal). The amount of talazoparib and polymer are varied to establish optimal particles with sufficient loading and appropriate size and polydispersity index (PdI). Next, the number of PICs-per-nanoparticle is optimized. The resulting construct is comprehensively characterized for stability, singlet oxygen generation, absorbance spectra, cancer cell selectivity, and photoactivity. In parallel, a fluorescent 3D coculture system is developed for validation of therapeutic effect. Cancer nodules are grown using the parental OVCAR8-DsRed cells and a chemo-resistant subline, NCI/ADR-RES-EGFP, which are seeded at equal densities and tracked up to 12 days. Consistent with previous

work in 2D cocultures, the 3D cocultures show domination of the chemo-sensitive cells in the absence of treatment. Results reveal that at low doses, NP-Tal induces chemo-resistant selection pressures by killing the chemo-sensitive parental cells and sparing the chemo-resistant subline. At higher doses of NP-Tal, the viability of both cell lines is reduced to equivalent degrees over time. Further studies reveal potent combinational effects of PIC and NP-Tal both when treated together (PIC + NP-Tal), though there are less impressive effects for the nanocomplex (PIC-NP-Tal).

To conclude this thesis, **chapters 6 and 7** overview the conclusions, future work, and scientific contributions. One area of expansion on the work in chapter 3 is the evaluation of PDT and EP4 inhibitor in the context of immune cell population and phenotype modulation. Both PDT and EP4 have long-established roles in anti-tumor immunity, though their combination in this context has yet to be explored. Further mechanistic rationale for this combination is expanded in chapter 6. Another future avenue for exploration is the direct quantification of fluid shear stress in the peritoneal cavity during HIPEC. While HIPEC is applied in the clinic across the globe, the fluid shear stress rates achieved during the procedure are unknown. This has been a major challenge for preclinical research seeking to recapitulate HIPEC-like conditions. A third area for future work is the *in vivo* evaluation of the PIC-NP-Tal construct invented in this thesis, particularly in the context of tolerability and bioavailability. To conclude, chapter 7 highlights a list of contributions to the field, which are encapsulated in the 10 expected publications and 8 conference presentations that have resulted from this thesis.

Chapter 2: Background

2.1 Ovarian Cancer

2.1.1 Scope and Pathogenesis

Ovarian cancer will account for approximately 13,000 deaths and over 20,000 new cases in the Unites States this year alone [2]. While the five-year survival rate for stage I disease is 92%, over 75% of patients are diagnosed at advanced stages (III-IV) with limited treatment options, bringing the overall five-year survival rate below 50% [3-5]. Ovarian cancer is a heterogenous disease that can originate at the ovary, fallopian tube, or peritoneum, and risk factors include genetics, oral contraceptive use, hormone replacement therapy, reproductive history, and diet, among others [5,6]. Additionally, there are multiple histological subtypes that vary in cellular origin, pathogenesis, and prognosis: high-grade serous, high-grade endometrioid, low-grade serous, low-grade endometrioid, clear-cell, and mucinous [5,6]. High-grade serous carcinoma (HGSC), which generally (80%) originates at the fallopian tube, is the most common histological subtype and accounts for 70% of diagnoses [5,7]. Unlike most epithelial cancers, HGSC does not require vascular or lymphatic transit for metastatic spread. Instead, the primary mechanism of HGSC metastasis, transcoelomic spread, involves the deposition of cancer cells and clusters throughout the peritoneal cavity, carried by the passive physiological movement of accumulated peritoneal fluids (ascites) [8,9]. Once ascites-carried cells and clusters are deposited along the peritoneum, metastatic niches form, and tumor-promoting microenvironments develop [8].

2.1.2 Ascites and Fluid Shear Stress

The accumulation of ascites in the peritoneal cavity is a hallmark of advanced stage ovarian cancer and is associated with chemoresistance, metastasis, disease recurrence, and overall poor prognosis [10,11] (**Figure 2.1**). Over 1/3 of patients experience ascites at diagnosis, and nearly all have ascites at recurrence [10]. This fluid development is primarily caused by increased vascular permeability, which is mediated by the accumulation of angiogenic factors such as VEGF and interleukin 6 and 8 [11,12]. Another proposed mechanism of ascites development is obstructed lymphatics. Under normal physiological conditions, lymphatic vessels reabsorb peritoneal fluid. Disseminated tumors obstruct these lymphatic portals on the peritoneal surface, enabling fluid accumulation [11]. While this is likely a contributing factor to the development of ascites, mouse models and clinical work show that ascites develops in the absence of bulk tumors obstructing lymphatic flow, suggesting that it is not the primary factor [11,13].

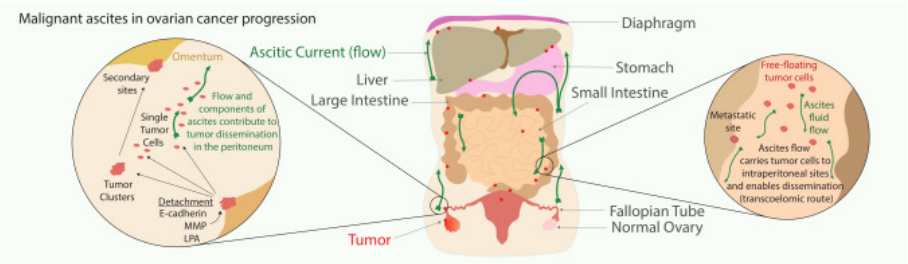

Figure 2.1: Malignant ascites in the dissemination and progression of ovarian cancer. Malignant ascites contributes to intraperitoneal tumor dissemination. Tumor cells detach from the primary tumor site as individual tumor cells or as tumor cell clusters, which can travel via currents of ascitic fluid to other intraperitoneal sites and create secondary cancer sites (transcoelomic route).[1]

[1] Figure and caption adapted from Rickard, B.P.; Conrad, C.; Sorrin, A.J.; Ruhi, M.K.; Reader, J.C.; Huang, S.A.; Franco, W.; Scarcelli, G.; Polacheck, W.J.; Roque, D.M., et al. Malignant Ascites in Ovarian Cancer: Cellular, Acellular, and Biophysical Determinants of Molecular Characteristics and Therapy Response. *Cancers (Basel)* 2021, *13*, 4318. Open access (CC BY). Figure is cropped from original print.

Ascites is a repository for cellular and acellular factors that stimulate biological deregulation and cultivate a microenvironment that facilitates cancer growth and metastasis [14]. Cellular factors in ascites include tumor cells and tumor-associated cells, such as such as cancer-associated fibroblasts (CAFs), tumor-associated macrophages (TAMs), and cancer-associated adipocytes [15]. Acellular factors include cytokines, proteins, metabolites, and exosomes, which mediate autocrine and paracrine signaling between cells [14,16]. Many of these factors dysregulate cell signaling pathways that are implicated in cell migration and ultimately drive the development of metastatic disease [17-21]. In addition to containing tumorigenic factors, ascites also mediates mechanical stimulation via fluid shear stress. Ascitic flow is induced by organ movement, gravity, breathing, and bodily movements. While human ascites shear stress rates have not been measured precisely, they are estimated to be in the range of 0.14-11 dynes/cm^2 based on a computational simulation of gastrointestinal wall shear stress values [22,23]. This continuous flow promotes metastasis through exfoliating cancer cells and clusters and stimulating cell signaling pathways [24].

2.1.3 Standard-of-Care for Advanced Ovarian Cancer

The standard-of-care treatment for advanced ovarian cancer involves surgical cytoreduction (debulking) for removal of gross macroscopic disease coupled with adjuvant chemotherapy (platinum-taxane cocktail) [25]. Chemotherapy can be delivered intravenously or intraperitoneally, and intraperitoneal administration can occur under static conditions or using a perfusion system to achieve HIPEC. Despite receiving the standard-of-care treatments, up to 80% of advanced ovarian cancer

patients will experience recurrent disease [26]. Relapse within 6 months indicates platinum-resistant disease and is linked to poor prognosis. Treatment options for platinum resistant disease include paclitaxel, polyethylene glycol (PEG)-ylated liposomal doxorubicin, topotecan, and gemcitabine, all of which offer similar response rates (~12 month overall survival) [27]. Patients that relapse at least 6 months after completion of initial therapy are deemed platinum-sensitive and will receive platinum-based treatment either alone or as part of a combination regimen. Unfortunately, response rates to platinum rechallenge typically worsen with each subsequent treatment until platinum resistance is developed [27].

2.2 Photodynamic Therapy[2]

2.2.1 Photochemistry and Mechanisms of Toxicity

PDT is a minimally invasive treatment modality that is used for oncologic and nononcologic applications and has been explored for the modulation of the TME [28,29]. The cytotoxic mechanism of PDT is based on inducing photodamage through the excitation of a nontoxic photoactive chemical, a photosensitizer (PS), using light of a specific wavelength [30]. A PS, in singlet ground state, absorbs a visible photon of appropriate energy and becomes electronically excited to a singlet excited state. The PS then either decays to the singlet ground state by generating fluorescence or undergoes intersystem crossing to the triplet excited state. From there, the molecule can interact directly with molecular oxygen or with another substrate via electron or proton transfer to return to the singlet ground state. When these photochemical reactions result in the generation of sufficient amounts of singlet oxygen or other

[2] Materials from this section are adapted from Sorrin, A.J., Kemal Ruhi, M., Ferlic, N.A., Karimnia, V., Polacheck, W.J., Celli, J.P., Huang, H.-C. and Rizvi, I. (2020), Photodynamic Therapy and the Biophysics of the Tumor Microenvironment. Photochem Photobiol, 96: 232-259. https://doi.org/10.1111/php.13209.

reactive molecular species to cross the threshold of cell survival, toxicity is conferred to the target tissue, such as cancer cells [30,31].

The modes of cell death activated by PDT (e.g., apoptosis, necrosis, necroptosis, lethal autophagy or paraptosis) depend strongly on the type of PS used and the subcellular and/or extracellular PS localization at the time of light activation. Mitochondrial photodamage generally leads to the initiation of apoptosis through the direct release of cytochrome c and degradation of the antiapoptotic Bcl family of proteins, without effects on proapoptotic Bax [32-34]. The initiation of apoptosis by direct mitochondrial photodamage is significant in cancer therapy because this pathway bypasses many of the escape and repair mechanisms through which cancer cells are able to develop resistance to traditional treatments. PDT can also cause toxicity by initiating necrosis, and causing white blood cells to release cytokines, such as necrosis factors [35,36]. Depending on the type of photodamage and the underlying biology of the target cells, PDT can also cause lethal levels of autophagy [37], or as has been reported more recently, can trigger paraptosis, a response, in part, to misfolded endoplasmic reticulum (ER) proteins [33]. Combining PS or PS formulations to enhance PDT efficacy by targeting complementary tumor compartments or subcellular sites has also shown promise [38-45]. Importantly, because the timing, location and intensity of light activation can be carefully controlled, PDT is inherently a targeted therapeutic modality. Exploitation of PDT-mediated cytotoxic mechanisms has been used in combination with conventional and emerging therapies to overcome chemoresistance [46] and to enhance efficacy [47-52].

2.2.2 Photodynamic Therapy and the Tumor Microenvironment

In addition to inducing spatially and temporally selective cytotoxicity, PDT can also alter the TME by targeting specific malignant and nonmalignant cells as well as extracellular components. This damage is highly dependent on PS localization, which is dictated by the structural and chemical properties of the PS and the PS-light interval (the time interval between PS administration and light exposure). Some PSs localize preferentially in specific tumor compartments, such as Tookad, which largely stays in the vasculature [53,54]. Other PSs, such as BPD, can target various tumor compartments (e.g., vasculature, ECM, cancer cells) depending, in part, on the PS-light interval. The use of Tookad and BPD in the context of vascular-targeted PDT is further discussed in a later section.

The localization of the PS directly influences the treatment outcome. For PDT targeted to the vasculature, there can be a range of effects, including vascular permeabilization for the enhanced delivery of nanoscale therapeutics, as well as blood vessel occlusion which can result in increased tumor hypoxia. [55-58]. Additionally, PDT that is targeted to the ECM can alter ECM composition through hyaluronic acid degradation and collagen crosslinking [59-61]. PDT-induced collagen crosslinking is being researched for the treatment of keratoconus of the cornea and intimal hyperplasia mediated vascular cell migration [62,63]. However, PDT can also lead to the degradation of collagen through damaging fibroblasts and causing the release of MMPs [64,65]. While the degradation of collagen prevents desmoplasia and increases drug penetration, it may also lead to increased invasion and metastasis of cancer cells [66-68]. Therefore, the effects of PDT on ECM composition can be highly varied, and

destruction of stromal components does not necessarily improve treatment outcomes. For example, previous work has shown that the depletion of the heterogeneous stroma results in more aggressive cancer behavior. In one study, a transgenic mouse was generated with the ability to delete αSMA^+ myofibroblasts in pancreatic cancer, and the depletion of the stroma caused invasive tumors with diminishing mouse survival [69]. Therefore, destruction of stromal components could aggravate disease progression, so PDT treatments designed to target stromal components must be carefully studied and optimized. A summary of PSs that are commonly used in clinics and in preclinical research is presented in **Table 2.1**, along with their localization characteristics [41,70-80].

Table 2.1: Photosensitizers that are commonly used in the clinic and in preclinical studies. *Hematoporphyrin Derivative (HpD); mono-l-aspartyl chlorin e6 (NPe6); zinc phthalocyanine* (ZnPc); Aminolevulinic Acid (ALA).

Photosensitizer	Family	Generation	Localization	References
HpD	Porphyrin	1st	Multiple organelles and cell membrane	[70,80]
BPD	Porphyrin	2nd	Mitochondria and ER, or vasculature depending on the photosensitizer-light interval	[71,72]
NPe6	Chlorin	2nd	Lysosomes	[41,78]
Tookad	Bacteriochlorin	2nd	Tumor vasculature	[73]

Photosensitizer	Family	Generation	Localization	References
Photofrin	Porphyrin	1st	Plasma membrane and Golgi apparatus	[74]
Foscan	Chlorin	2nd	ER and Golgi apparatus	[75,76]
ZnPc	Phthalocyanine	2nd	Mitochondria and lysosomes	[77]
ALA	Porphyrin	2nd	PpIX produced in mitochondria, some relocalizes to the plasma membrane and lysosomes	[79]

2.2.3 Targeting by Cellular and Tissue Modulation

Cellular and tissue modulation is among the most translationally relevant approaches to enhance selective treatment of target tissue. In the case of targeted PDT for cancer, a major goal of this targeting strategy is to increase the accumulation of PSs in tumors. Cellular and tissue modulation, also known as biomodulation, is the alteration of biological mechanisms by which cells metabolize, take up or retain PSs to selectively enhance PDT efficacy [81]. A focus of this section is the heme biosynthesis pathway utilized in mammalian cells, also known as the Shemin pathway, which involves the conversion of 5-ALA to heme [82-88]. The penultimate step in this pathway is the production of PpIX (**Figure 2.2a**) A preferential site of localization of PpIX is the mitochondria [89]. PpIX can also be transported into the cytosol by mitochondrial adenosine triphosphate (ATP)-binding cassette transporter G2 (ABCG2) [90,91]. The production of PpIX can be increased by modulating key

enzymes in the heme pathway, such as coproporphyrinogen (CPO) and ferrochelatase (FECH). ALA is a prodrug that is approved by the FDA for fluorescence-guided resection of gliomas and photodynamic treatment of actinic keratosis [92-94].

Preferential accumulation of PpIX in cancer cells results from dysfunctional activity of key enzymes in the heme pathway compared to healthy tissue. This includes decreased FECH activity and increased CPO activity, which increases the production of PpIX and limits its conversion to heme, leading to increased accumulation of the PS in target tissue [95]. In 1979, Malik and Djaldetti first showed that ALA enhanced the synthesis of hemoglobin as well as the intermediate precursor uroporphyrin and PpIX [96]. Later, in 1987, eighty basal cell carcinomas (BCC) were treated using ALA-induced PpIX-based PDT by Kennedy and Pottier, with a 90% response rate [97-99]. Among the advantages of PpIX is that it is rapidly cleared from the skin from topical, systemic, oral or intradermal administration, thereby minimizing skin phototoxicity [99,100]. Difficulties arise in using this treatment due to insufficient or nonuniform PpIX accumulation in the cancerous tissue, highlighting the need for approaches such as cellular and tissue modulation.

To overcome the problem of insufficient or nonuniform PpIX accumulation, various methods to modulate the heme pathway have been developed. Cells that are poorly differentiated and rapidly proliferating, as is common in many tumors, may produce insufficient amounts of PpIX [81]. One area of investigation to address this issue involves the use of cellular differentiators such as vitamin D or its analogues, methotrexate, retinoic acid, 5-fluorouracil acid, iron chelators and the androgens 5α-dihydrotestosterone (DHT) and R1881 [101-127].

Treatment efficacy can be influenced by microenvironmental factors such as temperature, pH and oxygen availability/hypoxia [128-133]. An emerging area of investigation is the role of mechanical stress on PpIX production and accumulation. A study by Niu *et al.* [134] using two glioma cell lines of bulk/solid tumors, U373 and U118, showed that cell proliferation rate increased in a nonlinear fashion as substrate stiffness increased. Their motivation was to study cell proliferation, and PpIX synthesis in glioma cells on substrates simulated the tissue stiffnesses of normal brain (1 kPa) and glioblastoma (12 kPa) [135-137]. The two cells used to evaluate the effects of mechanical stiffness were selected based on a previous study of PpIX production in a panel of 10 glioma cell lines. U373 was determined to produce the most PpIX, while U118 produced the least [138]. Evaluation of PpIX production in these two cell lines on substrates of varying stiffnesses showed that the mechanical properties of the underlying matrix affected each cell line differently. In the U118 cell line, a stiffer microenvironment led to increased PpIX accumulation with no change in the rate of cell growth [135]. In contrast, substrate stiffness had no significant effect on PpIX accumulation in the U373 cell line (**Figure 2.2b**) [135]. In another study by Ulrich *et al*., micromechanical cues from the ECM on glioma cells were evaluated by testing various ECM substrates with different mechanical and biochemical properties. It was found that ECM elasticity strongly affects glioma cell structure, motility and proliferation [136]. These findings highlight the impact of the ECM on cell morphology, cytoskeletal organization, motility and control of MMII-mediated intracellular contractility [136]. Further studies must be done to clarify the effects of mechanical stiffness on PpIX production in glioma and other cell types.

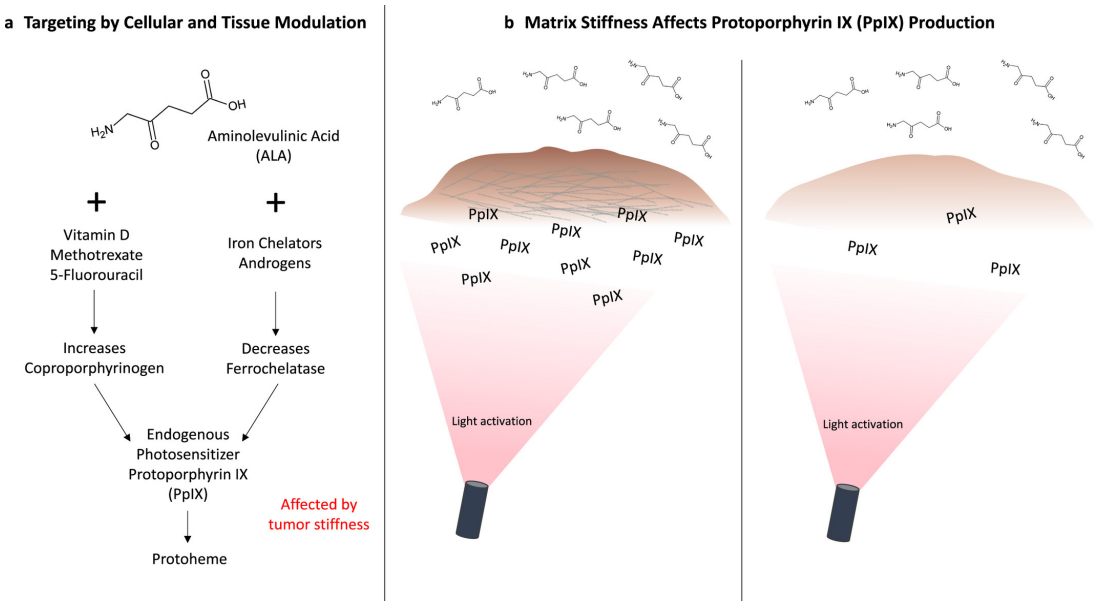

Figure 2.2: Protoporphyrin IX and Matrix Stiffness

(a) Summary of the pathways involved in targeting by cellular and tissue modulation, and (b) increased PpIX accumulation with higher substrate stiffness in glioma cells [134].

2.2.4 Functional Targeting

The TME acquires a unique set of biochemical traits which are closely connected to tumorigenesis [139]. While this distinct TME is linked to proliferation and metastasis, it also provides opportunities for the development of PSs that target these unique features through a strategy termed *functional targeting*. One aspect of functional targeting is the enhanced permeability and retention (EPR) effect, which causes an increase in nanoparticle accumulation and retention at the site of a tumor due to hyperpermeable tumor vasculature and insufficient lymphatic drainage. This phenomenon has been exploited for cancer treatment through the design of nanomedicines for drug targeting to tumors, though there is significant heterogeneity that limits the influence of the EPR effect on drug localization [140-142]. Various photochemistry-based strategies have been employed to enhance the EPR effect

through vascular permeabilization to improve nanomedicine extravasation in tumors. PDT has also been used clinically to occlude vasculature, with the goal of restricting the supply of blood to the tumor. Other unique features of the TME that are leveraged to achieve *functional targeting* include hypoxic and acidic conditions (**Figure 2.3**). As discussed in a previous section, tumors develop hypoxic conditions due to an imbalance in oxygen supply and consumption [143]. The abnormal, disorganized vascular network that develops in the TME provides limited oxygen supply despite an increasing demand for oxygen generated by the rapidly growing tumor. One of the byproducts of the hypoxic microenvironment is the development of acidic conditions [144]. In the absence of oxygen, cancer cells use anaerobic glycolysis, leading to lactic acid production and a decrease in pH [145]. Interestingly, even when oxygen is abundant and mitochondria are fully functional, cancer cells can utilize aerobic glycolysis, producing lactate despite the availability of oxygen. This is termed the Warburg effect, first described in the 1920s by Otto Warburg [146]. This section will discuss functional targeting, through which the unique features of the TME, such as abnormal vasculature, acidity and hypoxia, can be leveraged to achieve targeted PDT.

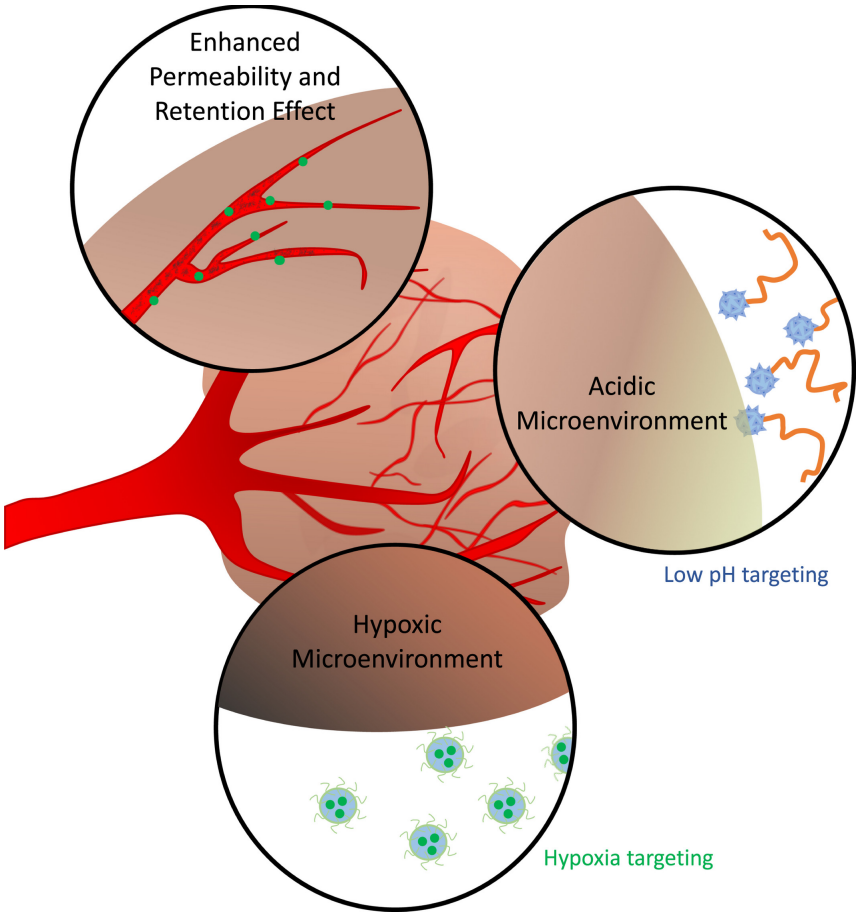

Figure 2.3: Mechanisms of functional targeting of photodynamic therapy Characteristics of the TME that are exploited for functional targeting.

2.2.4.1 Exploiting the enhanced permeability and retention effect and targeting the tumor vasculature

The EPR effect is a feature of the TME that is characterized by abnormally high leakage of blood plasma components from the tumor vasculature, as well as their increased retention in tumors [147]. Enhanced vessel wall permeability arises from the unique physiology of the tumor vasculature. Normal vasculature in healthy tissues is hierarchically organized, enabling the efficient delivery of oxygen and nutrients [148].Tumor vasculature, on the other hand, is disorganized, tortuous and hyperpermeable. The development of this vasculature occurs through aggressive

cancer cell growth and overexpression of proangiogenic factors to accommodate their high metabolic needs [147-149]. Tumor vessels are also immature, lacking a normal basement membrane, smooth muscle cells, and pericytes. Immature vessels, in combination with the presence of large fenestrations, cause hyperpermeability of the tumor vasculature to macromolecules and nanoparticles [148,150-152]. This enhanced extravasation is accompanied by poor lymphatic clearance, leading to the enhanced retention of extravasated particles [147,151]. The vasculature in most nonpathological tissues is less permeable than tumor vasculature, attenuating drug accumulation in healthy tissues [153] Therefore, the hyperpermeability of tumor vasculature and insufficient lymphatic drainage in tumors, in contrast to normal tissues, drive the EPR effect, which has been exploited for the selective delivery of anticancer drugs to tumor tissues [152].

The EPR effect is closely related to high interstitial fluid pressure (IFP) in tumors. The immature, hyperpermeable vasculature allows for extravasation of plasma fluid and proteins into the interstitial space, and the lack of lymphatic drainage prevents clearance, causing the fluid to accumulate [140,153]. Additionally, as the tumor grows, it compresses lymphatic vessels, further decreasing drainage of interstitial fluid [153,154]. As a result, while the IFP in normal tissue is around zero or slightly negative, tumor IFP is significantly higher and can reach above 90 mmHg [155]. High IFP at the tumor site hinders the EPR effect through decreasing the pressure gradient in the interstitial space, thereby limiting the convective flow that is normally the dominant mechanism of transport in tissue for macromolecules and nanoparticles [154,156]. Therefore, a consequence of high IFP is heterogeneity in the

extent of the EPR effect, limiting nanoparticle drug delivery and causing differences in therapeutic outcomes between patients. This relationship was confirmed in a mathematical model developed by Stapleton *et al.* [157] that associated liposome accumulation to the transport properties of solid tumors. They found that variations in peak IFP can cause interpatient heterogeneity in liposome accumulation. To address the influence of abnormal vasculature on tumor IFP, antiangiogenic therapies have been developed to normalize tumor vasculature [158]. According to a model by Jain *et al. [159]* such antiangiogenic therapies can modulate the TME through increasing intratumoral convection and decreasing fluid convection into the peritumor tissue or fluid. Increasing intratumor convection improves drug penetration and distribution, while decreasing fluid convection out of the tumor decreases the likelihood of lymphatic metastasis, peritumor edema, and ascites formation.

Knowledge of the EPR effect has had widespread effects on the development of drug delivery systems for cancer, and various PS delivery vehicles have been developed that leverage the EPR effect to increase intratumoral PS accumulation [160]. Examples of nanoparticle delivery vehicles that have been employed for PS delivery include liposomes [161-165], quantum dots [166,167], viruses [168,169], virus-like particles (VLPs) [170,171], polymeric nanoparticles [172], silica nanoparticles [173,174], metal nanoparticles [175], carbon nanoparticles [176,177] and others [178-180]. While the EPR effect has been used as the foundation for the development of a myriad of nanoparticle drug delivery systems, it has shown limitations in clinical practice due to high heterogeneity [140]. Due to this heterogeneity, predictive nanotechnology is being developed to determine if a tumor is likely to accumulate

nanoparticle drugs through EPR [181]. For example, ferumoxytol (FMX), a 30 nm magnetic nanoparticle, when administered intravenously and visualized with magnetic resonance imaging (MRI), was shown to predict both the intratumoral accumulation of therapeutic nanoparticles, as well as their antitumor effect [182,183]. Such technology could be used to stratify patients based on EPR effect and therefore has significant implications for personalized medicine in oncology.

The heterogeneity of the EPR effect occurs due to a variety of parameters that can differ widely between tumors, such as vascular maturation, tumor cell density, type of cancer and IFP, among many others [140,184,185]. Additionally, there are key limitations in how the EPR effect is studied. For example, it has primarily been evaluated in implanted tumors rather than metastatic tumors, despite the fact that metastases account for 90% of cancer deaths [186,187]. Additionally, the EPR effect is primarily studied in animal models that poorly recapitulate human tumors [188]. Due to heterogeneity in the extent of the EPR effect, methods to improve permeability of tumor vasculature are of great interest for improving drug delivery and therapeutic outcomes. PDT has been utilized as a novel method to achieve this. For example, through understanding pharmacokinetics following PS administration, PS-light interval can be optimized to activate PSs while they are accumulated in specific compartments to increase permeability to macromolecules and nanoparticles [49,52,189-191]. Moreover, targeting moieties can be utilized to achieve accumulation of PSs in the tumor vasculature and perivascular tumor cells to enhance the EPR effect [192-194].

A study by Snyder *et al.* [56] explored the ability of low-irradiance PDT to permeabilize vessels to macromolecular agents, including fluorescent microspheres and liposomal doxorubicin (Doxil). Using a murine colon cancer model, when fluorescent microspheres were administered immediately following PDT, there was an increase in intratumoral accumulation of microspheres in the range of 0.1–2 μm. When using low fluence rate PDT prior to Doxil administration, there was a significant increase in Doxil content in tumors, as well as up to 80% long-term tumor control. Additionally, a study by Gil *et al.* [57] used PDT as a method to improve the delivery and efficacy of oncolytic vaccinia virus (OVV) to primary and metastatic tumors in mice. Tumors that received PDT treatment (128 J cm^{-2} at 14 mW cm^{-2}) 12 h prior to OVV administration had an over 10-fold increase in viral titers compared to the control tumors. However, PDT with other light doses (135 J cm^{-2} at 75 mW cm^{-2} and 48 J cm^{-2} at 7 mW cm^{-2}) was less effective, underscoring the importance of treatment optimization when using PDT to increase intratumoral accumulation of therapeutics.

While PDT alone can be used to permeabilize tumor vasculature, targeting moieties can be incorporated to increase binding affinity to target cells. For example, Zhen *et al.* [193] synthesized PS-encapsulated ferritin nanocages with peptides targeted to $av\beta_3$, an integrin that is overexpressed in neoplastic endothelial cells. When used prior to nanoparticle administration, these endothelium-targeted PSs caused an increase in nanoparticle accumulation in tumor tissues by ~20-fold. When targeted PDT was used prior to treatment with the anticancer drug Doxil in a xenograft breast cancer tumor model, an increase in treatment efficacy of 75.3% was

observed. SEM images confirmed that the increased nanoparticle accumulation could be attributed to large fenestrae in the endothelial walls. Additionally, Sano *et al.* [194] showed that photoimmunotherapy (PIT) can be used to achieve an increase in the EPR effect, termed the super-enhanced permeability and retention (SUPR) effect. Following the light activation of panitumumab-IR700 constructs that accumulated in perivascular tumor cells, they observed significantly higher extravasation of a variety of nanoscale particles. This is attributed to the ability of PIT to cause necrosis specifically in the antigen-expressing cancer cells in the perivascular space while leaving nearby normal cells unharmed [195].

Previous work has also demonstrated that PDT can cause time-dependent changes in tumor IFP, which is normally a barrier to EPR-mediated drug accumulation in tumors [154,156,196]. A study by Leunig *et al.* [196] showed that PDT caused an initial increase in tumor IFP immediately following light administration, but 24 h after PDT, tumor IFP dropped to 50% of the control in a hamster melanoma model. In another study, Perentes *et al.* [58] investigated the IFP alterations caused by PDT as well as the resulting changes in the accumulation of liposomal doxorubicin. The authors showed that low-dose photodynamic therapy (L-PDT) reduces tumor IFP without impacting normal tissue IFP. Additionally, when liposomal doxorubicin was administered following L-PDT treatment, the drug penetrated significantly deeper into the tumor tissue compared to the control. Recently, Cavin *et al.* [197] explored the mechanism through which L-PDT alters vasculature to modulate IFP. Using a pericyte and endothelial cell coculture, they found that PDT alters the function of pericytes, strengthening their association with endothelial cells. Tumor vasculature

typically has poor pericyte coverage [150], so increasing pericyte–endothelial cell association causes vascular normalization, leading to a decrease in IFP and an increase in convective transport of drugs into the tumor. These studies illustrate that PDT can have significant effects on tumor IFP, though the effects are dependent on many factors, including PS-light interval, light dose and PS dose.

In addition to permeabilizing the vasculature to improve drug accumulation, vascular-targeted PDT has also been used to cut off blood supply to the tumor [198-201]. WST-09 (Tookad, palladium bacteriopheophorbide) and WST-11 (Tookad soluble, Padeliporfin) are PS with limited extravasation from vasculature, enabling spatially selective photodamage by confining PDT-mediated toxicity to the vascular compartment. When activated by light, Tookad can cause vascular occlusion, resulting in tumor necrosis [202-205]. Clinical trials have confirmed that PDT using Tookad is a well-tolerated and effective approach for the treatment of prostate cancer [206-208]. In one clinical trial, 28% of patients who received vascular-targeted PDT experienced disease progression after 24 months, compared to 58% of patients who underwent active surveillance [207]. An extended follow-up study analyzed the same cohort and found that, at four years, patients who had received vascular PDT experienced significantly lower disease progression rates and were less likely to convert to radiotherapy (24% *versus* 53%) [208].

A primary, nononcologic, application of PDT for vascular occlusion is in the treatment of age-related macular degeneration (AMD), the leading cause of blindness in elderly adults in western countries [209,210]. The neovascular form of AMD (also known as exudative or “wet”) leads to the formation of aberrant blood vessels from

the choriocapillaris under the foveal avascular zone below the retina (subfoveal choroidal neovascularization, CNV). These leaky blood vessels can cause loss of vision through subretinal hemorrhage and detachment of the retinal pigment epithelium [209]. Although thermal photocoagulation has been used as a primary treatment method for destroying CNVs, this treatment method has drawbacks, including retinal scar formation and immediate loss of visual acuity [210,211]. Preclinical and clinical studies demonstrated that CNV occlusion and improvements in visual acuity were achieved by activating intravenously administered BPD with nonthermal laser irradiation at short PS-light intervals (while the PS is in the vasculature) [71,212-216] to cause thrombosis of vessels and selective damage to endothelial cells [211]. Vascular-targeted PDT with a liposomal formulation of BPD, Visudyne, is approved worldwide for the treatment of wet AMD and has been used in millions of patients. PDT can therefore have multiple effects on the vasculature, including permeabilization and occlusion, depending on treatment parameters. This underscores the necessity for carefully optimizing vascular-targeted PDT treatment regiments to achieve specific, desired effects.

While PDT has great potential in the clinic to induce cytotoxicity in cancer cells, it has also emerged as a promising modality to improve the extravasation of nano- and microscale agents at the tumor site. This has been achieved either through targeting the vasculature directly, or through targeting the cells in the perivascular space. Additionally, localization of PS in specific regions, such as vasculature or perivascular cancer cells, can be achieved through the use of targeting moieties as well as through the optimization of PS-light interval. While preclinical studies are

promising, there is more work that must be done to bring this treatment strategy from benchtop to bedside. For example, light delivery methods can be further engineered to ensure that light is delivered uniformly to maximize access to target tissues. Additionally, the parameters for PDT treatment must be further optimized to improve drug delivery. For example, varying PS concentration and the amount of light delivered to the vasculature could potentially change the size and number of fenestrations created in the endothelial walls. Optimizing these parameters is critical because nanomedicines vary in size. Similarly, the optimal time after PDT to administer nano- and microscale therapeutics could differ based on particle size, so more work should be done to characterize this thoroughly. Moreover, combinational treatment regiments that pair carefully optimized EPR-enhancing PDT with nanoscale therapeutics still need to be evaluated in clinical trials to determine if this strategy can successfully overcome the heterogenous EPR that often limits nanomedicine efficacy. Overall, due to the potential of PDT as an adjuvant to nanoscale cancer drugs, the development of these technologies could have extremely widespread implications for cancer therapeutics.

2.2.4.2 Targeting the hypoxic microenvironment

Another feature that can be exploited for PS targeting is the hypoxic TME. Piao *et al.* [217] developed a PS that can only be activated under hypoxic conditions, such as those in solid tumors. They conjugated an azo moiety to a seleno-rosamine dye, blocking intersystem crossing and therefore blocking singlet oxygen generation. Under low oxygenated conditions, the moiety is cleaved from the dye, allowing

singlet oxygen generation upon light activation. The drug, therefore, has increased specificity for the hypoxic TME, where it can be light-activated.

Additionally, PDT can induce hypoxia in tumor tissues through both reducing vascular perfusion and consuming oxygen [55]. One study by Busch *et al.* [218]investigated how two different fluence rates, 38 and 75 mW cm^{-2}, differentially impacted Photofrin-PDT-mediated oxygen depletion. They found that in tumors treated with 75 mW cm^{-2}, there was significant hypoxia, even tissues in close proximity to the blood supply (vascular-adjacent tissues). Alternatively, in tumors treated with 38 mW cm^{-2}, there was an insignificant increase in hypoxia in vascular-adjacent tissues. The oxygen consumption associated with PDT presents an issue for repeated PDT treatments, where decreasing oxygen levels in the tissues might diminish the efficacy of subsequent treatments. While this oxygen consumption can exacerbate hypoxia-associated proliferation and metastasis, some groups have taken advantage of this by developing treatments that incorporate both PSs and hypoxia-activated prodrugs for a synergistic effect. For example, Feng *et al.* [219] developed a liposome containing chlorin-6 in the hydrophobic bilayer and AQ4N in the core. Chlorin-6 is a second-generation PS that is activated by 660 nm light, and AQ4N is a hypoxia-activated prodrug. In hypoxic conditions, nontoxic AQ4N is reduced first to AQ4M, then to AQ4, which intercalates DNA to inhibit topoisomerase II [220]. They found that following irradiation of the liposome, chlorin-6 is activated, inducing severe hypoxia. These hypoxic conditions catalyzed the activation of AQ4N, leading to significantly decreased tumor volume in a mouse model.

Similarly, Liu *et al.* [221] used upconversion nanoparticles (UCNPs) to encapsulate both a PS, silicon phthalocyanine dihydroxide (SPCD), and a bioreductive prodrug, tirapazamine (TPZ). Tirapazamine generates cytotoxic free radicals, which in aerobic conditions are oxidized back into the harmless parent compound. However, under hypoxic conditions, TPZ becomes highly reactive and causes strand breaks in DNA [222]. Liu *et al.* [221] found that under normal physiological oxygenation conditions, TPZ had little cytotoxicity, but following PDT-induced hypoxia, TPZ toxicity increased significantly. These studies illustrate that PSs can be functionally targeted to the hypoxic TME conditions, inducing specific toxicity.

Moreover, there are many studies that show that the therapeutic effect of PDT can improve when combined with methods for decreasing hypoxia [223,224]. Some methods focus on increasing the oxygen concentration by using oxygen carriers such as artificial red blood cells that contain PSs [225-227]. Mild heating also improves the intertumoral blood flow in PDT. The process is called photothermal therapy (PTT) in which the rapid increase in temperature above the threshold value of 42–45 degrees Celsius can kill cancer cells [228]. Performing fractional PDT treatment can also minimize the dependence on oxygen by allowing time for the replenishment of tissue oxygen [229].

2.2.4.3 Targeting the acidic microenvironment

The low pH of tumors has also been exploited in the development of functionally targeted PSs. For example, Luo *et al.* [230] developed a self-transformable pH-driven membrane anchoring photosensitizer (pHMAPS) for acidic

selectivity. The pHMAPS incorporates pH low insertion peptide (pHLIP), which adopts a random coil configuration in neutral physiological pH (~7.4), but changes conformation in a more acidic pH to an α-helix structure. This conformational change induces insertion into the cell membrane for selective delivery of the PS to cells in acidic environments such as the TME [230,231]. In an *in vivo* biodistribution analysis, pHMAPS localization was compared to a peptide without the ability to change conformation, nonmembrane anchoring photosensitizer (NMAPS). They found a significantly higher accumulation of the pHMAPS in the tumor compared to NMAPS, demonstrating successful targeting of the acidic TME.

Another study that leveraged the unique properties if pHLIP was done by Yu *et al.* [232], in which pH-responsive hollow gold nanoparticles loaded with PSs were synthesized to target the acidic microenvironment. In this study, pHLIP was conjugated to the nanoparticle surface for selective delivery to cells at low pH. Upon light activation, the nanoparticles produce heat for photothermal therapy and release the PS, chlorin-6. Following release, chlorin-6 interacts with oxygen in surrounding tissues to generate reactive oxygen species (ROS) for PDT.

Han *et al.* [233] engineered a chimeric peptide, PAPP-DMA, for targeted uptake by cells in the acidic TME. The peptide contains PpIX conjugated to a nuclear localization sequence (NLS) that has been modified with a negatively charged 2,3-dimethylmaleic anhydride (DMA). DMA detaches in acidic pH, increasing the charge of the peptide. This charge increase potentiates higher electrostatic interactions with the negatively charged cell membrane, facilitating internalization of the drug. Following cellular uptake, subcellular targeting of the nucleus is achieved through the

NLS. This targeting strategy employs multiple layers of specificity to achieve cellular uptake in acidic conditions, as well as subcellular specificity to translocate the PS to the nucleus for light-activated DNA damage. Gao *et al.* [234] also leveraged a masked targeting peptide to target the acidic TME. They decorated the surface of a PS-loaded polymeric nanoparticle with TAT, a cell-penetrating peptide [235]. To create specificity for low pH, the TAT peptide was modified with 2,3-dimethylmaleic anhydride to mask the cell-penetrating activity. Acidic pH reactivates the peptide's targeting activity, facilitating nanoparticle internalization by cells in the TME. Overall, these studies illustrate that biochemical interactions between the acidic TME and drug delivery vehicles can be leveraged to enable improved drug delivery to tumors.

2.2.4 Nanocarriers for Photosensitizer Targeting to Cancer and Stromal Cells

Nanotechnology-assisted PS delivery to tumors relies on the passive accumulation of PS-nanoparticle conjugates due to the EPR effect. However, upon accumulation at the tumor site, the PS can interact nonspecifically with cells in the TME. To achieve higher specificity for target cells and avoid damage to nearby healthy tissue, nanoparticle surfaces have been functionalized with various targeting moieties for molecular recognition. These functionalized nanoparticles rely on the high expression of molecular targets on the surface of target cells for specific delivery (**Figure 2.4**). Targeting moieties used for this purpose include folic acid, peptides, antibodies and carbohydrates [236-249] (**Table 2.2**), and can be either conjugated to a nanoparticle or directly to a PS.

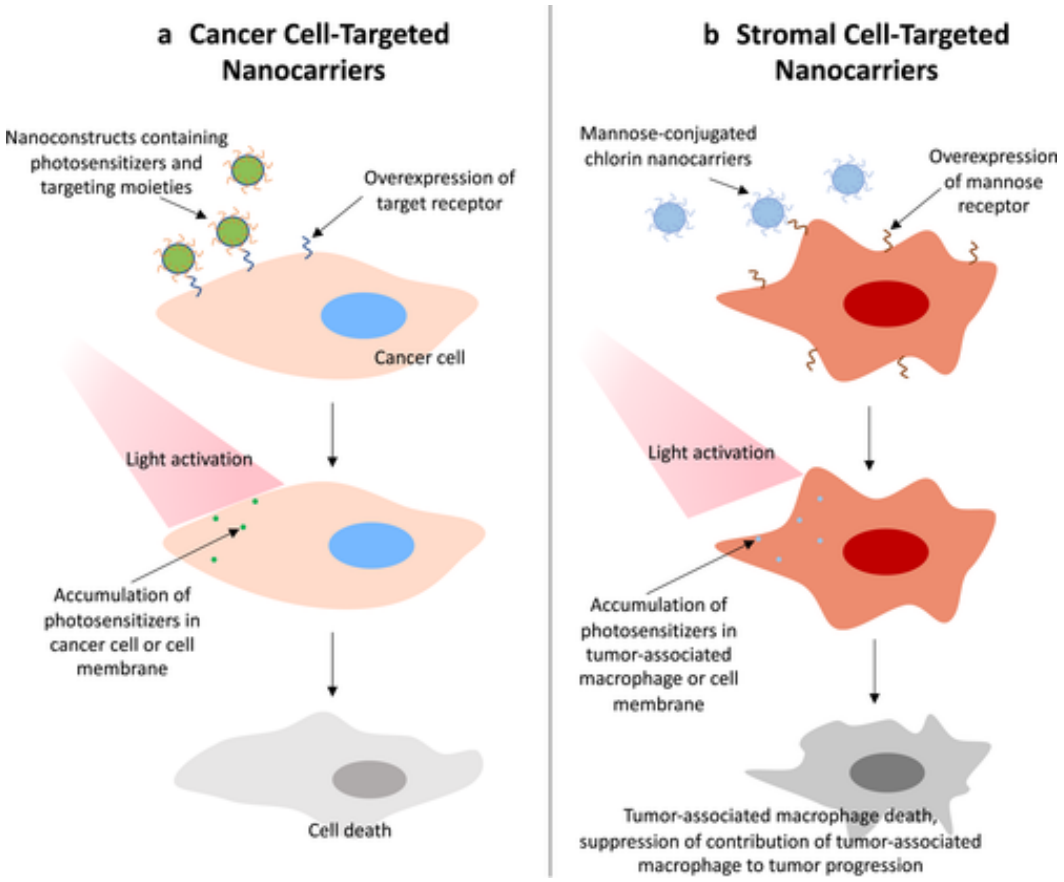

Figure 2.4: Cancer cell-targeted and stromal cell-targeted nanocarriers.

Depiction of the interactions between targeted photoactivatable nanocarriers and (a) cancer cells or (b) tumor-associated macrophages [240].

Table 2.2: A summary of various types of targeting moieties and details regarding their use.

Targeting moiety	Nanoparticle or molecule to which the moiety is conjugated	Target receptor	Target disease	References
Folic acid	Porphyrin-lipid nanoparticles (porphysomes), Hollow mesoporous silica nanoparticles, poly(lactic-co-glycolic acid) (PLGA) nanoparticles	Folate receptor	Lung cancer, Skin cancer, Colorectal cancer	[243-245]
Peptides and Proteins	Gold nanoparticles, PLGA nanoparticles	T antigen, $\alpha_v\beta_3$, EGFR	Colon cancer, Breast cancer, Melanoma, Glioma	[242,246,247]
Antibodies	Gold nanoparticles, Liposomes, PLGA nanoparticles	HER-2, EGFR	Colon cancer, Breast cancer, Epidermoid carcinoma, Ovarian cancer, Glioblastoma	[236,242,248,249]
Carbohydrates	Chlorin, Nanomicelles, Gold nanoparticles, PLGA nanoparticles	Mannose receptor, Galectin-1, CD44	Gastric cancer, Colon cancer, Breast cancer, Oral squamous cell carcinoma	[238-241]

Most PDT treatments that incorporate such targeting moieties are designed to directly target cancer cells. Selectively killing cancer cells can attenuate growth-

induced solid stress, which is generated through interactions between structural components of the microenvironment [250]. By attenuating growth-induced solid stress, cancer cell targeting can modulate the mechanical properties of the TME. Additionally, the noncancerous cellular components of the stroma can contribute to cancer progression and the mechanical stresses on the tumor. For example, CAFs and TAMs play key roles in tumor evolution through increasing malignant potential and chemoresistance [251]. The noncancerous cells in the tumor stroma are therefore attractive targets for cancer therapies, and PS delivery vehicles have been designed with targeting moieties against noncancerous stromal cells.

One method for cancer cell targeting is using carbohydrates as targeting moieties. Carbohydrates have a high binding affinity to lectins, which are endogenously overexpressed on the surface of cancer cells as well as noncancerous stromal cells [252]. A recent study in 2018 by García Calavia *et al.* [239] demonstrated that carbohydrates can serve dual functions as both targeting moieties and nanoparticle stabilizers. The investigators synthesized gold nanoparticles conjugated to zinc phthalocyanine, and the carbohydrate, lactose. Here, lactose conjugated to the surface was effective as a targeting moiety for the galectin-1 receptor on breast cancer cells and also helped to stabilize the nanoparticle in aqueous solutions. This is an example of "direct lectin targeting," where an exogenous carbohydrate is incorporated into the drug delivery system to target endogenously expressed carbohydrates. The binding affinity between carbohydrates and lectins can also be leveraged by decorating the nanoparticle surface with lectins in order to target carbohydrates overexpressed on the surface of cancer cells. This strategy is termed

"reverse lectin targeting" [253]. The latter strategy was investigated in a study by Obaid *et al*. [242] that compared using lectin for carbohydrate-targeted nanoparticles with using antibodies for protein receptor-targeted nanoparticles. To study this, gold nanoparticles were functionalized with either the lectin, jacalin or a monoclonal antibody. Both constructs used zinc phthalocyanine (C11Pc) as the PS, and efficacy of the constructs was evaluated in multiple cancer cell lines: HT-29 colon cancer cells and SK-BR-3 breast cancer cells. Here, the jacalin was used to target the cell surface molecule Thomsen–Friedenreich carbohydrate antigen (T antigen), and the monoclonal antibody was specific to HER-2. Results from this study demonstrated that PDT toxicity *in vitro* was comparable between both conjugates in both cancer cell lines, illustrating that targeting carbohydrates with lectins and targeting transmembrane proteins with antibodies can elicit similar toxicities when combined with PDT. The authors suggest that this outcome may be explained by the different binding affinities and cell surface receptor densities. While the dissociation constant of jacalin binding to HT-29 cells is higher than that of anti-HER-2 antibodies binding to SK-BR-3 cells, the HT-29 expression of T antigen is higher than the SK-BR-3 expression of HER-2 receptors. Thus, both binding affinity and target expression are critical parameters for the design of targeted nanotherapeutics.

Another common targeting moiety that is used to decorate the surface of nanoparticles is folate, which specifically targets folate receptors [243-245]. The folate receptor is a GPI-anchored cell surface receptor that is overexpressed in many cancers, making it an attractive receptor for targeted therapies [254]. The receptor is responsible for mediating the intracellular transport of folate via receptor-mediated

endocytosis. In a study by Kato *et al.* [243] folate receptor-targeted porphysomes were synthesized and studied as a lung cancer treatment *in vitro* and *in vivo*. In an orthotopic lung tumor model, both the nontargeted porphysomes and folate-targeted porphysomes (FPs) had higher accumulation in the tumor compared to the healthy lung tissue, but FP administration led to higher intracellular PS accumulation. This study illustrates that nanoparticles with and without targeting moieties are able to accumulate preferentially at the tumor, but the targeting moieties are key for improving uptake by target cells.

Similarly, peptides can also be conjugated to the nanoparticle surface to achieve tumor-specific drug delivery. The use of peptides for targeting has several potential benefits over antibodies, including lower risk of immune reactivity, smaller size, high stability and simple synthesis [255,256]. In a study by Sebak *et al.* [246], the peptide, cyclic (Arginine-Glycine-Aspartic acid-D-Tyrosine-Lysine) (cRGDyk), was conjugated to PLGA nanoparticles. The cRGDyk peptide served dual functions in this construct as both a targeting moiety and a quenching agent. Quenching agents like this are attractive features for PDT because they attenuate singlet oxygen generation outside of the tumor site, thereby improving specificity and limiting off-target cytotoxicity [257]. In another study, Gao *et al.* [258] investigated the effects of $\alpha v\beta_6$ integrin-targeted PDT on host immune response. The authors demonstrated that integrin-targeted PDT using IRDye700-streptavidin–biotin–HK peptide (DSAB-HK) could both inhibit tumor growth and stimulate the host antitumor response by promoting dendrite maturation and T-lymphocyte recruitment. While PDT can be used to target integrins for cancer cell destruction, PDT has also been shown to

modulate integrin expression in cancer cells. One study showed a significant reduction in the protein and mRNA expression of FAK and β1-integrin 12 h after PDT [259]. Similarly, Runnels and colleagues have shown that BPD-mediated PDT at a mild dose (0.5 J cm^{-2}) induces the loss of β1 integrin-containing focal adhesion plaques [72]. Because BPD was shown to localize in the mitochondria with no marked fluorescence at the membrane, and β1-containing integrins seemed to be structurally intact after photosensitization, the authors suggest that the PDT-mediated loss of integrin function occurred through intracellular damage rather than direct photodamage.

While the vast majority of targeted PDT strategies have focused on targeting cancer cells, there are a variety of stromal cells that contribute to cancer progression. TAMs are known to promote cancer proliferation and metastasis through a variety of mechanisms including inflammatory cytokine release, increased angiogenesis, suppression of T-cell response and ECM remodeling [260,261]. Due to the role of TAMs in ECM remodeling, strategies that target these tumor-promoting immune cells could potentially impact the stiffness of the TME.

Previous work by Hayashi *et al.* [240] has demonstrated that PDT can be used to target TAMs. The authors synthesized mannose-conjugated chlorin (M-chlorin) to target the overexpressed mannose receptors on TAMs (**Figure 2.4**). While these constructs were initially designed for specific toxicity in TAMs and not cancer cells, it was found that M-chlorin-PDT conferred cytotoxicity to tumor cells to a similar degree in vitro as the cancer cell-targeted control, glucose-conjugated chlorin (G-chlorin). This was attributed to the expression of mannose receptors on cancer cells.

However, *in vivo* studies showed that M-chlorin PDT led to significantly more tumor suppression than G-chlorin PDT, which was attributed to the affinity of M-chlorin for CD-206 expressing TAMs in addition to cancer cells. These results suggest exciting opportunities for future studies that target multiple cell types with a single targeting moiety to achieve enhanced antitumor effect. Such constructs could potentially achieve synergistic cytotoxicity by killing cancer cells as well as the nonmalignant cells that contribute to tumor maintenance, thereby providing an inherent mechanism for managing the cancer cells that survive initial treatment. Similarly, Wen and colleagues used a natural noninfectious nanocarrier, cowpea mosaic virus (CPMV), to target TAMs [262]. CPMV has been shown to have a preference for M2-polarized macrophages. However, they also have affinity for vimentin, which is overexpressed in certain epithelial cancers, including prostate cancer, gastrointestinal tumors, breast cancer, and lung cancer [263]. According to the results of the study, the PS-CPMV nanoconstruct (zinc ethynylphenyl porphyrin conjugated CPMV/ dendron hybrid) was effective on both cancer cells and macrophages but did not favor the M2 subpopulation, despite previous work suggesting that CPMV has a preference for M2-polarized macrophages [262].

2.2.5 Development and Applications of Photoimmunotherapy Technology

PIT is a form of targeted PDT that leverages the molecular targeting capabilities of antibodies and the selective phototoxicity of PSs to achieve cell-specific drug delivery. This is achieved through the synthesis of photoimmunoconjugates (PICs), which are drug conjugates composed of antibodies and PSs. Cell targeting is typically dependent on the presence of membrane proteins

that are differentially expressed on diseased versus normal tissue [264]. Ideally, these membrane proteins should have lower expression, or none at all, on healthy cells in order to maximize specificity and minimize systemic toxicity. An antibody binding to a target can trigger receptor-mediated endocytosis, followed by proteolytic cleavage to degrade the conjugate and release the PS [265]. Subsequent light irradiation leads to phototoxicity [264] (**Figure 2.5**). Some of the cell surface receptors that serve as targets for PIT are also implicated in metastasis and proliferation. Depending on the dose, binding of the PIC can also inhibit activation of these pathways. Therefore, PICs can serve dual functions through receptor inhibition and selective delivery of the PS for PDT [266].

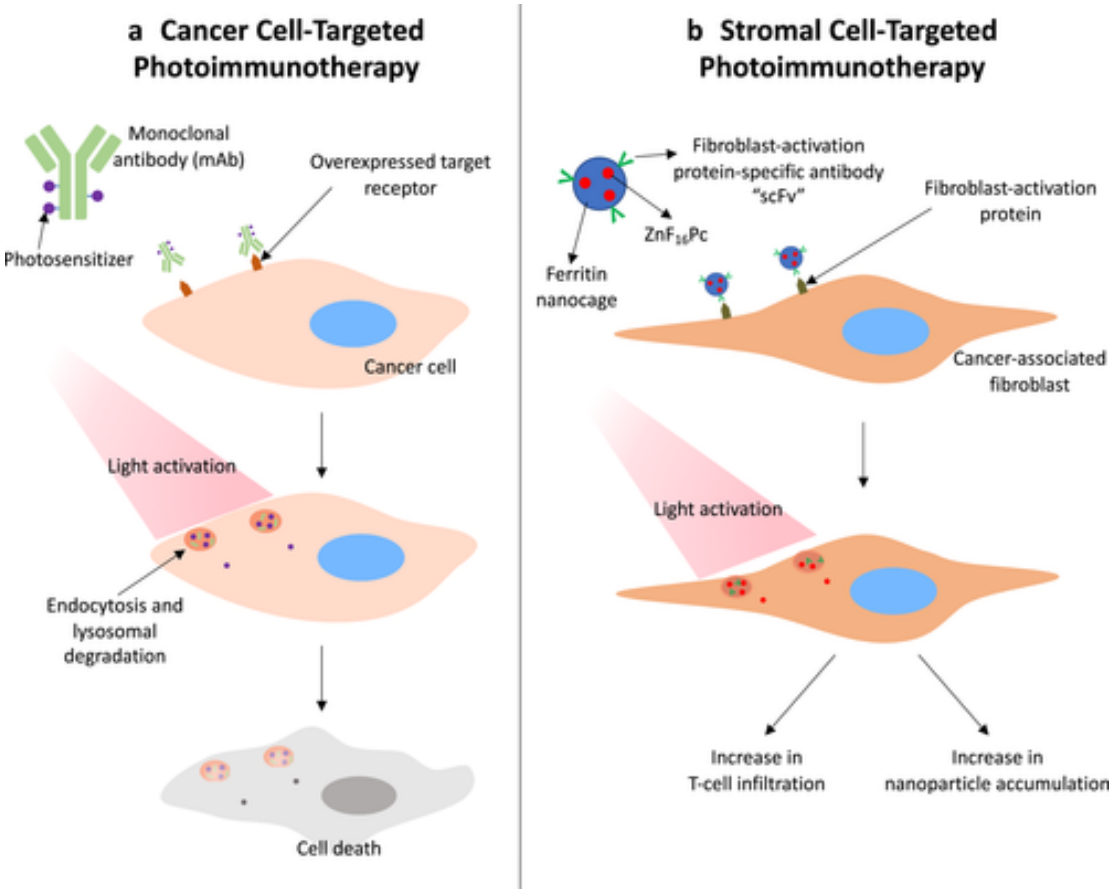

Figure 2.5: Photoimmunotherapy targeted to cancer cells and stromal cells.

(a) Schematic of photoimmunoconjugate uptake by a cancer cell. The antibody binds to the target cell and is internalized by receptor-mediated endocytosis. At certain photosensitizer:antibody ratios, lysosomal degradation mechanisms can be leveraged to dequench the photosensitizer, allowing for light activation. Following light activation, reactive molecular species are generated to induce cytotoxicity in target cells. (b) Cancer-associated fibroblast-targeted photoimmunotherapy and the associated effects on the TME [267,268].

PIT was first described in 1983 in the lab of Julia Levy by Mew *et al.* [269]. It was discovered that by conjugating the PS, hematoporphyrin, to monoclonal antibodies specific for myosarcoma, it was possible to more significantly inhibit cancer growth *in vivo* than treatment with either monotherapy alone, as well as treatment with the unconjugated antibody and PS, where all groups were light-activated. This study demonstrated for the first time that PICs can selectively enhance photodestruction of tumors. This discovery led to the development of many PICs incorporating a variety of antibody-PS combinations [270-274].

For example, in elegant work by Savellano and colleagues [275], the PIC conjugation and purification processes were optimized to produce highly pure PICs composed of the EGFR-specific antibody, C225, and the PS, BPD. Their optimization overcame previous issues with PIC development, including large amounts of impurities (unconjugated PSs), as well as the presence of insoluble aggregates. These issues presented a significant problem for earlier studies, because the therapeutic effects of the PICs cannot be clearly distinguished from the effects of the aggregates and impurities [275]. In another study, Mitsunaga *et al*. [276] synthesized PICs composed of EGFR-specific monoclonal antibodies (trastuzumab and panitumumab) and the PS, IRDye 700DX (IR700). It was shown that cytotoxicity was only conferred to EGFR-expressing target cells, demonstrating the selectivity of the conjugate. The authors hypothesized that fluorescence generated from light-activation

of the PIC could be used for theranostic applications. Similarly, Spring and colleagues used the Cet-BPD PIC developed by Savellano and colleagues to target EGFR expressing ovarian cancer micrometastases. In this PIC, the BPD molecules are self-quenched and not photoactivatable until they are internalized and proteolytically cleaved in target cells, further enhancing PIT selectivity and limiting off-target toxicity [277].

PIT has also been shown to trigger host antitumor immunity. A recent study by Ogawa *et al.* [278] explored a mechanistic understanding of cell death following PIT with mAb-IR700 PICs. The authors suggest that, unlike conventional PDT which is dependent on the generation of reactive oxygen species, cytotoxicity induced from PIT using near infrared light (NIR-PIT) is a result of membrane destabilization followed by water influx and cell bursting. This also elicits the maturation of immature dendritic cells, creating a concurrent immunological response to the tumor. A follow-up study was conducted to explore the cause of membrane destabilization [279]. It was shown that upon activation with NIR light, axial ligands on IR700 dissociate, decreasing the hydrophilicity of the dye. The authors postulate a conformational change in PIC–antigen complexes following PIT that confers stress to the cell membrane, resulting in water influx and cell bursting.

While PIT has been primarily targeted to malignant cells, it can also be used to target cancer-associated stromal components in the TME. For example, work by Zhen *et al.* [267] demonstrates that CAFs can be targeted using PIT. CAFs are present in the tumor stroma and support tumor growth and metastasis by remodeling the ECM and secreting growth factors, cytokines and chemokines [280]. In this study,

ferritin, which serves as a cage for the PS, $ZnF_{16}Pc$, is coated with fibroblast activation protein (FAP)-specific single-chain variable fragment (scFv) to target FAP, a protein overexpressed on the surface of CAFs. One particular feature of CAFs that the authors were interested in studying was CAF-mediated T-cell exclusion. By this mechanism, CAFs are able to prevent T cells from reaching the tumor through either the deposition of a dense ECM, or the production of CXCL12. It was found that CAF-targeted PIT led to a significant increase in T-cell infiltration into the tumor, demonstrating that PIT can be used to modulate the tumor stroma and potentiate an immune response (**Figure 2.5**). Importantly, the ECM deposited by CAFs is also known to provide a critical barrier to nanoparticle delivery to tumor cells [281]. Therefore, Li *et al. [268]* investigated the effect of CAF-targeted PIT on nanoparticle delivery to 4T1 tumors. The authors found that by treating with CAF-targeted PIT two days prior to nanoparticle injection, intratumoral nanoparticle accumulation was improved in a particle size-dependent manner. While the effects of CAF-targeted PIT on stromal properties have been investigated, more work is required to evaluate the impact of these treatments on the mechanical properties of the TME, as well as the inverse.

While PIT is a powerful tool for targeted PS delivery, PICs have several limitations, including a relatively low PS-to-antibody ratio (typically 2–7 PSs per Ab), poor intracellular PIC accumulation and limited target presentation on cells. However, PIT can be interfaced with nanotechnology to overcome these limitations. We have previously shown that multiple PICs can be conjugated to nanoparticles (PIC-NP) for enhanced PIC uptake, as has been shown in ovarian cancer and

glioblastoma cells [236]. PIC-NP increases the intracellular accumulation of PIC in cancer cells by at least twofold compared to PIC alone, which was attributed by the authors to the "carrier effect." This phenomenon describes the indirect endocytosis of multiple PICs that are conjugated to the nanoparticle surface. Therefore, one binding event between an antibody and a target cell leads to the uptake of multiple antibodies, each with multiple PSs.

2.3 Prostaglandin E2 Receptor 4 (EP4)

2.3.1 EP4 and Tumorigenic Signaling

EP4 is a G protein-coupled transmembrane protein that is linked to cyclic adenosine monophosphate (cAMP) production, protein kinase A (PKA) signaling, and phosphoinositide-3-kinase (PI3K) activation [282]. EP4 activation is closely linked to the inflammatory enzyme cyclo-oxygenase-2 (COX-2). The pathway begins with the conversion of plasma membrane phospholipids to arachidonic acid (AA) by phospholipase A (PLA2). AA is converted to prostaglandin E2 (PGE2) by the enzymatic activity of COX and PGE synthase enzymes [283]. PGE2 is then effluxed out of the cell via multiple drug resistance-associated protein 4 (MRP4), where it binds to prostaglandin E2 receptors (EP1-4) on the cell surface [284].

EP4 is expressed on various cell types including cancer cells, fibroblasts, and immune cells. Activation of EP4 has been linked to the onset and progression of multiple cancers including breast, colorectal, lung, prostate, ovarian, gallbladder, T cell leukemia, and renal cancers [285]. One of the preeminent roles of EP4 involves suppression of anti-tumor immunity through its expression on cells of the immune system including leukocytes, mononuclear cells, macrophages, T cells, B cells, and

dendritic cells, among others [285]. EP4 expression on cancer cells also drives numerous cancer-associated processes including migration, proliferation, metastasis, angiogenesis and lymphangiogenesis [286,287].

2.3.2 Clinical Applications of EP4 Inhibition

Clinical data support the development of EP4-based therapies. A phase I study (NCT01968070) evaluated an EP4 antagonist (LY3127760) at 20, 60, 200, and 300 mg, compared to celecoxib, an FDA-approved COX-2 inhibitor, in healthy patients [288]. LY3127760 was well tolerated and there were no deaths or serious adverse events. Gastrointestinal symptoms including abdominal pain, nausea, and indigestion were most common adverse events. *Ex vivo* blood TNF-α release was used as a target engagement marker for EP4 antagonism. These data demonstrated statistically significant increases in TNF-α at all LY3127760 doses over 20 mg, while no notable changes in TNF-α occurred in celecoxib treated patients. Results of this study support further evaluation of LY3127760 for phase II trials.

Another study recently evaluated EP4 antagonism using the inhibitor, E7046, in patients with advanced cancers (NCT02540291) [289]. Treatment with E7046 once daily demonstrated manageable tolerability and no dose-limiting toxicities. Importantly, serum levels of T-cell recruiting chemokines (CXCL10 and CCL5) were significantly upregulated after 15 days of treatment compared to baseline levels. Paired tumor biopsies taken before and after treatment revealed significant increases in T cell localization in tumor tissues after treatment. Taken together, these data suggest potent immunomodulatory effects of EP4 inhibitors for patients with advanced malignancies. There are currently at least eight clinical trials

(NCT05358691, NCT05205330, NCT04975958, NCT03658772, NCT04344795, NCT04432857, NCT05191667, NCT04432857) investigating EP4 inhibitors in combination with immunotherapy (pembrolizumab, durvalumab, balstilimab, Atezolizumab), PI3K inhibitor (buparlisib), or chemoradiotherapy. This thesis provides the first evidence of successful combinational effects of EP4 inhibition and PDT using multiple photosensitizer formulations (photosensitizer, PIC).

2.4 Poly(ADP-Ribose) Polymerase (PARP) Inhibitors

2.4.2 Poly(ADP) Ribose Polymerase (PARP)

There are 17 known members in the PARP superfamily of proteins, which hold a diverse array biological roles in DNA repair, transcription, and chromatin modulation, among many others [290]. They act through the modification of acceptor amino acids on target proteins via covalent attachment of mono(ADP-ribose) and poly(ADP-ribose) (PAR) chains [291,292]. This process is catalyzed by the hydrolysis of nicotinamide adenine dinucleotide (NAD^+), generating nicotinamide as a byproduct. PARP-1 is most well-studied for its role in DNA single strand break repair, specifically with regards to base excision repair [290,291]. Evidence also suggests more extensive roles of PARP-1 in nucleotide excision repair, classical non-homologous end-joining, alternative non-homologous end-joining, microhomology-mediated end-joining, homologous recombination, DNA mismatch repair, and replication fork stability maintenance [291].

PARP-1 is comprised of a DNA binding domain, an automodification domain, and the catalytic domain [293,294]. The DNA binding domain is composed of zinc fingers which recognize DNA damage and activate PARP in response to single strand

breaks [291,293]. Following binding to DNA, PARP catalytic activity is initiated and PAR chains are covalently attached to PARP itself, histones and non-histone proteins [294] (**Figure 2.6**). Next, proteins that are involved in the DNA damage response bind noncovalently to PAR chains, thereby recruiting them to the DNA strand break site [294]. For example, X-ray repair cross-complementing protein 1 (XRCC1) associates with PAR chains through its central BRCT domain (BRCT1) [295]. XRCC1 is a critical DNA damage repair protein that functions as a scaffold for association with other DNA repair proteins, DNA polymerase (Polβ) and a DNA ligase (Lig3α) [295].

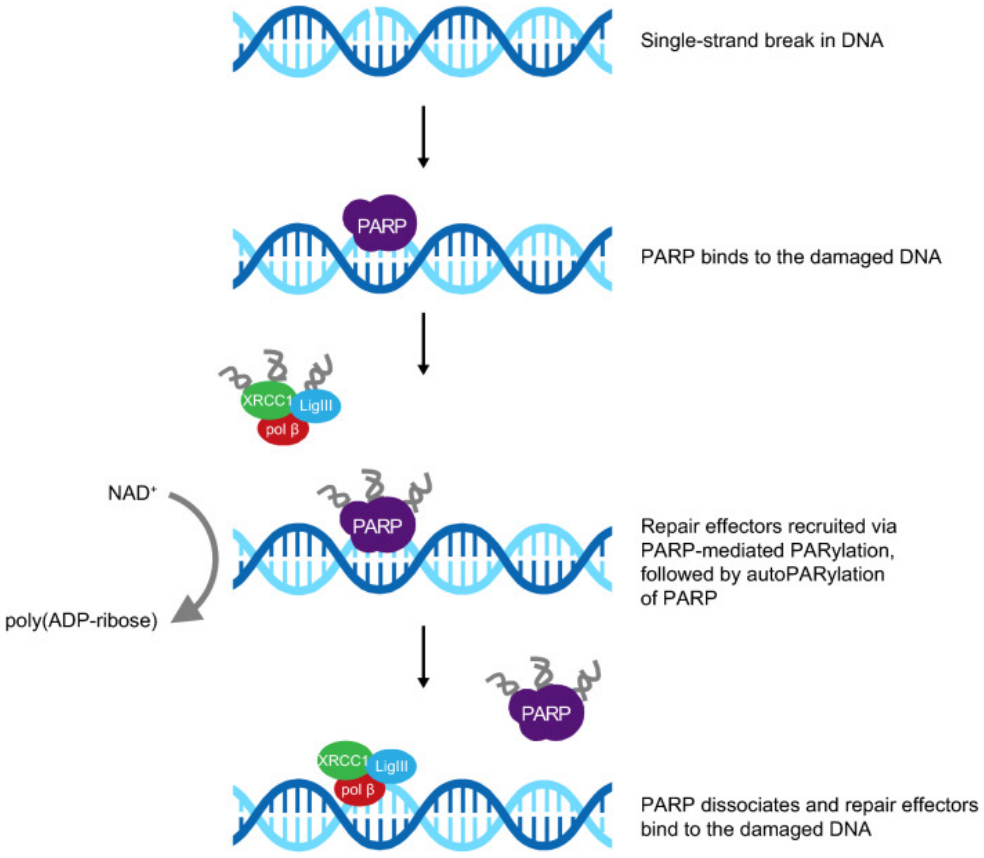

Figure 2.6: The role of PARP in base excision repair of single-strand breaks in DNA.[3]

[3] Figure and figure title adapted from Cortesi L, Rugo HS, Jackisch C. An Overview of PARP Inhibitors for the Treatment of Breast Cancer. Target Oncol. 2021 May;16(3):255-282. doi: 10.1007/s11523-021-00796-4. Open access (CC BY-NC 4.0).

PARP responds to single strand breaks by binding to the site of DNA damage. Auto-PARylation and trans-PARylation enable recruitment of effector proteins to repair the damaged segment of DNA.

2.4.3 Mechanism of PARP Inhibition

It was first discovered in 2005 that PARP inhibitors induce synthetic lethality in cells that are deficient in homologous recombination, particularly with regards to disfunction in BRCA-1 and BRCA-2 [296-298]. There are two proposed mechanisms through which PARP-mediated synthetic lethality arises: catalytic inhibition and PARP trapping. It was first proposed that PARP inhibitors prevent single strand break repair through competing with NAD+ at the PARP catalytic site. This catalytic competition leads to an accumulation of single strand breaks, which degenerate into double strand breaks. These double strand breaks are lethal to cells without effective homologous repair pathways, thereby explaining the synthetic lethality phenomenon. This hypothesis is challenged by the findings of Gottipati *et al*., who showed that PARP inhibition did not actually lead to an increase in DNA strand breaks [299].

According to the second hypothesis for PARP inhibitor-mediated cytotoxicity, PARP inhibitors trap PARP at DNA to produce lethal PARP-DNA complexes. Murai *at el.* [300] examined the association of PARP to DNA by quantifying nuclear-soluble versus chromatin-bound PARP1 in response to PARP inhibitors. They treated avian DT40 cells with olaparib in combination with alkylating agent, MMS, and found significantly enhanced levels of chromatin-bound PARP-1 with increasing concentrations of olaparib. In a follow-up study, Murai et al. compared the PARP trapping capabilities of three PARP inhibitors: olaparib, rucaparib, and BMN 673 (talazoparib) [301]. When investigating single agent toxicity in human cancer lines

EW8 and DU145, talazoparib was the most potent, with an IC_{90} 5-10 times lower than olaparib, where rucaparib did not reach an IC_{90}. They next examined PARP trapping efficiency by quantifying chromatin-bound PARP-1 and -2 following treatment with each PARP inhibitor from 0.1-10 μM. Western blotting data revealed that talazoparib was at least 100-times more potent as a PARP trapper than olaparib and rucaparib.

2.4.4 PARP Inhibitors in the Clinic

Currently, four PARP inhibitors are employed in the clinic in the United States and Europe: olaparib, rucaparib, niraparib, and talazoparib. Olaparib became the first clinically approved PARP inhibitor formulation in 2014, with approvals by the European Medicines Agency (EMA) and US Food and Drug Administration (FDA) [302]. EMA approval was granted for olaparib as a monotherapy maintenance treatment of BRCA-mutated high grade epithelial ovarian, fallopian tube, or primary peritoneal cancer patients who are in complete or partial response to platinum chemotherapy. FDA approval was granted for monotherapy olaparib treatment of BRCA-mutated advanced ovarian cancers that have been treated with at least 3 lines of chemotherapy. Since 2014, FDA approvals for olaparib have been extended for breast (2018), pancreatic (2019), and prostate cancers (2020).

Table 2.3: Summary of FDA and EMA approvals for PARP inhibitors.[4]

[4] Table reprinted from Rose, M.; Burgess, J.T.; O'Byrne, K.; Richard, D.J.; Bolderson, E. PARP Inhibitors: Clinical Relevance, Mechanisms of Action and Tumor Resistance. *Frontiers in Cell and Developmental Biology* 2020, *8*, doi:10.3389/fcell.2020.564601. Open access (CC BY).

PARP inhibitor	Approving organization	Year of approval	Indication	Mutational requirement	Relevant studies
Olaparib	FDA and EMA	2014	Advanced ovarian carcinoma	Germline BRCA1/2 Mutation	NCT0107662 (Kaufman et al., 2015)
	FDA and EMA	2017	Reoccurring ovarian, fallopian and primary peritoneal carcinoma	Independent of BRCA1/2 Mutational Status	SOLO-2 (Pujade-Lauraine et al., 2017) and Study 19 (Friedlander et al., 2018)
	FDA EMA	2018 2019	HER-2 negative breast cancer	BRCA1/2 Mutated	OlympiAD (Robson et al., 2017)
	FDA EMA	2018 2019	First-line treatment of advanced ovarian, fallopian and primary peritoneal carcinoma	Germline BRCA1/2 Mutation Complete or partial chemotherapy response.	SOLO-1 (Moore et al., 2018)
	FDA	2019	Metastatic pancreatic cancer	BRCA1/2 Mutated	POLO (Golan et al., 2019)
	FDA	2020	First-line treatment of advanced ovarian, fallopian and primary peritoneal carcinoma in combination with Bevacizumab	HRD-Positive Complete or partial chemotherapy response.	PAOLA-1 (Ray-Coquard et al., 2019)
	FDA	2020	Metastatic castration-resistant prostate cancer	HRD-positive	PROfound (de Bono et al., 2020)
Rucaparib	FDA EMA	2016 2018	Advanced ovarian carcinomas, following multiple chemotherapy treatments	BRCA1/2 Mutated	ARIEL2 and Study 10 (Oza et al., 2017)
	FDA EMA	2018 2019	Reoccurring ovarian, fallopian and primary peritoneal carcinoma	Independent of BRCA1/2 Mutational Status	ARIEL3 (Coleman et al., 2017)
	FDA	2020	Metastatic castration-resistant prostate cancer	BRCA1/2 Mutated	TRITON2 (Abida et al., 2019)
Niraparib	FDA and EMA	2017	Reoccurring ovarian, fallopian and primary peritoneal carcinoma	Complete or partial chemotherapy response.	ENGOT-OV16/NOVA Study (Mirza et al., 2016)
	FDA	2019	Reoccurring ovarian, fallopian and primary peritoneal carcinoma	HRD-positive Independent of chemotherapy response	QUADRA Study (Moore et al., 2019)
	FDA and EMA	2020	Advanced ovarian carcinomas and primary peritoneal carcinoma	Independent of biomarker status Complete or partial chemotherapy response.	PRIMA Study (Gonzalez-Martin et al., 2019)
Talazoparib	FDA and EMA	2018	Advanced or metastatic HER2-negative breast cancer	Germline BRCA1/2 Mutated	EMBRACA Study (Ettl et al., 2018)

In 2016, rucaparib received accelerated approval by the FDA for the treatment of BRCA-mutated advanced ovarian cancer patients that have been treated with two or more lines of chemotherapy. In 2020, based on the TRITON2 trial, approval of rucaparib was extended to *BRCA*-mutated, castration-resistant prostate cancer that has been treated with an androgen receptor-directed therapy and a taxane [303]. Niraparib was first approved by the FDA in 2017 for the maintenance treatment of recurrent epithelial ovarian, fallopian tube, or primary peritoneal cancers that are in response (complete or partial) to first-line platinum-based chemotherapy. Interestingly, niraparib was the first PARP inhibitor to not require biomarker testing or BRCA mutations.

FDA approval for niraparib was extended in 2019 for epithelial ovarian, fallopian tube, or primary peritoneal cancers that have received at least three prior lines of chemotherapy and have a homologous recombination deficiency. Approval

for niraparib was later extended in 2020 as a maintenance treatment for all women with epithelial ovarian, fallopian tube, or primary peritoneal cancers that are platinum-responsive, regardless of biomarker status. The most recently approved PARP inhibitor, talazoparib, was approved by the FDA in 2018 for BRCA-mutated, HER2-negative locally advanced or metastatic breast cancer.

Chapter 3: Sub-cytotoxic PDT (Photodynamic Priming, PDP) Harmonizes with EP4 Inhibitors to Attenuate Metastatic Phenotype in Ovarian Cancer Cells[5]

One of the major challenges in the treatment of advanced ovarian cancer is the development of metastatic lesions throughout the peritoneal cavity and its associated organs. This chapter reports the invention and development of a new combination of low dose PDT (PDP) EP4 inhibition to address this challenge. Benchmarks for success of this therapeutic strategy include inhibition of metastasis-associated behaviors and metastasis-associated cell signaling. These benchmarks are tested using immunoblotting, gap closure assay, and transwell invasion assay. Work in this chapter provides new knowledge indicating that the combination of PDP and EP4 inhibitor could play a major role in blocking ovarian cancer metastasis.

3.1 Introduction

PDP is a powerful tool that leverages subtherapeutic photochemistry alone or in combination with chemotherapy or radiation therapy for cancer treatment. Its mechanism of action relies on the light activation of a photosensitizer molecule and subsequent generation of ROS, resulting in biomolecule oxidation [304]. While the direct cell death brought about in this manner is associated with photodynamic therapy (PDT), PDP is achieved through sub-lethal effects [305]. These effects range

[5] Contents of this section are adapted from Sorrin, A.J.; Liu, C.; Cicalo, J.; Reader, J.; Najafali, D.; Zhang, Y.; Roque, D.M.; Huang, H.-C. Photodynamic Priming Improves the Anti-Migratory Activity of Prostaglandin E Receptor 4 Antagonist in Cancer Cells In Vitro. *Cancers* **2021**, *13*, 5259. https://doi.org/10.3390/cancers13215259. Open access (CC BY).

widely from vascular modulation and chemo-sensitization to antitumor immune activation and remain under active investigation. Snyder et al. first showed that low dose photodynamic therapy could enhance macromolecule drug delivery through vascular permeabilization [56]. Several in vivo studies of rodent lung tumors revealed that low dose photodynamic therapy improved the distribution and delivery of liposomal chemotherapies [306-308]. Work by Debefve et al. further explored photochemical modulation of vasculature in the context of combination therapies [309,310], and later revealed that leukocytes play a major role in the vascular permeabilizing effects of photochemistry [311]. In addition to vascular modulation, PDP has also been shown to decrease tumor interstitial fluid pressure [58], attenuate chemotherapy selection pressure [49], overcome tumor desmoplasia by modulating tumor collagen content and extracellular matrix [312], enable chemotherapy dose-reduction [312,313], and enhance the cytotoxicity of radiation therapy [314]. A recent study also found that PDP using a triple-receptor-targeted formulation promoted antitumor immunity in pancreatic ductal adenocarcinoma spheroid cocultures with pancreatic CAFs and human peripheral blood mononuclear cells [315]. PDP upregulated the expression of antitumor immunogenic signals (Hsp60, Hsp70, CRT, and HMGB1) and induced activation of CD4+ and CD8+ T cells.

PDP-based combination regimens are currently under rapid development [49,312-316], and this chapter combines PDP with the inhibition of an emerging therapeutic target, EP4. As discussed in Chapter 2, EP4 is a G protein-coupled receptor that contributes to cancer progression and metastasis by promoting cancer cell invasion and migration, inducing tumor-associated angiogenesis, and attenuating

the anti-cancer immune response [285,286,317]. EP4 is implicated in the onset and progression of numerous cancers including ovarian, lung, breast, uterine, colorectal, cervical, and prostate, among others [285,318,319]. A study by Spinella et al. showed that EP4 activation stimulates vascular endothelial growth factor (VEGF) production, cell migration, and matrix metalloproteinase activity in HEY human ovarian cancer cells [320]. Tonisen and colleagues also demonstrated that activation of EP4 was linked to invasive capabilities, invadopodia maturation, and matrix degradation in MDA-MB-231 breast cancer cells [317].

At the molecular level, EP4 has also been shown to intracellularly transactivate the epithelial growth factor receptor (EGFR) through the recruitment of β-arrestin (β-arr) and subsequent activation of membrane-bound Src in cancer cells [317,321]. EGFR signaling is linked to proliferation, migration, invasion, angiogenesis, and resistance to apoptosis in cancer cells [322,323]. Signaling pathways downstream of EP4 and EGFR are also overlapping; therefore, inhibiting EGFR alone may be insufficient. For example, preclinical work has shown that the simultaneous blockade of EGFR and EP4 outperforms the inhibition of EGFR alone in attenuating the tumorigenic cervical cancer cell signaling of mitogen-activated protein kinase (MAPK), CREB, protein kinase B (also called AKT), and glycogen synthase kinase (GSK) [324]. A recent study analyzed EP4 expression in ovarian tumor samples and found that EP4 was expressed in nearly 40% of the samples [325]. They also identified EP4 overexpression in several human ovarian cancer cell lines including OVCAR-3, CAOV3, SKOV3, and Kuramochi cells. EGFR is also overexpressed in 30–98% of

epithelial ovarian malignancies [322]. This study develops a combination treatment of EGFR-targeted PDP and EP4 inhibition for ovarian cancer.

In this chapter, EGFR-targeted PDP is achieved by light activation of an antibody–photosensitizer conjugate using FDA-approved Cet and photosensitizer, BPD. The Cet-BPD conjugates used in this study are "cancer-activatable", meaning that BPD molecules are quenched (inactivated) when conjugated to Cet, and can be un-quenched (activated) by cancer cells upon EGFR-mediated endocytosis and lysosomal proteolysis [275,277,326]. Preclinical studies showed that light activation of Cet-BPD is most effective when combined with chemotherapy for enhanced ovarian tumor burden reduction in vivo [277] and in vitro [327]. In 2020, a Cet-IRDye700 conjugate (also known as Cet saratolacan sodium, RM-1929, or ASP-1929) was approved for photoimmunotherapy of head and neck cancer in Japan [276,328,329]. The Cet-photosensitizer conjugate is an emerging therapeutic armamentarium against cancer, and its photodynamic efficacy may be further improved when combined with other treatment modalities.

As discussed in chapter 2, despite aggressive standard treatments consisting of platinum-taxane chemotherapy and cytoreductive surgery, roughly 80 percent of ovarian cancer patients will still develop recurrent disease [330]. Patients with resistant disease have a paucity of therapeutic options, and the need for novel treatment approaches is clear [331]. In this chapter, we evaluated the combination treatment of EGFR-targeted PDP and EP4 inhibition in the context of ovarian cancer migration, invasion, and metastasis-related cell signaling pathways linked to EP4 and EGFR. Gap closure and transwell invasion assays were used to characterize the anti-

metastatic effects of BPD-based PDP, Cet-BPD-based PDP, and EP4 inhibition, alone and in combination, in two high-grade serous ovarian adenocarcinoma lines (OVCAR-5, CAOV3). Immunoblotting and enzyme-linked immunosorbent assays (ELISAs) are also conducted to further characterize molecular alterations induced by the treatments. This chapter provides new evidence that EGFR-targeted PDP coupled with EP4 inhibition attenuates cancer-promoting cell signaling and behaviors linked to metastasis in ovarian cancer cells.

3.2 Materials and Methods

3.2.1 Cell Culture

The high-grade serous ovarian adenocarcinoma cell lines, OVCAR-5 and CAOV3, were used in this chapter. OVCAR-5 cells were purchased from ATCC (Manasses, VA, USA) and the CAOV3 cell line was obtained from Dr. Giuliano Scarcelli (University of Maryland, College Park) who purchased the cells from ATCC (Manasses, VA, USA). Both cell lines were cultured in a 37 °C, 5% CO_2 incubator. Cell lines were propagated for less than 40 passages, and cells were confirmed to be mycoplasma-free using the MycoAlert™ PLUS Mycoplasma Detection Kit (Lonza, Basel, Switzerland). RPMI-1640 medium with L-glutamine (Corning, Corning, MA, USA) containing 10% fetal bovine serum (FBS) (Gibco, Gaithersburg, MD), 100 U/mL penicillin, and 100 μg/mL streptomycin (Corning, Corning, MA, USA) were used to maintain OVCAR-5 cells. DMEM medium (Corning, Corning, MA, USA) supplemented with 10% FBS (Gibco, Gaithersburg, MD, USA) was used to maintain CAOV3 cells.

3.2.2 Gap Closure and Metabolic Activity Studies

For gap closure assays, OVCAR-5 cells were plated at 40,000 cells per well in 96-well plates, then treated with 2% serum-containing media containing DMSO (vehicle, < 0.5 %), BPD, Cet-BPD, AH23848, or a combination. After 24 hours, cells were irradiated with a 690-nanometer laser (0.1 J/cm^2, 10 mW/cm^2, Modulight, Inc., Tampere, Finland). Irradiance was measured at the illuminated surface for each experiment, and black-walled wells were used for all studies to minimize reflected light. Monolayer cultures were scratched using an AutoScratch™ Wound Making Tool (Biotek, Winooski, VT, USA), and 5% serum-containing media was added to each well. AH23848 was re-added to the wells that had received prior AH23848 treatment. Imaging was performed with a Lionheart™ FX Automated Microscope (Biotek, Winooski, VT, USA), and image analysis was accomplished using Gen5 software (Biotek, Winooski, VT, USA). Gap closure percentage was calculated using the following equation: (initial gap area-final gap area)/initial gap area. Cellular metabolic activity studies, cell plating, and treatments were conducted the same as described in the gap closure protocol. An MTT (3-(4,5-dimethylthiazol-2-yl)-2,5-diphenyltetrazolium bromide) assay (Invitrogen, Waltham, MA, USA) was performed following the vendor's protocol to assess relative metabolic activity for viability studies. For gap closure and metabolic activity studies, all experimental conditions were performed at least three times in triplicate.

3.2.3 Lysate Collection and Western Blotting

OVCAR-5 cells (1.1×10^6) were plated in 35-millimeter cell culture dishes and treated with DMSO (vehicle), BPD, Cet-BPD, AH23848, or a combination in

serum-free medium. After 24 h, dishes were irradiated with a 690-nanometer laser (0.1 J/cm^2, 10 mW/cm^2, Modulight, Inc., Tampere, Finland). After another 24 hours, dishes were primed with 1 μM PGE_2 and 50 ng/mL epithelial growth factor (EGF) (R&D, Minneapolis, MN, USA) in serum-free media for 10 min, then lysates were collected in RIPA buffer supplemented with 1% protease and phosphatase inhibitor cocktails (Thermo Fisher, Waltham, MA, USA). For CAOV3 lysate collections, 5 × 10^5 cells were plated and PGE_2 and epidermal growth factor (EGF) were not added. Western blotting was performed as previously described [332]. Proteins were detected using antibodies against EGFR (1:1000, Cell Signaling #4267), Phospho-EGFR (1:500, R&D MAB89671), ERK1 (1:1000, R&D AF1879), ERK2 (1:500, R&D MAB1230), and Phospho-Erk1/Erk2 (1:2000, R&D AF1018), CREB (1:1000, Cell Signaling #9104), Phospho-CREB (1:1000, Cell Signaling #9198), COX-2 (1:1000, Cell Signaling #12282), EP4 (1:500, Cayman #101775), MRP4 (1:500, Invitrogen #MA1-35681), and glyceraldehyde-3-phosphate dehydrogenase GAPDH (1:1000, Cell Signaling #2118). Membranes were imaged using the FluorChem E system (ProteinSimple, San Jose, CA, USA). For Western blotting, all experimental conditions were evaluated a minimum of four times. Signaling intensity of each protein marker was analyzed against GAPDH using ImageJ.

3.2.4 Photoimmunoconjugate Synthesis and Drugs

Photoimmunoconjugates Cet-BPD were synthesized at a ratio of ~4:1 (BPD:Cet) by carbodiimide crosslinking of Cet to BPD, as described previously [327]. Total protein was quantified using a BCA assay and the BPD concentration was characterized using UV–Vis spectroscopy for photoimmunoconjugate

characterization. AH23848 and PGE_2 were obtained from Cayman Chemical (Ann Arbor, MI, USA). EGF was obtained from R&D Systems (Minneapolis, MN, USA).

3.2.5 Extraction Methods to Quantify Photosensitizer Uptake in Cells

OVCAR-5 cells were plated in 35-millimeter dishes at 1.1×10^6 cells per dish, then treated with BPD or Cet-BPD. After 24 h, cells were lysed in RIPA buffer supplemented with 1% protease and phosphatase inhibitor cocktails (Thermo Fisher, Waltham, MA, USA) and then BPD fluorescence signal was measured using a plate reader (Synergy Neo2; Biotek, Winooski, VT, USA; Ex/Em: 435 nm/700 nm). Intracellular BPD concentrations were quantified by correlating fluorescence to a standard curve, then normalized to total protein level (grams) as determined using a BCA assay. All experimental conditions were performed at least three times in duplicate.

3.2.6 Transwell Invasion Assay and PGE_2 ELISA

CAOV3 cells were plated in 35-millimeter dishes at 150,000 cells per dish (for invasion assay) or 500,000 cells per dish (for PGE_2 ELISA). Cells were treated with vehicle (DMSO), BPD, Cet-BPD, AH23848, or a combination regimen in serum-free media for 24 h, then irradiated at 690 nm (0.1 J/cm^2, 10 mW/cm^2, Modulight, Inc., Tampere, Finland). For invasion assays, dishes were trypsinized and plated at 25,000 cells per well in the CultreCoat® 96-Well Medium BME Cell Invasion Assay (R&D, Minneapolis, MN, USA). The remainder of the assay was conducted as per the manufacturer's instructions. For the PGE_2 ELISA, cell culture supernatants were collected 1 and 4 h after light-activation, then supernatants were

assayed for PGE_2 using the Prostaglandin E_2 ELISA Kit (514010, Cayman Chemical, Ann Arbor, MI, USA). For transwell assays and ELISAs, all conditions were performed a minimum of three times in triplicate.

3.2.7 Statistical Analysis

Statistical analysis was conducted using GraphPad PRISM version 9.0.2 for MacOS, and ImageJ was used to quantify immunoblotting bands. Data for gap closure, transwell invasion, Western blotting, ELISA, and MTT studies were analyzed using one-way ANOVA followed by a post hoc Tukey's test. F-tests were used to quantify changes in variance between groups. A value of $p \leq 0.05$ was considered statistically significant.

3.3 Results

3.3.1 Combination of BPD-Based PDP and EP4 Inhibitor (AH23848) Decreases Ovarian Cancer Cell Migration and Invasion

To assess the effects of combination therapy with BPD-based PDP and AH23848 on human ovarian cancer cell migration, we performed the gap closure and transwell cell invasion assays using OVCAR-5 and CAOV3 cell lines (**Figure 3.1**). The concentrations of BPD and AH23848 were fixed at 0.5 and 40 μM, respectively, to maintain sublethal dosing (< 15% reduction in metabolic activity) upon light aviation (**Figure 3.2**). The OVCAR-5 cells incubated with BPD without light activation showed no significant change in gap closure compared to the vehicle control (**Figure 3.1A**). When the OVCAR-5 cells were exposed to AH23848 with or without BPD, the cells migrated ~18% slower than that of the vehicle control ($p <$

0.05), demonstrating sensitivity to EP4 inhibition. PDP using light-activated BPD decreased gap closure by ~33% ($p \leq 0.0001$). When the OVCAR-5 cells were treated with both BPD-based PDP and AH23848, there was a ~65% reduction in gap closure, which is significantly lower than that of the vehicle control and monotherapies ($p \leq 0.001$). A stronger combination effect was observed in the CAOV3 cells using the transwell cell invasion assay (**Figure 3.1B**). Treatments with AH23848, BPD, their combination, or BPD-based PDP did not significantly alter CAOV3 migration compared to the vehicle control ($p > 0.05$). In contrast, the combination of BPD-based PDP and AH23848 greatly reduced the invasion of the CAOV3 cells by ~92%, and this was significantly lower than all the control groups ($p \leq 0.0001$). Our data show that the combination of AH23848 and BPD-based PDT at sub-cytotoxic doses reduce the migration and invasion of two ovarian cancer cell lines in vitro.

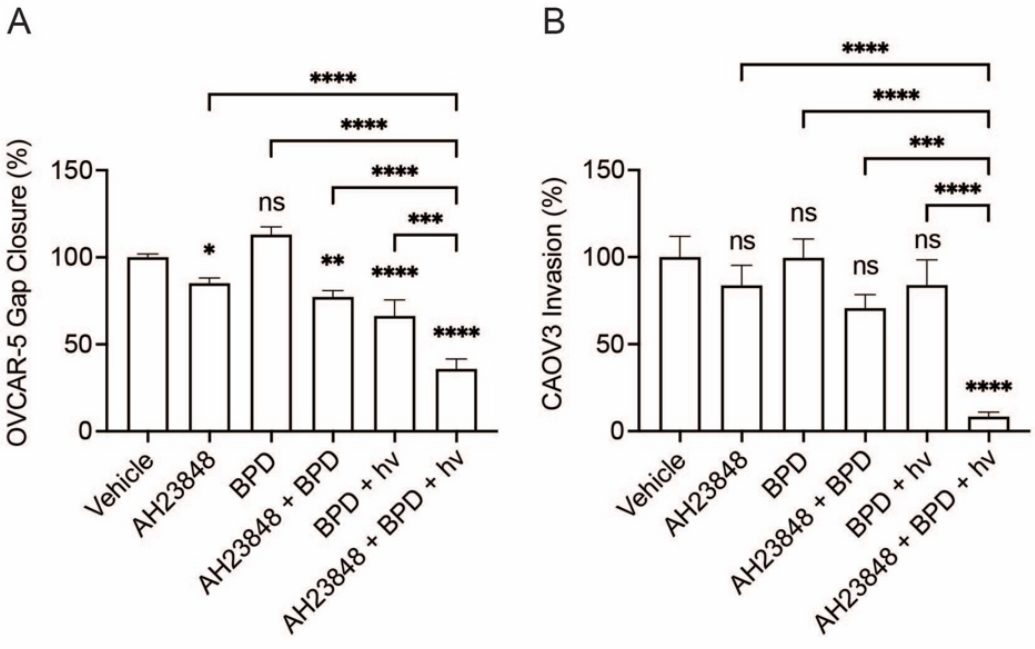

Figure 3.1: Anti-migratory effects of BPD-based PDP, EP4 inhibitor (AH23848), and their combination.

Agents were evaluated in (**A**) a gap closure assay using OVCAR-5 cells and (**B**) a transwell invasion assays using CAOV3 cells. All data are normalized to the vehicle (DMSO) control, and statistical analysis was performed using a one-way ANOVA and post hoc Tukey's test. Error bars represent the standard error of the mean. * $p \leq 0.05$; ** $p \leq 0.01$; *** $p \leq 0.001$; **** $p \leq 0.0001$; ns: nonsignificant. Each bar is representative of at least 9 individual 96-well plate wells.

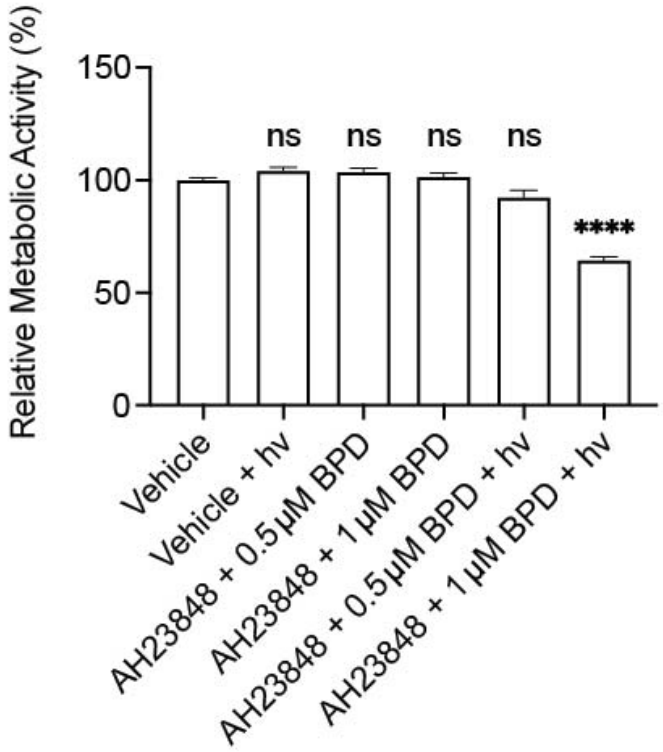

Figure 3.2: Quantification of cellular metabolic activity.

OVCAR-5 cells were treated for 24 hours with the indicated agents (AH23848 dose was fixed at 40 µM), then the light activated groups received 690 nm light (0.1 J/cm^2, 10 mW/cm^2). Metabolic activity was quantified 24 hours later using the MTT assay. Data is normalized to the vehicle (DMSO) control, then statistical analysis was performed using a one-way ANOVA and post hoc Tukey's test. Error bars represent the standard error of the mean. ****$p \leq 0.0001$; ns: nonsignificant. Each bar is representative of 16 individual 96-well plate wells.

3.3.2 BPD-Based PDP Combined with EP4 Inhibition Does Not Attenuate Cell Signaling Pathways Linked to EP4 and EGFR

Considering the tumorigenic role of EP4 signaling and EP4-EGFR crosstalk, we investigated the expression of pCREB, CREB, pEGFR, EGFR, p-ERK1/2, ERK1, ERK2, EP4, and MRP4 in OVCAR-5 cancer cells following the combination

treatment of BPD-based PDP and AH23848 (**Figure 3.3A**). Briefly, OVCAR-5 cells were treated with AH23848, BPD, or their combination for 24 h followed by light activation (hv, 0.1 J/cm^2, 10 mW/cm^2). Cells lysates were then collected at 24 h after treatment and used for Western blot analyses. Dark controls were included for comparison. Cells treated with BPD, with and without light and AH23848, showed an average of a two-fold increase in CREB expression. However, further analysis suggested that changes in pCREB expression was not statistically significant (**Figure 3.3B**). The only statistically significant change observed was an increase in CREB expression following BPD-based PDP ($p \leq 0.05$, **Figure 3.3C**). The expression of p-EGFR, EGFR, p-ERK1/2, ERK1, ERK2, EP4, and MRP4 in OVCAR-5 cells did not change significantly following any treatment compared to the vehicle control (**Figure 3.3 D–K**). Our data suggested that the combination of BPD-based PDP and AH23848 has minimal impact on the EGFR and EP4 signaling pathways. These findings motivated us to further investigate PDP using EGFR-targeted Cet-BPD in combination with AH23848 in subsequent studies to achieve the co-inhibition of EGFR and EP4.

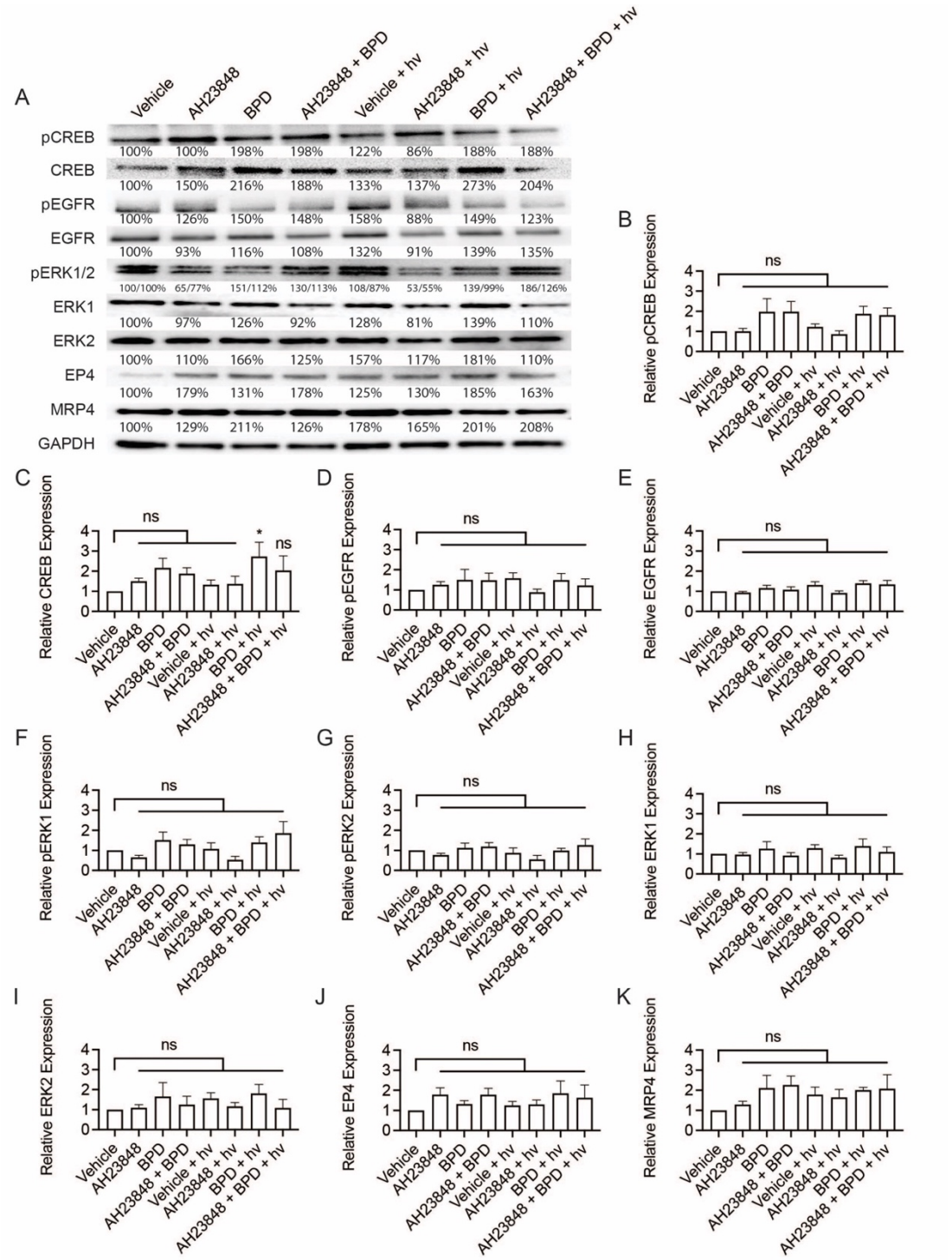

Figure 3.3: Western blot analysis of p-CREB, CREB, p-EGFR, EGFR, p-ERK1/2, ERK1, ERK2, EP4, and MRP4 in OVCAR-5 cells.

Cells were treated with the indicated agents for 24 h, then light-activated (0.1 J/cm^2, 10 mW/cm^2) or maintained in dark conditions. After 24 h, cells were agonized with EGF (50 ng/mL) and PGE2 (1 μM) for 10 min, then whole extracts were collected and analyzed using Western blot. (A) Representative Western blot images and (B–K)

relative densitometric bar graphs of phosphorylated and total proteins were shown. Results are normalized to the vehicle control group. Statistical analysis was performed using a one-way ANOVA and post hoc Tukey's test. Percentages below each band represent the average change in intensity relative to the vehicle control across all experiments. For pERK1 and pERK2 bands, the first number corresponds to pERK1, and the second number corresponds to pERK2. Error bars represent the standard error of the mean. * $p \leq 0.05$; ns: nonsignificant. Each bar is representative of at least 4 individual western blots.

3.3.3 Cet-BPD-PDP and BPD-PDP Have Similar Effects on Gap Closure When Compared at Equivalent Intracellular Photosensitizer Concentrations

The uptake of Cet-BPD and effects on metastasis-related phenotype were assessed in the OVCAR-5 cells (**Figure 3.4**). Extraction studies showed that the intracellular accumulation of Cet-BPD was ~2.5-fold lower than that of free BPD (**Figure 3.4A**, $p \leq 0.001$). At a fixed photosensitizer incubation concentration of 1 μM, a 24-hour incubation of free BPD resulted in an intracellular photosensitizer concentration of ~0.5 μmoles of BPD per grams (g) of protein, compared to ~0.2 μmoles of BPD per grams (g) of protein for the OVCAR-5 cells treated with Cet-BPD. When the photosensitizer incubation concentration was fixed at 0.5 μM, the uptake concentrations for free BPD and Cet-BPD were ~0.2 and ~0.1 μmol BPD/g protein, respectively. Interestingly, treatment with 1 μM Cet-BPD and 0.5 μM BPD led to statistically equivalent amounts of photosensitizer uptake. As a result, these doses were further compared in gap closure assays (**Figure 3.4B,C**). PDP with light (hv) activation of 1 and 0.5 μM BPD reduced the gap closure by ~75 and ~35%, respectively, compared to the vehicle control ($p \leq 0.0001$). Similarly, light (hv) activation of 1 μM Cet-BPD reduced the gap closure by ~24% ($p \leq 0.0001$) compared to the control. Further analysis showed that there is no statistically significant

difference between the anti-migratory effects of PDP using 0.5 µM BPD or 1 µM Cet-BPD (e.g., photosensitizer doses that result in equivalent intracellular concentrations). The 1 µM Cet-BPD treatment was, therefore, selected for use in subsequent studies to evaluate combination effects with EP4 inhibition.

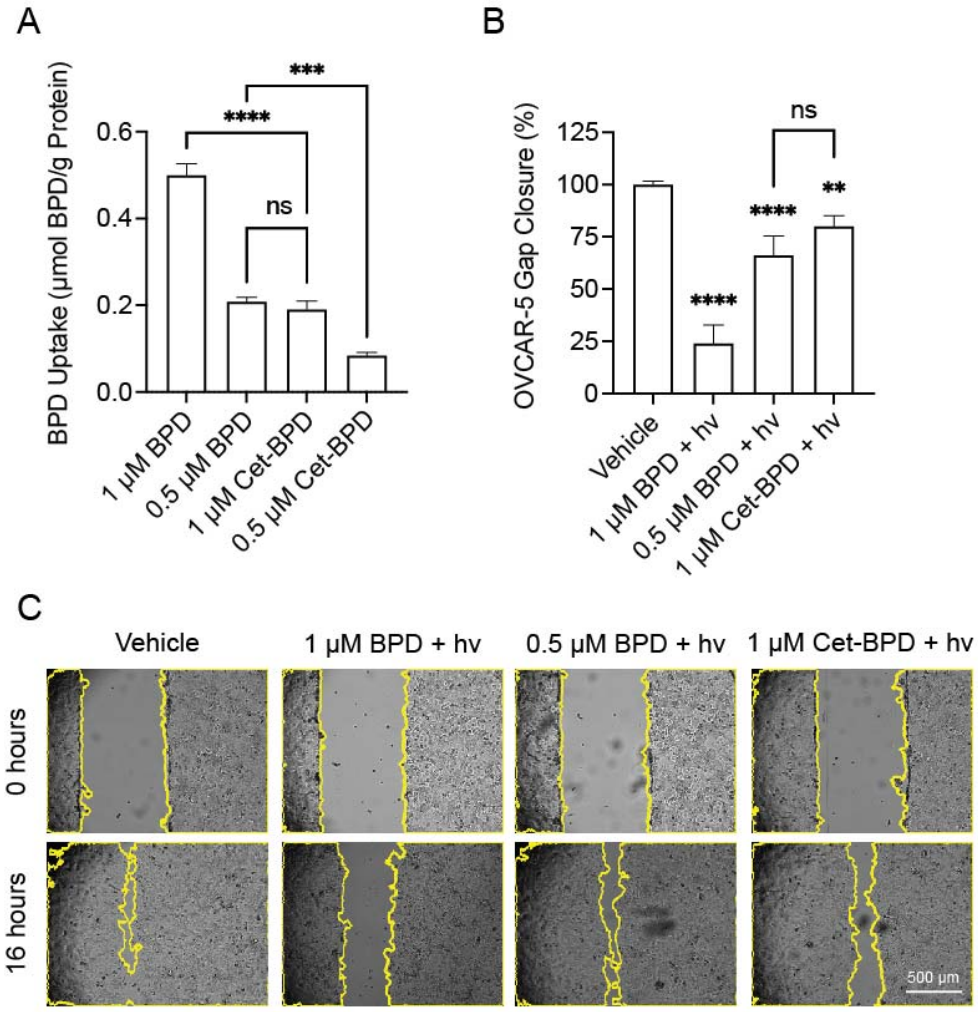

Figure 3.4: Conjugation of BPD to Cet impacts uptake and gap closure.

OVCAR-5 cells were plated in 96-well plates, treated with the indicated BPD or Cet-BPD doses for 24 h, then (**A**) agents were extracted from cells to quantify cellular photosensitizer uptake, or (**B**) cells were light-activated at 690 nm and scratched for gap-closure analysis. Representative gap closure images are included (**C**). Statistical analysis was performed using a one-way ANOVA and post hoc Tukey's test. Error bars represent the standard error of the mean. ** $p \leq 0.01$; *** $p \leq 0.001$; **** $p \leq$

0.0001; ns: nonsignificant. Each bar is representative of at least 6 35-mm dishes (**A**) or 96-well plate wells (**B**).

3.3.4 Cet-BPD-Based PDP Combined with EP4 Inhibition Attenuates Migration, Invasion, and Cell Signaling Linked to EP4 and EGFR.

In **Figure 3.1**, we showed that BPD-based PDP enhances the anti-migratory activity of EP4 inhibitors in ovarian cancer cells (**Figure 3.1**). We next investigated if Cet-BPD-based PDP combined with AH23848 also inhibited migration as measured using a gap closure assay or invasion as measured using a transwell assay (**Figure 3.5**). Cet-BPD alone at 1 μM did not induce significant alterations in gap closure ($p > 0.05$) in the OVCAR-5 cells; however, Cet-BPD-based PDP induced a 20% reduction in migration relative to the control (**Figure 3.5A**). EP4 inhibition using 40 μM AH23848 with and without Cet-BPD (1 μM) reduced gap closure by approximately 15% compared to the control OVCAR-5 cells. A combination of Cet-BPD-based PDP and AH23848 (40 μM) significantly reduced the OVCAR-5 gap closure by up to 50% of all the control groups ($p < 0.0001$). Similar effects were observed when combining Cet-BPD-based PDP with a lower concentration of AH23848 at 20 μM (**Figure 3.6**). These data show that Cet-BPD-based PDP combined with AH23848 significantly inhibited ovarian cancer cell migration compared to both Cet-BPD-based PDP or AH23848 alone, demonstrating the superior potency of this combination regimen. Next, transwell invasion assays were conducted using the same treatment groups to characterize effects on CAOV3 invasion (**Figure 3.5B**). Treatment with AH23848 alone, Cet-BPD alone, a combination of Cet-BPD with an EP4 inhibitor, Cet-BPD-based PDP (Cet-BPD + hv), all resulted in a modest (4–30%) (but statistically

insignificant) reduction in invasion. Only when the CAOV3 cells were treated with the combination of Cet-BPD-based PDP and AH23848 was a significantly reduction in the CAOV3 cell invasion ($p \leq 0.0001$) by 76% observed, demonstrating a potent combination effect in the context of cell invasion.

Cell signaling pathways associated with the activation of EGFR and EP4 were next evaluated using immunoblotting of the OVCAR-5 cells following treatment with Cet-BPD-based PDP and AH23848, alone and in combination (**Figure 3.7**). Representative images are displayed in **Figure 3.7A**. Cet-BPD combined with AH23848 attenuated pCREB signaling to 60% of the control and adding light further reduced pCREB activation to 35% ($p \leq 0.05$). All the groups with Cet-BPD, regardless of the inclusion of AH23848, showed significant reductions in EGFR phosphorylation ($p \leq 0.01$). In pERK1 and pERK2 signaling, the combination of Cet-BPD and AH23848 reduced signaling drastically by over 80% ($p \leq 0.05$). Cet-BPD-based PDP combined with AH23848 further reduced pERK1/2 by 90% ($p \leq 0.01$). None of the changes to total protein in CREB, EGFR, ERK1, ERK2, EP4, or MRP4 reached statistical significance. The molecular effects of co-inhibition of EP4 and EGFR using AH23848 and Cet-BPD are summarized in **Figure 3.8**.

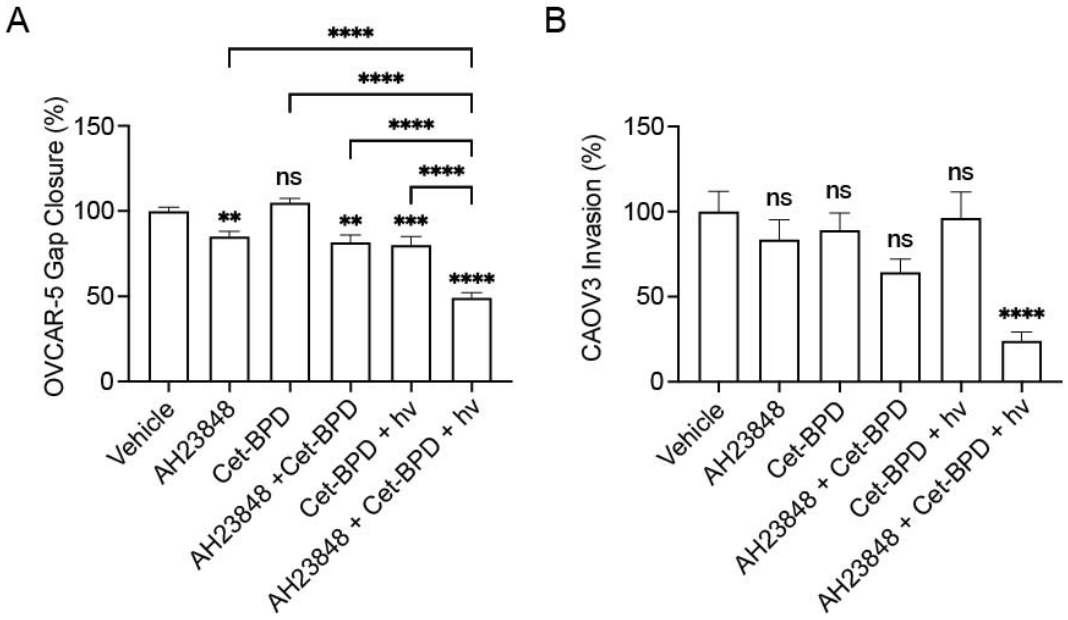

Figure 3.5: Investigation of anti-metastatic effects of Cet-BPD-based PDP combined with EP4 inhibition (AH23848).

Treatments are evaluated in gap closure assays using OVCAR-5 cells (**A**) and transwell invasion assays using CAOV3 cells (**B**). All data are normalized to the vehicle (DMSO) control, and statistical analysis was performed using a one-way ANOVA and post hoc Tukey's test. Error bars represent the standard error of the mean. ** $p \leq 0.01$; *** $p \leq 0.001$; **** $p \leq 0.0001$; ns: nonsignificant. Each bar is representative of at least 12 individual 96-well plate wells.

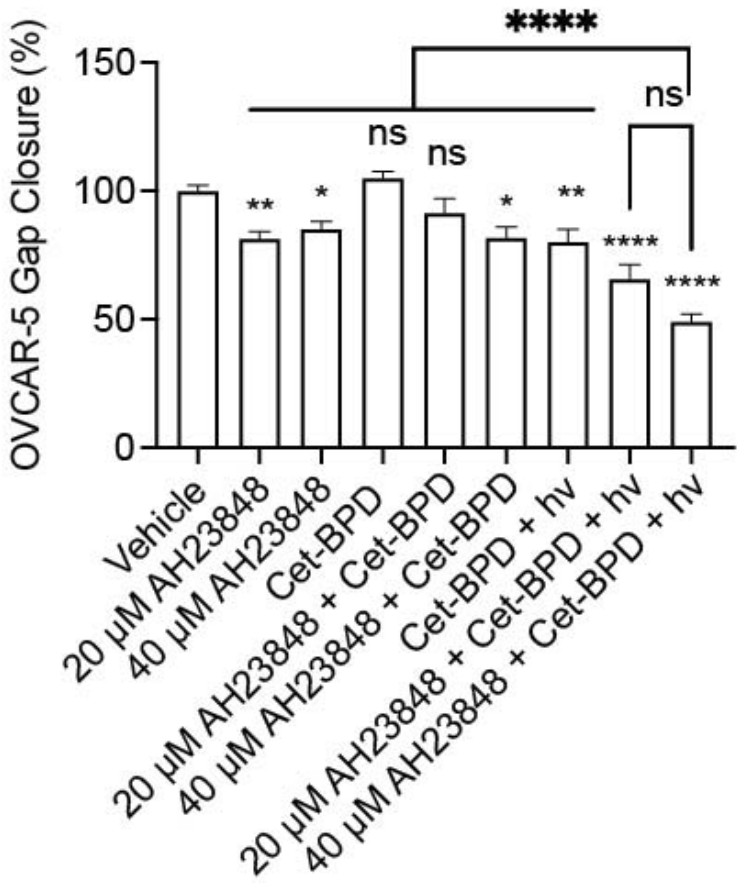

Figure 3.6: Gap closure analysis at 20 μM and 40 μM AH23848.

OVCAR-5 cells were treated with the indicated agents for 24 hours, then light-activated at 690 nm (0.1 J/cm^2, 10 mW/cm^2). Following irradiation, cells were scratched for gap closure analysis and normalized to the vehicle (DMSO) control. Statistical analysis was performed using a one-way ANOVA and post hoc Tukey's test. Error bars represent the standard error of the mean. *$p \leq 0.05$; **$p \leq 0.01$; ****$p \leq 0.0001$; ns: nonsignificant. Each bar is representative of at least 11 individual 96-well plate wells.

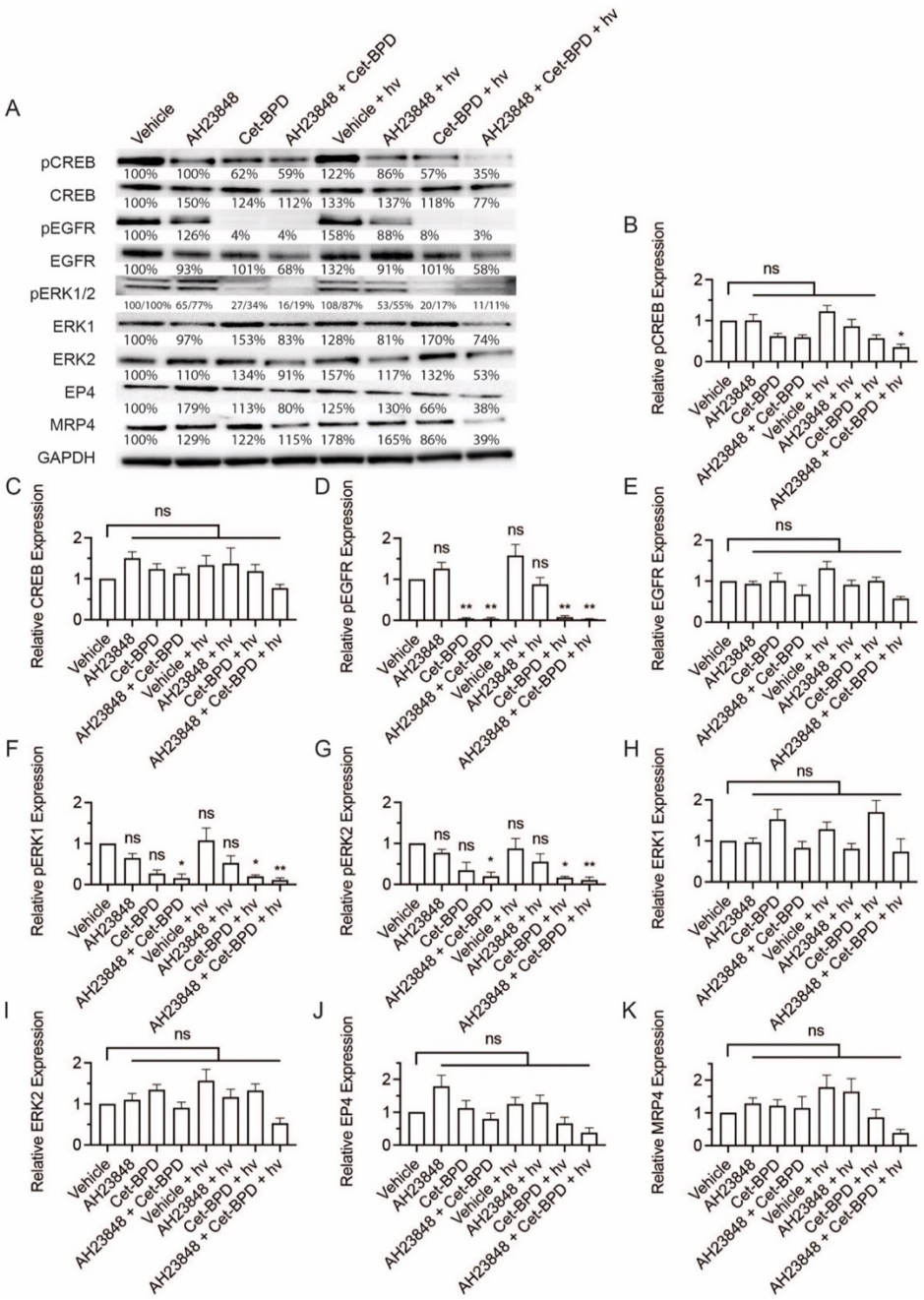

Figure 3.7: Western blot analysis of p-CREB, CREB, p-EGFR, EGFR, p-ERK1/2, ERK1, ERK2, EP4, and MRP4 in OVCAR-5 cells.

Cells were treated with the indicated agents for 24 h, then light-activated (0.1 J/cm^2, 10 mW/cm^2) or maintained in dark conditions. After 24 h, cells were agonized with EGF (50 ng/mL) and PGE_2 (1 μM) for 10 min, then whole extracts were collected and analyzed using Western blot. (A) Representative Western blot images and (B–K) relative densitometric bar graphs of phosphorylated and total proteins were shown. Results are normalized to the vehicle control group. Statistical analysis was performed using a one-way ANOVA and post hoc Tukey's test. Percentages below each band represent the average change in intensity relative to the vehicle control

across all experiments. For pERK1 and pERK2 bands, the first number corresponds to pERK1, and the second number corresponds to pERK2. Error bars represent the standard error of the mean. * $p \leq 0.05$; ** $p \leq 0.01$; ns: nonsignificant. Each bar is representative of at least 5 individual western blots.

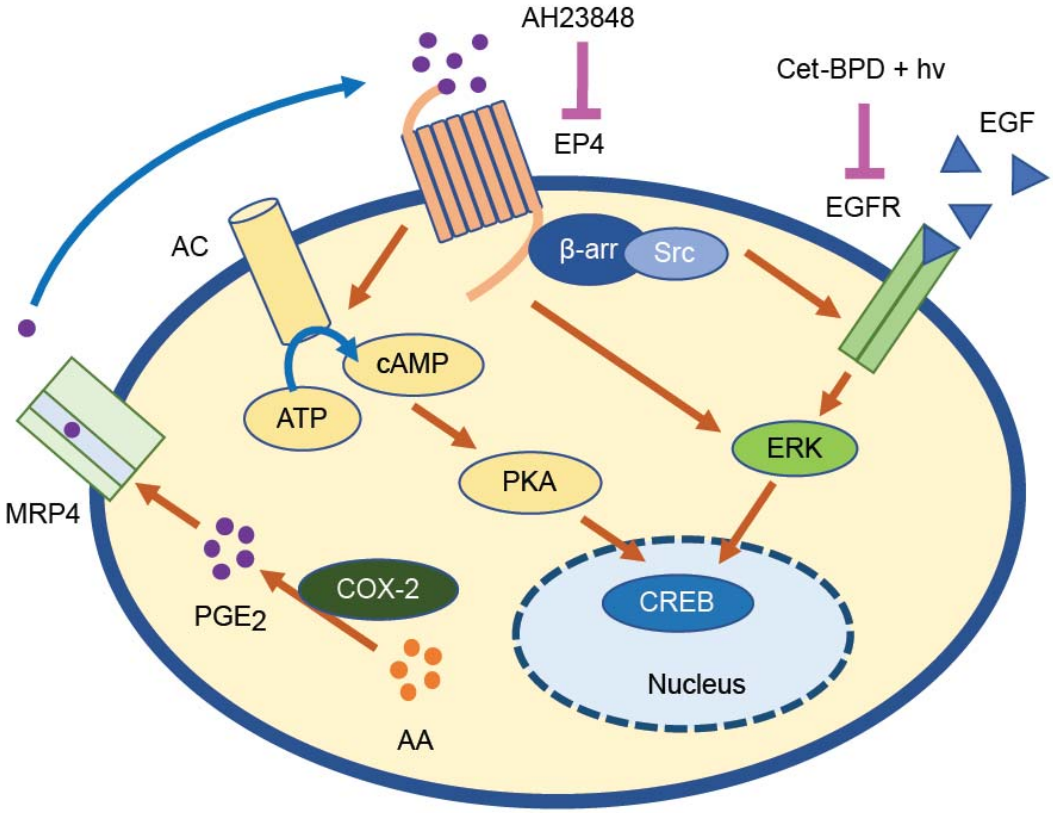

Figure 3.8: Proposed relationship between the combination treatment (Cet-BPD-based PDP and AH23848) and EGFR-EP4 signal transduction pathways.

Arachidonic acid is converted to PGE_2 by COX-1, COX-2, and PGE synthase [333]. PGE_2 is exported from the cell via multiple drug resistance-associated protein 4 (MRP4), where it can bind to the G-protein coupled receptors, EP1–4 [334]. EP4 is coupled to the G protein alpha stimulator (G_S), which activates adenylyl cyclase. Adenylyl cyclase converts ATP to cyclic adenosine monophosphate (cAMP), which subsequently activates Protein Kinase A (PKA). When PKA is activated, its catalytic subunits translocate into the nucleus and activate CREB, a transcription factor with complex roles in cancer [335]. EGFR can be activated extracellularly via EGF binding and intracellularly via the EP4/β-arr/Src complex [317]. Activated EGFR causes a variety of downstream effects including ERK phosphorylation, which is linked to CREB activation. EP4 has also been shown to induce ERK activation independently of EGFR [336]. The Cet-BPD and EP4 inhibitor combination regimen is designed to simultaneously abrogate EGFR and EP4 signaling to block tumorigenic crosstalk

along with overlapping signaling pathways. Abbreviations: AA (arachidonic acid); COX2 (cyclooxygenase-2); PGE2 (prostaglandin E2); MRP4 (multidrug resistance-associated protein 4); EP4 (prostaglandin E2 receptor 4); ATP (adenosine triphosphate); cAMP (cyclic adenosine monophosphate); PKA (protein kinase A); CREB (cyclic AMP response element-binding protein); ERK1/2 (extracellular signal-regulated kinases 1/2); *β-arr (β-Arrestin); EGFR (epidermal growth factor receptor); EGF (epidermal growth factor); BPD (benzoporphyrin derivative); Cet (Cet).*

3.4 Discussion

In this chapter, we show that PDP significantly attenuates gap closure in OVCAR-5 cells. This is consistent with previous work by Jiang et al., who showed, using an invasion assay, that Photofrin®-based subcytotoxic photochemistry inhibited glioblastoma transit through a Matrigel membrane [337]. Yang et al. demonstrated that sub-lethal photodynamic therapy (10–20% cell killing) using 5-Aminolevulinic acid (5-ALA) induced significant decreases in the migration and invasion of multiple head and neck cancer cell lines [338]. In our study, PDP was evaluated using two platforms: freeform BPD, as well as the EGFR-targeted Cet-BPD conjugate. The porphyrin-based BPD was selected due to its FDA approval status and because most earlier PDP studies use BPD or other porphyrin-based photosensitizers. However, Overchuk et al. recently used a bacteriochlorin-based photosensitizer to achieve PDP [312]. More work is warranted to characterize differences in priming effects between photosensitizers, or if a combinational approach of multiple photosensitizers may be beneficial. **Figure 3.4** revealed that approximately two times more BPD is internalized compared to Cet-BPD. However, when compared at equal intracellular concentrations, BPD and Cet-BPD had similar effects on gap closure. Cet-photosensitizer conjugates are rapidly gaining traction in the clinical sphere. In September 2020, Japan approved a Cet-IR700 construct, Akalux®, for the treatment

of unresectable locally advanced or recurrent head and neck cancer. A Cet-IR700 construct (ASP-1929) is also under evaluation in multiple clinical trials.

We further demonstrated, for the first time, that incorporating EP4 inhibition into a PDP treatment led to additional reductions in migration along with a drastic attenuation of cell invasion (**Figures 3.1 and 3.5**). To inhibit EP4, we used AH23848, which was first reported by Coleman et al. to antagonize EP4 in 1994 [339]. While AH23848 is commonly used in vitro, numerous EP4 antagonists have been developed with higher selectivity (CJ-023,423 (grapiprant), L-161982, ONO AE3-208, etc.) [321]. In this study, AH23848 was used as a model drug to validate the combination effect of EP4 inhibition with EGFR-targeted PDP. In addition to lowering migration and invasion, AH23848 combined with PDP also demonstrated a substantial increase in treatment consistency compared to PDP alone. To quantify this, F-tests were performed to compare the variances of BPD-based PDP and Cet-BPD-based PDP with and without AH23848. The analyses revealed statistically significant decreases in variance (alpha = 0.05) when AH23848 was added to both BPD-based PDP and Cet-BPD-based PDP in both migration studies and invasion studies (**Figures 3.1 and 3.5**). The potent combination effects demonstrated here motivate future work using newer EP4 antagonists that are currently in clinical trials, including grapiprant, TPST-1495, and AN0025 (previously E7046).

Previous work supports our findings that EP4 plays a fundamental role in cancer progression. In murine breast cancer models, EP4 antagonism has been shown to reduce primary tumor growth, stem cell-like functions, tumor-associated angiogenesis and lymphangiogenesis, and metastasis to the lymph nodes and lungs [340,341]. Xu et

al. showed in PC-3 prostate cancer cells that EP4 antagonism (or EP4 siRNA) attenuates the PGE2-mediated expression of matrix metalloproteinases, nuclear factor-κB ligand, and runt-related transcription factor 2, which promote cell growth and metastasis in multiple cancers [342]. We also recently showed that EP4 antagonism significantly reduced SK-UT-1 (leiomyosarcoma) cell migration and sensitized cells to docetaxel (half-maximal inhibition concentration [IC_{50}] decreased from 1.47 to 0.46 nM) [343]. Additionally, the intracellular crosstalk between EP4 and EGFR via EP4/β-arr/Src is well characterized [317,321,344]. In light of this, the co-inhibition of both receptors is a promising prospect that has been studied previously in cervical cancer cells by Parida et al. [324]. Cells were stimulated with PGE_2 and treated with either an EP4 inhibitor (GW627368X), an EGFR monoclonal antibody, or both, then screened via Western blot for MAPK, CREB, AKT, and GSK phosphorylation. While the monotherapies produced potent downregulation in phosphorylation, the simultaneous blockade of EGFR and EP4 led to further reductions for multiple targets. This supports the notion that silencing compensatory signaling pathways can enhance treatment effects. Our study expands on this concept by coupling the co-inhibition of EP4 and EGFR with PDP.

While BPD-based PDP combined with EP4 inhibition (**Figure 3.3**) did not block the tumorigenic signaling of CREB, EGFR, ERK1, or ERK2, the EGFR-EP4 co-inhibition strategy resulted in potent downregulations (**Figure 3.7**). We show that phosphorylated EGFR is decreased in the presence of Cet-BPD, regardless of the addition of AH23848 or light-activation (**Figure 3.7C**). This is consistent with previous work by Abu-Yousif et al., who showed that Cet-BPD blocked EGFR

phosphorylation in EGF-primed OVCAR-5 cells with and without light-activation [345]. The same study also looked at p-MAPK/ERK signaling and their Cet-BPD treatment only inhibited ERK phosphorylation when light-activated. Similarly, our study also showed that Cet-BPD-based PDP attenuates ERK phosphorylation. Unlike their study, we found that Cet-BPD without light activation also blocked ERK phosphorylation, though it was not a statistically significant decrease relative to the vehicle control. This difference can likely be attributed to the higher Cet concentration used in our study (~250 nM vs. 37 nM). Work by Cherukuri et al. showed that PGE_2 stimulates ERK and CREB phosphorylation in colon cancer cells, and this can be blocked using a selective EP4 inhibitor (L-161,982) [346]. Our study is partially consistent with this, as we show that EP4 inhibition using AH23848 attenuates ERK1 and ERK2 phosphorylation to ~60% of the vehicle control. Unlike their study, inhibition of EP4 alone did not block the phosphorylation of CREB, likely due to the presence of the EGF-mediated stimulation of EGFR. In fact, multiple studies have linked EGFR to CREB activation [347,348], which is consistent with our data showing that Cet-BPD alone can modestly attenuate CREB phosphorylation with or without light activation. Importantly, the only treatment to induce significant reductions in CREB phosphorylation was Cet-BPD-based PDP combined with AH23848, demonstrating potent combination effects (**Figure 3.7B**). While previous work suggests that photochemistry upregulates both PGE_2 and COX-2 [349-351], we did not observe the stimulation of either in our experiments (**Figure 3.9**). Work by Ferrario et al. shows that the effects of photochemistry on COX-2 and PGE_2 are highly dependent on dosage [349]; this likely explains our results because the light

dose used (0.1 J/cm^2) was relatively low. In contrast, we observed a notable downregulation of PGE_2 in the supernatants following all treatments, particularly at 4 h.

PDP is a promising modality that leverages subtherapeutic (below the usually delivered dose) photodynamic therapy alone or as part of a combination regimen for cancer treatment. We envision that PDP can be in incorporated into the clinic in two ways. First, PDP can be achieved in the tissues surrounding photodynamic therapy-treated areas, as shown by Vincent et al. [352]. While these surrounding tissues receive subtherapeutic photochemistry, the PDP effects may be leveraged to enhance overall outcomes either through activating antitumor immunity or increasing the accumulation of another agent. Second, PDP can be used in the clinic as a tool to precisely enhance the delivery and selectivity of chemotherapy to tumors. Wang et al. showed that while high fluence PDT (30, 50 J/cm^2) induced vascular occlusion in rodent mesothelioma xenograft tumors, using an intermediate fluence (10 J/cm^2) improved FITC-Dextran leakage in tumors but not normal tissues [353]. Importantly, using a lower fluence (5 J/cm^2) did not improve tumor uptake of FITC-Dextran, highlighting the importance of careful light dose selection for achieving the desired effects. They further demonstrated that photochemistry at 10 J/cm^2 combined with liposomal cisplatin outperformed the monotherapies in inhibiting tumor growth. The use of PDP for selective chemotherapy delivery to tumors is therefore a promising avenue through which we envision PDP may be incorporated into a clinical setting.

It is important to acknowledge several limitations of the work in this chapter. Transwell migration assays are subject to irregular migration and reproducibility

issues, and in gap closure assays there can be mechanical damage to the cells and plate surface caused by the scratch as well as general reproducibility issues [354]. Both transwell and scratch assays are also performed on cells plated in two-dimensional monolayers, which do not replicate the three-dimensional structure of tumors. Future studies can be performed using 3D cultures and co-cultures that mimic the collective cell migration of cancer cells due to tumor cell-specific intercellular connections, tissue scaffold environment interactions, and interactions with tumor-associated cells.

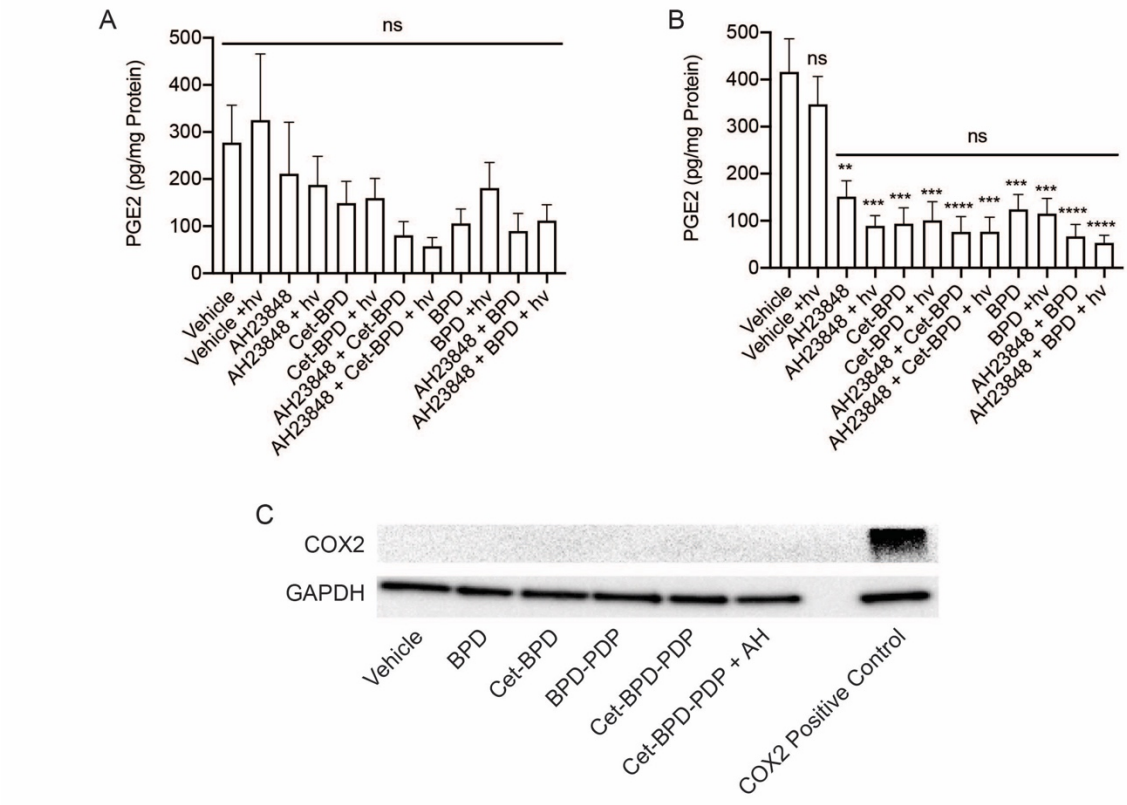

Figure 3.9: Investigation of PGE2 release and COX-2 regulation in CAOV3 cells.

CAOV3 cells were treated with serum-free media supplemented with the indicated agents, and light-activated 24 hours later (0.1 J/cm^2, 10 mW/cm^2). Supernatants were

collected at **(A)** 1 and **(B)** 4 hours post-PDP and assayed for PGE2 using the Prostaglandin E_2 ELISA Kit (514010, Cayman) **(C)** Lysates were collected at 24 hours post-PDP and probed for COX-2. GAPDH was included as a loading control. Statistical analysis was performed using a one-way ANOVA and post hoc Tukey's test. Error bars represent the standard error of the mean. $^{**}p \leq 0.01$; $^{***}p \leq 0.001$; $^{****}p \leq 0.0001$; ns: nonsignificant. Each bar is representative of 9 wells of the ELISA plate. Western blot image is representative of three western blots.

3.5 Conclusions

This chapter demonstrates that PDP improves the anti-migratory activity of a prostaglandin E receptor 4 antagonist in ovarian cancer cells. We confirm this using two models of metastatic behavior (gap closure and invasion assays), two ovarian cancer cell lines (OVCAR-5 and CAOV3), and two photosensitizer formulations (non-targeted BPD and EGFR-targeted Cet-BPD). Molecular analysis indicates that EGFR, ERK1/2, and CREB signaling are implicated in these treatment outcomes. Based on these promising functional and mechanistic in vitro assays, further experiments to verify in vivo efficacy are warranted. It is also important to mention that cell migration and invasion are two parts of the complex, multi-step metastatic cascade. This cascade involves proteolytic remodeling of the basement membrane, cross-talk with stromal cells, invasion, transport along vascular and lymphatic routes, extravasation, and formation of metastatic niches [355]. Therefore, further studies to investigate the role of the PDP-EP4 combination in the context of these other steps would elucidate the holistic impact of the treatment in regulating cancer metastasis. Importantly, in addition to overexpression in cancer cells, EP4 is also expressed in various immune cells (i.e., macrophages, T cells, NK cells, and B cells), and PGE_2-EP4 signaling plays a major role in evasion of the antitumor immune response [285,356,357]. Future *in vivo* work to study the PDP-EP4 inhibitor combination

regimen should therefore evaluate anti-metastatic effects as well as the modulation of the antitumor immune response.

Chapter 4: Transient fluid flow improves photoimmunoconjugate delivery and photoimmunotherapy efficacy

Circulating drugs in the abdominal cavity at the time of surgery is an effective strategy for the treatment of peritoneal metastases from ovarian cancer. While fluid flow can increase the effective contact of drugs with the peritoneal surface, fluid flow-induced shear stress has been reported to improve cellular uptake of therapeutic entities. However, a major gap in knowledge exists regarding the potential role of fluid flow-induced shear stress as a delivery vehicle for photoimmunotherapy. This chapter addresses this gap using a microfluidic cell culture model to study how fluid flow-induced shear stress affects the delivery, subcellular localization, and phototoxicity of photoimmunoconjugates in human ovarian cancer cells. Photoimmunoconjugate delivery is evaluated at 0, .5, 1, and 5 dyne/cm^2 at varying time points (10 minutes to 5 hours), and data are validated in multiple human ovarian cancer cell lines (OVCAR8, OVCAR3). Data from this chapter reveal that delivery at 0.5 and 1 dynes/cm^2, compared to static conditions, doubles the cellular delivery of photoimmunoconjugates. Subsequent studies validate that fluid flow-mediated treatment with three different photosensitizer formulations BPD, photoimmunoconjugates, and photoimmunoconjugate-coated liposomes) led to enhanced phototoxicity compared to static conditions. This chapter confirms a fundamental role of fluid flow-induced shear stress in the anti-cancer effects of photoimmunotherapy, supporting further study of this delivery method.

4.1 Introduction

As described in Chapter 2, cancer cells in the abdominal cavity are continuously exposed to fluid shear stress (FSS) from accumulated malignant fluids (ascites). Patients with advanced stage or recurrent ovarian cancer can present with over two liters of ascites in the peritoneal cavity [358]. The shear stresses conferred by currents of ascitic fluid resulting from organ mobility, gravity, breathing and other bodily movements, are estimated to be 5 dynes/cm^2 or less [22,23,359,360]. To date, most research has been dedicated to exploring the impact of ascitic FSS on cell proliferation, migration, vitality, metabolism, expression of genes and proteins, and other cellular functions. Overall, these studies have found that "continuous" (days or weeks) FSS may induce epithelial-mesenchymal transition, increased motility, morphological changes, or treatment resistance [361-364]. On the other hand, "transient" (minutes to hours) fluid flow is already used medically to distribute the chemotherapy solution in the abdomen of patients with peritoneal carcinomatosis for improved outcomes [365]. With new molecular-targeted theranostic agents and nanomedicines under development for peritoneally disseminated tumors, there is a need to enhance our basic understanding of transient FSS as a potential tool in the arsenal against cancer.

An emerging theranostic treatment for peritoneally disseminated ovarian cancer is PIT. As described in Chapter 2, PIT is a molecular-targeted modality that leverages targeting properties of antibodies for selective delivery of photosensitizers via their conjugation as photoimmunoconjugates (PICs) [277,366]. Upon light absorption by photosensitizers, highly cytotoxic ROS are generated for the ablation of

cancer cells and priming of the surviving cells for adjuvant treatments [366]. In addition to the cytotoxic effects of PIT, the fluorescent signal generated from the photosensitizers on the PIC can be used for cancer imaging [277]. PIT was first described by Mew *et al.* who conjugated myosarcoma-targeted monoclonal antibodies to hematoporphyrin [269]. Since then, several antibody-photosensitizer combinations have been developed for the photochemical treatment and diagnosis of cancer [366].

Much of the preclinical and clinical research on PIT targets EGFR [322,367,368]. EGFR-targeted PIT was shown to selectively induce killing of EGFR-expressing ovarian cancer cells while mitigating EGFR signaling pathways [345]. Importantly, these findings highlight that antibodies used in PIT retain biological functions to achieve multi-pronged anti-cancer effects of both photosensitizer delivery and inhibition of tumor-promoting cell signaling. Consistent with these dual functions, we and others have shown that PICs targeting the EGFR can attenuate EGFR and ERK1/2 signaling [345,369]. Nonetheless, one of the major challenges associated with PIT is limited photosensitizer delivery to cancer cells [236,327,369]. This can be attributed to several factors including finite antigen numbers per cancer cell, limited number of photosensitizer-to-antibody payload, and poor tumor accessibility of antibodies [236]. The work in this chapter overcomes this limitation through the rigorous examination of transient flow as a drug delivery platform to enhance total cellular PIC delivery and thereby bolster cytotoxic effects.

In addition to total cellular PIC delivery, the subcellular localization is another key determinant of PIT treatment effect [370-373]. Upon antibody-EGFR binding in the plasma membrane, the complex rapidly undergoes receptor-mediated endocytosis

followed by localization in the endosome, lysosome, endoplasmic reticulum, and nucleus [374-377]. Prior work shows that lysosomal digestion of EGFR-targeted PIC dequenches the photosensitizer, enabling applications for PIT and imaging [277,378]. Despite extensive investigations of subcellular PIC accumulation under static conditions, the role of transient flow as a modulator of these processes remains largely unknown. Results from this study confirm time- and FSS-dependent effects of transient flow on PIC subcellular accumulation.

PIT is achieved in this study using FDA-approved agents: Cet, an EGFR-targeted antibody, and the photosensitizer, BPD. A perfusion system is used to treat OVCAR8 ovarian cancer cells at varying FSS (0.5-5 dynes/cm^2, 1.16-11.55 mL/minute; **Supplementary Table 1**). Microfluidic models strike an optimal balance between the simplicity/reductionism of in vitro models with the complexity/realism of animal models, making them ideal to study the effects of FSS [359,379]. Longitudinal binding studies reveal time-dependent changes in subcellular uptake that vary between static and FSS conditions. The results also reveal significant effects of FSS in promoting total cellular photosensitizer uptake while modulating subcellular compartmentalization. Toxicity studies are performed with multiple photosensitizer formulations including free BPD, PIC, and PIC-Nal [327]. Across all formulations, FSS-mediated delivery induces heightened cell killing. Results from this chapter implicate transient flow as a fundamental property for consideration in the implementation of photochemical treatments for locally disseminated metastases.

4.2 Materials and Methods

4.2.1 Cell Culture

OVCAR8 cells were obtained courtesy of Dr. Jocelyn Reader (University of Maryland School of Medicine; University of Maryland Eastern Shore), and OVCAR3 cells were obtained from Dr. Michael M. Gottesman (National Cancer Institute, National Institutes of Health). OVCAR8 and OVCAR3 cells were maintained in RPMI-1640 medium with L-glutamine (Corning) supplemented with 10% (OVCAR8) or 20% (OVCAR3) fetal bovine serum (Gibco), 100 U/mL penicillin and 100 μg/mL streptomycin (Lonza). J774 cells (ATCC) were maintained in DMEM (ATCC) supplemented with 10% fetal bovine serum, 100 U/mL penicillin and 100 μg/mL streptomycin. Cells were maintained at 37 °C, 5% CO_2 incubator and subcultured at 80-90% confluence for less than 30 passages. Cells were confirmed free of mycoplasma using MycoAlert^{TM} PLUS Mycoplasma Detection Kit (Lonza). Cell line biological identities were verified using STR profiling.

4.2.2 Photosensitizer Delivery Under Laminar Flow

The *in vitro* laminar flow model parameters are summarized in **Table 4.1**, and experimental workflow is shown in **Figure 4.1**. OVCAR8 cells were plated in the μ-Slide $I^{0.6}$ Luer chips at 250,000 cells/chip and incubated overnight. The following day, 1 μM photosensitizer was administered under flow using the Fluidic Unit Quad pump system and Pump Control Software (ibidi). The Fluidic Unit Quad pump system contains 4 perfusion sets, each accommodating one chip. Next, chips were either immediately collected for photosensitizer uptake analysis or light-activated for

subsequent viability experiments. Static controls were collected by pipetting 200 µL treated medium directly into the chip. All treatments were conducted at 37 °C, 5% CO_2, and dark controls were shielded from light throughout the treatment process. For each replicate in subcellular uptake studies, two chips were combined to accrue quantifiable amounts of BPD and protein within each fraction. Chips were not combined for total cellular uptake and cytotoxicity analyses.

Table 4.1: Parameters for *in vitro* modeling of fluid shear stress.

Fluid Shear Stress (τ; dynes/cm^2)	**Flow Rate (Φ; mL/min)**	**Dynamic Viscosity at 37°C (η; dynes·s/cm^2)**	**Channel Height (mm)**	**Channel Length (mm)**	**Channel Width (mm)**	**Growth Area (cm^2)**	**Cell chamber volume (µL)**
0	0	0.0072	0.6	50	5	2.5	150
0.5	1.16						
1	2.31						
5	11.55						

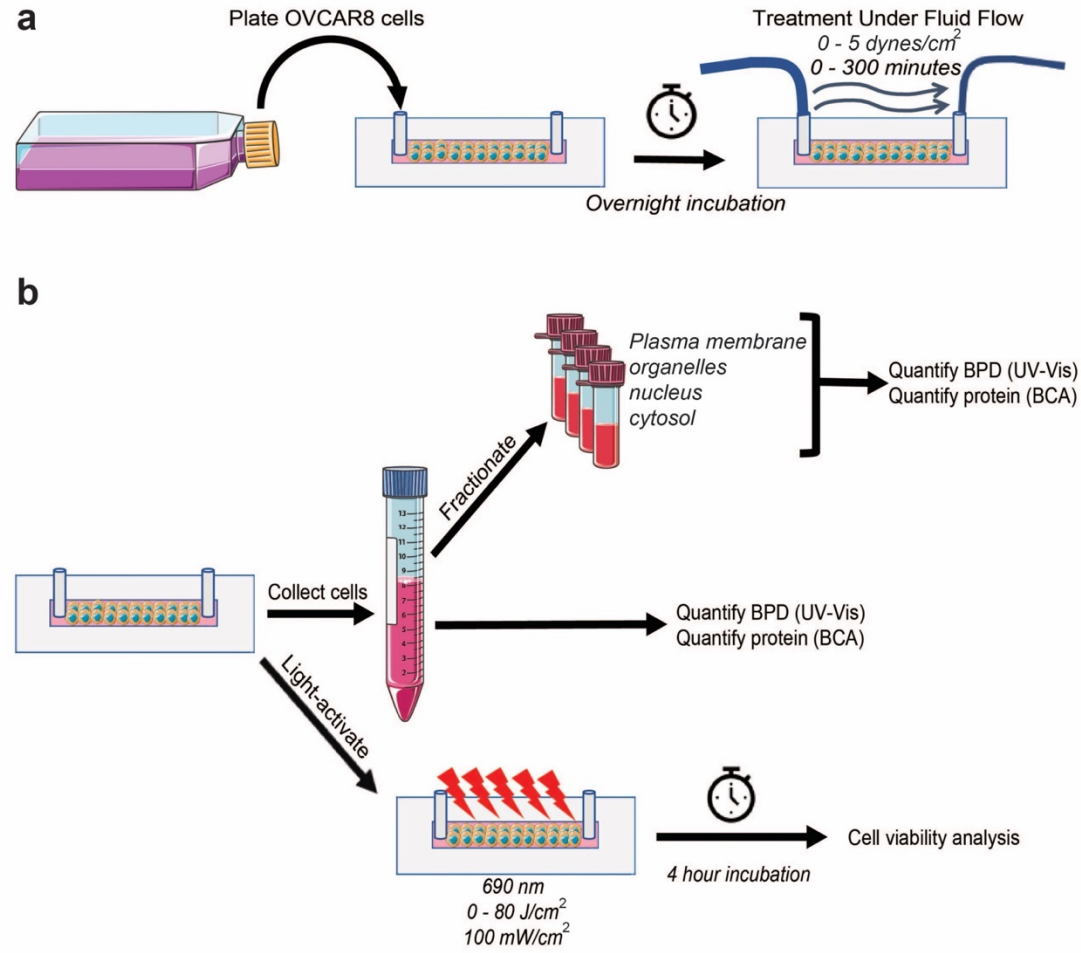

Figure 4.1: Experimental workflow for FSS experiments.

(a) 250,000 OVCAR8 cells were plated in the µ-Slide $I^{0.6}$ Luer chips. Following overnight incubation, flow was initiated with or without 1 µM photosensitizer. (b) Next, cells in chips were either immediately collected for total or subcellular analysis or light-activated for viability quantification 4 hours post-irradiation. Figure graphics were created using images courtesy of smart.servier.com.

4.2.3 Total and Subcellular Photosensitizer Delivery Analysis

Following photosensitizer treatment in static or flow conditions as described above, cells were lysed in radioimmunoprecipitation assay buffer (RIPA) (ThermoFisher) for

total cellular analyses. For isolation of subcellular compartments (plasma membrane, organelle, cytosol, and nucleus) cell pellets were fractionated using the Minute™ Plasma Membrane Protein Isolation and Cell Fractionation Kit (Invent Biotechnologies, Inc.). Fluorescence (Ex/Em: 435 nm/700 nm; gain: 150) was measured using the synergy Neo2 (Biotek), and fluorescence values were compared to a standard curve to quantify BPD concentration in units of pmoles/L. Next, the Pierce™ BCA Protein Assay Kit (ThermoFisher Scientific) was used to quantify protein content in units of µgrams/L. Concentrations of BPD and protein were divided to determine pmoles BPD/µgrams protein. All fluorescence measurements were performed in black 96-well plates. The purity of the plasma membrane and organelle fractions has been previously characterized by Vázquez-Medina, *et al.* who showed that the plasma membrane fraction is enriched with plasma membrane markers such as Na^+/K^+-ATPase and flotillin, whereas the organelle fraction is enriched with markers for the mitochondria, Golgi, and endoplasmic reticulum[380]. Additionally, work by Kutluay *et al.* demonstrated that the cytosol fraction is enriched with cytosol marker LC3A/B [381].

4.2.4 Cytotoxicity Analysis

Following photosensitizer treatment, cells were irradiated using a 690-nanometer laser (10-80 J/cm^2, 100 mW/cm^2; Modulight, Inc.) and incubated for 4 hours prior to cytotoxicity analysis by Neutral Red Assay Kit (abcam). Briefly, after washing each chip with phosphate buffered saline (PBS), neutral red staining solution (prepared at 1x in cell culture media) was added to the chips and incubated for 2 hours at 37 °C. The staining solution was then aspirated, and cells were washed and solubilized using

buffers provided in the kit. The solubilized product was transferred to a 96 well plate, and absorbance at 540 nm was measured using the Synergy Neo2 (Biotek). Background-subtracted values were normalized to the untreated control to quantify lysosomal integrity.

4.2.5 Synthesis and Characterization of Photoimmunoconjugates

PICs were synthesized using carbodiimide chemistry as previously described [327]. 10kDa methoxy PEG succinimidyl carboxymethyl ester (mPEG-NHS; JenKem Technology) was reacted with Cet, BPD *N*-hydroxysuccinimidyl ester (BPD-NHS), and azide-PEG4-*N*-hydroxysuccinimidyl ester (azide-PEG-NHS) at a 3:1:6:2.5 molar ratio. Purification and buffer exchange were performed with 7 kDa MWCO Zeba™ spin desalting column (ThermoFisher) and 30 kDa MWCO Amicon® Ultra-15 Centrifugal Filter (Millipore Sigma), respectively. Final antibody and BPD concentrations were determined using Pierce™ BCA Protein Assay Kit (ThermoFisher Scientific) and UV-Vis spectroscopy. SDS-PAGE was used to measure purity. Final BPD:Cet ratio was ~3:1, representing between 3- to 5-fold quenching [275,277]. To measure PIC stability under flow, PICs were flowed through cell-free chips for 30 minutes at 1 dynes/cm^2. The perfusate was collected for purity analysis via SDS-PAGE. Photoactivity was determined by dividing the maximum fluorescence intensity of PIC in PBS by the maximum fluorescence intensity of PIC in DMSO following excitation at 435 nm (Synergy Neo2, Biotek).

4.2.6 Synthesis and characterization of Nanoliposomes (Nal) and Photoimmunoconjugate-Nanoliposomes (PIC-Nal)

For Nal synthesis, a mixture of dipalmitoylphosphatidylcholine (DPPC), dioleoylglycerophosphoglycerol (DOPG), cholesterol, distearoyl-phosphatidylethanolamine-methoxy polyethylene glycol (DSPE-mPEG2000), and distearoyl-glycerophosphoethanolamine-N-dibenzocyclooctyl polyethylene glycol (DSPE-mPEG2000-DBCO) was prepared at a 5.9:0.7:2.9:0.5:0.05 molar ratio in chloroform. All liposome components were purchased from Avanti. Chloroform was removed by rotary evaporation, then the dry lipid films were rehydrated in UltraPure™ DNase/RNase-Free Distilled Water (Invitrogen™). For liposome sizing, extrusion was performed through a 0.1 μm Nuclepore™ Track-Etched Polycarbonate Membrane Filter (Whatman). Copper-free click chemistry was used to generate PIC-Nal. PIC (containing azide) and Nal (containing DBCO) were mixed at a 90:1 molar ratio then purified using Sepharose CL-4B size exclusion chromatography. Size and zeta potential were quantified using the Nanobrook Omni (Brookhaven Instruments). PIC-Nal stability under flow and photoactivity were analyzed using the same methods as PIC.

4.2.7 Lysate Collection and Western Blotting

Cellular proteins for western blotting were extracted as described previously [369]. Briefly, pelleted cells were lysed in radioimmunoprecipitation buffer (Thermo Fisher) supplemented with protease and phosphatase inhibitors (Thermo Fisher). Proteins were separated on NuPAGE™ 4 to 12% Bis-Tris gels (Invitrogen) then transferred to PVDF membranes (Thermo Scientific). Membranes were blocked in milk at room

temperature for one hour, then probed overnight for EGFR (1:1000, Cell Signaling #4267) and GAPDH (1:1000, Cell Signaling #2118). Primary antibody solutions were prepared in 5% bovine serum albumin (Fisher Scientific) dissolved in Pierce™ TBS Tween™ 20 Buffer (Thermo Fisher). Chemiluminescence was generated using SuperSignal™ West Pico PLUS Chemiluminescent Substrate (Thermo Fisher), then detected using the Azure 500 imager (Azure Biosystems). Image analysis was performed using imageJ. Background-subtracted EGFR band intensity was normalized first to GAPDH, then to the static control for quantification of relative protein expression.

4.2.8 Confocal Microscopy

OVCAR8 cells were seeded in μ-Slide $I^{0.6}$ Luer chips (ibidi) at 250,000 cells/chip and incubated overnight for attachment. Next, 5 μM PIC treatment was administered under static or flow (1 dyne/cm^2) conditions for 5 hours. Cells were immediately fixed in 10% neutral buffered formalin (Millipore Sigma) for 15 minutes then stained with NucBlue™ Live ReadyProbes™ Reagent (Invitrogen). Confocal images were collected using a 405 nm laser with emission windows of 430-470 nm (nuclei) and 650-750 (BPD).

4.2.9 Statistical Analysis

In this study, PRISM version 9.0.2 for MacOS was used for statistical analysis. ImageJ was used for quantification of photoimmunoconjugate purity and western blotting. Data were analyzed using unpaired t-test (where two groups are compared)

and one-way ANOVA (where three or more groups are compared). Post-hoc tests used within each figure are specified in the figure captions. P values ≤ 0.05 were considered statistically significant, where * $p \leq 0.05$; ** $p \leq 0.01$; *** $p \leq 0.001$; **** $p \leq 0.0001$; ns: nonsignificant.

4.3 Results

4.3.1 Photoimmunoconjugate stability and cell viability are maintained under transient fluid shear stress, while EGFR expression is modestly attenuated

A model for the delivery of photodynamic agents under FSS culture was established using the ibidi Pump System and μ-Slide $I^{0.6}$ Luer chips (ibidi). This model was first implemented for the evaluation of flow-induced changes in PIC purity and cellular properties **(Figure 4.2A-C)**. Purity was evaluated to ensure that treatment under FSS conditions would not compromise PIC conjugation. In these experiments, PIC was run through the pump for 30 minutes at 1 dynes/cm^2 in cell culture medium or PBS. Perfusate was then collected and subjected to gel electrophoresis for imaging of fluorescence (ex/em: 435/700) and total protein **(Figure 4.2A-B)**. The quantified purity data (**Figure 4.2C)** revealed that PICs retained purity following FSS culture conditions. Next, drug-free experiments were performed to evaluate the cellular effects of transient FSS (30 minutes, 1 dynes/cm^2). **Figure 4.2D** shows that flow conditions did not cause significant alterations in cell viability (analyzed by NRU assay) compared to static controls. Images of cells following culture in static and flow conditions showed no significant morphological differences. (**Figure 4.2E**) Quantification of cellular EGFR expression revealed a

13% decrease ($p < 0.05$) following FSS culture (30 minutes, 1 dynes/cm^2) (**Figure 4.2F-G**).

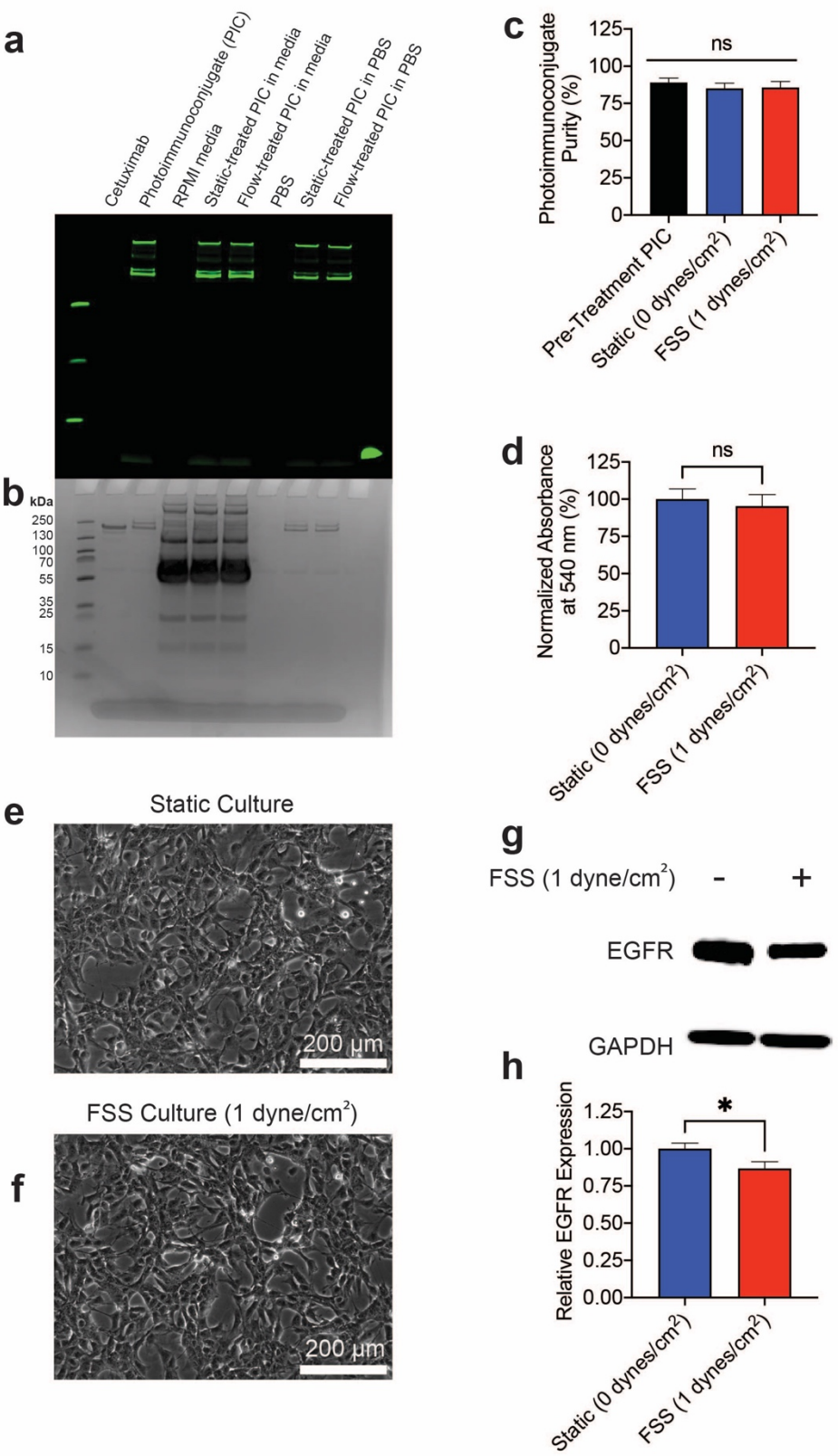

Figure 4.2: Transient fluid shear stress-induced effects on PIC purity, cell viability, and EGFR expression.

(a-c) Comparison of PIC purity following incubation under static or flow conditions. This data is representative of three gels. Cell viability (d), morphology (e-f), and EGFR expression (g-h) were evaluated following drug-free treatment under static or 1 dynes/cm^2 conditions for 30 minutes. Viability and western blot data are representative of at least 3 ibidi chips. Statistical analysis was performed using one-way ANOVA (c) and t-tests (d, h). Error bars represent the standard error of the mean. * $p \leq 0.05$; ns: nonsignificant. All data shown is representative of at least three datapoints.

4.3.2 Longitudinal binding analysis reveals that transient fluid shear stress modulates PIC-based BPD localization in a time-dependent manner.

Next, the role of FSS in longitudinally modulating subcellular photosensitizer compartmentalization was examined. Data in the plasma membrane and organelle compartments revealed a time-dependent increase in BPD accumulation over time, reaching an observable plateau by 3 hours at ~0.24 pmoles and ~0.28 pmoles, respectively (**Figure 4.3A-B**). No significant differences in plasma membrane protein levels were observed, though a significant increase from 4.08 to 11.34 μgrams protein ($p < 0.01$) was observed for the organelle compartment at 30 minutes. Longitudinal data for the nuclear compartment reveals overall more BPD following FSS culture, with statistically significant increases at 30 minutes and 300 minutes ($p < 0.01$) (**Figure 4.3C**). Nuclear protein remained unchanged longitudinally between static and flow conditions. In the cytosolic compartment, which contains the most cellular proteins, higher amounts of BPD are observed under FSS treatment conditions compared to static, with a significant increase at 240 minutes ($p < 0.05$) (**Figure 4.3D**). Total BPD was normalized to protein (**Figure 4.4**) to analyze changes in BPD with consideration for protein modulation within each compartment. Fold changes in BPD/protein averaged across all time points from 10-300 minutes revealed that FSS-

mediated PIC delivery changes uptake by 1.01-fold, 0.97-fold, 2.52-fold and 7.03-fold in the plasma membrane, organelle, nuclear, and cytosol fractions, respectively.

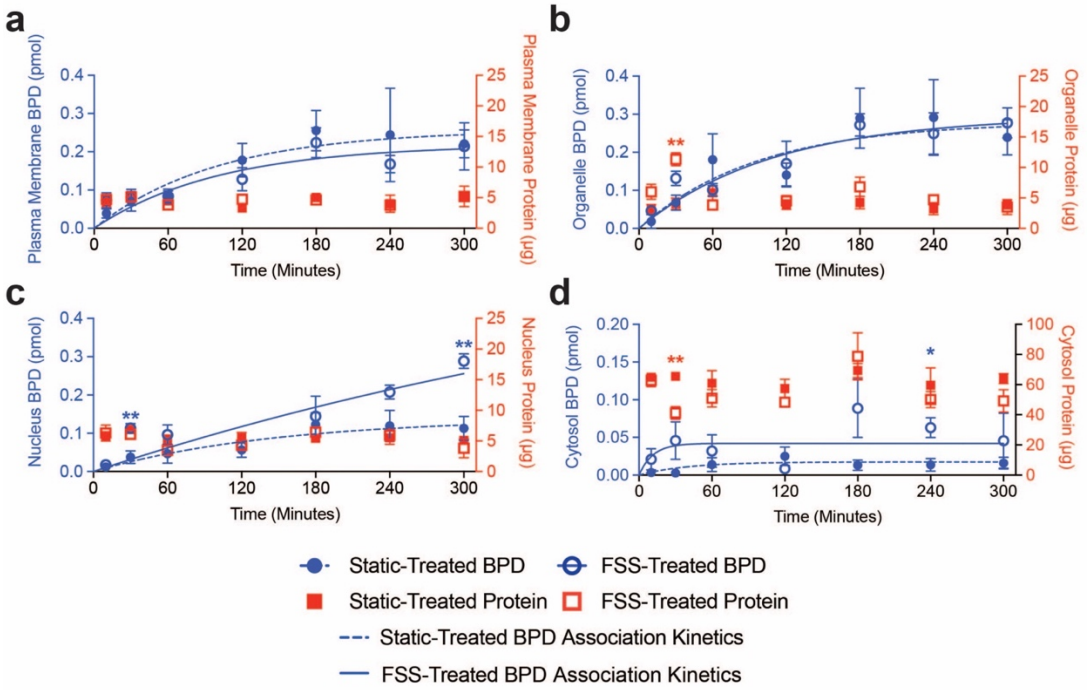

Figure 4.3: Longitudinal monitoring of subcellular photosensitizer and protein under transient fluid shear stress.

Confluent monolayers of OVCAR8 cells were treated with 1 uM PIC under static or FSS (5 dynes/cm^2) conditions for 10, 30, 60, 120, 180, 240, and 300 minutes. At each time point, cells were fractionated using Minute™ Plasma Membrane Protein Isolation and Cell Fractionation Kit (Invent Biotechnologies, Inc.). Longitudinal data for total BPD and protein are plotted for the plasma membrane (a), organelle compartment (b), nucleus (c), and cytosol (d). BPD association profiles are shown for the groups treated under static and FSS conditions with a dotted blue line and a solid blue line, respectively. Statistical analysis was performed using t-tests at each time point. Error bars represent the standard error of the mean. * $p \leq 0.05$; ** $p \leq 0.01$; *ns: nonsignificant.* Each point is representative of at least 6 ibidi chips.

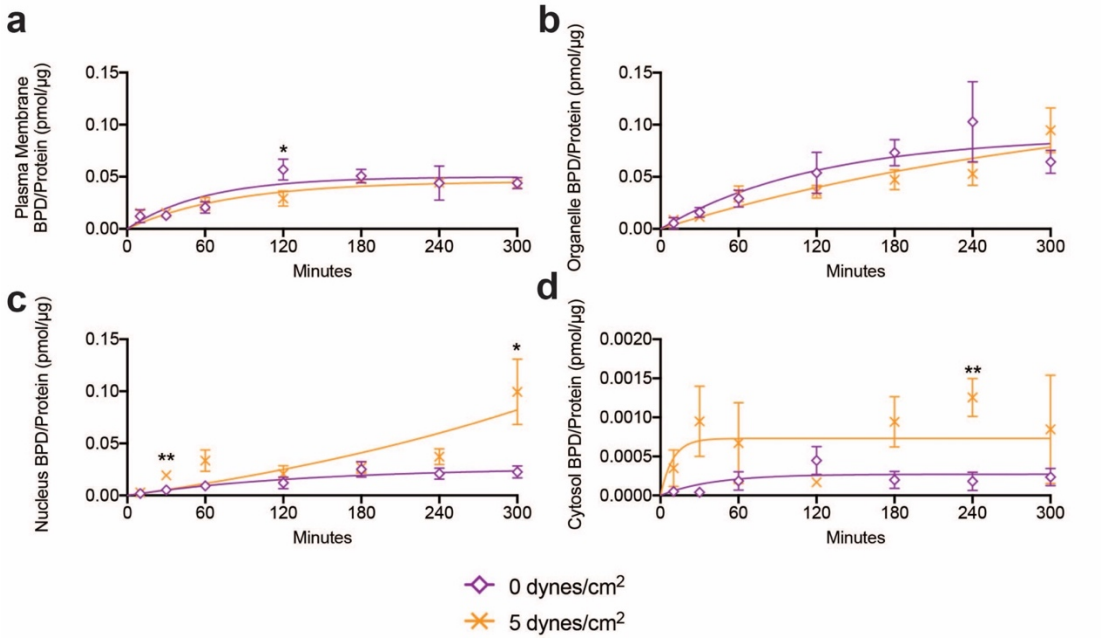

Figure 4.4: Longitudinal monitoring of BPD/Protein under transient fluid shear stress.

The total BPD is normalized to the total protein at each compartment: plasma membrane (a), organelle (b), nucleus (c), and cytosol (d). Data points are plotted at each time point along with kinetic association profiles. Statistical analysis was performed using unpaired t-tests at each time point, and error bars represent the standard error of the mean. * $p \leq 0.05$; ** $p \leq 0.01$ *ns: nonsignificant.* Each point is representative of at least 6 individual ibidi chips.

4.3.3 Total cellular uptake varies with fluid shear stress.

Following PIC treatment under 0, 0.5, 1, or 5 dynes/cm^2, total cellular BPD and protein were quantified (**Figure 4.5**). While FSS-mediated PIC treatment did not induce significant changes in total cellular protein, cellular BPD increased from 0.42 to 0.79 pmoles ($p < 0.05$), 0.74 pmoles ($p < 0.01$), and 0.63 pmoles for 0.5, 1, and 5 dynes/cm^2, respectively (**Figure 4.5A**). Results for total BPD vs. total cellular protein are plotted in **Figure 4.5B**. Groups treated under FSS tend to cluster higher on the graph with respect to the y-axis (BPD). Normalized BPD/protein increased under FSS conditions by 1.95-fold ($p < 0.01$), 1.71-fold ($p < 0.01$), and 1.62-fold for 0.5, 1, and 5 dynes/cm^2, respectively (**Figure 4.5C**). Considering the heterogeneity of ovarian

cancers, we next investigated PIC uptake under static versus FSS conditions (1 dyn/cm^2) of a secondary high grade serous cell line, OVCAR3 (**Figure 4.6**). PIC delivery to OVCAR3 cells, measured in BPD normalized to protein, increased under FSS by ~70%.

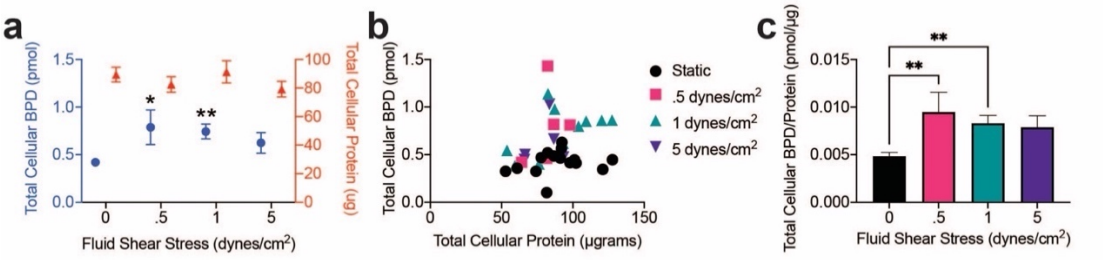

Figure 4.5: Comparison of total BPD, total protein, and BPD/protein at varying fluid shear stresses.

OVCAR8 cell monolayers plated µ-Slide I$^{0.6}$ Luer chips were treated with 1 µM PIC for 30 minutes under static or FSS (0.5, 1, 5 dynes/cm^2) conditions. Total BPD and protein were quantified by UV-Vis spectrophotometry and BCA, respectively. Averaged data (a) and individual datapoints (b) are shown, as well as the normalized BPD/protein (c). Statistical analysis was performed using a one-way ANOVA, and FSS data were compared to static controls using post hoc Dunnet test. Error bars represent the standard error of the mean. ** $p \leq 0.05$; ** $p \leq 0.01$; ns: nonsignificant.* Each point is representative of at least 5 individual ibidi chips (a,c).

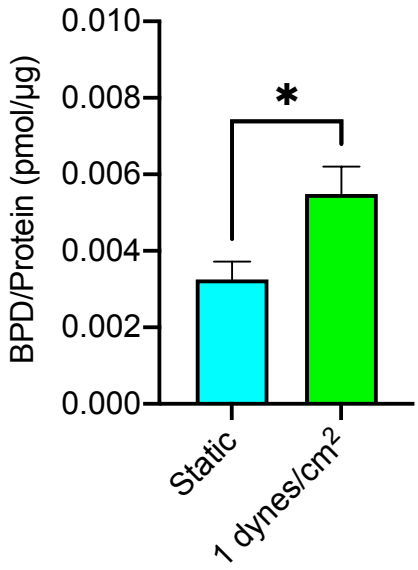

Figure 4.6: PIC uptake by OVCAR3 under static and FSS conditions

OVCAR3 cells were seeded at 250,000 cells per chip in µ-Slide $I^{0.6}$ Luer chips, and after overnight incubation, treated with 1 µM PIC under 0 or 1 dyne/cm2 for 30 minutes. BPD/Protein was quantified as described in *Materials and Methods*. Each bar is representative of five individual ibidi chips.

4.3.4 Varying fluid shear stress modulates subcellular photosensitizer localization and compartmentalization.

FSS-dependent variations in subcellular localization (**Figure 4.7**) and compartmentalization (**Figure 4.8**) were characterized. For all subcellular compartments, FSS culture during photosensitizer treatment enhanced BPD accumulation at all flow rates compared to the static control (**Figure 4.7 A-D**). BPD localization in the plasma membrane increased from 0.057 pmoles at 0 dynes/cm^2 to 0.079, 0.135, and 0.081 pmoles for 0.5, 1, and 5 dynes/cm^2, respectively. In the organelle compartment, BPD in static groups averaged 0.087 pmoles, whereas increases in moles of BPD to 0.125, 0.187 ($p < 0.01$), and 0.131 pmoles were observed with at 0.5, 1, and 5 dynes/cm^2, respectively. Nuclear BPD localization

increased drastically under FSS-mediated treatment, with 0.037 pmoles under static conditions increasing to 0.147 ($p < 0.01$), 0.191 ($p < 0.0001$), and 0.113 ($p < 0.05$), pmoles at 0.5, 1, and 5 dynes/cm^2, respectively. Cytosolic BPD was approximately 0 pmoles following PIC incubation under static culture for 30 minutes, but increased to 0.049, 0.152 ($p < 0.001$), and 0.046 pmoles with increasing FSS. Variations in compartmental protein levels were less consistent, though some significant changes were revealed. In the plasma membrane, protein increased significantly between 0 and 1 dynes/cm^2 (5.22 to 10.57 μgrams, $p < 0.05$). In the organelle compartment, protein increased from 4.78 to 11.34 μgrams ($p < 0.05$) at 0 and 5 dynes/cm^2, respectively. No significant changes in nuclear protein were observed, though cytosolic protein decreased from 65.51 μgrams at 0 dynes/cm^2 to 41.20 μgrams at 5 dynes/cm^2 ($p < 0.05$).

Trends in BPD vs. protein were next explored (**Figure 4.7 E-H**). Plasma membrane data revealed that FSS conditions enhanced BPD and protein levels compared to static conditions. In the organelle compartment, nearly all the FSS-cultured groups showed higher amounts of total protein, and most showed higher amounts of BPD uptake, with respect to the static controls. Within the nuclear fraction, FSS data are loosely grouped above static with respect to the y-axis, without consistent differences along the x-axis (protein). In the cytosol, there are no clear trends in grouping of protein levels with varied FSS, though BPD is observably higher for most groups treated under FSS. Next, BPD was normalized to protein (**Figure 4.7 I-L**), revealing notable increases in the nuclear compartment from 0.005 at 0 dynes/cm^2 to 0.019, 0.024 ($p < 0.01$), and 0.019 ($p < 0.05$) pmoles/μgram at 0.5,

1, and 5 dynes/cm^2, respectively. In the cytosol compartment, BPD/protein increased from ~4e-5 pmoles/μgram at the static condition by 50-fold at 1 dynes/cm^2 ($p < 0.01$), and ~20 fold at 0.5 and 5 dynes/cm^2. Percentage of total cellular BPD and protein contained within each subcellular compartment was next investigated (**Figure 4.8**). BPD and protein values were summed across all fractions, then values in each fraction were divided by the sum to determine percentages. Under flow, percent BPD decreased in the organelle fraction and increased in nuclear and cytosol fractions (**Figure 4.8 A)**. Organelle-localized percent protein increases under flow from 6% under static treatment to ~13% under flow **(Figure 4.8 B)**. Cytosolic percent protein reveals a concomitant decrease from 80% under static treatment to an average of 68% under flow. Confocal microscopy was used to further confirm enhanced PIC delivery under FSS conditions (**Figure 4.9**).

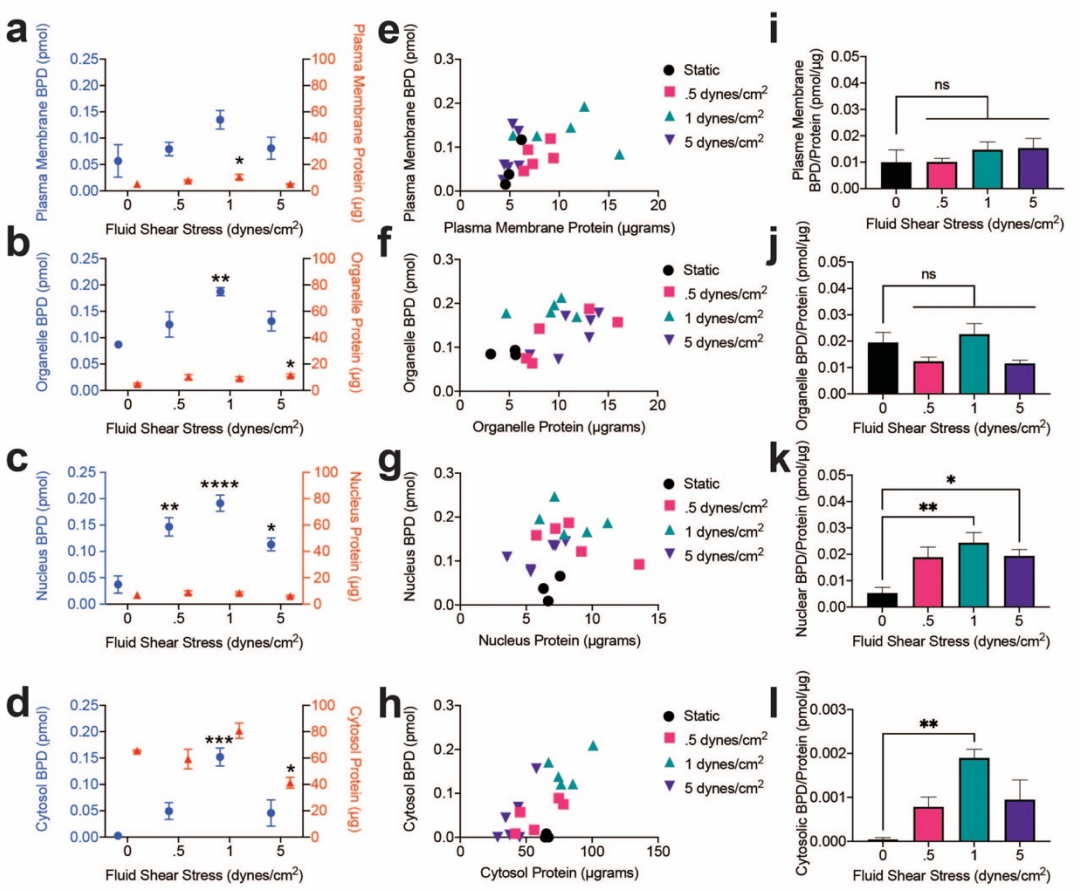

Figure 4.7: Fluid shear stress-dependent changes in subcellular BPD and protein compartmentalization.

Monolayers of OVCAR8 cells were treated with 1 µM PIC under static or FSS (0.5, 1, 5 dynes/cm^2) conditions, then fractionated for subcellular analysis of BPD, protein, and BPD/protein. FSS-dependent changes in BPD and protein (a-d). Individual datapoints for BPD versus protein (e-h). Normalized BPD/protein in each compartment (i-l). Statistical analysis was performed using a one-way ANOVA, and FSS data were compared to static controls using post hoc Dunnet test. Error bars represent the standard error of the mean. * $p \leq 0.05$; ** $p \leq 0.01$; *** $p \leq 0.001$; **** $p \leq 0.0001$; *ns: nonsignificant.* Each datapoint shown is representative of at least three ibidi chips (a-d, i-l).

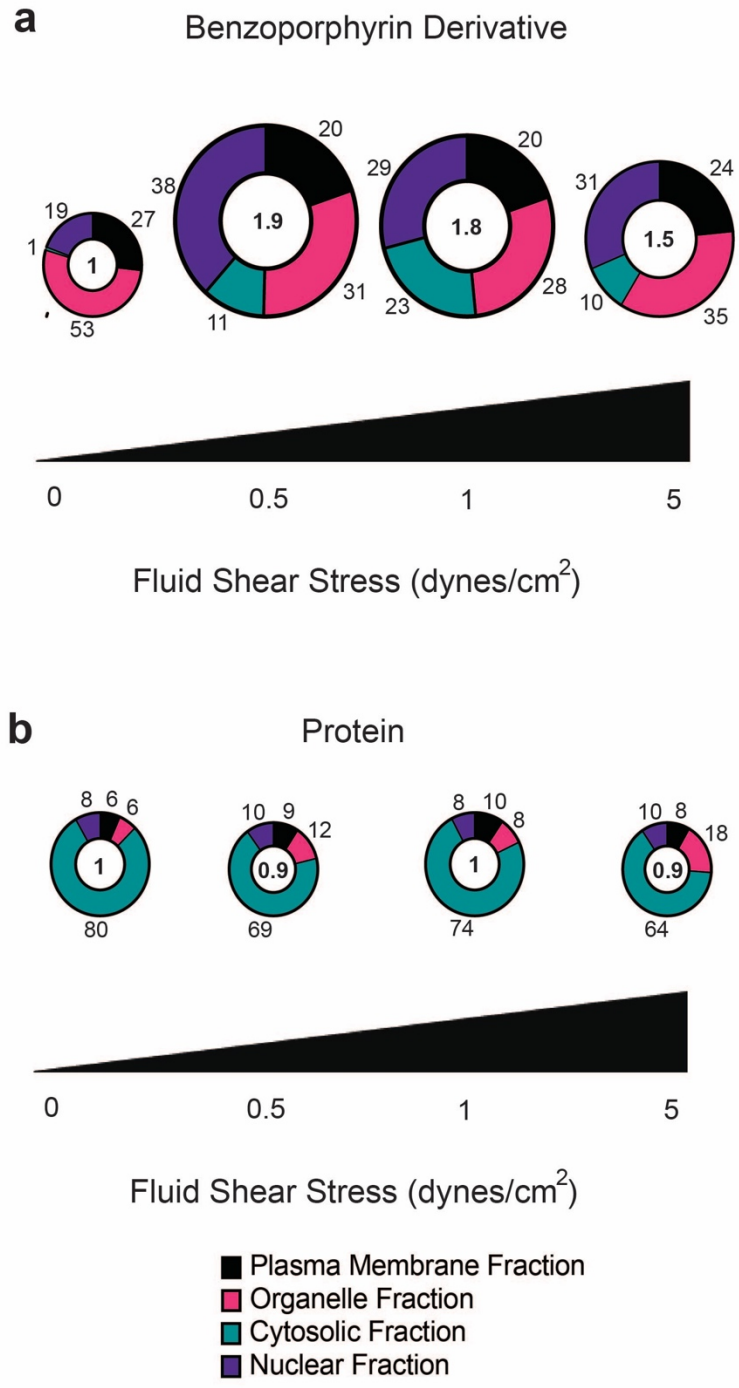

Figure 4.8: Percent distribution of BPD and protein among subcellular compartments.

Total BPD (a) and total protein (b) values were summed across all compartments, then values in each compartment were divided by the sum to determine percentage.

Circle diameter is equal to the fold change in total BPD or protein compared to static condition. Fold change is listed inside each circle. Compartment percentages are listed outside each segment.

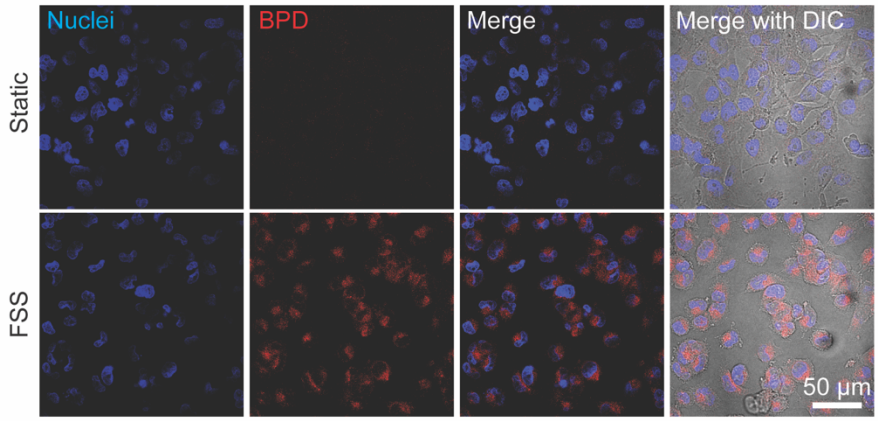

Figure 4.9: Confocal fluorescence imaging of PIC uptake.

250,000 OVCAR8 cells were seeded in µ-Slide $I^{0.6}$ Luer chips and incubated overnight for attachment. Chips were next treated with 5 µM PIC under static or FSS (1 dyne/cm^2) conditions for five hours. Chips were fixed in 10% neutral buffered formalin and stained for nuclei prior to confocal imaging. The scale bar represents 50 µm.

4.3.5 Transient flow-mediated delivery enhances cytotoxicity of three photosensitizer formulations in a light-dose dependent manner

Next, cytotoxicity of photodynamic agents delivered under static or FSS conditions was assessed. Multiple formulations were included to evaluate variations across free photosensitizer (BPD), antibody-conjugated photosensitizer (PIC), and liposome-conjugated PIC (PIC-Nal) (**Figure 4.10**). The PIC-Nal formulation was previously developed by us [327]. PIC-Nal size, PDI, zeta potential, and stability under FSS were tested (**Table 4.2; Figure 4.11**). There were no significant differences in size and PDI between FSS-treated and static-treated PIC-Nal after 30 minutes or 2 hours, indicating overall stability. Photoactivity was quantified for all formulations (**Figure 4.12**), revealing 0.6%, 3.4%, and 10.6% photoactivity for BPD,

PIC, and PIC-Nal, respectively. For PIC-treated groups, cell viability decreased with flow treatment from 89 to 74%, 80% to 65.5% ($p < 0.05$), 76% to 64.25% ($p < 0.001$), and 62.7% to 51% ($p < 0.05$) for 10, 20, 40, and 80 J/cm^2, respectively (**Figure 4.13 A**). For cells treated with PIC-Nal, flow treatment decreased viability from 88% to 86.3%, 81% to 67.7%, 73% to 65%, and 67.7% to 50% ($p < 0.01$) at 10, 20, 40, and 80 J/cm^2, respectively (**Figure 4.13 B**). Free BPD induced the most potent cytotoxicity, which was improved further still by flow-mediated delivery from 60% to 45%, 47.7% to 27.3% ($p < 0.05$), 35% to 15.3% ($p < 0.01$), and 12.7% to 5% at each increasing light dose (**Figure 4.13 C**). Next, total cellular photosensitizer uptake profiles were compared between each photosensitizer formulation (**Figure 4.13 D-F**). Consistent with the cytotoxicity data, FSS-mediated delivery enhanced total cellular uptake across all formulations. Uptake improved under flow by ~67% for BPD ($p < 0.001$), 60% for PIC ($p < 0.001$), and ~43% for PIC-Nal. We also confirmed, using EGFR-negative cells (J774), that the FSS-enhanced uptake of PIC is dependent on EGFR-expression. While BPD uptake by J774 cells increased significantly under FSS, PIC uptake did not change. (**Figure 4.14**).

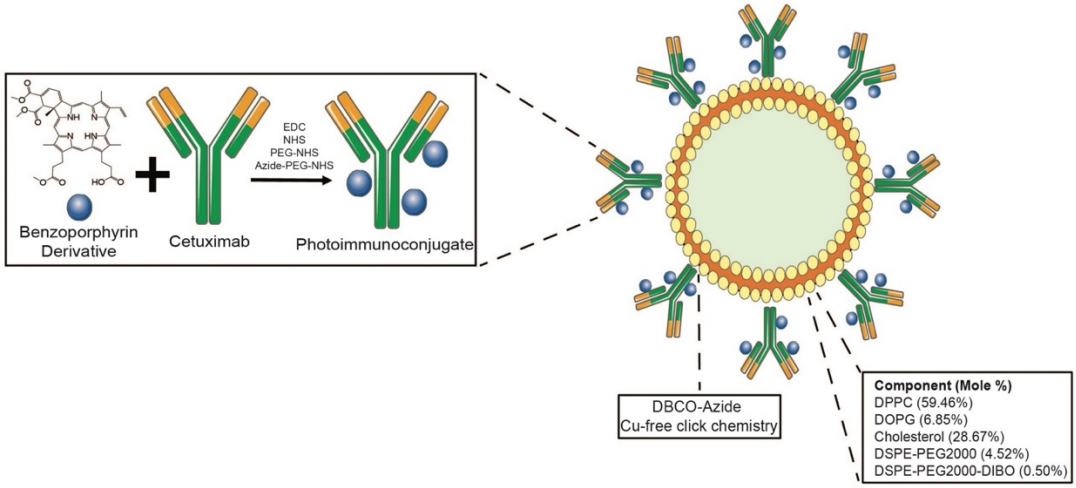

Figure 4.10: Photosensitizer formulation schematic.

BPD, PEG-NHS, and Azide-PEG-NHS are conjugated to Cet using carbodiimide chemistry to generate photoimmunoconjugates. The photoimmunoconjugate is then linked to liposomes using copper-free click chemistry. Figure graphics were created using images courtesy of smart.servier.com.

Table 4.2: Physical characterization of liposomal formulations. Data is representative of at least 3 nanoparticle batches.

Sample	Diameter (nm)	PDI	Zeta Potential (mV)	PIC Conjugation Efficiency (%)
Nal	121.38 ± 3.58	0.09 ±0.008	-12.57 ±0.88	N/A
PIC-Nal	135.11 ± 0.79	0.15 ± 0.005	-15.39 ±0.213	33.75 ± 1.76

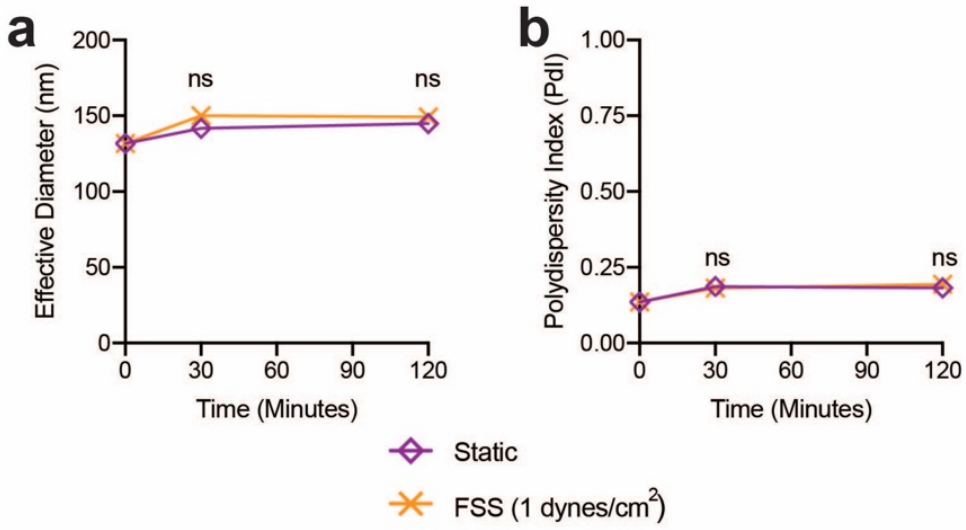

Figure 4.11: Stability of PIC-Nal under FSS.

PIC-Nal (1 μM) was run through cell-free chips in UltraPure distilled water at 1 dynes/cm^2. The perfusate was sampled at 30 and 120 minutes, then size (a) and PdI (b) were quantified. Statistical analysis was performed using unpaired t-tests at each time point, and error bars represent the standard error of the mean. *ns: nonsignificant.* Each point shown is representative of at least 3 nanoparticle batches.

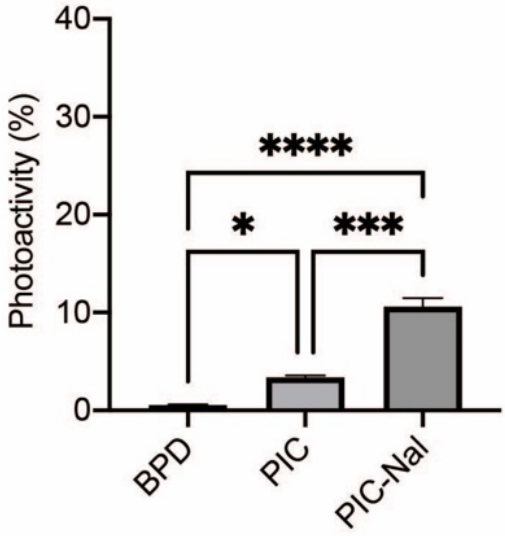

Figure 4.12: Photoactivity of three photosensitizer formulations.

Photoactivity was quantified for BPD, PIC, and PIC-Nal by dividing the maximum fluorescence intensity in water by the maximum fluorescence intensity by in DMSO. Statistical analysis was performed using a one-way ANOVA with post-hoc Tukey test. Error bars represent the standard error of the mean. * $p \leq 0.05$; *** $p \leq 0.001$; **** $p \leq 0.0001$ *ns: nonsignificant.* Each bar shown is representative of 3 individual datapoints.

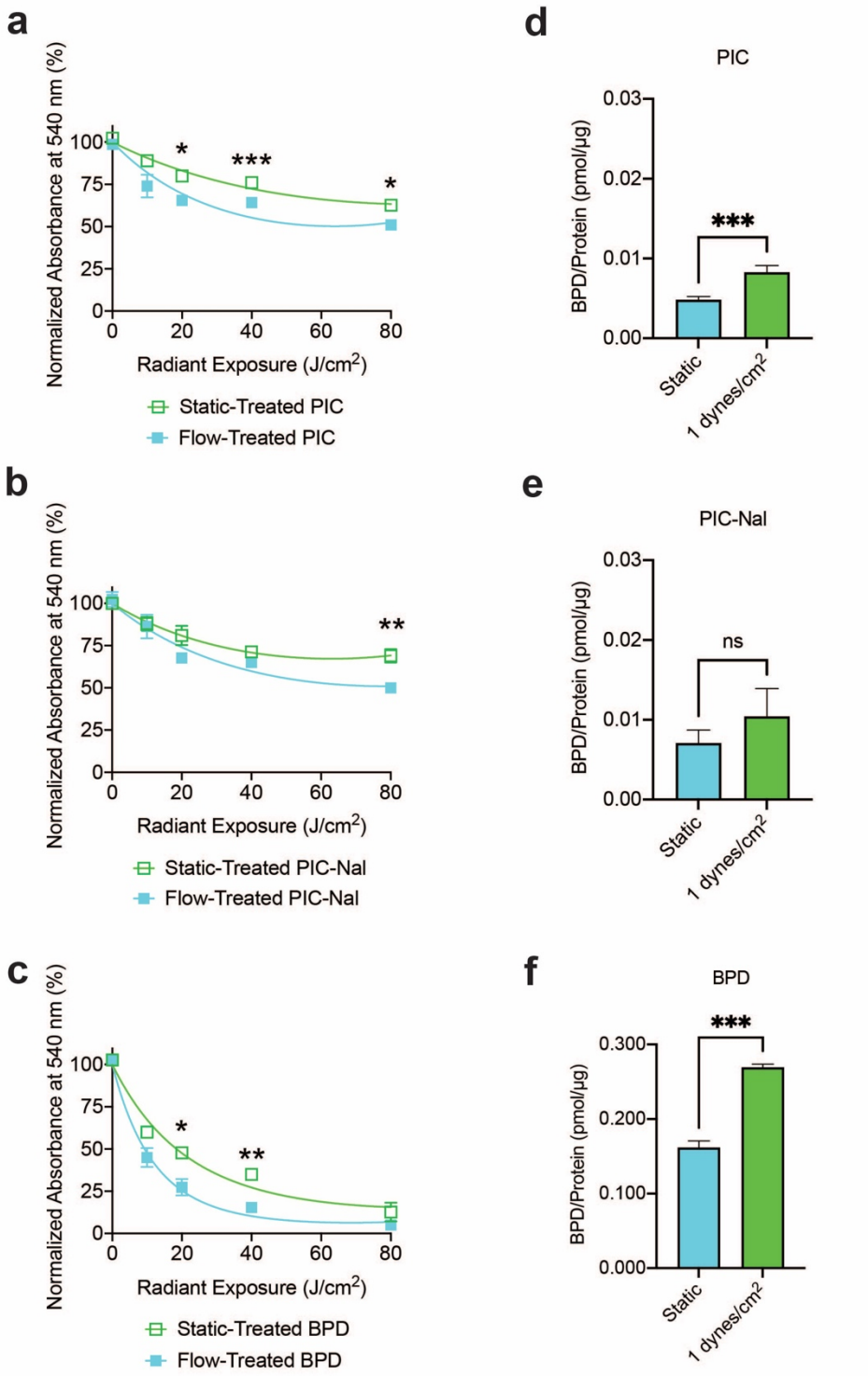

Figure 4.13: Cytotoxicity and uptake of three photosensitizer formulations following transient flow-mediated treatment.

Confluent monolayers of OVCAR8 cells were treated with 1 µM PIC (a), 1 µM PIC-Nal (b), or 1 µM free BPD (c) for 30 minutes under static or FSS (1 dynes/cm^2)

conditions. Next, medium was exchanged and chips were irradiated with a 690 nm laser at 10, 20, 40, or 80 J/cm^2 (100 mW/cm^2). After 4 hours, cell viability was analyzed by NRU. For uptake studies, cells were incubated under static or FSS conditions with PIC (d), PIC-Nal (e), or BPD (f), then immediately washed, collected, and analyzed as described in *Methods*. Statistical analysis was performed using unpaired t-tests. Error bars represent the standard error of the mean. *$* p \leq 0.05$; **$* p \leq 0.01$; ***$* p \leq 0.001$ *ns: nonsignificant.* Each bar shown is representative of 3 individual ibidi chips.

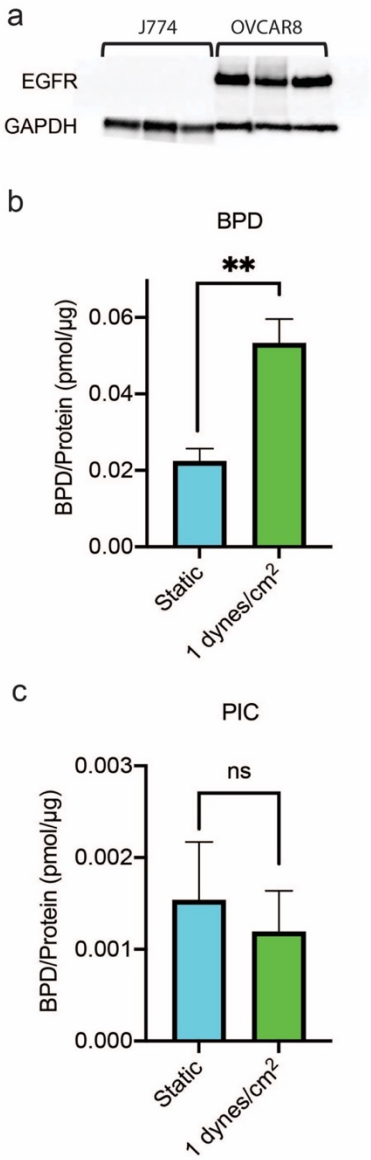

Figure 4.14: Fluid shear stress-mediated uptake evaluation in EGFR-negative J774 cells.

Expression of EGFR by OVCAR8 and J774 cells was evaluated by western blotting (a). Next, J774 cells were treated with 1 μM BPD (b) or PIC (c) under static or FSS conditions (1 dynes/cm^2) for 30 minutes. Cellular BPD (pmoles) was normalized to total protein (μg) to quantify photosensitizer uptake. ** $p \leq 0.01$; *ns: nonsignificant.* Western blot data is representative of three 35-mm dishes. Uptake data is representative of three ibidi chips.

4.4 Discussion

Cancers in the peritoneal cavity are currently treated with fluid flow-based drug delivery in the HIPEC procedure, but the potential of transient flow as an amplifier of photochemical efficacy remains largely unknown. This chapter sheds light on the potential application of transient flow in PIC delivery and the efficacy of EGFR-targeted PIT. Numerous models of flow-mediated drug delivery have been examined in previous work [361,363,364,382-390]. Recently, using a perfusion model with adherent 3D ovarian cancer nodules, we found that FSS (3 dynes/cm^2) induced resistance to carboplatin, but not photoimmunotherapy [364]. The same study also showed that extended exposure to FSS (7 days) resulted in upregulation of phosphorylated ERK 1/2 and EGFR. In contrast, **Figure 4.2** shows a 13% decrease ($p < 0.05$) in EGFR expression following 30 minutes of exposure to FSS. There may, therefore, be kinetic variations in the biological effects of FSS on protein expression, internalization, and degradation. As recently reviewed by López-Hernández et al. [391], cells may increase cellular endocytosis and subsequent lysosomal degradation of plasma membrane proteins in response to environmental stresses. In support of this, He et al. anchored hairpin-type fluorescent DNA probes to the cell surface to track the internalization of cell surface proteins under FSS [392]. They found that FSS enhanced the endocytosis of plasma membrane proteins, resulting in probe

localization at the mitochondria and lysosomes. Time-dependent effects of FSS on endothelial cell uptake of PECAM-targeted nanoparticles were previously examined by Han et al. [363]. They compared acute (30 minutes) versus chronic (16 hours) FSS and uncovered opposing effects on uptake. Chronic FSS caused decreased nanoparticle uptake that was linked to morphological cellular alignment in the direction of flow and the formation of actin stress fibers. Treatment under acute FSS caused increases in nanoparticle uptake that were dependent on flow rate and number of antibodies per nanoparticle.

This is the first study, to our knowledge, to evaluate the dynamics of PIC binding and internalization in EGFR-expressing cancer cells under FSS. (**Figure 4.3; Figure 4.4**). Previous studies show that Cet-EGFR binding induces internalization of the Cet-EGFR complex, followed by trafficking to intracellular compartments including the endosome, lysosome, endoplasmic reticulum, and nucleus [374-377]. Work by Patel et al. found that when Cet binds to the EGFR-expressing cell surface, it begins internalization within minutes [376]. Localization increases gradually over the course of four hours. Similarly, we showed that photosensitizer localization was detectable in the plasma membrane and organelles in as early as 10 minutes after incubation/treatment, and accumulation plateaued after roughly 3 hours (**Figure 4.3**). Our studies also revealed rapid nuclear localization, which was significantly enhanced under FSS culture after a 30-minute incubation. Consistent with these findings, Liao et al. showed, by western blot, that EGFR localizes to the nucleus as early as 30 minutes following incubation of MDA-MB-468 cells with Cet.

We next evaluated the effect of varying FSS (0.5, 1, 5 dynes/cm^2; 1.16, 2.31, 11.55 mL/minute) on the total cellular (**Figure 4.5**) and subcellular (**Figures 4.7, 4.8**) BPD, protein, and BPD/protein. The total cellular BPD and BPD/protein increased significantly under 0.5 and 1 dynes/cm^2 compared to the static control (**Figure 4.5**). The total BPD and BPD/protein also increased at 5 dynes/cm^2, however these changes did not reach statistical significance. Similar trends are seen within all subcellular compartments (**Figure 4.7**), where pmoles BPD increased at 0.5 and 1 dynes/cm^2 compared to the static condition, and then began to decrease at 5 dynes/cm^2. This highlights a phenomenon previously shown in literature in which a FSS "sweet spot" is achieved. Samuel et al. examined the effects of varying flow rate on the HUVEC uptake of 2.7 nm quantum dots, 4.5 nm quantum dots, and 50 nm silica particles [382]. Uptake was most notably enhanced at moderate flow rates (0.05, 0.1 Pa), but the increase in uptake was less pronounced at the highest flow rate (0.5 Pa). Han et al. investigated the role of varying flow rate in the internalization of PECAM-targeted nanocarriers [363]. It was found that for particles with 50 antibody per nanocarrier, uptake increased significantly between 1-4 dynes/cm^2, but not below (0.5 dynes/cm^2) or above (8 dynes/cm^2). Recently, Charwat et al. leveraged a complementary *in silico* and *in vitro* approach to evaluate the dynamic changes in uptake of 249 nm nanoparticles by endothelial cells under varying FSSs. They identified 1.8 dynes/cm^2 as the critical rate at which uptake is at a maximum. Above this rate, nanoparticle uptake decreased despite an increasing number of nanoparticles entering the system.

With increasing global use of HIPEC for intraperitoneal malignancies, FSS-based cancer treatment is a growing field of study. However, despite prior clinical use of photodynamic therapy for peritoneally disseminated cancers, the impact of FSS on photochemical treatments is largely unknown. In this study, three photosensitizer formulations were tested under FSS for the treatment of ovarian cancer *in vitro*. Multiple light doses were evaluated to account for light dose-dependent changes. All formulations exhibited trends toward greater cytotoxicity under FSS, with free BPD inducing the most cell killing compared to PIC and PIC-Nal (**Figure 4.13**). This is attributed to greatly enhanced uptake of free BPD compared to the antibody-based formulations. This is consistent with previous work that has shown enhanced uptake and anti-cancer effects of free photosensitizer compared to antibody-conjugated photosensitizer, though with the trade-off of poor cancer selectivity [236,327,345,369,378]. Additionally, unlike BPD and PIC, PIC-Nal uptake is not significantly enhanced under FSS-based treatment, though it trends towards an increase. Consistent with these observations, changes in toxicity under FSS are more modest for PIC-Nal compared to the other formulations. These formulation-based variations in uptake and cell killing are expected. As recently reviewed by Shurbaji et al., the effects of FSS on drug delivery and treatment effect are variable and depend on multiple factors including particle size, shape, charge, and elasticity [359]. Antibody-functionalized nanoparticles also vary in binding under FSS based on the number of antibodies per nanoparticle [363]. Based on these data, the clinical implementation of FSS-based photodynamic treatment will require careful

consideration of nanoparticle properties and treatment parameters to enhance treatment outcomes.

It is critical to acknowledge several limitations of the work in this chapter. One such consideration is that the clinical relevance of EGFR-targeted therapies for ovarian cancer remains ambiguous. Overexpression of the EGFR protein by ovarian cancers ranges widely from 9-62% [393]. Furthermore, efficacy of EGFR-targeted therapies for ovarian cancer has been limited [394]. As expertly reviewed by Bhandari et al. [395], previous work shows that while the binding of EGFR-targeted photoimmunoconjugates correlates with cellular EGFR expression, phototoxicity does not correlate with EGFR expression. This suggests that more factors are at play, such as the sensitivity of individual cancer cell lines. Still, EGFR-targeted photoimmunoconjugates are at the forefront of clinical photoimmunotherapy, with one clinically used formulation in Japan and four clinical trials in the United States. Additionally, photoimmunotherapy is a platform technology, where various photosensitizers and antibodies can be conjugated to target specific tumor antigens that are relevant for different cancers. Therefore, information from this study could help to advance the development of photoimmunoconjugates that target non-EGFR antigens for the treatment of ovarian cancer. Another limitation of this study is the variation between our flow model and physiological intraperitoneal flow. In this study, experiments are conducted under carefully controlled laminar flow, whereas flow in the peritoneal cavity is expected to be more turbulent. Further *in vivo* work is warranted to evaluate more physiologically-relevant flow as a carrier for photoimmunoconjugates.

4.5 Conclusion

In conclusion, this chapter examines the role of transient fluid shear stress as mediator of photoimmunoconjugate delivery and interrogates the subsequent treatment effects with three photosensitizer formulations. We first confirm that the conjugation of the photoimmunoconjugate remains stable and cell viability is not altered during treatment under transient fluid shear stress (**Figure 4.2**). Next, kinetic variations in photosensitizer delivery to subcellular compartments under static versus flow conditions are examined, revealing time-dependent changes in the BPD accumulation at the nucleus and cytosol (**Figure 4.3**). In contrast, BPD at the plasma membrane and organelles remains largely unchanged by treatment under fluid shear stress. Fluid shear stress-dependent changes in total and subcellular BPD and protein are next evaluated, demonstrating the most significant increases in BPD accumulation at 0.5 and 1 dynes/cm^2 (**Figures 4.5, 4.7**). We next evaluated subcellular compartmentalization of BPD and protein, revealing fluid shear stress-induced trends towards lower percent BPD at the organelles and higher percent BPD at the nucleus and cytosol fractions (**Figure 4.8**). Total protein values do not change significantly in flow-treated cells, however the compartmentalization of protein decreases at the cytosol by up to 16% and increases at the organelles by up to 12% between static and fluid shear stress conditions. **Figure 4.13** shows the enhancement in phototoxicity of three photosensitizer formulations when treated under fluid shear stress compared to static conditions. Cell killing caused by free photosensitizer, photoimmunoconjugate, and photoimmunoconjugate-coated liposomes are all enhanced when administered at 1 dyne/cm^2. Overall, these preclinical data implicate flow-based treatment as a

powerful parameter in the use of photoimmunotherapy for the treatment of peritoneally metastasized cancers.

Chapter 5: The Role of PARP Inhibition in Evolutionary Dynamics of Ovarian Cancer

In our previous work, a dual-fluorescent co-culture model was developed to study the population dynamics of the drug sensitive human ovarian cancer cell line (OVCAR8-DsRed2) and its resistant subline that overexpresses P-gp (NCI/ADR-RES-EGFP) during photodynamic therapy (PDT)-PARP inhibitor combination therapies [396]. The combination of olaparib treatment and BPD-PDT significantly reduced viability and enhanced DNA damage, but resulted in substantial selection pressures for the chemo-resistant subpopulation. In contrast, the use of lipid-conjugated BPD with olaparib mitigated these selection pressures by up to 18-fold. This work supports the use of PDT-PARP inhibitor combinational therapies, while motivating the use of lipid-conjugated photosensitizers to overcome multidrug resistance. Chapter 5 further realizes the PDT-PARP inhibitor combinational strategy through the invention of a novel nanotechnology. The most potent clinical PARP inhibitor, talazoparib, is loaded into the core of a polymeric nanoparticle, which is subsequently surface-decorated with photoimmunoconjugates to form PIC-NP-Tal. In parallel, a new 3-dimensional fluorescent co-culture model is developed using OVCAR-8-DsRed2 and NCI/ADR-RES-EGFP plated at equal ratios and tracked up to 12 days. PIC-NP-Tal and all relevant controls are evaluated in the 3D coculture model at multiple irradiation doses to thoroughly characterize combination and monotherapy effects on total spheroid ablation and relative changes in parental and subline cell population dynamics.

5.1 Introduction

As discussed in Chapter 2, the poly(ADP-ribose) (PAR) post-translational modification is a major biological regulator with broad roles in cell survival, gene expression, and energy metabolism [292]. The transfer of PAR chains to target proteins is accomplished by PAR polymerases (PARPs), which use NAD^+ as a substrate and generate nicotinamide as a byproduct. PARP-1 binds to DNA single-strand breaks (SSBs), initiating PARylation of acceptor proteins including PARP-1, histones, and other DNA repair proteins [293]. These appended PAR chains recruit additional DNA repair molecules for SSB rectification, such as XRCC1 [293,294]. In recent years, there has been increasing clinical interest in PARP inhibitors (PARPi) for oncologic applications, particularly in patients with *BRCA* mutations where synthetic lethality can be achieved [296]. Mechanistically, PARPi function through 1) directly competing with NAD+ at the PARP catalytic site and 2) trapping PARP at the SSB site, forming toxic PARP-DNA complexes [397].

PARPi first entered the clinical sphere in 2014 with the FDA and EMA approvals of olaparib for the treatment of advanced ovarian cancer [296]. Since then, three additional PARPi (rucaparib, niraparib, and talazoparib) have been FDA-approved for clinical use. These agents have been used for the treatment of numerous malignancies including ovarian, breast, pancreatic, prostate, fallopian, and primary peritoneal cancers [296]. Talazoparib, the most recently FDA-approved PARPi, exhibits the greatest potency compared to olaparib, rucaparib, and niraparib, with lower IC_{50} values for PARPs-1, -2, -3, -4, and the strongest PARP trapping capabilities [398,399]. While talazoparib is the most potent PARPi, it is also the most

toxic to normal cells and the most poorly tolerated. As a result, maximum tolerated dose of talazoparib is at least 300-fold lower than that of other clinically used PARPi [400]. Combinational therapeutic strategies are a cornerstone in cancer therapeutics that may be leveraged to enable dose reductions of the individual therapies while maximizing anti-cancer effects [401]. In this study, a novel nanoplatform is engineered for ovarian cancer-targeted codelivery of talazoparib with photodynamic therapy (PDT).

PDT, as explained in Chapter 2, involves the light-activation of photosensitive dyes (photosensitizers) resulting in the generation of reactive molecular species which can induce direct cytotoxicity and modulate biological processes [366]. Prior work has established harmonization between PDT and PARPi as an anti-cancer combination regimen for applications in ovarian, gastric, pancreatic, and skin cancers [396,402-404]. Tanaka *et al.* found that talaporfin-mediated PDT enhanced PARP-trapping capabilities of olaparib; and their combination significantly suppressed gastric tumor growth in a xenograft murine model [402]. Lei *et al.* codelivered chlorin e6 and olaparib to pancreatic cancer cells and demonstrated that their combination enhanced cytotoxicity, ROS generation, and DNA damage [403]. We have previously demonstrated that olaparib in combination with PDT using BPD effectively reduced survival and clonogenicity of a coculture system of chemo-sensitive and chemo-resistant ovarian cancer cells [396]. In the same study, we further demonstrated that a lipidated photosensitizer formulation reduced selective survival advantage of the chemo-resistant cells, effectively redirecting cancer evolution dynamics [396]. This exemplifies the potential of nanoengineered combination therapies for overcoming

critical barriers to clinical translation such as multidrug resistance. This is particularly relevant for PARP inhibitors, which have been shown in preclinical studies to induce acquired drug resistance through overexpression of multidrug resistance protein 1 (MDR1, P-gp, ABCB1). Rottenberg *et al.* compared olaparib-sensitive and olaparib-resistant tumors by quantifying the *abcb1a/b* genes that encode for murine and found up to 85-fold increase in over 70% of resistant tumors compared to those sensitive[405]. They further demonstrated that olaparib resistance could be reversed by the addition of a P-gp inhibitor, tariquidar. In another study, Oplustilova *et al.* showed, using a proliferation assay, that the P-gp inhibitor verapamil sensitized HCT116 colon cancer cells to PARP inhibitor KU 58948 [406].

In this study, nanoengineering approaches are leveraged for encapsulation of talazoparib in polymeric nanoparticles (NP-Tal). NP-Tal is surface-decorated with antibody-photosensitizer conjugates (photoimmunoconjugates, PIC) using click chemistry for dual functionalization with cancer-targeting capabilities and PDT (PIC-NP-Tal). Optimal synthesis parameters are established to determine the masses of polymer and talazoparib added to the synthesis, as well as PIC-to-nanoparticle ratio. In parallel, a three-dimensional coculture model of fluorescently labelled ovarian cancer cells is developed to examine evolution of multi-drug resistance. The model is comprised of the parental OVCAR8-DsRed2 cells grown with their chemo-resistant P-gp overexpressing subline, NCI/ADR-RES-EGFP. This model enables fluorescence-based longitudinal viability tracking of each cell line in response to treatment, potentiating precise dose optimization. Results demonstrate that low dose NP-Tal (0.01 μM) trends towards selection of the drug-resistant populations by

killing the parental OVCAR8-DsRed2 but sparing the NCI/ADR-RES-EGFP subline. In contrast, higher doses of NP-Tal (> 0.01 μM) kill both cell lines to similar degrees. Next, the combination of PIC and NP-Tal is compared to the conjugated PIC-NP-Tal to evaluate the role of conjugation on therapeutic effect. Results demonstrate potent combination effects of PIC and NP-Tal when mixed, but less potent effects when conjugated together. Additionally, treatment with PIC, BPD + NP-Tal, PIC + NP-Tal, and PIC-NP-Tal demonstrated selection pressures for the chemo-resistant subline, whereas NP-Tal alone and BPD alone kill both cell lines to equivalent degrees across all light doses tested. Results from this work provide fundamental implications for the combination of photoimmunotherapy (PIT) and PARP inhibition in the context of drug-resistant ovarian cancer.

5.2 Materials and Methods

5.2.1 Synthesis of Photoimmunoconjugates

PIC synthesis was performed as previously described [327]. First, 10 kDa methoxy PEG succinimidyl carboxymethyl ester (mPEG-NHS; JenKem Technology) was added dropwise to Cet at a 3:1 molar ratio and reacted overnight under continuous stirring. Next, BPD *N*-hydroxysuccinimidyl ester (BPD-NHS) and azide-PEG4-*N*-hydroxysuccinimidyl ester (azide-PEG-NHS; Thermo Scientific) were added to the reaction to a final ratio of 9 and 2.5 moles per 1 mole Cet, respectively. After another 20 hours of stirring, the mixture was purified using a 30 kDa Zeba spin desalting column (7 kDa MWCO; Thermo Scientific) and concentrated using an Amicon centrifugal filter unit (30 kDa MWCO, Millipore Sigma). Final Cet concentration was

determined by Pierce™ BCA Protein Assay Kit (ThermoFisher Scientific), and final BPD concentration was determined by UV-vis spectroscopy.

5.2.2 Synthesis of PIC-Functionalized Polymeric Nanoparticles

For talazoparib-loaded nanoparticles (NP-Tal), synthesis parameters were initially varied for protocol optimization (**Table 5.1**). PLGA-PEG-COOH and PLGA-PEG-DBCO were obtained from PolySciTech, and talazoparib (Tal) was obtained from MedChemExpress. Polymer was first co-dissolved with talazoparib in 1 mL of acetone, then added to 10 mL of ultrapure water (Invitrogen) containing 0.1% Pluronic F-68 (Gibco). The solution was sonicated with a probe sonicator for 3 minutes and acetone was evaporated at room temperature for 4-6 hours under continuous stirring at 400 rpm. The obtained NP-Tal were filtered through 0.22 μm syringe filter units (Millipore) and concentrated in an Amicon centrifugal filter unit (30 kDa MWCO, Millipore Sigma). Next, PIC was conjugated to the DBCO-containing nanoparticles through copper-free click chemistry. For conjugation, PIC and nanoparticles were mixed overnight at volume ratios of 0.5:1, 1:1, 2:1, and 3:1, then purified *via* Sepharose CL-4B size exclusion chromatography.

Table 5.1: Varying parameters in nanoparticle formulation

Parameter	**Values**
PLGA-PEG-COOH (mg)	10.7, 21.4, 42.8, 85.6
Tal (mg)	0, 0.107, 0.535, 1.07, 2.675
PLGA-PEG-DBCO/total polymer (%)	0, 25, 50, 100

5.2.3 Photophysical and Photochemical Nanoparticle Characterization

Talazoparib concentration was determined using a fluorescence-based standard curve (ex/em; 312/416 nm, Synergy neo2, Biotek). BPD concentration was calculated

similarly (ex/em; 435/700nm). Loading capacity (%) was calculated as the mass of polymer divided by the mass of loaded talazoparib. The talazoparib encapsulation efficiency (%) was calculated as the ratio of nanoparticle-loaded talazoparib to the initial talazoparib added to the nanoparticle synthesis reaction. Talazoparib retention (%) was calculated as the ratio of talazoparib after and before PIC conjugation. PIC conjugation efficiency (%) was determined by calculating the ratio of BPD loaded onto the nanoparticle to the initial BPD added to the conjugation reaction. PIC per nanoparticle was calculated by first determining molecules of PIC using Pierce™ BCA Protein Assay Kit (ThermoFisher Scientific), then dividing by the number of nanoparticles as determined by NanoSight LM10 (Malvern Instruments). Talazoparib per nanoparticle was calculated as molecules of talazoparib divided by number of nanoparticles. Nanoparticle size, PdI, and zeta potential were determined using the Nanobrook Omni (Brookhaven Instruments). To quantify photoactivity, compounds were dissolved in PBS or DMSO, then fluorescence emission was collected upon light-activation at 435 nm. Maximum fluorescence emission in PBS was divided by maximum fluorescence emission in DMSO for photoactivity values. Singlet oxygen generation was determined using the Singlet Oxygen Sensor Green (SOSG) probe (Invitrogen). Selectivity and uptake studies of PIC versus PIC-NP-Tal were performed with OVCAR8 (EGFR+) and J774 (EGFR-) cells. First, 300,000 cells were plated and incubated overnight. Next, dishes were treated with 1 μM PIC or PIC-NP-Tal for 30 minutes. Cells were lysed using radioimmunoprecipitation assay buffer, then BPD fluorescence was measured at ex/em 435/700 nm.

5.2.4 3D Ovarian Cancer Coculture System Development and Treatment Regimen

High grade serous ovarian cancer cell lines OVCAR8-DsRed2 and NCI/ADR-RES-EGFP were obtained courtesy of Dr. Michael M. Gottesman (National Cancer Institute, National Institutes of Health). Both cell lines were cultured in RPMI-1640 medium (Corning) supplemented with 10% fetal bovine serum (Gibco), 100 U/mL penicillin and 100 μg/mL streptomycin (Corning). Every four passages, media was supplemented with G418 (Invitrogen) at 500 μg/mL (OVCAR8-DsRed2) or 200 μg/mL (NCI-ADR-RES-EGFP). The growth dynamics of these cell lines on 2D substrates was described previously by our group [396]. In the present study, 3D spheroidal cocultures were generated by plating equal numbers of OVCAR8-DsRed2 and NCI/ADR-RES-EGFP to a final cell number of 1,000, 2,000, or 5,000 cells per well in ultra-low-attachment, round bottom 96 well plates (PerkinElmer). The Lionheart FX Automated Microscope (Biotek) was used for imaging 4 hours after plating, 24 hours after plating, and then every two days up to day 12. For treatment evaluation, 2,000 cells (1,000 of each cell line) were treated on day 4 for 24 hours prior to light activation (690 nm, Modulight, Inc.) on day 5. Longitudinal imaging was conducted as described above, and final cell viability analysis was conducted on day 12 using the CellTiter-Glo® Cell Viability Assay (Promega). Total killing controls were achieved by treating spheroids on day 12 with 5% bleach for four hours prior to viability analysis.

5.2.5 Statistical Analysis

GraphPad Prism version 9.0.2 was used for statistical analysis. All data shown were collected at least in triplicate and plotted as mean ± standard error of the mean.

Details regarding statistical testing are elaborated in figure captions, and statistical significance was determined as $P < 0.05$.

5.3 Results

5.3.1 Development of Talazoparib-Loaded Polymeric Nanoparticles

NP-Tal were prepared by nanoprecipitation methods, where acetone and ultrapure water were used for the organic and aqueous phase, respectively (**Figure 5.1a**). A representative TEM image of the NP-Tal is shown in **Figure 5.1b**. The development of nanoparticle synthesis optimization began with varying the initial amount of talazoparib added to the reaction (**Figure 5.1c-g; Figure 5.2**). For these studies, the amount of polymer (PLGA-PEG-COOH) added to the reaction was fixed at 10.7 mg. Tested masses of talazoparib included 0, 0.107, 0.535, 1.070, and 2.675 mg. The loading capacity was first measured (**Figure 5.1c**). Loading capacity initially increases, then plateaus, where a maximum is reached at 0.535 mg. This is further shown by encapsulation efficiency data (**Figure 5.1d**), calculated as the percent of initially added talazoparib that is successfully encapsulated in the nanoparticles. Encapsulation efficiency is consistently at ~3% when 0.107 and 0.535 mg are added ($p < 0.01$), then decreases at higher values. NP-Tal are ~15 nm larger than empty nanoparticles (**Figure 5.1e**), and sizes remain stable across formulations for up to 24 weeks (**Figure 5.2a**). PdI of all formulations was initially below 0.16 (**Figure 5.1f)** and remained stable at or below 0.21 for up to 24 weeks (**Figure 5.2b**). Zeta potentials (**Figure 5.1g**) remain relatively consistent across batches. For subsequent reactions, 0.535 mg was set as the talazoparib mass due to maximum loading being reached.

Next, the mass of PLGA-PEG-COOH added in the nanoparticle synthesis reaction was varied (**Figure 5.1h-l**). The initial mass of talazoparib was fixed at 0.535 mg, and polymer was added at 10.7, 21.4, 42.8 or 85.6 mg. No significant changes in loading capacity were calculated (**Figure 5.1h**), encapsulation efficiency increased with increasing polymer mass (**Figure 5.1i**), and size increased significantly for nanoparticles made with 42.8 and 85.6 mg polymer (**Figure 5.1j**). Up to 24 weeks, size of all groups remained stable (**Figure 5.3a**). The PdI remained relatively consistent (~0.16) at 10.7, 21.4, 42.8 mg polymer but increased significantly at 85.6 mg polymer to 0.22 ($p < 0.01$) (**Figure 5.1k**). PdI for all groups remained consistent for up to 24 weeks (**Figure 5.3b**). Zeta potential remained relatively consistent across formulations (**Figure 5.1l**). Based on these results, 42.8 mg polymer was selected as the optimal mass of polymer due to the significant increase in PdI at 85.6 mg.

In order to later 'click' azide-functionalized photoimmunoconjugates (PIC) onto the nanoparticle, PLGA-PEG-DBCO was incorporated into the formulation. PLGA-PEG-DBCO was mixed with PLGA-PEG-COOH to a final total polymer mass of 42.8 mg, and the relative mass of PLGA-PEG-DBCO was varied from 0, 25, 50, and 100% (**Figure 5.1m-q**). The talazoparib loading capacity and encapsulation efficiency remained relatively consistent with increasing mass of PLGA-PEG-DBCO (**Figure 5.1m-n**). In contrast, size, PdI, and zeta potential increased significantly when nanoparticles were prepared with 100% PLGA-PEG-DBCO (**Figure 5.1o-q**). Size and PdI remained stable across 24 weeks for groups where the mass percent of PLGA-PEG-DBCO was below 100% (**Figure 5.4a-b**). However, for 100% PLGA-PEG-DBCO nanoparticles, after 24 weeks, size decreased from ~300 nm to below

200 nm, and PdI decreased from ~0.3 to 0.22. Due to the instability and high PdI of 100% PLGA-PEG-DBCO, the 50% PLGA-PEG-DBCO condition was selected for subsequent experiments.

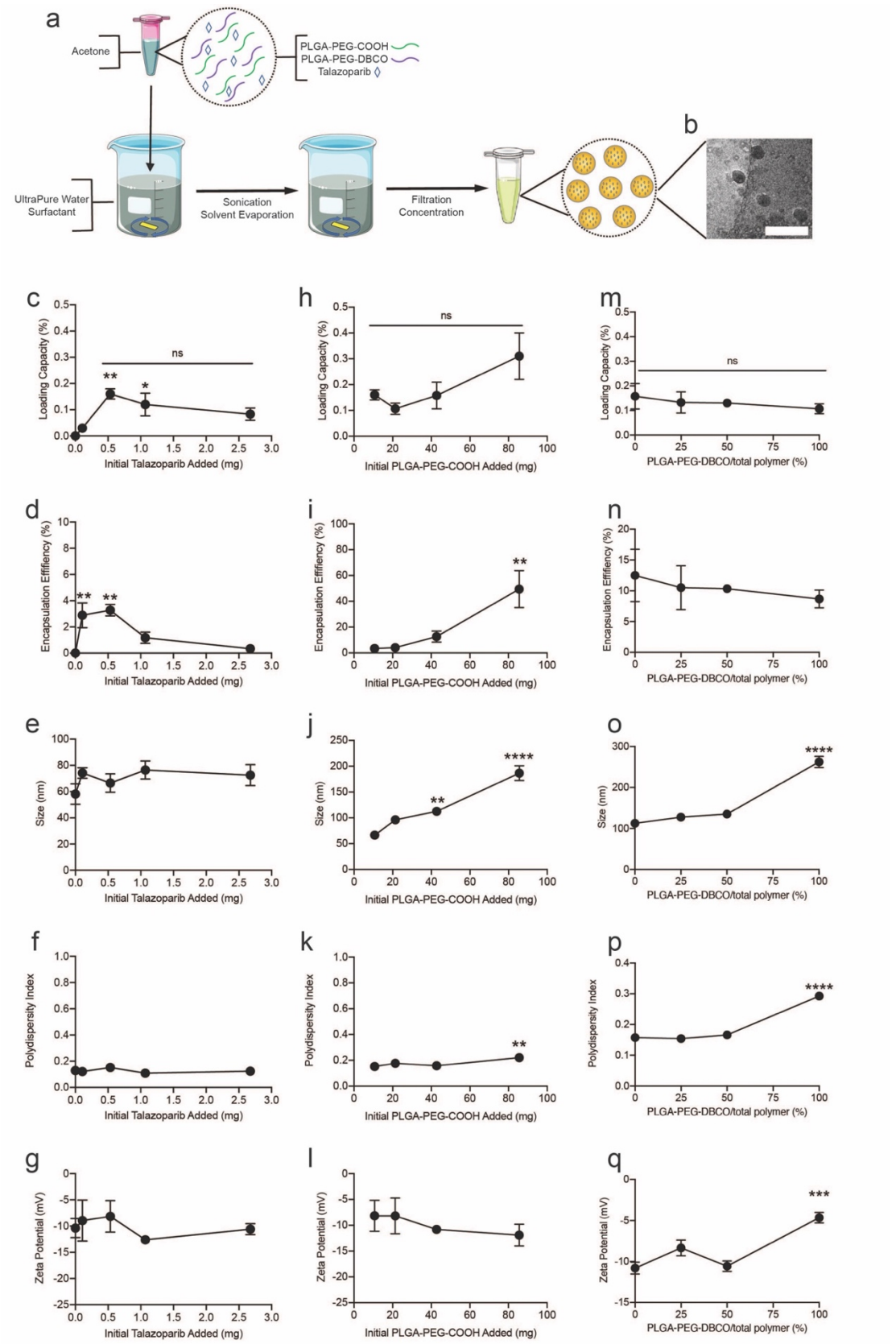
a
Acetone
PLGA-PEG-COOH
PLGA-PEG-DBCO
Talazoparib
UltraPure Water
Surfactant
Sonication
Solvent Evaporation
Filtration
Concentration
b
c
Loading Capacity (%)
ns
**
*
Initial Talazoparib Added (mg)
h
Loading Capacity (%)
ns
Initial PLGA-PEG-COOH Added (mg)
m
Loading Capacity (%)
ns
PLGA-PEG-DBCO/total polymer (%)
d
Encapsulation Effiency (%)
**
**
Initial Talazoparib Added (mg)
i
Encapsulation Effiency (%)
**
Initial PLGA-PEG-COOH Added (mg)
n
Encapsulation Effiency (%)
PLGA-PEG-DBCO/total polymer (%)
e
Size (nm)
Initial Talazoparib Added (mg)
j
Size (nm)
**
****
Initial PLGA-PEG-COOH Added (mg)
o
Size (nm)
****
PLGA-PEG-DBCO/total polymer (%)
f
Polydispersity Index
Initial Talazoparib Added (mg)
k
Polydispersity Index
**
Initial PLGA-PEG-COOH Added (mg)
p
Polydispersity Index
****
PLGA-PEG-DBCO/total polymer (%)
g
Zeta Potential (mV)
Initial Talazoparib Added (mg)
l
Zeta Potential (mV)
Initial PLGA-PEG-COOH Added (mg)
q
Zeta Potential (mV)
***
PLGA-PEG-DBCO/total polymer (%)

Figure 5.1: Schematic and characterization of talazoparib-loaded nanoparticles

NP-Tal is prepared by co-dissolution of polymers and talazoparib in acetone, which is added into surfactant-containing water. The mixture is sonicated and solvent is evaporated under constant spinning for 4-6 hours, then nanoparticles are concentrated using 30 kDa MWCO centrifugal filter (**a**). Representative TEM images are shown (**b**). Scale bar: 250 μm. During optimization procedures, initial talazoparib (mg) was varied (**c-g**) and initial PLGA-PEG-COOH (mg) was varied (**h-l**). (**m-q**) Next PLGA-PEG-DBCO was mixed in with PLGA-PEG-COOH at varying amounts from 0-100% where total polymer mass remained fixed at 42.8 mg. The characterized parameters include loading capacity (%), encapsulation efficiency (%), size (nm), polydispersity index, and zeta potential. * $p \leq 0.05$; ** $p \leq 0.01$; *** $p \leq 0.001$; **** $p \leq 0.0001$.

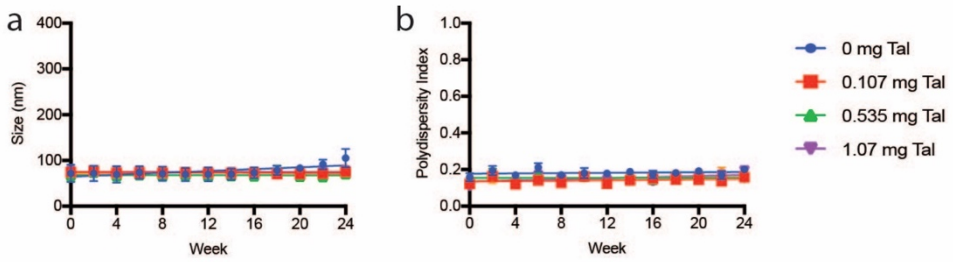

Figure 5.2: Stability of nanoparticles with varying initial talazoparib amounts

Polymeric nanoparticles were prepared with 10.7 mg PLGA-PEG-COOH and 0, 0.107, 0.535, or 1.07 mg of talazoparib. Particle size (**a**) and PdI (**b**) were tracked longitudinally for up to 24 weeks. All datapoints are representative of three nanoparticle batches.

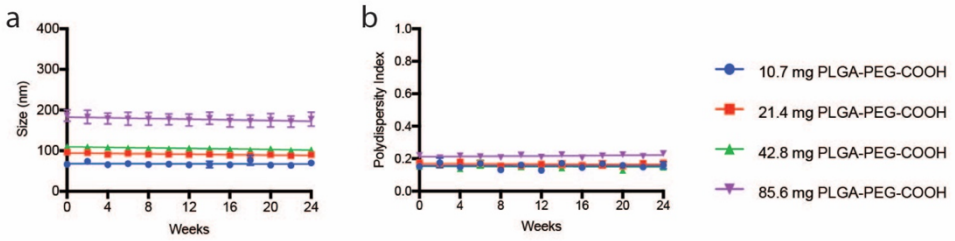

Figure 5.3: Stability of nanoparticles with varying initial PLGA-PEG-COOH amounts

Polymeric nanoparticles were prepared with 0.535 mg of talazoparib and varied amounts of PLGA-PEG-COOH from 10.7 to 85.6 mg. Particle size (**a**) and PdI (**b**) were tracked longitudinally for up to 24 weeks. All datapoints are representative of three nanoparticle batches.

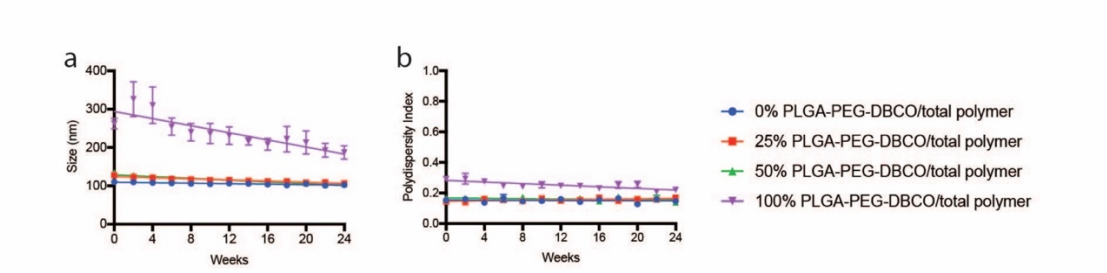

Figure 5.4: Stability of nanoparticles with varying PLGA-PEG-DBCO/total polymer percentages

Polymeric nanoparticles were prepared with 0.535 mg of talazoparib and 42.8 total mg polymer. The polymer component was either PLGA-PEG-COOH, PLGA-PEG-DBCO, or a mixture. Particle size (**a**) and PdI (**b**) were tracked longitudinally for up to 24 weeks. All datapoints are representative of three nanoparticle batches.

5.3.2 Optimization and Characterization of PIC-Conjugated Nanoparticles

Azide-functionalized PICs composed of Cet and BPD were 'clicked' onto the surface of DBCO-functionalized nanoparticles (**Figure 5.5a-b**). PICs were first prepared using carbodiimide chemistry at a 4:1 final BPD:Cet ratio. Next, 100 µL of nanoparticles were reacted overnight with PIC at varying volumes (50, 100, 200, 300 µL) resulting in volume ratios of 0.5:1, 1:1. 2:1, and 3:1 (PIC:NP). PIC-conjugated nanoparticles (PIC-NP) were purified by size exclusion chromatography and characterized for size, PIC conjugation efficiency (based on BPD concentration), and PIC per nanoparticle (**Figure 5.5c-e**). Dynamic light scattering data revealed that PIC conjugation to nanoparticles increased particle diameter by ~10 nm (**Figure 5.5c**). PIC conjugation efficiency (amount of photosensitizer conjugated to the nanoparticle relative to the amount added to the synthesis reaction) increased with higher PIC:NP reaction volume ratios, reaching a plateau at the 2:1 volume ratio around ~32% (**Figure 5.5d**). Next, the number of PICs per nanoparticle was calculated, revealing a range from ~30-330 PIC/NP at varying reaction volumes (**Figure 5.5e**). Due to the

plateau in reaction efficiency occurring at a 2:1 PIC:NP volume ratio, this condition was selected for subsequent studies. Stability of PIC-NP and PIC-NP-Tal in size and PdI was confirmed for up to 12 weeks (**Figure 5.6)**.

PIC-NP-Tal was next prepared and characterized (**Figure 5.5f-k, Table 5.2**). Absorbance spectra were recorded (**Figure 5.5f-g**), demonstrating that all BPD-containing agents (BPD, PIC, PIC-NP, PIC-NP-Tal) have the characteristic BPD absorbance peaks at ~435 nm and ~700 nm. Tal-containing formulations show characteristic absorbance peaks at ~312 nm. Next, quenching in aqueous solution was evaluated by comparing absorbance at 690 nm in PBS (quenched) versus DMSO (unquenched) (**Figure 5.5h**). BPD, PIC, PIC-NP, and PIC-NP-Tal all exhibit quenching, shown as significant reductions (~20-50%) in absorbance in PBS compared to DMSO. Free BPD and PIC show low photoactivity (<7%) due to quenching in aqueous solution, whereas the photoactivity of PIC-NP and PIC-NP-Tal is significantly higher, at 42% and 33%, respectively **(Figure 5.5i**). In **Figure 5.5j**, singlet oxygen generation based on SOSG fluorescence signal is shown. Compared to BPD, PIC-NP and PIC-NP-Tal show significantly higher fluorescence emission intensity ($P < 0.01$), representing elevated singlet oxygen yield.

EGFR-dependent uptake was next evaluated by treating EGFR-negative J774 cells and EGFR-positive OVCAR8 cells with PIC or PIC-NP-Tal for 30 minutes, then collecting cells and quantifying internalized BPD (**Figure 5.5k**). PIC uptake by OVCAR8 cells was significantly ($P < 0.01$) greater than PIC uptake by J774 cells

with a 3.5-fold increase in photosensitizer uptake, demonstrating EGFR-enhanced uptake. For PIC-NP-Tal, uptake by OVCAR8 cells was over double that of J774 ($P < 0.05$).

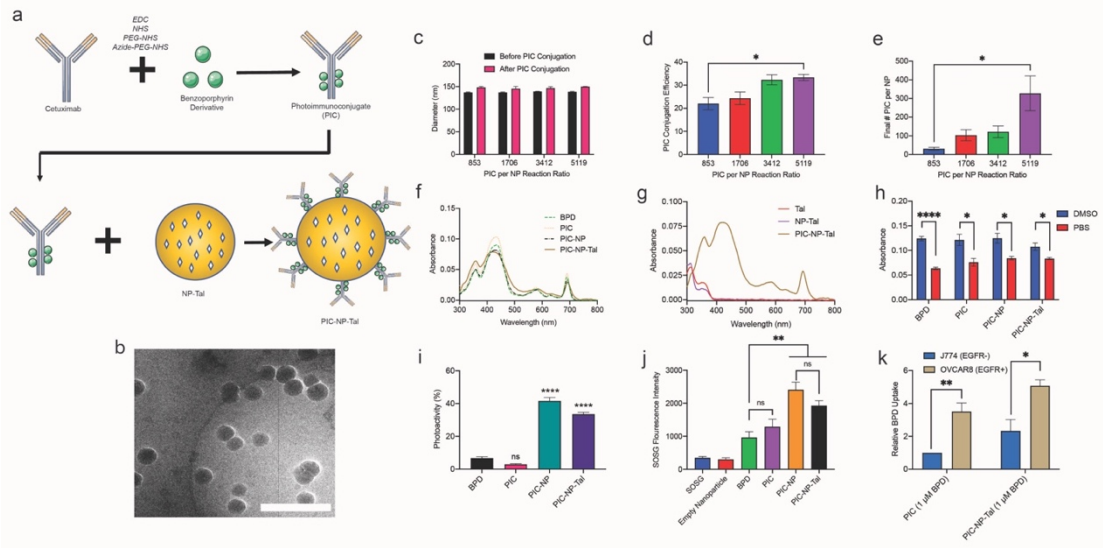

Figure 5.5: Optimization and characterization of PIC-conjugated nanoparticles.

Azide-functionalized photoimmunoconjugates were conjugated to DBCO-containing nanoparticles *via* copper-free click chemistry (**a**) and visualized by cryoEM (**b**). Scale bar: 500 μm. Volume ratio of PIC:NP was varied and changes in size (**c**), PIC conjugation efficiency (**d**), and number of PICs per nanoparticle (**e**) were characterized. Data in **c-e** are representative of three individual nanoparticle batches. The absorbance spectra are shown for BPD-containing formulations (**f**) and talazoparib-containing formulations (**g**) from 300-800 nm in DMSO. Next, comparison of 690 nm absorbance was performed in DMSO versus PBS (**h**). Photoactivity was evaluated, as described in *Materials & Methods,* for BPD, PIC, PIC-NP, and PIC-NP-Tal (**i**). Singlet oxygen was next quantified using SOSG (Invitrogen) (**j**). For studies **h-j**, data is representative of three individual nanoparticle batches. Uptake of 1 μM PIC versus 1 μM PIC-NP-Tal in EGFR-negative J774 cells compared to EGFR-positive OVCAR8 cells after 30 minute incubation (**k**)**.** Data is normalized to J774 uptake of PIC. This data is representative of three 35-mm dishes. * $p \leq 0.05$; ** $p \leq 0.01$; *** $p \leq 0.001$; **** $p \leq 0.0001$.

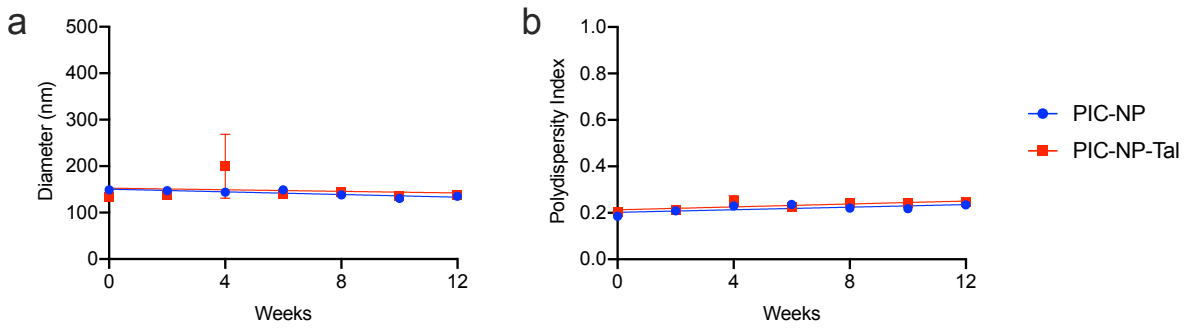

Figure 5.6: Stability of PIC-conjugated nanoparticles.

Polymeric nanoparticles were functionalized with PIC to establish PIC-NP and PIC-NP-Tal formulations. Both formulations were tracked for 12 weeks and particle size and PdI were recorded. All datapoints are representative of three nanoparticle batches.

Nanoparticle properties are summarized in **Table 5.2**. Empty nanoparticles (NP) are ~140 nm, whereas talazoparib loaded nanoparticles (NP-Tal) are ~126 nm. This difference in size is not statistically significant (P = 0.30), and upon PIC conjugation, both nanoparticles increase in size by 5-7 nm. PdI for empty and talazoparib-loaded nanoparticles is around ~0.18, whereas PIC conjugated nanoparticles have PdI just under 0.20. For all formulations, zeta potential is consistently around -7 mV. Talazoparib loading into nanoparticles was determined as 8.5%, and molecules of talazoparib per nanoparticle were calculated as 5295.1 and 2104.4 for NP-Tal and PIC-NP-Tal, respectively. PIC conjugation efficiency is ~30% for PIC-NP and PIC-NP-Tal and the number of PIC per nanoparticle is consistent between both formulations at ~115 PIC/NP.

Table 5.2: Characterization of nanoparticle physical properties and drug loading.

Talazoparib loading efficiency is defined as the moles of talazoparib loaded into the nanoparticle divided by the moles of talazoparib added to the nanoparticle synthesis reaction. # talazoparib per NP is defined as the molecules of talazoparib divided by the number of nanoparticles. PIC conjugation efficiency is defined as the moles of BPD conjugated to the nanoparticle divided by the moles of BPD added to the initial

conjugation reaction. # PIC per NP is defined as the molecules of PIC (based on antibody) divided by the number of nanoparticles. Each datapoint is representative of at least four individual nanoparticle batches.

	Size (d. nm)	Polydispersity Index	Zeta Potential (mV)	Talazoparib Loading Efficiency (%)	# Talazoparib per NP	PIC Conjugation Efficiency (%)	# PIC per NP
	Mean	*Mean*	*Mean*	*Mean*	*Mean*	*Mean*	*Mean*
NP	139.5 ±3.2	0.181 ±0.002	-7.3 ±1.0	N/A	N/A	N/A	N/A
PIC-NP	146.3 ±2.5	0.199 ±0.006	-6.7 ±1.9	N/A	N/A	32.0 ±1.9	119.9 ±19.7
NP-Tal	126.4 ±9.3	0.179 ±0.008	-6.6±0.5	8.5 ±1.5	5295.1 ±706.6	N/A	N/A
PIC-NP-Tal	131.7 ±3.7	0.197 ±0.006	-7.5 ±0.9	N/A	2104.4 ±578.9	30.2 ±1.0	108.1 ±24.5

5.3.3 Development of 3-Dimensional Ovarian Cancer Coculture Model

A 3D coculture model of a parental (OVCAR8-DsRed2) and a chemo-resistant subline (NCI/ADR-RES-EGFP) was developed by seeding 1,000, 2,000, or 5,000 cells at a 1:1 ratio in ultra-low attachment round bottom plates and tracking fluorescence over the course of 12 days (**Figure 5.7a-c**). Representative longitudinal images of spheroids with a 2000 cell seeding density are shown in **Figure 5.7d**. The parental OVCAR8-DsRed2 cells grew drastically faster than NCI/ADR-RES-EGFP at all seeding densities, reaching 48-, 58-, and 215-fold increases in RFU by day 12 in 5000, 2000, and 1000 cell seeding densities, respectively. NCI/ADR-RES-EGFP cells, in contrast reach 1-, 2-, and 6-fold increases in growth by day 12 for 5,000, 2,000, and 1,000 seeding density groups. The growth ratios of OVCAR8-DsRed2:NCI/ADR-RES-EGFP were calculated as the fold change in OVCAR8-DsRed2 RFU relative to day 1 divided by the fold change in NCI/ADR-RES-EGFP RFU relative to day 1 (**Figure 5.7e**). Across all starting seeding densities, this ratio remained relatively consistent over the course of the experiment, with day 12 values at 40, 25, and 41 at 1,000, 2,000, and 5,000 densities, respectively ($P > 0.4$). Fluorescence-based viability tracking was next validated by preparing a total killing control (5% bleach, 4 hours) and comparing fluorescence emission intensity values with an ATP-based cell viability assay (CellTiter-Glo® Cell Viability Assay) (**Figure**

5.7f-g). Fluorescence intensity of OVCAR8-DsRed2 and NCI/ADR-RES-EGFP decreased significantly for total killing controls to 13% and 28%, respectively. In contrast, the ATP-based assay showed reductions in viability down to <1%. The residual fluorescence values for total killing controls are likely resulting from auto-fluorescent contributions. Representative images of total killing controls are shown in **Figure 5.7h**.

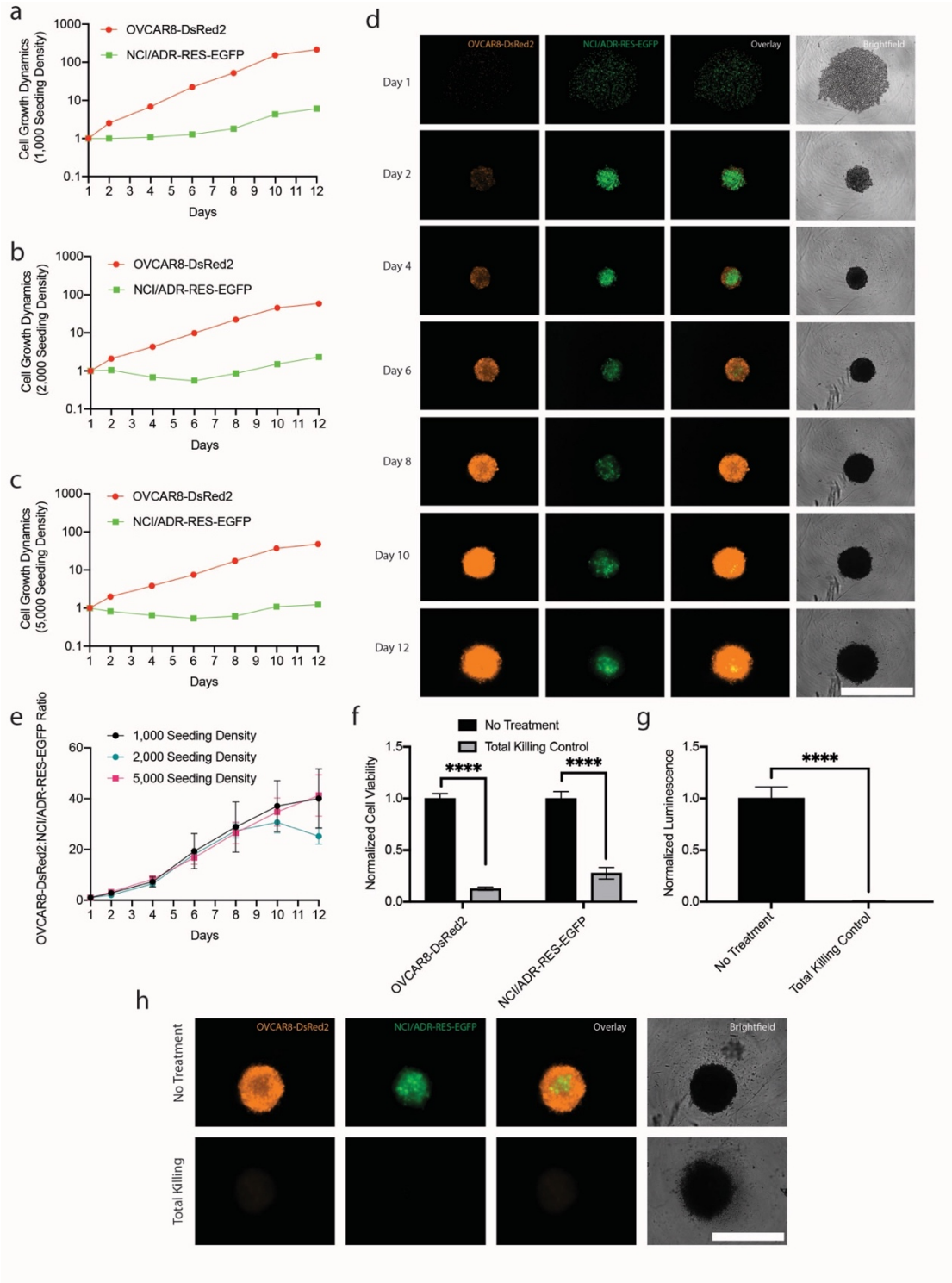

Figure 5.7: Optimization of 3D coculture model.

OVCAR8-DsRed2 and NCI/ADR-RES-EGFP cells were plated at a 1:1 ratio to final seeding cell densities of 1,000-5,000. Fluorescence signal from cells was recorded up to 12 days and plotted as fold change from day 1 for 1000 (**a**), 2000 (**b**), and 5000 (**c**) cell seeding densities. Representative longitudinal imaging for spheroids with 2000

seeded cells are shown (**d**). Next, fold change in OVCAR8-DsRed2 fluorescence was divided by fold change in NCI/ADR-RES-EGFP fluorescence to get the cell growth ratio €. Total killing controls (5% bleach) were included, and viability is plotted as a function of fluorescence (**f**) and CellTiter-Glo® Cell Viability Assay (**g**). Representative images of total killing controls are shown (**h**). Scale bar = 1000 μm. * $p \leq 0.05$; ** $p \leq 0.01$; *** $p \leq 0.001$; **** $p \leq 0.0001$. All data shown are representative of at least 6 individual spheroids.

5.3.4 Comparative Dosage Analysis of NP-Tal in Ovarian Cancer 3D Cocultures

Next, treatment effect of NP-Tal in spheroids (2,000 cell seeding density) was evaluated using concentrations from 0.01 to 3 μM (**Figure 5.8**. On day 4, when spheroids were fully established, they were treated with varying doses of NP-Tal until day 12. Images were taken longitudinally, and the fluorescence emission intensity of each spheroid was normalized to the untreated spheroid on each respective day to determine viability (**Figure 5.8a-f**). Representative images of spheroids on day 12 are shown (**Figure 5.8g**). Results at the lower NP-Tal doses (0.01 – 0.11 μM) demonstrate a decrease in viability for the parental cell line whereas the resistant subline was spared (**Figure 5.8a-c**). On the other hand, higher doses (0.33 – 3 μM) killed both parental and subline cells to a similar degree (**Figure 5.8d-f**). **Figure 5.9a-b** shows fluorescence-based viability analysis of OVACR8-DsRed2 cells and NCI/ADR-RES-EGFP cells, revealing decreases in viability with increasing NP-Tal dosing. On day 12, 3 μM treatment resulted in ~14% and ~25% viability for OVACR8-DsRed2 cells and NCI/ADR-RES-EGFP cells, respectively. Next, growth curves were calculated based on changes in fluorescence relative to day 1 for each cell line (**Supplementary Figure 5.9c-d**). Untreated cells show day 12 growth increases at 58-fold and 2-fold for OVACR8-DsRed2 cells and NCI/ADR-RES-EGFP cells, respectively. Increasing NP-Tal dosage caused decreasing fold changes

in growth, with day 12 values at 8-fold and 0.6-fold for OVCAR8-DsRed2 cells and NCI/ADR-RES-EGFP cells, respectively, with 3 μM treatment. Dose-dependent effects of NP-Tal are shown in **Supplementary Figure 5.10a-b** using fluorescence-based and ATP-based viability assays. Fluorescence-based data shows a rightward shift of the NCI/ADR-RES-EGFP cells, representing increased resistance to NP-Tal relative to the parental OVCAR8-DsRed22 cell line.

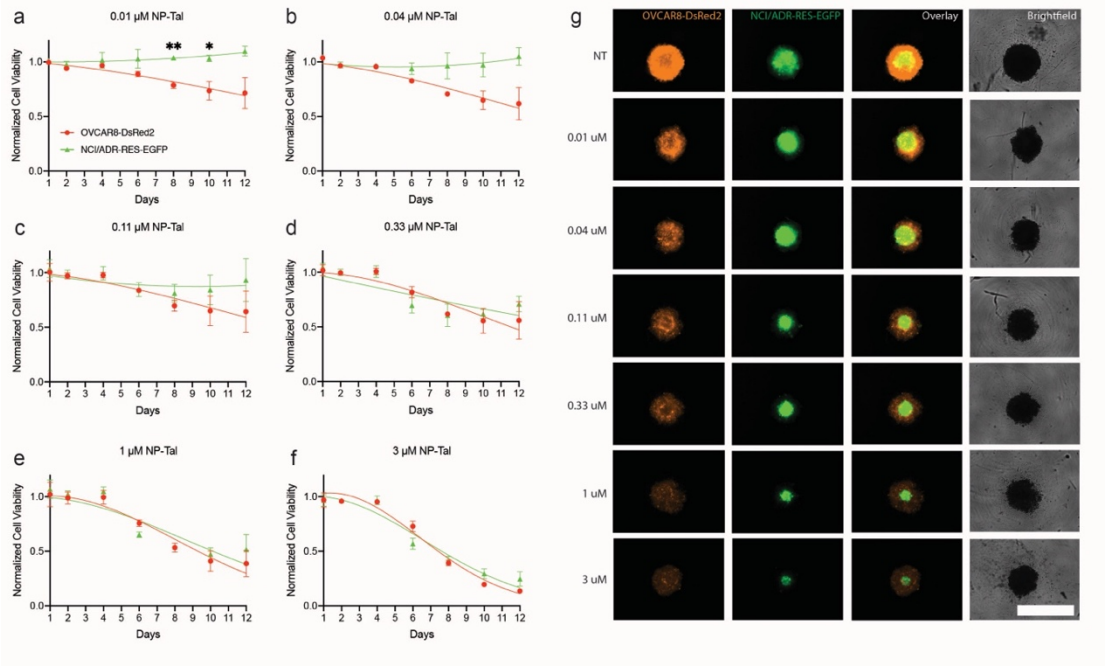

Figure 5.8: Spheroid toxicity analysis of NP-Tal at varying doses.

Spheroids composed of OVCAR8-DsRed2 cells and NCI/ADR-RES-EGFP cells were treated with NP-Tal at varying doses three days after seeding. Fluorescence was recorded up to 12 days, and intensity values for each cell line were normalized to the untreated spheroids to calculate cell viability. Longitudinal viability for parental and subline cells are shown from days 1-12 for NP-Tal doses at 0.01 μM (**a**), 0.04 μM (**b**), 0.11 μM (**c**), 0.33 μM (**d**) 1 μM (**e**), and 3 μM (**f**). Representative images of spheroids on day 12 at each treatment dose are shown (**g**). Scale bar = 1000 μm. * $p \leq 0.05$; ** $p \leq 0.01$; *** $p \leq 0.001$; **** $p \leq 0.0001$. All datapoints are representative of 11 individual spheroids.

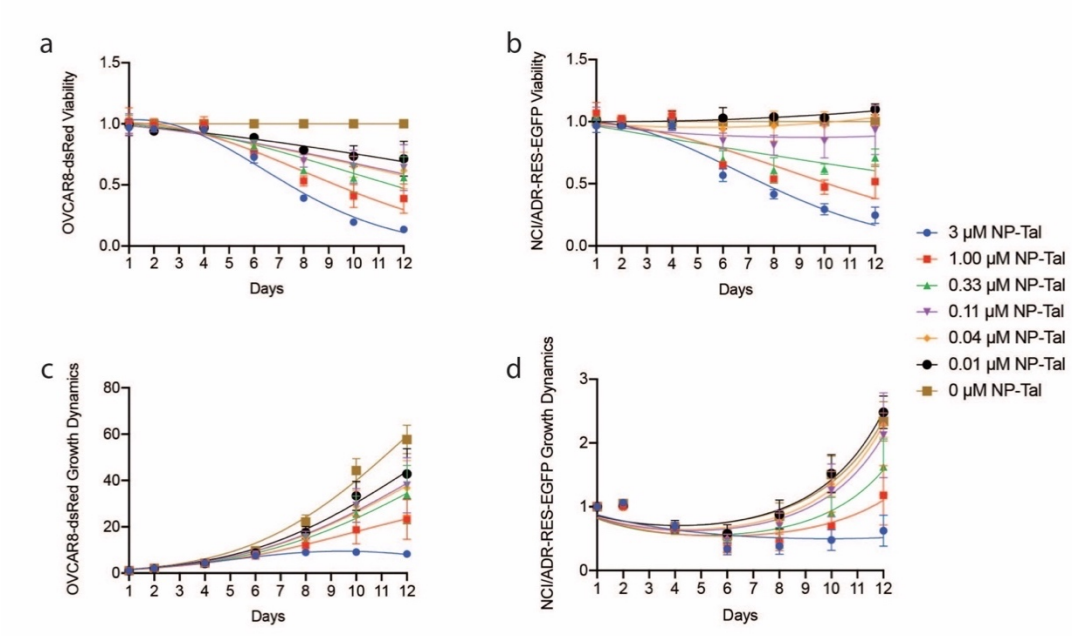

Figure 5.9: Longitudinal spheroid viability and growth tracking.

Coculture spheroids were treated with NP-Tal up to 3 µM and imaged on days 1, 2, 4, 6, 8, 10, and 12. Fluorescence values were normalized to untreated cells on each respective day to quantify viability for OVCAR8-DsRed cells (a) and NCI/ADR-RES-EGFP cells (b). Growth dynamic of the parental cells (a) and subline (b) are calculated as the fold-change in RFU relative to day 1. All datapoints are representative of 11 individual spheroids.

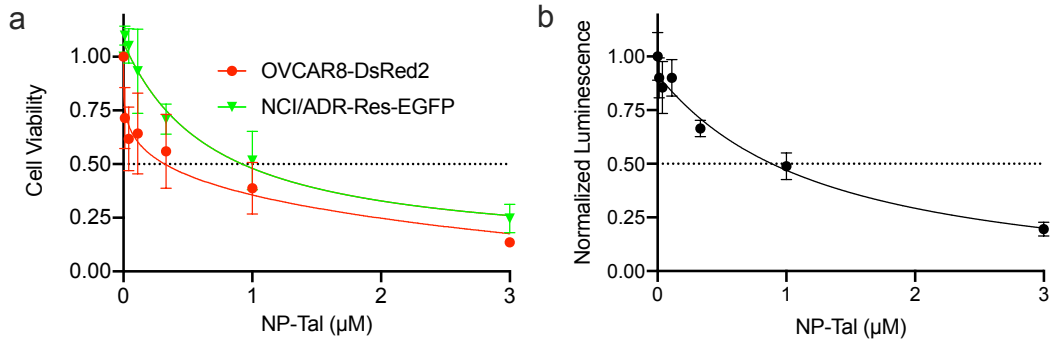

Figure 5.10: Day 12 spheroid viability curves.

On day 12 after seeding, spheroids treated with varying doses of NP-Tal were characterized for viability based on fluorescence of each cell line (**a**) and luminescence in the CellTiter-Glo® Cell Viability Assay (**b**). All datapoints are representative of at least 6 individual spheroids.

5.3.5 Treatment Outcomes in Coculture Spheroids

PIC-NP-Tal and monotherapy controls were next tested in the 3D coculture model (**Figure 5.11**). Luminescence-based viability analysis in **Figure 5.11a** shows that there are light-dose dependent effects of BPD, PIC, BPD mixed with NP-Tal (BPD+NP-Tal), and PIC mixed with NP-Tal (PIC+NP-Tal). In contrast, there were no significant light-dose dependent toxicities for the no treatment (NT), NP-Tal, and PIC-NP-Tal groups. Analysis of treatment groups within light doses is shown in **Figures 5.11b-d**. At all light doses, PIC-NP-Tal does not induce significant reductions in viability. In contrast, when PIC and NP-Tal are mixed as an unconjugated pair (PIC+NP-Tal), spheroid viability is reduced to 84% ($P < 0.05$), 53% ($P < 0.0001$), and 17% ($P < 0.0001$) at 0, 20, and 50 J/cm^2. Notably, at 20 J/cm^2, PIC+NP-Tal significantly outperforms PIC and NP-Tal alone. BPD alone, PIC alone, and BPD+NP-Tal caused significant reductions in viability at 20 and 50 J/cm^2, and PIC+NP-Tal significantly outperformed PIC-NP-Tal at 20 and 50 J/cm^2. Next, parental and subline fluorescence intensities were normalized to untreated spheroids and plotted in **Figure 5.11 e-j**. NP-Tal and BPD did not cause significant differences in viability between cell lines across all light doses, demonstrating a lack of selection pressures for either cell line. Interestingly, BPD+NP-Tal does select for chemoresistance, as determined by significantly higher viability of the NCI/ADR-RES-EGFP line compared to the OVCAR8-DsRed2 line at 0 and 20 J/cm^2. PIC alone, PIC+NP-Tal, and PIC-NP-Tal induce selection pressures towards drug resistance at 20 and 50 J/cm^2, but not at 0 J/cm^2.

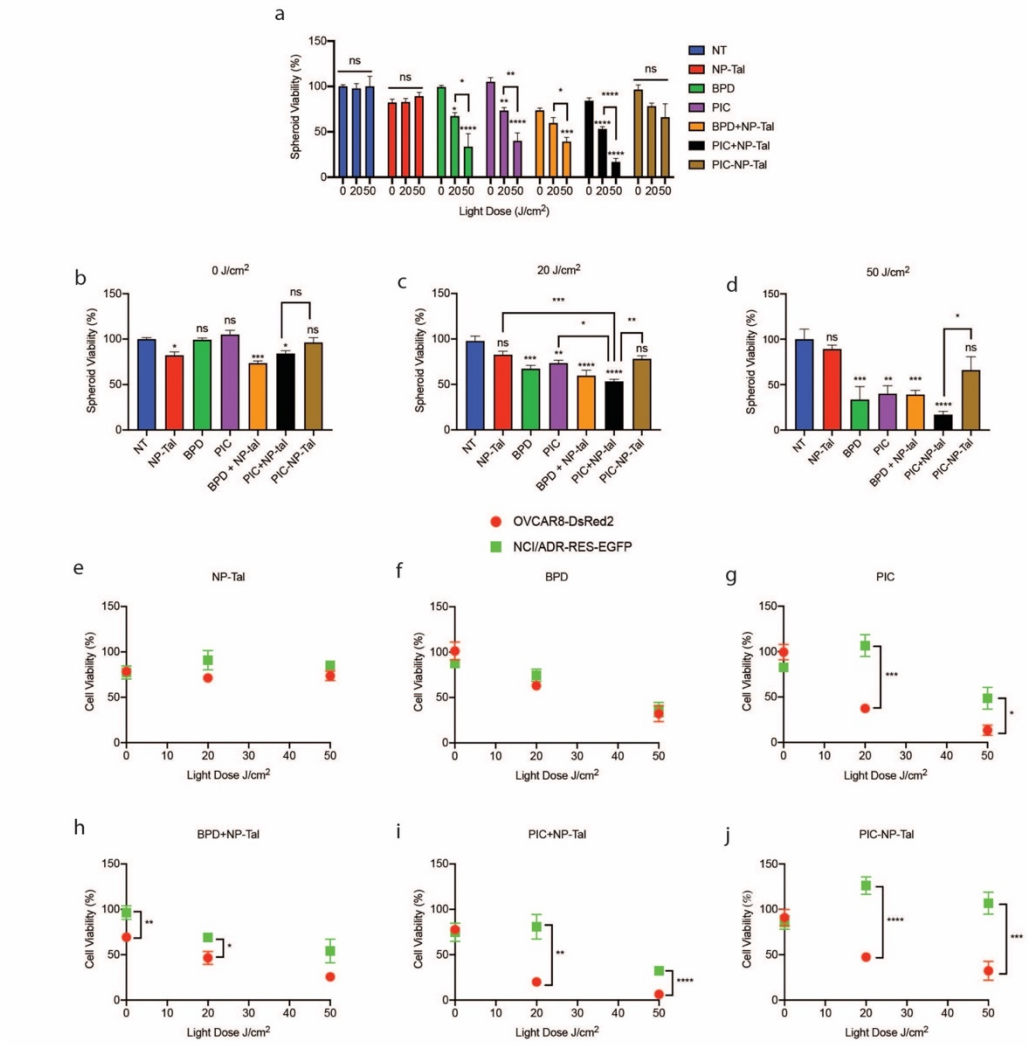

Figure 5.11: Treatment of 3D Cocultures with PIC-NP-Tal:

Spheroid cocultures of OVCAR8-DsRed2 and NCI/ADR-RES-EGFP cells were treated with PIC-NP-Tal or relevant controls three days after seeding. Light-activation was performed at 0 (dark control), 20, or 50 J/cm^2. Viability analysis using the CellTiter-Glo® Cell Viability Assay was performed, where luminescence values were normalized to the no treatment (NT) 0 J/cm^2 control (**a**). Normalized luminescence is further analyzed within light doses for 0 (**b**), 20 (**c**), and 50 J/cm^2 (**d**). Fluorescence-based viability of each cell line, normalized to untreated spheroids, is shown at each light dose for NP-Tal (**e**), BPD (**f**), PIC (**g**), BPD+NP-Tal (**h**), PIC+NP-Tal (**i**), and PIC-NP-Tal (**j**). * $p \leq 0.05$; ** $p \leq 0.01$; *** $p \leq 0.001$; **** $p \leq 0.0001$. All datapoints are representative of at least five spheroids.

5.4 Discussion

PARP inhibition has emerged in recent years as a powerhouse chemotherapy for numerous malignancies. In the clinic, PARP inhibitors are used to treat a growing list of indications that currently includes ovarian, breast, pancreatic, prostate, fallopian, and primary peritoneal cancers. Of the currently FDA-approved PARP inhibitors, studies show that talazoparib has the lowest IC_{50} and greatest PARP trapping capabilities. However, talazoparib is also the most toxic, with at least 300-fold lower maximum tolerated dose compared to the other clinically-prescribed PARP inhibitors. Nanoengineering approaches have emerged as a promising strategy to overcome this obstacle and strengthen PARP inhibition as an anti-cancer modality [407-409].

The nanoengineering approach in this study is unique in that it combines talazoparib with photoimmunotherapy to achieve codelivery of PDT and PARP inhibition within a targeted formulation. Work by Spring *et al.* has demonstrated the capabilities of photoimmunotherapy for ovarian cancer treatment *in vivo* [277]. They showed that anti-EGFR photoimmunoconjugates composed of Cet and BPD could selectively accumulate in ovarian cancer metastases, enabling precise imaging and treatment. We have previously shown that photoimmunotherapy-functionalized nanoparticles promote enhanced photosensitizer delivery [236] and possess combination-treatment capabilities through co-encapsulation of additional therapeutic entities [327]. Additionally, the clinical relevance of photoimmunotherapy-based anti-cancer approaches has recently been elevated with the clinical use of Cet-IR700 conjugates for the treatment of head and neck cancer in Japan [410].

The present study combines two clinically relevant modalities, photoimmunotherapy and PARP inhibition, in a targeted polymeric nanoparticle for the treatment of ovarian cancer spheroids. First, the nanoformulation was optimized through modulating various synthesis parameters including talazoparib mass, polymer mass, and ratio of two polymers (PLGA-PEG-COOH and PLGA-PEG-DBCO) (**Table 5.1, Figure 5.1**). The optimized formulation was then functionalized with photoimmunoconjugates *via* copper-free click chemistry for targeting and photoactivity capabilities (**Figure 5.5**). Consistent with previous work, the final formulation (PIC-NP-Tal) retained the 690 nm Q-band of BPD for light activation and showed superior singlet oxygen generation compared to free BPD [236,327]. Like PIC, PIC-NP-Tal also demonstrated selectivity for EGFR-expressing cells. Importantly, uptake of PIC-NP-Tal by EGFR-expressing cells was greater than uptake of PIC alone by 45%, demonstrating our previously described "carrier effect" phenomenon in 2-dimensional cultures.

In parallel, we developed a novel fluorescent 3D coculture system of the parental OVCAR8-DsRed2 cells and the drug resistant subline, NCI/ADR-RES-EGFP (**Figure 5.7**). In a previous study, these cell lines were cocultured on 2D substrate, leading to rapid domination of the parental subline [396]. For example, after 7 days, the parental line outnumbered the subline by nearly 5-fold, and by 14 days this difference increased to ~20-fold. Similarly, in 3D growth conditions, the parental cell line rapidly outgrows the chemo-resistant subline, and this trend is consistent when cells are plated at varying seeding densities (1000, 2000, 5000 cells per well). Spheroids with lower seeding densities showed greater increases in cellular

fluorescence compared to spheroids plated at higher seeding densities, representative of greater spheroid growth (**Figure 5.7a-c**). For example, at the 1000 cell seeding density, the fluorescence emission intensity of OVCAR8-DsRed2 and NCI/ADR-Res-EGFP increased by 215-fold and 6-fold relative to day 1, respectively. In contrast, at the 5000 cell seeding density, OVCAR8-DsRed2 and NCI/ADR-RES-EGFP cell fluorescence changed by 48-fold and 1-fold. However, regardless of seeding density, the parental-to-subline growth ratio remains remarkably consistent throughout the study (**Figure 5.7e**).

We next established dose-response studies of NP-Tal in the spheroid coculture model to evaluate the role of talazoparib dose in spheroid evolution (**Figure 5.8**). On the lower dose range, the NCI/ADR-RES-EGFP cell line is spared throughout the study, while the parental OVCAR8-DsRed2 line succumbs to the treatment. In contrast, higher doses kill both cell lines to equivalent degrees. This demonstrates a trend towards acquired chemoresistance where sublethal treatment is applied, a phenomenon consistently observed in prior studies [411]. Next, the PIC-NP-Tal nanocomplex is tested in the 3D coculture model (**Figure 5.11**). PIC mixed with NP-Tal significantly outperformed the nanocomplex (PIC-NP-Tal) in spheroid killing at 20 and 50 J/cm^2, though both treatments drove chemoresistance. Similarly, treatment with PIC alone and BPD+NP-Tal both drove chemoresistance. In contrast, NP-Tal and BPD as monotherapies were the only groups to kill both the parental and resistant subline to equivalent degrees across all light doses, thereby avoiding domination of the chemo-resistant subline.

5.5 Conclusion

Photoimmunotherapy and PARP inhibition are clinically relevant cancer treatment modalities with synergistic potential. In this study, these modalities are combined to achieve a novel nanocomplex for codelivery of Cet-BPD PICs and talazoparib. First, formulation parameters were optimized to establish a polymeric nanoparticle loaded with talazoparib with capabilities for click chemistry to attach PIC. The PIC-to-nanoparticle reaction ratio was next optimized, and the formulation was thoroughly characterized for photochemical and biological properties. In parallel, a 3D model of ovarian cancer with fluorescently labeled chemo-sensitive (OVCAR8-DsRed2) and chemo-resistant (NCI/ADR-RES-EGFP) subpopulations was developed and tracked up to 12 days. Treatment of spheroids with varying doses of NP-Tal revealed that lower doses induce selection pressures in favor of the chemo-resistant subline, whereas higher doses are similarly cytotoxic to both cell lines. Evaluation of PIC-NP-Tal in the 3D spheroid model revealed inferior therapeutic effects compared to co-treatment of PIC and NP-Tal. Additionally, PIC, BPD+NP-Tal, PIC+NP-Tal, and PIC-NP-Tal all drove chemoresistance, whereas NP-Tal and BPD as monotherapies did not. Overall, these data provide new insights into combinational therapies in the context of 3D spheroids, indicating that conjugation of multiple therapeutic entities may not always outperform the unconjugated combination. Results from this study also indicate that while combinational therapies may enhance total cell killing compared to monotherapies, they may also drive chemoresistance, reinforcing the fundamental importance of preclinical models of multidrug resistance.

Chapter 6: Future Directions and Outlook

6.1 Combination of PDT and EP4 Inhibition in Anti-Tumor Immune Response

Results from Chapter 3 establish that photochemistry can be effectively paired with EP4 inhibition to attenuate metastasis-related behaviors and protein expression in ovarian cancer cells. One important aspect that can be further exploited is the role of the PDT/EP4i combination in the anti-tumor immune response. This line of investigation could shed light on powerful synergistic effects between PDT and EP4i. One of the fundamental benefits of PDT for cancer treatment is the recruitment and activation of immune cells to the tumor site. This occurs through multiple mechanisms, including generation of damage-associated molecular patterns, activation of antigen presenting cells, and vascular permeabilization for entry of inflammatory cells [412].

However, part of the physiological PDT response is the activation of the PGE2/COX-2 pathway [349-351], which has a well-established role in cancer initiation and progression [413]. Therefore, COX-2 inhibitors have been strategically coupled with PDT to overcome PDT-mediated PGE2/COX-2 activation [349-351]. Despite this promising therapeutic strategy, COX-2 inhibition has had limited clinical success due to hematologic risks (e.g., leukopenia, thrombocytopenia, anemia) and cardiovascular toxicities [414-416]. In contrast, EP4 inhibitors have been posed as an alternative to COX-2 inhibitors that might provide similar therapeutic benefits while sparing cardiovascular toxicities [286]. Thus, combinations of EP4 inhibitors with PDT may enhance therapeutic effect through the blockade of the PGE2/COX-2 pathway without involving critical risks to cardiovascular health. The PDT-EP4i

combinational effects on anti-tumor immune response can be explored through various perspectives, including 1) direct effects on cancer cells and immune cells in coculture or *in vivo*, 2) establishment of anti-tumor immunologic memory, 3) abscopal effects, and 4) cancer metastasis.

6.2 Quantifying Intraperitoneal Fluid Shear Stress During HIPEC

Chapter 4 establishes that flow-mediated photosensitizer delivery enhances binding, uptake, and cytotoxicity of multiple photodynamic agents. The fluid shear stresses evaluated in Chapter 4 are within the range of 0-5 dynes/cm^2, which was based on peritoneal flow approximations of previous studies [22,23,359,360]. However, these estimations are descriptive of baseline peritoneal flow, where additional flow is not being applied for drug delivery. Therefore, the actual fluid shear stress rate within the peritoneal cavity during a HIPEC procedure remains unknown. This is a major gap in the field that should be addressed to bolster the progress of flow-based delivery systems. To this end, we have explored several methods for measuring fluid shear stress during the HIPEC procedure and there are two key components to be determined: 1) the model and 2) the measurement tool.

Regarding model selection, Helderman et al. has eloquently summarized the use of animal models for evaluation of HIPEC treatment effect [417]. These same models that are used to evaluate therapeutic effect could also be used for quantification of HIPEC-induced fluid shear stress. The review by Helderman et al. summarizes 60 articles which used various animal models including rats, mice, pigs, and rabbits, which represented 47%, 27%, 22%, and 5% of studies, respectively [417]. To study fluid shear stress, an ideal model should bear similar size and anatomy to the

human peritoneal cavity, making pigs an optimal candidate compared to smaller animals. Additionally, pig peritoneal cavities can accommodate commensurate volumes of fluid compared to the human peritoneal cavity, which is an important parameter when considering fluid shear stresses experienced.

In addition to selecting a model, a major question still remains: how can fluid shear stress be measured? Several fluid shear stress sensing technologies have emerged in recent decades, which could potentially be strategically implanted into various sectors of the porcine peritoneal cavity during a HIPEC procedure. Yu and colleagues designed a flexible polymer sensor for measurement of intravascular shear stress [418]. The sensor determines shear stresses by measuring changes in electrical resistance caused by flow-induced heat dissipation. In another study, Baldwin et al. designed a biocompatible sensor that relies on the flow-induced transfer of heat from a heating element to electrodes [419]. Electrode heating modulates impedance, which is measured and used to calculate fluid shear stresses.

However, technical challenges still remain when considering leveraging these sensor technologies for this particular application. For example, current fluid shear stress sensors are designed to measure flow that moves in one direction, whereas peritoneal flow moves in multiple directions. Secondly, considering the complex physiological landscape of the peritoneal cavity, multiple sensors would be needed to be implanted in various locations to achieve a holistic understanding of intraperitoneal flow during a HIPEC procedure. Thus, the sensors would need to be implantable but also small enough to not disturb movement of fluid in the cavity.

To summarize this future direction, a porcine model would be an ideal candidate for evaluation of HIPEC-induced fluid shear stress due to physiological similarities to humans. A sensor will be needed, where the design considerations include biocompatibility, implantability, measurements of fluid shear stress in all directions, and miniature size to avoid flow disruption. With these considerations in place, major advances can be made to the field through establishing a fundamental understanding of fluid shear stress rates in the peritoneal cavity during flow-mediated drug delivery.

6.3 NP-Tal *In Vivo* Evaluation of Tolerability, Bioavailability, and Therapeutic Effect

Despite being the most potent of the FDA-approved PARP inhibitors, talazoparib remains the most poorly tolerated, as evidenced by it's 300-fold lower maximum tolerated dose compared to olaparib. Converting free talazoparib into nanoparticle formulations has the potential to revolutionize its therapeutic potential. Zhang and colleagues recently showed in a murine model that liposomal talazaoprib demonstrated enhanced tolerability compared to free talazoparib, based on changes in animal weight [420]. Pathade and colleagues showed, using olaparib, that nanoformulations overcame hematologic toxicities of the PARP inhibitor [421]. Thus, a crucial next step for the NP-Tal work will be to evaluate tolerability *in vivo* compared to free talazoparib, with metrics such as animal weight and immune cell population dynamics. Another benefit of nanomedicines compared to free drug is enhancements in bioavailability. Pathade found than nanoformulations of olaparib enhanced bioavailability by up to 1.9-fold based on AUC measurements. They further

showed that olaparib-loaded lipospheres increased the maximum plasma concentration by up to 3-fold. Similar studies should be performed using NP-Tal to evaluate key pharmacokinetic parameters *in vivo*.

Chapter 7: Scientific Contributions

The work completed in this dissertation has resulted in 10 expected publications (4 first-author), 8 presentations (national and international), and the following contributions to scientific knowledge:

- Established novel treatment strategy combining PDP with EP4 inhibition (Chapter 3).
- Demonstrated using multiple assays (gap closure, transwell invasion) and multiple cell lines (OVCAR8, CAOV3) that PDP combined with inhibition of the EP4 receptor attenuates metastasis-related behaviors (Chapter 3).
- Confirmed that combinational effects of PIT-PDP and EP4 inhibitor can be attributed, in part, to blocking activation of EGFR, ERK1/2, and CREB (Chapter 3).
- Established and optimized a flow-based drug delivery strategy for enhancement of multiple photodynamic agents (Chapter 4).
- Demonstrated that flow-mediated photoimmunoconjugate delivery changes subcellular localization of photosensitizer compared to static conditions (Chapter 4).
- Confirmed that delivery of free BPD, PIC, and PIC-Nal is enhanced under flow-based treatment by 66, 71%, and 47%, respectively (Chapter 4).
- Demonstrated that cytotoxicity of BPD, PIC, and PIC-Nal are significantly enhanced by up to 1.4-fold, 2.4-fold, and 1.7-fold, respectively, when delivered under flow compared to static treatment (Chapter 4).

- Established a novel 3D model of cancer evolutionary dynamics using a coculture of fluorescently-labelled ovarian cancer cell lines OVCAR8-DsRed and NCI/ADR-RES-EGFP (Chapter 5).
- Invented and characterized a novel nanoformulation composed of talazoparib-loaded polymeric nanoparticles with PIC decorating the surface (PIC-NP-Tal) (Chapter 5).
- Demonstrated that low-dose Tal-NP drives chemoresistance through killing chemo-sensitive cells while sparing chemo-resistant cells (Chapter 5).
- Confirmed potent anti-tumor combination effects of PIC and NP-Tal in 3D model of ovarian cancer (Chapter 5).

7.1 Peer Reviewed Journal Publications

Published Manuscripts:

1. **Sorrin, A.J.**; Liu, C.; Cicalo, J.; Reader, J.; Najafali, D.; Zhang, Y.; Roque, D.M.; Huang, H.C. Photodynamic Priming Improves the Anti-Migratory Activity of Prostaglandin E Receptor 4 Antagonist in Cancer Cells In Vitro. *Cancers (Basel)* **2021**, *13*, 5259.
2. Baglo, Y.; **Sorrin, A.J**.; Xiaocong, P.; Liu, C.; Reader, J.; Roque, D.M.; Huang, H.C. Evolutionary dynamics of cancer multidrug resistance in response to olaparib and photodynamic therapy. *Translational Oncology* **2021**, *14*, 101198.
3. Rickard, B.P.; Conrad, C.; **Sorrin, A.J**.; Ruhi, M.K.; Reader, J.; Huang, S.A.; Franco, W.; Scarcelli, G.; Polacheck, W.J.; Roque, D.M.; del Carmen, M.G.; Huang, H.C.; Demirci, U.; Rizvi, I. Malignant Ascites in Ovarian Cancer:

Cellular, Acellular, and Biophysical Determinants of Molecular Characteristics and Therapy Response. *Cancers* **2021**, *13*, 4318.

4. **Sorrin, A.J.** Ruhi, M.K.; Ferlic, N.A.; Karimnia, V.; Polacheck, W.J.; Celli, J.P.; Huang, H.C.; Rizvi, I. Photodynamic Therapy and the Biophysics of the Tumor Microenvironment. *Photochemistry and Photobiology* **2020**, *96*, 232-259.
5. Inglut, C.T.; **Sorrin, A.J.**; Kuruppu, T.; Vig, S.; Cicalo, J.; Ahmad, H.; Huang, H.C. Immunological and Toxicological Considerations for the Design of Liposomes. *Nanomaterials* **2020**, *10*.
6. (Book Chapter) Stabile, J.*; Najafali, D.*; Cheema, Y.; Inglut, C.T.; Liang, B.J.; Vaja, S.; **Sorrin, A.J.**; Huang, H.-C. Chapter 12 - Engineering gold nanoparticles for photothermal therapy, surgery, and imaging. In *Nanoparticles for Biomedical Applications*, Chung, E.J., Leon, L., Rinaldi, C., Eds. Elsevier: 2020.
7. Baglo, Y.; **Sorrin, A.J.**; Liang, B.J.; Huang, H.C. Harnessing the Potential Synergistic Interplay Between Photosensitizer Dark Toxicity and Chemotherapy. *Photochem Photobiol* **2019**, *96*, 636-645.

Publications In-Progress:

1. **Sorrin, A.J.**; Dasgupta, A.; McNaughton, K.; Liu, C.; Zhou, K.; Arnau Del Valle, C.; Roque, D.M.; Huang, H.C. Co-Packaged PARP Inhibitor and Photosensitizer for Targeted Photo-Chemotherapy of 3D Ovarian Cancer Spheroids. ***In Preparation.***

2. Liang, B.J.; Pang, S.; Perttila, R.; Ma, C.H., Srivastava, P; Gaitan, B.; **Sorrin, A.J.**; Fadul, N.; Ylöniemi, Z.; Roque D.M.; Hasan, T.; Uusimaa, P.; Huang, H.C. Fluorescence-guided phototherapy using targeted nanotechnology and ML7710 minimizes heterogeneous treatment effects in peritoneal carcinomatosis. ***Submitted.***
3. **Sorrin, A.J.** Zhou, K.; May, K.; Liu, C.; McNaughton, K.; Rahman, I.; Liang, B.J.; Rizvi, I.; Roque, D.M.; Huang. H.C. Transient fluid flow improves photoimmunoconjugate delivery and photoimmunotherapy efficacy. *iScience* **2023***,* ***Submitted.***

7.2 National and International Conference Presentations

1. **Sorrin, A.J.**; McNaughton, K.; Dasgupta, A.; Zhou, K.; Liu, C.; Roque, D.M.; Huang, H.C. (July 2023). *Preventing and overcoming resistance to PARP inhibitors in cancer cells using photodynamic therapy.* IPA, Tampere, Finland. (Oral)
2. **Sorrin, A.J.**; Zhou, K.; May, K.; Liu, C.; McNaughton, K.; Rahman, I.; Liang, B.J.; Rizvi, I.; Roque, D.M.; Huang. H.C. (July 2023). *Examining the Role of Fluid Shear Stress in Intraperitoneal Photoimmunotherapy Delivery and Efficacy.* IPA, Tampere, Finland. (Oral)
3. **Sorrin, A.J.**; Zhou, K.; May, K.; Liu, C.; Liang, B.J.; Roque, D.M.; Huang, H.C. (February 2023). *The role of fluid shear stress in regulating photoimmunotherapy efficacy and immunogenic cell death.* SPIE Photonics West, San Francisco, CA. (Oral, <u>invited talk</u>)

4. **Sorrin, A.J.**; Zhou, K.; May, K.; Liu, C.; Liang, B.J.; Roque, D.M.; Huang, H.C. (April 2022). *Examining the role of fluid shear stress in intraperitoneal photoimmunotherapy delivery and efficacy.* SPIE Photonics Europe, Strasbourg, France. (Oral)
5. **Sorrin, A.J.**; Reader, J; Liu, C.; Cicalo, J.; Najafali, D.; Roque, D.M.; Huang, H.C. (March 2021). *Photodynamic therapy-based combination regimen with EP4 inhibitors attenuates metastatic behavior in ovarian cancer.* SPIE Photonics West Conference, San Francisco, CA. (Oral).
6. Roque, D.M.; **Sorrin, A.J.;** Reader, J.; Huang, H.C. (March 2020). *Photoimmunoconjugate nanoparticle, mechanism-based therapy for intraperitoneal treatment of carcinomatosis*. Society of Gynecologic Oncology 2020 Annual Meeting on Women's Cancer, Ontario, Canada. (Poster).
7. **Sorrin, A.J.**; Reader, J.; Najafali, D.; Liang, B.J.; Baglo, Y.; Roque, D.M.; Huang, H.C. (February 2020). *Light-Activatable, Mechanism-Based Combination Regimen to Attenuate Ovarian Cancer Migration.* 16th Annual USM PROMISE AGEP Research Symposium, College Park, MD. (Poster).
8. **Sorrin, A.J.**; Reader, J.; Najafali, D.; Liang, B.J.; Baglo, Y.; Roque, D.M.; Huang, H.C. (January 2020). *Light-Activatable, Mechanism-Based Combination Regimen to Attenuate Ovarian Cancer Migration.* SPIE Photonics West Conference, San Francisco, CA. (Poster).

Bibliography

1. Hahn, S.M.; Fraker, D.L.; Mick, R.; Metz, J.; Busch, T.M.; Smith, D.; Zhu, T.; Rodriguez, C.; Dimofte, A.; Spitz, F., et al. A Phase II Trial of Intraperitoneal Photodynamic Therapy for Patients with Peritoneal Carcinomatosis and Sarcomatosis. *Clinical Cancer Research* **2006**, *12*, 2517-2525, doi:10.1158/1078-0432.CCR-05-1625.
2. Siegel, R.L.; Miller, K.D.; Wagle, N.S.; Jemal, A. Cancer statistics, 2023. *CA: A Cancer Journal for Clinicians* **2023**, *73*, 17-48, doi:10.3322/caac.21763.
3. Badgwell, D.; Bast, R.C., Jr. Early detection of ovarian cancer. *Dis Markers* **2007**, *23*, 397-410, doi:10.1155/2007/309382.
4. Torre, L.A.; Trabert, B.; DeSantis, C.E.; Miller, K.D.; Samimi, G.; Runowicz, C.D.; Gaudet, M.M.; Jemal, A.; Siegel, R.L. Ovarian cancer statistics, 2018. *CA: a cancer journal for clinicians* **2018**, *68*, 284-296, doi:10.3322/caac.21456.
5. Reid, B.M.; Permuth, J.B.; Sellers, T.A. Epidemiology of ovarian cancer: a review. *Cancer Biol Med* **2017**, *14*, 9-32, doi:10.20892/j.issn.2095-3941.2016.0084.
6. Matulonis, U.A.; Sood, A.K.; Fallowfield, L.; Howitt, B.E.; Sehouli, J.; Karlan, B.Y. Ovarian cancer. *Nature Reviews Disease Primers* **2016**, *2*, 16061, doi:10.1038/nrdp.2016.61.
7. Lalwani, N.; Prasad, S.R.; Vikram, R.; Shanbhogue, A.K.; Huettner, P.C.; Fasih, N. Histologic, Molecular, and Cytogenetic Features of Ovarian Cancers: Implications for Diagnosis and Treatment. *RadioGraphics* **2011**, *31*, 625-646, doi:10.1148/rg.313105066.
8. Yeung, T.-L.; Leung, C.S.; Yip, K.-P.; Au Yeung, C.L.; Wong, S.T.C.; Mok, S.C. Cellular and molecular processes in ovarian cancer metastasis. A Review in the Theme: Cell and Molecular Processes in Cancer Metastasis. *Am J Physiol Cell Physiol* **2015**, *309*, C444-C456, doi:10.1152/ajpcell.00188.2015.
9. Latifi, A.; Luwor, R.B.; Bilandzic, M.; Nazaretian, S.; Stenvers, K.; Pyman, J.; Zhu, H.; Thompson, E.W.; Quinn, M.A.; Findlay, J.K., et al. Isolation and characterization of tumor cells from the ascites of ovarian cancer patients: molecular phenotype of chemoresistant ovarian tumors. *PLoS One* **2012**, *7*, e46858, doi:10.1371/journal.pone.0046858.
10. Ahmed, N.; Stenvers, K. Getting to Know Ovarian Cancer Ascites: Opportunities for Targeted Therapy-Based Translational Research. *Front Oncol* **2013**, *3*, 1-12, doi:10.3389/fonc.2013.00256.
11. Kipps, E.; Tan, D.S.P.; Kaye, S.B. Meeting the challenge of ascites in ovarian cancer: new avenues for therapy and research. *Nature Reviews Cancer* **2013**, *13*, 273-282, doi:10.1038/nrc3432.
12. Smolle, E.; Taucher, V.; Haybaeck, J. Malignant Ascites in Ovarian Cancer and the Role of Targeted Therapeutics. *Anticancer Res.* **2014**, *34*, 1553.
13. Garrison, R.N.; Galloway, R.H.; Heuser, L.S. Mechanisms of malignant ascites production. *J Surg Res* **1987**, *42*, 126-132, doi:10.1016/0022-4804(87)90109-0.

14. Rickard, B.P.; Conrad, C.; Sorrin, A.J.; Ruhi, M.K.; Reader, J.C.; Huang, S.A.; Franco, W.; Scarcelli, G.; Polacheck, W.J.; Roque, D.M., et al. Malignant Ascites in Ovarian Cancer: Cellular, Acellular, and Biophysical Determinants of Molecular Characteristics and Therapy Response. *Cancers (Basel)* **2021**, *13*, 4318, doi:10.3390/cancers13174318.
15. Worzfeld, T.; Pogge von Strandmann, E.; Huber, M.; Adhikary, T.; Wagner, U.; Reinartz, S.; Müller, R. The Unique Molecular and Cellular Microenvironment of Ovarian Cancer. *Front Oncol* **2017**, *7*, 24-24, doi:10.3389/fonc.2017.00024.
16. Kim, S.; Kim, B.; Song, Y.S. Ascites modulates cancer cell behavior, contributing to tumor heterogeneity in ovarian cancer. *Cancer Sci* **2016**, *107*, 1173-1178, doi:10.1111/cas.12987.
17. Lane, D.; Matte, I.; Garde-Granger, P.; Bessette, P.; Piché, A. Ascites IL-10 Promotes Ovarian Cancer Cell Migration. *Cancer microenvironment : official journal of the International Cancer Microenvironment Society* **2018**, *11*, 115-124, doi:10.1007/s12307-018-0215-3.
18. Lane, D.; Matte, I.; Laplante, C.; Garde-Granger, P.; Carignan, A.; Bessette, P.; Rancourt, C.; Piché, A. CCL18 from ascites promotes ovarian cancer cell migration through proline-rich tyrosine kinase 2 signaling. *Molecular cancer* **2016**, *15*, 58-58, doi:10.1186/s12943-016-0542-2.
19. Kim, E.K.; Yun, S.J.; Do, K.H.; Kim, M.S.; Cho, M.; Suh, D.-S.; Kim, C.D.; Kim, J.H.; Birnbaum, M.J.; Bae, S.S. Lysophosphatidic acid induces cell migration through the selective activation of Akt1. *Experimental & Molecular Medicine* **2008**, *40*, 445-452, doi:10.3858/emm.2008.40.4.445.
20. Meunier, L.; Puiffe, M.L.; Le Page, C.; Filali-Mouhim, A.; Chevrette, M.; Tonin, P.N.; Provencher, D.M.; Mes-Masson, A.M. Effect of ovarian cancer ascites on cell migration and gene expression in an epithelial ovarian cancer in vitro model. *Transl Oncol* **2010**, *3*, 230-238, doi:10.1593/tlo.10103.
21. Kim, S.; Gwak, H.; Kim, H.S.; Kim, B.; Dhanasekaran, D.N.; Song, Y.S. Malignant ascites enhances migratory and invasive properties of ovarian cancer cells with membrane bound IL-6R in vitro. *Oncotarget* **2016**, *7*, 83148-83159, doi:10.18632/oncotarget.13074.
22. Avraham-Chakim, L.; Elad, D.; Zaretsky, U.; Kloog, Y.; Jaffa, A.; Grisaru, D. Fluid-flow induced wall shear stress and epithelial ovarian cancer peritoneal spreading. *PLoS One* **2013**, *8*, e60965, doi:10.1371/journal.pone.0060965.
23. Jeffrey, B.; Udaykumar, H.S.; Schulze, K.S. Flow fields generated by peristaltic reflex in isolated guinea pig ileum: impact of contraction depth and shoulders. *American Journal of Physiology-Gastrointestinal and Liver Physiology* **2003**, *285*, G907-G918, doi:10.1152/ajpgi.00062.2003.
24. Novak, C.; Horst, E.; Mehta, G. Review: Mechanotransduction in ovarian cancer: Shearing into the unknown. *APL Bioeng* **2018**, *2*, 031701, doi:10.1063/1.5024386.
25. Lisio, M.-A.; Fu, L.; Goyeneche, A.; Gao, Z.-H.; Telleria, C. High-Grade Serous Ovarian Cancer: Basic Sciences, Clinical and Therapeutic Standpoints. *Int J Mol Sci* **2019**, *20*, 952, doi:10.3390/ijms20040952.

26. Pignata, S.; C Cecere, S.; Du Bois, A.; Harter, P.; Heitz, F. Treatment of recurrent ovarian cancer. *Annals of Oncology* **2017**, *28*, viii51-viii56, doi:10.1093/annonc/mdx441.
27. Luvero, D.; Milani, A.; Ledermann, J.A. Treatment options in recurrent ovarian cancer: latest evidence and clinical potential. *Therapeutic advances in medical oncology* **2014**, *6*, 229-239, doi:10.1177/1758834014544121.
28. Besic Gyenge, E.; Forny, P.; Lüscher, D.; Laass, A.; Walt, H.; Maake, C. Effects of hypericin and a chlorin based photosensitizer alone or in combination in squamous cell carcinoma cells in the dark. *Photodiagnosis Photodyn Ther* **2012**, *9*, 321-331, doi:10.1016/j.pdpdt.2012.03.006.
29. Nishita, M.; Park, S.Y.; Nishio, T.; Kamizaki, K.; Wang, Z.; Tamada, K.; Takumi, T.; Hashimoto, R.; Otani, H.; Pazour, G.J., et al. Ror2 signaling regulates Golgi structure and transport through IFT20 for tumor invasiveness. *Sci Rep* **2017**, *7*, 1, doi:10.1038/s41598-016-0028-x.
30. Castano, A.P.; Demidova, T.N.; Hamblin, M.R. Mechanisms in photodynamic therapy: part one-photosensitizers, photochemistry and cellular localization. *Photodiagnosis Photodyn Ther* **2004**, *1*, 279-293, doi:10.1016/s1572-1000(05)00007-4.
31. Lucky, S.S.; Soo, K.C.; Zhang, Y. Nanoparticles in photodynamic therapy. *Chem Rev* **2015**, *115*, 1990-2042, doi:10.1021/cr5004198.
32. Oleinick, N.L.; Morris, R.L.; Belichenko, I. The role of apoptosis in response to photodynamic therapy: what, where, why, and how. *Photochemical & Photobiological Sciences* **2002**, *1*, 1-21, doi:10.1039/b108586g.
33. Kessel, D. Apoptosis and associated phenomena as a determinants of the efficacy of photodynamic therapy. *Photochem Photobiol Sci* **2015**, *14*, 1397-1402, doi:10.1039/c4pp00413b.
34. Li, D.; Li, L.; Li, P.; Li, Y.; Chen, X. Apoptosis of HeLa cells induced by a new targeting photosensitizer-based PDT via a mitochondrial pathway and ER stress. *Onco Targets Ther* **2015**, *8*, 703-711, doi:10.2147/ott.S76370.
35. Allison, R.R.; Moghissi, K. Photodynamic Therapy (PDT): PDT Mechanisms. *Clin Endosc* **2013**, *46*, 24-29, doi:10.5946/ce.2013.46.1.24.
36. Kawczyk-Krupka, A.; Czuba, Z.; Szliszka, E.; Król, W.; Sieroń, A. The role of photosensitized macrophages in photodynamic therapy. *Oncol Rep* **2011**, *26*, 275-280, doi:10.3892/or.2011.1262.
37. Mroz, P.; Yaroslavsky, A.; Kharkwal, G.B.; Hamblin, M.R. Cell death pathways in photodynamic therapy of cancer. *Cancers (Basel)* **2011**, *3*, 2516-2539, doi:10.3390/cancers3022516.
38. Cincotta, L.; Szeto, D.; Lampros, E.; Hasan, T.; Cincotta, A.H. Benzophenothiazine and Benzoporphyrin Derivative Combination Phototherapy Effectively Eradicates Large Murine Sarcomas. *Photochemistry and Photobiology* **1996**, *63*, 229-237, doi:10.1111/j.1751-1097.1996.tb03019.x.
39. Villanueva, A.; Stockert, J.C.; Cañete, M.; Acedo, P. A new protocol in photodynamic therapy: enhanced tumour cell death by combining two different photosensitizers. *Photochemical & Photobiological Sciences* **2010**, *9*, 295-297, doi:10.1039/b9pp00153k.

40. Acedo, P.; Stockert, J.C.; Cañete, M.; Villanueva, A. Two combined photosensitizers: a goal for more effective photodynamic therapy of cancer. *Cell Death & Disease* **2014**, *5*, e1122-e1122, doi:10.1038/cddis.2014.77.
41. Kessel, D.; Reiners Jr, J.J. Enhanced Efficacy of Photodynamic Therapy via a Sequential Targeting Protocol. *Photochemistry and Photobiology* **2014**, *90*, 889-895, doi:10.1111/php.12270.
42. Rizvi, I.; Obaid, G.; Bano, S.; Hasan, T.; Kessel, D. Photodynamic therapy: Promoting in vitro efficacy of photodynamic therapy by liposomal formulations of a photosensitizing agent. *Lasers in Surgery and Medicine* **2018**, *50*, 499-505, doi:10.1002/lsm.22813.
43. Rizvi, I.; Nath, S.; Obaid, G.; Ruhi, M.K.; Moore, K.; Bano, S.; Kessel, D.; Hasan, T. A Combination of Visudyne and a Lipid-anchored Liposomal Formulation of Benzoporphyrin Derivative Enhances Photodynamic Therapy Efficacy in a 3D Model for Ovarian Cancer. *Photochemistry and Photobiology* **2019**, *95*, 419-429, doi:10.1111/php.13066.
44. Obaid, G.; Jin, W.; Bano, S.; Kessel, D.; Hasan, T. Nanolipid Formulations of Benzoporphyrin Derivative: Exploring the Dependence of Nanoconstruct Photophysics and Photochemistry on Their Therapeutic Index in Ovarian Cancer Cells. *Photochemistry and Photobiology* **2019**, *95*, 364-377, doi:10.1111/php.13002.
45. Inglut, C.T.; Baglo, Y.; Liang, B.J.; Cheema, Y.; Stabile, J.; Woodworth, G.F.; Huang, H.-C. Systematic Evaluation of Light-Activatable Biohybrids for Anti-Glioma Photodynamic Therapy. *Journal of Clinical Medicine* **2019**, *8*, doi:10.3390/jcm8091269.
46. Duska, L.R.; Hamblin, M.R.; Miller, J.L.; Hasan, T. Combination Photoimmunotherapy and Cisplatin: Effects on Human Ovarian Cancer Ex Vivo. *JNCI: Journal of the National Cancer Institute* **1999**, *91*, 1557-1563, doi:10.1093/jnci/91.18.1557.
47. Rizvi, I.; Celli, J.P.; Evans, C.L.; Abu-Yousif, A.O.; Muzikansky, A.; Pogue, B.W.; Finkelstein, D.; Hasan, T. Synergistic Enhancement of Carboplatin Efficacy with Photodynamic Therapy in a Three-Dimensional Model for Micrometastatic Ovarian Cancer. *Cancer Research* **2010**, *70*, 9319-9328, doi:10.1158/0008-5472.Can-10-1783.
48. del Carmen, M.G.; Rizvi, I.; Chang, Y.; Moor, A.C.E.; Oliva, E.; Sherwood, M.; Pogue, B.; Hasan, T. Synergism of Epidermal Growth Factor Receptor–Targeted Immunotherapy With Photodynamic Treatment of Ovarian Cancer In Vivo. *JNCI: Journal of the National Cancer Institute* **2005**, *97*, 1516-1524, doi:10.1093/jnci/dji314.
49. Huang, H.-C.; Rizvi, I.; Liu, J.; Anbil, S.; Kalra, A.; Lee, H.; Baglo, Y.; Paz, N.; Hayden, D.; Pereira, S., et al. Photodynamic Priming Mitigates Chemotherapeutic Selection Pressures and Improves Drug Delivery. *Cancer research* **2018**, *78*, 558-571, doi:10.1158/0008-5472.CAN-17-1700.
50. Spring, B.Q.; Bryan Sears, R.; Zheng, L.Z.; Mai, Z.; Watanabe, R.; Sherwood, M.E.; Schoenfeld, D.A.; Pogue, B.W.; Pereira, S.P.; Villa, E., et al. A photoactivable multi-inhibitor nanoliposome for tumour control and

simultaneous inhibition of treatment escape pathways. *Nature Nanotechnology* **2016**, *11*, 378-387, doi:10.1038/nnano.2015.311.
51. Pigula, M.; Huang, H.-C.; Mallidi, S.; Anbil, S.; Liu, J.; Mai, Z.; Hasan, T. Size-dependent Tumor Response to Photodynamic Therapy and Irinotecan Monotherapies Revealed by Longitudinal Ultrasound Monitoring in an Orthotopic Pancreatic Cancer Model. *Photochemistry and Photobiology* **2019**, *95*, 378-386, doi:10.1111/php.13016.
52. Huang, H.-C.; Mallidi, S.; Liu, J.; Chiang, C.-T.; Mai, Z.; Goldschmidt, R.; Ebrahim-Zadeh, N.; Rizvi, I.; Hasan, T. Photodynamic Therapy Synergizes with Irinotecan to Overcome Compensatory Mechanisms and Improve Treatment Outcomes in Pancreatic Cancer. *Cancer research* **2016**, *76*, 1066-1077, doi:10.1158/0008-5472.CAN-15-0391.
53. van Straten, D.; Mashayekhi, V.; de Bruijn, H.S.; Oliveira, S.; Robinson, D.J. Oncologic Photodynamic Therapy: Basic Principles, Current Clinical Status and Future Directions. *Cancers (Basel)* **2017**, *9*, doi:10.3390/cancers9020019.
54. Solban, N.; Rizvi, I.; Hasan, T. Targeted photodynamic therapy. *Lasers in Surgery and Medicine* **2006**, *38*, 522-531, doi:10.1002/lsm.20345.
55. Wang, H.-W.; Putt, M.E.; Emanuele, M.J.; Shin, D.B.; Glatstein, E.; Yodh, A.G.; Busch, T.M. Treatment-Induced Changes in Tumor Oxygenation Predict Photodynamic Therapy Outcome. *Cancer Research* **2004**, *64*, 7553-7561, doi:10.1158/0008-5472.Can-03-3632.
56. Snyder, J.W.; Greco, W.R.; Bellnier, D.A.; Vaughan, L.; Henderson, B.W. Photodynamic Therapy: A Means to Enhanced Drug Delivery to Tumors. *Cancer Research* **2003**, *63*, 8126-8131.
57. Gil, M.; Bieniasz, M.; Seshadri, M.; Fisher, D.; Ciesielski, M.J.; Chen, Y.; Pandey, R.K.; Kozbor, D. Photodynamic therapy augments the efficacy of oncolytic vaccinia virus against primary and metastatic tumours in mice. *Br J Cancer* **2011**, *105*, 1512-1521, doi:10.1038/bjc.2011.429.
58. Perentes, J.Y.; Wang, Y.; Wang, X.; Abdelnour, E.; Gonzalez, M.; Decosterd, L.; Wagnieres, G.; van den Bergh, H.; Peters, S.; Ris, H.-B., et al. Low-Dose Vascular Photodynamic Therapy Decreases Tumor Interstitial Fluid Pressure, which Promotes Liposomal Doxorubicin Distribution in a Murine Sarcoma Metastasis Model. *Translational Oncology* **2014**, *7*, 393-399, doi:10.1016/j.tranon.2014.04.010.
59. Lapčík, L.; Schurz, J. Photochemical degradation of hyaluronic acid by singlet oxygen. *Colloid and Polymer Science* **1991**, *269*, 633-635, doi:10.1007/BF00659919.
60. Alageel, S.A.; Arafat, S.N.; Salvador-Culla, B.; Kolovou, P.E.; Jahanseir, K.; Kozak, A.; Braithwaite, G.J.C.; Ciolino, J.B. Corneal Cross-Linking With Verteporfin and Nonthermal Laser Therapy. *Cornea* **2018**, *37*, 362-368, doi:10.1097/ico.0000000000001473.
61. Abbas, S.; Barbara, R.; Barbara, A. Water Soluble Tetrazolium Salt-11 as an Alternative to Riboflavin for Corneal Collagen Cross-linking for the Treatment of Keratoconus. *International Journal of Keratoconus and Ectatic Corneal Diseases* **2017**, *6*, 42-44, doi:10.5005/jp-journals-10025-1141.

62. Waterman, P.R.; Overhaus, M.; Heckenkamp, J.; Nigri, G.R.; Fungaloi, P.F.; Landis, M.E.; Kossodo, S.C.; LaMuraglia, G.M. Mechanisms of reduced human vascular cell migration after photodynamic therapy. *Photochem Photobiol* **2002**, *75*, 46-50, doi:10.1562/0031-8655(2002)075<0046:morhvc>2.0.co;2.
63. Overhaus, M.; Heckenkamp, J.; Kossodo, S.; Leszczynski, D.; LaMuraglia, G.M. Photodynamic Therapy Generates a Matrix Barrier to Invasive Vascular Cell Migration. *Circ. Res.* **2000**, *86*, 334-340, doi:10.1161/01.RES.86.3.334.
64. Karrer, S.; Bosserhoff, A.K.; Weiderer, P.; Landthaler, M.; Szeimies, R.-M. Influence of 5-Aminolevulinic Acid and Red Light on Collagen Metabolism of Human Dermal Fibroblasts. *Journal of Investigative Dermatology* **2003**, *120*, 325-331, doi:10.1046/j.1523-1747.2003.12037.x.
65. Tanaka, H.; Okada, T.; Konishi, H.; Tsuji, T. The effect of reactive oxygen species on the biosynthesis of collagen and glycosaminoglycans in cultured human dermal fibroblasts. *Archives of Dermatological Research* **1993**, *285*, 352-355, doi:10.1007/BF00371836.
66. Fleming, J.M.; Yeyeodu, S.T.; McLaughlin, A.; Schuman, D.; Taylor, D.K. In Situ Drug Delivery to Breast Cancer-Associated Extracellular Matrix. *ACS Chemical Biology* **2018**, *13*, 2825-2840, doi:10.1021/acschembio.8b00396.
67. Gomer, C.J.; Ferrario, A.; Luna, M.; Rucker, N.; Wong, S. Photodynamic therapy: Combined modality approaches targeting the tumor microenvironment. *Lasers in Surgery and Medicine* **2006**, *38*, 516-521, doi:https://doi.org/10.1002/lsm.20339.
68. Pazos, M.; Nader, H.B. Effect of photodynamic therapy on the extracellular matrix and associated components. *Braz J Med Biol Res* **2007**, *40*, 1025-1035, doi:10.1590/s0100-879x2006005000142.
69. Özdemir, Berna C.; Pentcheva-Hoang, T.; Carstens, Julienne L.; Zheng, X.; Wu, C.-C.; Simpson, Tyler R.; Laklai, H.; Sugimoto, H.; Kahlert, C.; Novitskiy, Sergey V., et al. Depletion of Carcinoma-Associated Fibroblasts and Fibrosis Induces Immunosuppression and Accelerates Pancreas Cancer with Reduced Survival. *Cancer Cell* **2014**, *25*, 719-734, doi:10.1016/j.ccr.2014.04.005.
70. Malham, G.M.; Thomsen, R.J.; Finlay, G.J.; Baguley, B.C. Subcellular distribution and photocytotoxicity of aluminium phthalocyanines and haematoporphyrin derivative in cultured human meningioma cells. *British Journal of Neurosurgery* **1996**, *10*, 51-57, doi:10.1080/02688699650040520.
71. Miller, J.W.; Walsh, A.W.; Kramer, M.; Hasan, T.; Michaud, N.; Flotte, T.J.; Haimovici, R.; Gragoudas, E.S. Photodynamic Therapy of Experimental Choroidal Neovascularization Using Lipoprotein-Delivered Benzoporphyrin. *Archives of Ophthalmology* **1995**, *113*, 810-818, doi:10.1001/archopht.1995.01100060136048.
72. Runnels, J.M.; Chen, N.; Ortel, B.; Kato, D.; Hasan, T. BPD-MA-mediated photosensitization in vitro and in vivo: cellular adhesion and beta1 integrin expression in ovarian cancer cells. *Br J Cancer* **1999**, *80*, 946-953, doi:10.1038/sj.bjc.6690448.

73. Kawczyk-Krupka, A.; Wawrzyniec, K.; Musiol, S.K.; Potempa, M.; Bugaj, A.M.; Sieroń, A. Treatment of localized prostate cancer using WST-09 and WST-11 mediated vascular targeted photodynamic therapy—A review. *Photodiagnosis and Photodynamic Therapy* **2015**, *12*, 567-574, doi:10.1016/j.pdpdt.2015.10.001.
74. Hsieh, Y.-J.; Wu, C.-C.; Chang, C.-J.; Yu, J.-S. Subcellular localization of Photofrin® determines the death phenotype of human epidermoid carcinoma A431 cells triggered by photodynamic therapy: When plasma membranes are the main targets. *J. Cell. Physiol.* **2003**, *194*, 363-375, doi:10.1002/jcp.10273.
75. Marchal, S.; François, A.; Dumas, D.; Guillemin, F.; Bezdetnaya, L. Relationship between subcellular localisation of Foscan® and caspase activation in photosensitised MCF-7 cells. *Br J Cancer* **2007**, *96*, 944-951, doi:10.1038/sj.bjc.6603631.
76. Teiten, M.H.; Bezdetnaya, L.; Morlière, P.; Santus, R.; Guillemin, F. Endoplasmic reticulum and Golgi apparatus are the preferential sites of Foscan® localisation in cultured tumour cells. *Br J Cancer* **2003**, *88*, 146-152, doi:10.1038/sj.bjc.6600664.
77. Tynga, I.M.; Houreld, N.N.; Abrahamse, H. The primary subcellular localization of Zinc phthalocyanine and its cellular impact on viability, proliferation and structure of breast cancer cells (MCF-7). *Journal of Photochemistry and Photobiology B: Biology* **2013**, *120*, 171-176, doi:10.1016/j.jphotobiol.2012.11.009.
78. Kessel, D.; Woodburn, K.; Gomer, C.J.; Jagerovic, N.; Smith, K.M. Photosensitization with derivatives of chlorin p6. *Journal of Photochemistry and Photobiology B: Biology* **1995**, *28*, 13-18, doi:10.1016/1011-1344(94)07085-3.
79. Gaullier, J.-M.; Gèze, M.; Santus, R.; Melo, T.S.e.; Mazière, J.-C.; Bazin, M.; Morlière, P.; Dubertret, L. SUBCELLULAR LOCALIZATION OF AND PHOTOSENSITIZATION BY PROTOPORPHYRIN IX IN HUMAN KERATINOCYTES AND FIBROBLASTS CULTIVATED WITH 5-AMINOLEVULINIC ACID. *Photochemistry and Photobiology* **1995**, *62*, 114-122, doi:10.1111/j.1751-1097.1995.tb05247.x.
80. Shulok, J.R.; Wade, M.H.; Lin, C.-W. SUBCELLULAR LOCALIZATION OF HEMATOPORPHYRIN DERIVATIVE IN BLADDER TUMOR CELLS IN CULTURE. *Photochemistry and Photobiology* **1990**, *51*, 451-457, doi:10.1111/j.1751-1097.1990.tb01736.x.
81. Anand, S.; Ortel, B.J.; Pereira, S.P.; Hasan, T.; Maytin, E.V. Biomodulatory approaches to photodynamic therapy for solid tumors. *Cancer Letters* **2012**, *326*, 8-16, doi:10.1016/j.canlet.2012.07.026.
82. Shemin, D.; Rittenberg, D. The utilization of glycine for the synthesis of a porphyrin. *J. Biol. Chem.* **1945**, *159*, 567-568.
83. Shemin, D.; Russell, C.S. δ-Aminolevulinic acid, its role in the biosynthesis of Porphyrins and Purines1. *Journal of the American Chemical Society* **1953**, *75*, 4873-4874.
84. Radin, N.S.; Rittenberg, D.; Shemin, D. The role of acetic acid in the biosynthesis of heme. *J. Biol. Chem.* **1950**, *184*, 755-767.

85. Muir, H.M.; Neuberger, A. The biogenesis of porphyrins. 2. The origin of the methyne carbon atoms. *Biochemical Journal* **1950**, *47*, 97.
86. Gibson, K.; Laver, W.; Neuberger, A. Initial stages in the biosynthesis of porphyrins. 2. The formation of δ-aminolaevulic acid from glycine and succinyl-coenzyme A by particles from chicken erythrocytes. *Biochemical Journal* **1958**, *70*, 71.
87. Kikuchi, G.; Kumar, A.; Talmage, P.; Shemin, D. The enzymatic synthesis of δ-aminolevulinic acid. *J. Biol. Chem.* **1958**, *233*, 1214-1219.
88. Shemin, D.; Kumin, S. The mechanism of porphyrin formation: the formation of a succinyl intermediate from succinate. *J. Biol. Chem.* **1952**, *198*, 827-837.
89. Gaullier, J.M.; Gèze, M.; Santus, R.; Melo, T.S.e.; Mazière, J.C.; Bazin, M.; Morlière, P.; Dubertret, L. Subcellular localization of and photosensitization by protoporphyrin IX in human keratinocytes and fibroblasts cultivated with 5-aminolevulinic acid. *Photochemistry and Photobiology* **1995**, *62*, 114-122, doi:10.1111/j.1751-1097.1995.tb05247.x.
90. Yamamoto, M. Improvement of the efficacy of 5-aminolevulinic acid-mediated photodynamic treatment in human oral squamous cell carcinoma HSC-4. **2013**, 10.18926/AMO/50408, doi:10.18926/AMO/50408.
91. Kobuchi, H.; Moriya, K.; Ogino, T.; Fujita, H.; Inoue, K.; Shuin, T.; Yasuda, T.; Utsumi, K.; Utsumi, T. Mitochondrial localization of ABC transporter ABCG2 and its function in 5-aminolevulinic acid-mediated protoporphyrin IX accumulation. *PLoS One* **2012**, *7*, e50082, doi:10.1371/journal.pone.0050082.
92. Hadjipanayis, C.G.; Stummer, W. 5-ALA and FDA approval for glioma surgery. *Journal of neuro-oncology* **2019**, *141*, 479-486, doi:10.1007/s11060-019-03098-y.
93. Dirschka, T.; Radny, P.; Dominicus, R.; Mensing, H.; Brüning, H.; Jenne, L.; Karl, L.; Sebastian, M.; Oster-Schmidt, C.; Klövekorn, W. Photodynamic therapy with BF-200 ALA for the treatment of actinic keratosis: results of a multicentre, randomized, observer-blind phase III study in comparison with a registered methyl-5-aminolaevulinate cream and placebo. *British Journal of Dermatology* **2012**, *166*, 137-146, doi:10.1111/j.1365-2133.2011.10613.x.
94. Dirschka, T.; Radny, P.; Dominicus, R.; Mensing, H.; Brüning, H.; Jenne, L.; Karl, L.; Sebastian, M.; Oster-Schmidt, C.; Klövekorn, W. Long-term (6 and 12 months) follow-up of two prospective, randomized, controlled phase III trials of photodynamic therapy with BF-200 ALA and methyl aminolaevulinate for the treatment of actinic keratosis. *British Journal of Dermatology* **2013**, *168*, 825-836, doi:10.1111/bjd.12158.
95. Wachowska, M.; Muchowicz, A.; Firczuk, M.; Gabrysiak, M.; Winiarska, M.; Wańczyk, M.; Bojarczuk, K.; Golab, J. Aminolevulinic acid (ALA) as a prodrug in photodynamic therapy of cancer. *Molecules* **2011**, *16*, 4140-4164, doi:10.3390/molecules16054140.
96. Malik, Z.; Djaldetti, M. 5-aminolevulinic acid stimulation of porphyrin and hemoglobin synthesis by uninduced friend erythroleukemic cells. *Cell Differentiation* **1979**, *8*, 223-233, doi:10.1016/0045-6039(79)90049-6.
97. Kennedy, J.; Pottier, R.; Pross, D. Photodynamic therapy with endogenous protoporphyrin: IX: basic principles and present clinical experience. *Journal*

of Photochemistry and Photobiology B: Biology **1990**, *6*, 143-148, doi:10.1016/1011-1344(90)85083-9.
98. Pottier, R.H. Photodynamic therapy with ALA: a clinical handbook. **2006**.
99. Kennedy, J.C.; Pottier, R.H. New trends in photobiology: endogenous protoporphyrin IX, a clinically useful photosensitizer for photodynamic therapy. *Journal of Photochemistry and Photobiology B: Biology* **1992**, *14*, 275-292, doi:10.1016/1011-1344(92)85108-7.
100. Gad, F.; Viau, G.; Bousbira, M.; Bertrand, R.; Bissonnette, R. Photodynamic therapy with 5-aminolevulinic acid induces apoptosis and caspase activation in malignant T cells. *Journal of cutaneous medicine and surgery* **2001**, *5*, 8-13, doi:10.1177/120347540100500103.
101. Anand, S.; Wilson, C.; Hasan, T.; Maytin, E.V. Vitamin D3 Enhances the Apoptotic Response of Epithelial Tumors to Aminolevulinate-Based Photodynamic Therapy. *Cancer Research* **2011**, *71*, 6040-6050, doi:10.1158/0008-5472.Can-11-0805.
102. Maytin, E.V.; Anand, S.; Wilson, C.; Iyer, K. 5-Fluorouracil as an enhancer of aminolevulinate-based photodynamic therapy for skin cancer: New use for a venerable agent? In Proceedings of BiOS.
103. Rollakanti, K.R.; Anand, S.; Maytin, E.V. Vitamin D enhances the efficacy of photodynamic therapy in a murine model of breast cancer. *Cancer Med* **2015**, *4*, 633-642, doi:10.1002/cam4.361.
104. Tahmasebi, H.; Khoshgard, K.; Sazgarnia, A.; Mostafaie, A.; Eivazi, M.T. Enhancing the efficiency of 5-aminolevulinic acid-mediated photodynamic therapy using 5-fluorouracil on human melanoma cells. *Photodiagnosis and Photodynamic Therapy* **2016**, *13*, 297-302, doi:10.1016/j.pdpdt.2015.08.011.
105. Benito-Miguel, M.; Blanco, M.D.; Gómez, C. Assessment of sequential combination of 5-fluorouracil-loaded-chitosan-nanoparticles and ALA-photodynamic therapy on HeLa cell line. *Photodiagnosis and Photodynamic Therapy* **2015**, *12*, 466-475, doi:10.1016/j.pdpdt.2015.05.001.
106. Maytin, E.V.; Anand, S.; Riha, M.; Lohser, S.; Tellez, A.; Ishak, R.; Karpinski, L.; Sot, J.; Hu, B.; Denisyuk, A., et al. 5-Fluorouracil Enhances Protoporphyrin IX Accumulation and Lesion Clearance during Photodynamic Therapy of Actinic Keratoses: A Mechanism-Based Clinical Trial. *Clinical Cancer Research* **2018**, *24*, 3026-3035, doi:10.1158/1078-0432.Ccr-17-2020.
107. Salim, A.; Leman, J.A.; McColl, J.H.; Chapman, R.; Morton, C.A. Randomized comparison of photodynamic therapy with topical 5-fluorouracil in Bowen's disease. *British Journal of Dermatology* **2003**, *148*, 539-543, doi:10.1046/j.1365-2133.2003.05033.x.
108. Blake, E.; Curnow, A. The Hydroxypyridinone Iron Chelator CP94 Can Enhance PpIX-induced PDT of Cultured Human Glioma Cells. *Photochemistry and Photobiology* **2010**, *86*, 1154-1160, doi:10.1111/j.1751-1097.2010.00770.x.
109. Hanania, J.; Malik, Z. The effect of EDTA and serum on endogenous porphyrin accumulation and photodynamic sensitization of human K562 leukemic cells. *Cancer Letters* **1992**, *65*, 127-131, doi:10.1016/0304-3835(92)90156-P.

110. Pye, A.; Campbell, S.; Curnow, A. Enhancement of methyl-aminolevulinate photodynamic therapy by iron chelation with CP94: an in vitro investigation and clinical dose-escalating safety study for the treatment of nodular basal cell carcinoma. *Journal of Cancer Research and Clinical Oncology* **2008**, *134*, 841-849, doi:10.1007/s00432-008-0358-6.
111. Campbell, S.M.; Morton, C.A.; Alyahya, R.; Horton, S.; Pye, A.; Curnow, A. Clinical investigation of the novel iron-chelating agent, CP94, to enhance topical photodynamic therapy of nodular basal cell carcinoma. *British Journal of Dermatology* **2008**, *159*, 387-393, doi:10.1111/j.1365-2133.2008.08668.x.
112. Pye, A.; Curnow, A. Direct Comparison of δ-Aminolevulinic Acid and Methyl-Aminolevulinate-Derived Protoporphyrin IX Accumulations Potentiated by Desferrioxamine or the Novel Hydroxypyridinone Iron Chelator CP94 in Cultured Human Cells. *Photochemistry and Photobiology* **2007**, *83*, 766-773, doi:10.1562/2006-05-30-RA-906.
113. Anand, S.; Rollakanti, K.R.; Horst, R.L.; Hasan, T.; Maytin, E.V. Combination of Oral Vitamin D3 with Photodynamic Therapy Enhances Tumor Cell Death in a Murine Model of Cutaneous Squamous Cell Carcinoma. *Photochemistry and Photobiology* **2014**, *90*, 1126-1135, doi:10.1111/php.12286.
114. Berg, K.; Anholt, H.; Bech, Ø.; Moan, J. The influence of iron chelators on the accumulation of protoporphyrin IX in 5-aminolaevulinic acid-treated cells. *Br J Cancer* **1996**, *74*, 688-697, doi:10.1038/bjc.1996.423.
115. Bech, Ø.; Phillips, D.; Moan, J.; MacRobert, A.J. A hydroxypyridinone (CP94) enhances protoporphyrin IX formation in 5-aminolaevulinic acid treated cells. *Journal of Photochemistry and Photobiology B: Biology* **1997**, *41*, 136-144, doi:10.1016/S1011-1344(97)00095-X.
116. Curnow, A.; MacRobert, A.J.; Bown, S.G. Comparing and combining light dose fractionation and iron chelation to enhance experimental photodynamic therapy with aminolevulinic acid. *Lasers in Surgery and Medicine* **2006**, *38*, 325-331, doi:10.1002/lsm.20328.
117. Chang, S.-C.; MacRobert, A.J.; Porter, J.B.; Brown, S.G. The efficacy of an iron chelator (CP94) in increasing cellular protoporphyrin IX following intravesical 5-aminolaevulinic acid administration: an in vivo study. *Journal of Photochemistry and Photobiology B: Biology* **1997**, *38*, 114-122, doi:10.1016/S1011-1344(96)07441-6.
118. Casas, A.; Batlle, A.M.d.C.; Butler, A.R.; Robertson, D.; Brown, E.H.; MacRobert, A.; Riley, P.A. Comparative effect of ALA derivatives on protoporphyrin IX production in human and rat skin organ cultures. *Br J Cancer* **1999**, *80*, 1525-1532, doi:10.1038/sj.bjc.6690556.
119. Choudry, K.; Brooke, R.C.C.; Farrar, W.; Rhodes, L.E. The effect of an iron chelating agent on protoporphyrin IX levels and phototoxicity in topical 5-aminolaevulinic acid photodynamic therapy. *British Journal of Dermatology* **2003**, *149*, 124-130, doi:10.1046/j.1365-2133.2003.05351.x.
120. Inoue, K.; Karashima, T.; Kamada, M.; Shuin, T.; Kurabayashi, A.; Furihata, M.; Fujita, H.; Utsumi, K.; Sasaki, J. Regulation of 5-Aminolevulinic Acid-

Mediated Protoporphyrin IX Accumulation in Human Urothelial Carcinomas. *Pathobiology* **2009**, *76*, 303-314, doi:10.1159/000245896.
121. Ortel, B.; Sharlin, D.; O'Donnell, D.; Sinha, A.K.; Maytin, E.V.; Hasan, T. Differentiation enhances aminolevulinic acid-dependent photodynamic treatment of LNCaP prostate cancer cells. *Br J Cancer* **2002**, *87*, 1321-1327, doi:10.1038/sj.bjc.6600575.
122. Maytin, E.V.; Honari, G.; Khachemoune, A.; Taylor, C.R.; Ortel, B.; Pogue, B.W.; Sznycer-Taub, N.; Hasan, T. The Vitamin D Analog Calcipotriol Combined with Aminolevulinate-Mediated Photodynamic Therapy for Human Psoriasis: A Proof-of-Principle Study. *Israel Journal of Chemistry* **2012**, *52*, 767-775, doi:10.1002/ijch.201200005.
123. Seo, J.-W.; Song, K.-H. Topical calcipotriol before ablative fractional laser-assisted photodynamic therapy enhances treatment outcomes for actinic keratosis in Fitzpatrick grades III-V skin: A prospective randomized clinical trial. *Journal of the American Academy of Dermatology* **2018**, *78*, 795-797, doi:10.1016/j.jaad.2017.11.027.
124. Momma, T.; Hamblin, M.R.; Hasan, T. Hormonal modulation of the accumulation of 5-aminolevulinic acid-induced protoporphyrin and phototoxicity in prostate cancer cells. *International Journal of Cancer* **1997**, *72*, 1062-1069, doi:10.1002/(SICI)1097-0215(19970917)72:6<1062::AID-IJC22>3.0.CO;2-5.
125. Sinha, A.K.; Anand, S.; Ortel, B.J.; Chang, Y.; Mai, Z.; Hasan, T.; Maytin, E.V. Methotrexate used in combination with aminolaevulinic acid for photodynamic killing of prostate cancer cells. *Br J Cancer* **2006**, *95*, 485-495, doi:10.1038/sj.bjc.6603273.
126. Anand, S.; Honari, G.; Hasan, T.; Elson, P.; Maytin, E.V. Low-dose methotrexate enhances aminolevulinate-based photodynamic therapy in skin carcinoma cells in vitro and in vivo. *Clin Cancer Res* **2009**, *15*, 3333-3343, doi:10.1158/1078-0432.Ccr-08-3054.
127. Yang, D.F.; Lee, J.W.; Chen, H.M.; Hsu, Y.C. Topical methotrexate pretreatment enhances the therapeutic effect of topical 5-aminolevulinic acid-mediated photodynamic therapy on hamster buccal pouch precancers. *J Formos Med Assoc* **2014**, *113*, 591-599, doi:10.1016/j.jfma.2014.03.002.
128. Juzeniene, A.; Juzenas, P.; Bronshtein, I.; Vorobey, A.; Moan, J. The influence of temperature on photodynamic cell killing in vitro with 5-aminolevulinic acid. *Journal of Photochemistry and photobiology B: Biology* **2006**, *84*, 161-166, doi:10.1016/j.jphotobiol.2006.02.009.
129. Juzeniene, A.; Juzenas, P.; Iani, V.; Moan, J. Topical Application of 5-Aminolevulinic Acid and its Methylester, Hexylester and Octylester Derivatives: Considerations for Dosimetry in Mouse Skin Model. *Photochemistry and Photobiology* **2002**, *76*, 329-334, doi:10.1562/0031-8655(2002)0760329TAOAAA2.0.CO2.
130. Piot, B.; Rousset, N.; Lenz, P.; Eléouet, S.; Carré, J.; Vonarx, V.; Bourré, L.; Patrice, T. Enhancement of Delta Aminolevulinic Acid–Photodynamic Therapy In Vivo by Decreasing Tumor pH With Glucose and Amiloride. *The*

Laryngoscope **2001**, *111*, 2205-2213, doi:10.1097/00005537-200112000-00026.
131. Bech, Ø.; Berg, K.; Moan, J. The pH dependency of protoporphyrin IX formation in cells incubated with 5-aminolevulinic acid. *Cancer Letters* **1997**, *113*, 25-29, doi:10.1016/S0304-3835(96)04558-2.
132. Wyld, L.; Reed, M.W.R.; Brown, N.J. The influence of hypoxia and pH on aminolaevulinic acid-induced photodynamic therapy in bladder cancer cells in vitro. *Br J Cancer* **1998**, *77*, 1621-1627, doi:10.1038/bjc.1998.265.
133. Uehlinger, P.; Zellweger, M.; Wagnières, G.; Juillerat-Jeanneret, L.; van den Bergh, H.; Lange, N. 5-Aminolevulinic acid and its derivatives: physical chemical properties and protoporphyrin IX formation in cultured cells. *Journal of Photochemistry and Photobiology B: Biology* **2000**, *54*, 72-80, doi:10.1016/S1011-1344(99)00159-1.
134. Niu, C.; Fisher, C.; Scheffler, K.; Wan, R.; Maleki, H.; Liu, H.; Sun, Y.; A. Simmons, C.; Birngruber, R.; Lilge, L. Polyacrylamide gel substrates that simulate the mechanical stiffness of normal and malignant neuronal tissues increase protoporphyin IX synthesis in glioma cells. *Journal of Biomedical Optics* **2015**, *20*, 098002, doi:10.1117/1.JBO.20.9.098002.
135. Niu, C.J.; Fisher, C.; Scheffler, K.; Wan, R.; Maleki, H.; Liu, H.; Sun, Y.; A. Simmons, C.; Birngruber, R.; Lilge, L. Polyacrylamide gel substrates that simulate the mechanical stiffness of normal and malignant neuronal tissues increase protoporphyin IX synthesis in glioma cells. *Journal of biomedical optics* **2015**, *20*, 098002-098002, doi:10.1117/1.JBO.20.9.098002.
136. Ulrich, T.A.; de Juan Pardo, E.M.; Kumar, S. The mechanical rigidity of the extracellular matrix regulates the structure, motility, and proliferation of glioma cells. *Cancer research* **2009**, *69*, 4167-4174, doi:10.1158/0008-5472.CAN-08-4859.
137. Murphy, M.C.; Huston III, J.; Jack Jr, C.R.; Glaser, K.J.; Manduca, A.; Felmlee, J.P.; Ehman, R.L. Decreased brain stiffness in Alzheimer's disease determined by magnetic resonance elastography. *Journal of magnetic resonance imaging* **2011**, *34*, 494-498, doi:10.1002/jmri.22707.
138. Fisher, C.J.; Niu, C.J.; Lai, B.; Chen, Y.; Kuta, V.; Lilge, L.D. Modulation of PPIX synthesis and accumulation in various normal and glioma cell lines by modification of the cellular signaling and temperature. *Lasers in surgery and medicine* **2013**, *45*, 460-468, doi:10.1002/lsm.22161.
139. Wang, M.; Zhao, J.; Zhang, L.; Wei, F.; Lian, Y.; Wu, Y.; Gong, Z.; Zhang, S.; Zhou, J.; Cao, K. Role of tumor microenvironment in tumorigenesis. *J Cancer* **2017**, *8*, 761, doi:10.7150/jca.17648.
140. Golombek, S.K.; May, J.-N.; Theek, B.; Appold, L.; Drude, N.; Kiessling, F.; Lammers, T. Tumor targeting via EPR: Strategies to enhance patient responses. *Advanced Drug Delivery Reviews* **2018**, *130*, 17-38, doi:https://doi.org/10.1016/j.addr.2018.07.007.
141. Greish, K. Enhanced permeability and retention (EPR) effect for anticancer nanomedicine drug targeting. *Cancer nanotechnology: Methods and protocols* **2010**, 10.1007/978-1-60761-609-2_3, 25-37, doi:10.1007/978-1-60761-609-2_3.

142. Rosenblum, D.; Joshi, N.; Tao, W.; Karp, J.M.; Peer, D. Progress and challenges towards targeted delivery of cancer therapeutics. *Nature communications* **2018**, *9*, 1410, doi:10.1038/s41467-018-03705-y.
143. Vaupel, P.; Harrison, L. Tumor hypoxia: causative factors, compensatory mechanisms, and cellular response. *The oncologist* **2004**, *9*, 4-9, doi:10.1634/theoncologist.9-90005-4.
144. Thews, O.; Riemann, A. Tumor pH and metastasis: a malignant process beyond hypoxia. *Cancer and Metastasis Reviews* **2019**, *38*, 113-129, doi:10.1007/s10555-018-09777-y.
145. Kato, Y.; Ozawa, S.; Miyamoto, C.; Maehata, Y.; Suzuki, A.; Maeda, T.; Baba, Y. Acidic extracellular microenvironment and cancer. *Cancer cell international* **2013**, *13*, 1-8, doi:10.1186/1475-2867-13-89.
146. Liberti, M.V.; Locasale, J.W. The Warburg Effect: How Does it Benefit Cancer Cells? *Trends Biochem Sci* **2016**, *41*, 211-218, doi:10.1016/j.tibs.2015.12.001.
147. Iyer, A.K.; Khaled, G.; Fang, J.; Maeda, H. Exploiting the enhanced permeability and retention effect for tumor targeting. *Drug Discovery Today* **2006**, *11*, 812-818, doi:10.1016/j.drudis.2006.07.005.
148. Siemann, D.W. The unique characteristics of tumor vasculature and preclinical evidence for its selective disruption by Tumor-Vascular Disrupting Agents. *Cancer Treatment Reviews* **2011**, *37*, 63-74, doi:10.1016/j.ctrv.2010.05.001.
149. Kobayashi, H.; Watanabe, R.; Choyke, P.L. Improving conventional enhanced permeability and retention (EPR) effects; what is the appropriate target? *Theranostics* **2013**, *4*, 81-89, doi:10.7150/thno.7193.
150. Heldin, C.H.; Rubin, K.; Pietras, K.; Ostman, A. High interstitial fluid pressure - an obstacle in cancer therapy. *Nat Rev Cancer* **2004**, *4*, 806-813, doi:10.1038/nrc1456.
151. Maeda, H. The enhanced permeability and retention (EPR) effect in tumor vasculature: the key role of tumor-selective macromolecular drug targeting. *Adv Enzyme Regul* **2001**, *41*, 189-207, doi:10.1016/s0065-2571(00)00013-3.
152. Ngoune, R.; Peters, A.; von Elverfeldt, D.; Winkler, K.; Pütz, G. Accumulating nanoparticles by EPR: A route of no return. *J Control Release* **2016**, *238*, 58-70, doi:10.1016/j.jconrel.2016.07.028.
153. Nehoff, H.; Parayath, N.N.; Domanovitch, L.; Taurin, S.; Greish, K. Nanomedicine for drug targeting: strategies beyond the enhanced permeability and retention effect. *Int J Nanomedicine* **2014**, *9*, 2539-2555, doi:10.2147/ijn.S47129.
154. Jain, R.K.; Stylianopoulos, T. Delivering nanomedicine to solid tumors. *Nat Rev Clin Oncol* **2010**, *7*, 653-664, doi:10.1038/nrclinonc.2010.139.
155. Jain, R.K. Delivery of molecular and cellular medicine to solid tumors. *Advanced Drug Delivery Reviews* **2001**, *46*, 149-168, doi:10.1016/S0169-409X(00)00131-9.
156. Dewhirst, M.W.; Secomb, T.W. Transport of drugs from blood vessels to tumour tissue. *Nature Reviews Cancer* **2017**, *17*, 738-750, doi:10.1038/nrc.2017.93.

157. Stapleton, S.; Milosevic, M.; Allen, C.; Zheng, J.; Dunne, M.; Yeung, I.; Jaffray, D.A. A mathematical model of the enhanced permeability and retention effect for liposome transport in solid tumors. *PLoS One* **2013**, *8*, e81157, doi:10.1371/journal.pone.0081157.
158. Goel, S.; Wong, A.H.; Jain, R.K. Vascular normalization as a therapeutic strategy for malignant and nonmalignant disease. *Cold Spring Harb Perspect Med* **2012**, *2*, a006486, doi:10.1101/cshperspect.a006486.
159. Jain, R.K.; Tong, R.T.; Munn, L.L. Effect of Vascular Normalization by Antiangiogenic Therapy on Interstitial Hypertension, Peritumor Edema, and Lymphatic Metastasis: Insights from a Mathematical Model. *Cancer Research* **2007**, *67*, 2729-2735, doi:10.1158/0008-5472.Can-06-4102.
160. Lim, C.-K.; Heo, J.; Shin, S.; Jeong, K.; Seo, Y.H.; Jang, W.-D.; Park, C.R.; Park, S.Y.; Kim, S.; Kwon, I.C. Nanophotosensitizers toward advanced photodynamic therapy of Cancer. *Cancer Letters* **2013**, *334*, 176-187, doi:10.1016/j.canlet.2012.09.012.
161. Weijer, R.; Broekgaarden, M.; Kos, M.; van Vught, R.; Rauws, E.A.J.; Breukink, E.; van Gulik, T.M.; Storm, G.; Heger, M. Enhancing photodynamic therapy of refractory solid cancers: Combining second-generation photosensitizers with multi-targeted liposomal delivery. *Journal of Photochemistry and Photobiology C: Photochemistry Reviews* **2015**, *23*, 103-131, doi:10.1016/j.jphotochemrev.2015.05.002.
162. Kim, J.; Santos, O.A.; Park, J.-H. Selective photosensitizer delivery into plasma membrane for effective photodynamic therapy. *Journal of Controlled Release* **2014**, *191*, 98-104, doi:10.1016/j.jconrel.2014.05.049.
163. Baglo, Y.; Liang, B.J.; Robey, R.W.; Ambudkar, S.V.; Gottesman, M.M.; Huang, H.-C. Porphyrin-lipid assemblies and nanovesicles overcome ABC transporter-mediated photodynamic therapy resistance in cancer cells. *Cancer Letters* **2019**, *457*, 110-118, doi:10.1016/j.canlet.2019.04.037.
164. Huynh, E.; Zheng, G. Porphysome nanotechnology: A paradigm shift in lipid-based supramolecular structures. *Nano Today* **2014**, *9*, 212-222, doi:10.1016/j.nantod.2014.04.012.
165. Huang, H.C.; Mallidi, S.; Obaid, G.; Sears, B.; Tangutoori, S.; Hasan, T. 23 - Advancing photodynamic therapy with biochemically tuned liposomal nanotechnologies. In *Applications of Nanoscience in Photomedicine*, Hamblin, M.R., Avci, P., Eds. Chandos Publishing: Oxford, 2015; DOI: 10.1533/9781908818782.487.pp. 487-510.
166. Hsu, C.-Y.; Chen, C.-W.; Yu, H.-P.; Lin, Y.-F.; Lai, P.-S. Bioluminescence resonance energy transfer using luciferase-immobilized quantum dots for self-illuminated photodynamic therapy. *Biomaterials* **2013**, *34*, 1204-1212, doi:10.1016/j.biomaterials.2012.08.044.
167. Shao, L.; Gao, Y.; Yan, F. Semiconductor Quantum Dots for Biomedicial Applications. *Sensors* **2011**, *11*, 11736-11751.
168. Lee, K.L.; Carpenter, B.L.; Wen, A.M.; Ghiladi, R.A.; Steinmetz, N.F. High Aspect Ratio Nanotubes Formed by Tobacco Mosaic Virus for Delivery of Photodynamic Agents Targeting Melanoma. *ACS Biomaterials Science & Engineering* **2016**, *2*, 838-844, doi:10.1021/acsbiomaterials.6b00061.

169. Gandra, N.; Abbineni, G.; Qu, X.; Huai, Y.; Wang, L.; Mao, C. Bacteriophage Bionanowire as a Carrier for Both Cancer-Targeting Peptides and Photosensitizers and its use in Selective Cancer Cell Killing by Photodynamic Therapy. *Small* **2013**, *9*, 215-221, doi:10.1002/smll.201202090.
170. Stephanopoulos, N.; Tong, G.J.; Hsiao, S.C.; Francis, M.B. Dual-Surface Modified Virus Capsids for Targeted Delivery of Photodynamic Agents to Cancer Cells. *ACS Nano* **2010**, *4*, 6014-6020, doi:10.1021/nn1014769.
171. Rhee, J.-K.; Baksh, M.; Nycholat, C.; Paulson, J.C.; Kitagishi, H.; Finn, M.G. Glycan-Targeted Virus-like Nanoparticles for Photodynamic Therapy. *Biomacromolecules* **2012**, *13*, 2333-2338, doi:10.1021/bm300578p.
172. Bae, B.-c.; Na, K. Development of Polymeric Cargo for Delivery of Photosensitizer in Photodynamic Therapy. *International Journal of Photoenergy* **2012**, *2012*, 431975, doi:10.1155/2012/431975.
173. Yang, G.; Gong, H.; Qian, X.; Tan, P.; Li, Z.; Liu, T.; Liu, J.; Li, Y.; Liu, Z. Mesoporous silica nanorods intrinsically doped with photosensitizers as a multifunctional drug carrier for combination therapy of cancer. *Nano Research* **2015**, *8*, 751-764, doi:10.1007/s12274-014-0558-0.
174. Bharathiraja, S.; Moorthy, M.S.; Manivasagan, P.; Seo, H.; Lee, K.D.; Oh, J. Chlorin e6 conjugated silica nanoparticles for targeted and effective photodynamic therapy. *Photodiagnosis and Photodynamic Therapy* **2017**, *19*, 212-220, doi:10.1016/j.pdpdt.2017.06.001.
175. Sun, J.; Kormakov, S.; Liu, Y.; Huang, Y.; Wu, D.; Yang, Z. Recent Progress in Metal-Based Nanoparticles Mediated Photodynamic Therapy. *Molecules* **2018**, *23*, 1704.
176. Lee, D.J.; Park, S.Y.; Oh, Y.T.; Oh, N.M.; Oh, K.T.; Youn, Y.S.; Lee, E.S. Preparation of chlorine e6-conjugated single-wall carbon nanotube for photodynamic therapy. *Macromolecular Research* **2011**, *19*, 848-852, doi:10.1007/s13233-011-0816-x.
177. Huang, P.; Wang, S.; Wang, X.; Shen, G.; Lin, J.; Wang, Z.; Guo, S.; Cui, D.; Yang, M.; Chen, X. Surface Functionalization of Chemically Reduced Graphene Oxide for Targeted Photodynamic Therapy. *J Biomed Nanotechnol* **2015**, *11*, 117-125, doi:10.1166/jbn.2015.2055.
178. Huang, H.C.; Hasan, T. The "Nano" World in Photodynamic Therapy. *Austin J Nanomed Nanotechnol* **2014**, *2*.
179. Yin, R.; Wang, M.; Huang, Y.-Y.; Huang, H.-C.; Avci, P.; Chiang, L.Y.; Hamblin, M.R. Photodynamic therapy with decacationic [60]fullerene monoadducts: Effect of a light absorbing electron-donor antenna and micellar formulation. *Nanomedicine: Nanotechnology, Biology and Medicine* **2014**, *10*, 795-808, doi:10.1016/j.nano.2013.11.014.
180. Obaid, G.; Broekgaarden, M.; Bulin, A.L.; Huang, H.C.; Kuriakose, J.; Liu, J.; Hasan, T. Photonanomedicine: a convergence of photodynamic therapy and nanotechnology. *Nanoscale* **2016**, *8*, 12471-12503, doi:10.1039/c5nr08691d.
181. Shi, J.; Kantoff, P.W.; Wooster, R.; Farokhzad, O.C. Cancer nanomedicine: progress, challenges and opportunities. *Nature Reviews Cancer* **2017**, *17*, 20-37, doi:10.1038/nrc.2016.108.

182. Miller, M.A.; Arlauckas, S.; Weissleder, R. Prediction of Anti-cancer Nanotherapy Efficacy by Imaging. *Nanotheranostics* **2017**, *1*, 296-312, doi:10.7150/ntno.20564.
183. Miller, M.A.; Gadde, S.; Pfirschke, C.; Engblom, C.; Sprachman, M.M.; Kohler, R.H.; Yang, K.S.; Laughney, A.M.; Wojtkiewicz, G.; Kamaly, N., et al. Predicting therapeutic nanomedicine efficacy using a companion magnetic resonance imaging nanoparticle. *Science Translational Medicine* **2015**, *7*, 314ra183-314ra183, doi:10.1126/scitranslmed.aac6522.
184. Maeda, H. Toward a full understanding of the EPR effect in primary and metastatic tumors as well as issues related to its heterogeneity. *Advanced Drug Delivery Reviews* **2015**, *91*, 3-6, doi:10.1016/j.addr.2015.01.002.
185. Rajora, A.K.; Ravishankar, D.; Osborn, H.M.I.; Greco, F. Impact of the Enhanced Permeability and Retention (EPR) Effect and Cathepsins Levels on the Activity of Polymer-Drug Conjugates. *Polymers* **2014**, *6*, 2186-2220, doi:10.3390/polym6082186.
186. Chaffer, C.L.; Weinberg, R.A. A Perspective on Cancer Cell Metastasis. *Science* **2011**, *331*, 1559-1564, doi:10.1126/science.1203543.
187. Prabhakar, U.; Maeda, H.; Jain, R.K.; Sevick-Muraca, E.M.; Zamboni, W.; Farokhzad, O.C.; Barry, S.T.; Gabizon, A.; Grodzinski, P.; Blakey, D.C. Challenges and Key Considerations of the Enhanced Permeability and Retention Effect for Nanomedicine Drug Delivery in Oncology. *Cancer Research* **2013**, *73*, 2412-2417, doi:10.1158/0008-5472.Can-12-4561.
188. Nichols, J.W.; Bae, Y.H. EPR: Evidence and fallacy. *Journal of Controlled Release* **2014**, *190*, 451-464, doi:10.1016/j.jconrel.2014.03.057.
189. Spring, B.Q.; Rizvi, I.; Xu, N.; Hasan, T. The role of photodynamic therapy in overcoming cancer drug resistance. *Photochemical & Photobiological Sciences* **2015**, *14*, 1476-1491, doi:10.1039/C4PP00495G.
190. Chen, B.; Pogue, B.W.; Luna, J.M.; Hardman, R.L.; Hoopes, P.J.; Hasan, T. Tumor Vascular Permeabilization by Vascular-Targeting Photosensitization: Effects, Mechanism, and Therapeutic Implications. *Clinical Cancer Research* **2006**, *12*, 917-923, doi:10.1158/1078-0432.Ccr-05-1673.
191. Chen, B.; Pogue, B.W.; Hoopes, P.J.; Hasan, T. Combining vascular and cellular targeting regimens enhances the efficacy of photodynamic therapy. *International Journal of Radiation Oncology*Biology*Physics* **2005**, *61*, 1216-1226, doi:10.1016/j.ijrobp.2004.08.006.
192. Gao, W.; Wang, Z.; Lv, L.; Yin, D.; Chen, D.; Han, Z.; Ma, Y.; Zhang, M.; Yang, M.; Gu, Y. Photodynamic Therapy Induced Enhancement of Tumor Vasculature Permeability Using an Upconversion Nanoconstruct for Improved Intratumoral Nanoparticle Delivery in Deep Tissues. *Theranostics* **2016**, *6*, 1131-1144, doi:10.7150/thno.15262.
193. Zhen, Z.; Tang, W.; Chuang, Y.-J.; Todd, T.; Zhang, W.; Lin, X.; Niu, G.; Liu, G.; Wang, L.; Pan, Z., et al. Tumor Vasculature Targeted Photodynamic Therapy for Enhanced Delivery of Nanoparticles. *ACS Nano* **2014**, *8*, 6004-6013, doi:10.1021/nn501134q.

194. Sano, K.; Nakajima, T.; Choyke, P.L.; Kobayashi, H. Markedly Enhanced Permeability and Retention Effects Induced by Photo-immunotherapy of Tumors. *ACS Nano* **2013**, *7*, 717-724, doi:10.1021/nn305011p.
195. Kobayashi, H.; Choyke, P.L. Super enhanced permeability and retention (SUPR) effects in tumors following near infrared photoimmunotherapy. *Nanoscale* **2016**, *8*, 12504-12509, doi:10.1039/c5nr05552k.
196. Leunig, M.; Goetz, A.E.; Gamarra, F.; Zetterer, G.; Messmer, K.; Jain, R.K. Photodynamic therapy-induced alterations in interstitial fluid pressure, volume and water content of an amelanotic melanoma in the hamster. *Br J Cancer* **1994**, *69*, 101-103, doi:10.1038/bjc.1994.15.
197. Cavin, S.; Riedel, T.; Rosskopfova, P.; Gonzalez, M.; Baldini, G.; Zellweger, M.; Wagnières, G.; Dyson, P.J.; Ris, H.-B.; Krueger, T., et al. Vascular-targeted low dose photodynamic therapy stabilizes tumor vessels by modulating pericyte contractility. *Lasers in Surgery and Medicine* **2019**, *51*, 550-561, doi:10.1002/lsm.23069.
198. Fingar, V.H.; Kik, P.K.; Haydon, P.S.; Cerrito, P.B.; Tseng, M.; Abang, E.; Wieman, T.J. Analysis of acute vascular damage after photodynamic therapy using benzoporphyrin derivative (BPD). *Br J Cancer* **1999**, *79*, 1702-1708, doi:10.1038/sj.bjc.6690271.
199. Engbrecht, B.W.; Menon, C.; Kachur, A.V.; Hahn, S.M.; Fraker, D.L. Photofrin-mediated Photodynamic Therapy Induces Vascular Occlusion and Apoptosis in a Human Sarcoma Xenograft Model1. *Cancer Research* **1999**, *59*, 4334-4342.
200. Madar-Balakirski, N.; Tempel-Brami, C.; Kalchenko, V.; Brenner, O.; Varon, D.; Scherz, A.; Salomon, Y. Permanent occlusion of feeding arteries and draining veins in solid mouse tumors by vascular targeted photodynamic therapy (VTP) with Tookad. *PLoS One* **2010**, *5*, e10282, doi:10.1371/journal.pone.0010282.
201. Buzzá, H.H.; Fialho de Freitas, L.C.; Moriyama, L.T.; Teixeira Rosa, R.G.; Bagnato, V.S.; Kurachi, C. Vascular Effects of Photodynamic Therapy with Curcumin in a Chorioallantoic Membrane Model. *Int J Mol Sci* **2019**, *20*, 1084, doi:10.3390/ijms20051084.
202. Bugaj, A.M. Vascular targeted photochemotherapy using padoporfin and padeliporfin as a method of the focal treatment of localised prostate cancer - clinician's insight. *World J Methodol* **2016**, *6*, 65-76, doi:10.5662/wjm.v6.i1.65.
203. Zilberstein, J.; Schreiber, S.; Bloemers, M.C.W.M.; Bendel, P.; Neeman, M.; Schechtman, E.; Kohen, F.; Scherz, A.; Salomon, Y. Antivascular Treatment of Solid Melanoma Tumors with Bacteriochlorophyll–serine-based Photodynamic Therapy. *Photochemistry and Photobiology* **2001**, *73*, 257-266, doi:10.1562/0031-8655(2001)0730257ATOSMT2.0.CO2.
204. Azzouzi, A.R.; Barret, E.; Bennet, J.; Moore, C.; Taneja, S.; Muir, G.; Villers, A.; Coleman, J.; Allen, C.; Scherz, A., et al. TOOKAD® Soluble focal therapy: pooled analysis of three phase II studies assessing the minimally invasive ablation of localized prostate cancer. *World Journal of Urology* **2015**, *33*, 945-953, doi:10.1007/s00345-015-1505-8.

205. Eggener, S.E.; Coleman, J.A. Focal Treatment of Prostate Cancer with Vascular-Targeted Photodynamic Therapy. *TheScientificWorldJOURNAL* **2008**, *8*, 172368, doi:10.1100/tsw.2008.127.
206. Trachtenberg, J.; Weersink, R.A.; Davidson, S.R.H.; Haider, M.A.; Bogaards, A.; Gertner, M.R.; Evans, A.; Scherz, A.; Savard, J.; Chin, J.L., et al. Vascular-targeted photodynamic therapy (padoporfin, WST09) for recurrent prostate cancer after failure of external beam radiotherapy: a study of escalating light doses. *BJU International* **2008**, *102*, 556-562, doi:10.1111/j.1464-410X.2008.07753.x.
207. Azzouzi, A.-R.; Vincendeau, S.; Barret, E.; Cicco, A.; Kleinclauss, F.; van der Poel, H.G.; Stief, C.G.; Rassweiler, J.; Salomon, G.; Solsona, E., et al. Padeliporfin vascular-targeted photodynamic therapy versus active surveillance in men with low-risk prostate cancer (CLIN1001 PCM301): an open-label, phase 3, randomised controlled trial. *The Lancet Oncology* **2017**, *18*, 181-191, doi:10.1016/S1470-2045(16)30661-1.
208. Gill, I.S.; Azzouzi, A.-R.; Emberton, M.; Coleman, J.A.; Coeytaux, E.; Scherz, A.; Scardino, P.T. Randomized Trial of Partial Gland Ablation with Vascular Targeted Phototherapy versus Active Surveillance for Low Risk Prostate Cancer: Extended Followup and Analyses of Effectiveness. *Journal of Urology* **2018**, *200*, 786-793, doi:10.1016/j.juro.2018.05.121.
209. Bressler, N.M.; Bressler, S.B.; Fine, S.L. Age-related macular degeneration. *Survey of Ophthalmology* **1988**, *32*, 375-413, doi:10.1016/0039-6257(88)90052-5.
210. Prasad, P.S.; Schwartz, S.D.; Hubschman, J.-P. Age-related macular degeneration: Current and novel therapies. *Maturitas* **2010**, *66*, 46-50, doi:10.1016/j.maturitas.2010.02.006.
211. Schmidt-Erfurth, U.; Hasan, T. Mechanisms of Action of Photodynamic Therapy with Verteporfin for the Treatment of Age-Related Macular Degeneration. *Survey of Ophthalmology* **2000**, *45*, 195-214, doi:10.1016/S0039-6257(00)00158-2.
212. Schmidt-Erfurth, U.; Hasan, T.; Gragoudas, E.; Michaud, N.; Flotte, T.J.; Birngruber, R. Vascular targeting in photodynamic occlusion of subretinal vessels. *Ophthalmology* **1994**, *101*, 1953-1961, doi:10.1016/s0161-6420(13)31079-3.
213. Kramer, M.; Miller, J.W.; Michaud, N.; Moulton, R.S.; Hasan, T.; Flotte, T.J.; Gragoudas, E.S. Liposomal Benzoporphyrin Derivative Verteporfin Photodynamic Therapy: Selective Treatment of Choroidal Neovascularization in Monkeys. *Ophthalmology* **1996**, *103*, 427-438, doi:10.1016/S0161-6420(96)30675-1.
214. Bressler, N.M. Photodynamic therapy of subfoveal choroidal neovascularization in age-related macular degeneration with verteporfin: two-year results of 2 randomized clinical trials-tap report 2. *Arch Ophthalmol* **2001**, *119*, 198-207, doi:10-1001/pubs.Ophthalmol.
215. Group, T.o.A.-r.M.D.W.P.T.S. Photodynamic Therapy of Subfoveal Choroidal Neovascularization in Age-related Macular Degeneration With Verteporfin: One-Year Results of 2 Randomized Clinical Trials—TAP Report

1. *Archives of Ophthalmology* **1999**, *117*, 1329-1345, doi:10.1001/archopht.117.10.1329.
216. Barbazetto, I.; Burdan, A.; Bressler, N.M.; Bressler, S.B.; Haynes, L.; Kapetanios, A.D.; Lukas, J.; Olsen, K.; Potter, M.; Reaves, A., et al. Photodynamic therapy of subfoveal choroidal neovascularization with verteporfin: fluorescein angiographic guidelines for evaluation and treatment--TAP and VIP report No. 2. *Arch Ophthalmol* **2003**, *121*, 1253-1268, doi:10.1001/archopht.121.9.1253.
217. Piao, W.; Hanaoka, K.; Fujisawa, T.; Takeuchi, S.; Komatsu, T.; Ueno, T.; Terai, T.; Tahara, T.; Nagano, T.; Urano, Y. Development of an Azo-Based Photosensitizer Activated under Mild Hypoxia for Photodynamic Therapy. *Journal of the American Chemical Society* **2017**, *139*, 13713-13719, doi:10.1021/jacs.7b05019.
218. Busch, T.M.; Wileyto, E.P.; Emanuele, M.J.; Del Piero, F.; Marconato, L.; Glatstein, E.; Koch, C.J. Photodynamic Therapy Creates Fluence Rate-dependent Gradients in the Intratumoral Spatial Distribution of Oxygen. *Cancer Research* **2002**, *62*, 7273-7279.
219. Feng, L.; Cheng, L.; Dong, Z.; Tao, D.; Barnhart, T.E.; Cai, W.; Chen, M.; Liu, Z. Theranostic Liposomes with Hypoxia-Activated Prodrug to Effectively Destruct Hypoxic Tumors Post-Photodynamic Therapy. *ACS Nano* **2017**, *11*, 927-937, doi:10.1021/acsnano.6b07525.
220. Albertella, M.R.; Loadman, P.M.; Jones, P.H.; Phillips, R.M.; Rampling, R.; Burnet, N.; Alcock, C.; Anthoney, A.; Vjaters, E.; Dunk, C.R., et al. Hypoxia-Selective Targeting by the Bioreductive Prodrug AQ4N in Patients with Solid Tumors: Results of a Phase I Study. *Clinical Cancer Research* **2008**, *14*, 1096-1104, doi:10.1158/1078-0432.Ccr-07-4020.
221. Liu, Y.; Liu, Y.; Bu, W.; Cheng, C.; Zuo, C.; Xiao, Q.; Sun, Y.; Ni, D.; Zhang, C.; Liu, J., et al. Hypoxia Induced by Upconversion-Based Photodynamic Therapy: Towards Highly Effective Synergistic Bioreductive Therapy in Tumors. *Angew Chem Int Ed Engl* **2015**, *54*, 8105-8109, doi:10.1002/anie.201500478.
222. Marcu, L.; Olver, I. Tirapazamine: from bench to clinical trials. *Curr Clin Pharmacol* **2006**, *1*, 71-79, doi:10.2174/157488406775268192.
223. Jahanban-Esfahlan, R.; de la Guardia, M.; Ahmadi, D.; Yousefi, B. Modulating tumor hypoxia by nanomedicine for effective cancer therapy. *J. Cell. Physiol.* **2018**, *233*, 2019-2031, doi:10.1002/jcp.25859.
224. Song, X.; Feng, L.; Liang, C.; Yang, K.; Liu, Z. Ultrasound Triggered Tumor Oxygenation with Oxygen-Shuttle Nanoperfluorocarbon to Overcome Hypoxia-Associated Resistance in Cancer Therapies. *Nano Letters* **2016**, *16*, 6145-6153, doi:10.1021/acs.nanolett.6b02365.
225. Modery-Pawlowski, C.L.; Tian, L.L.; Pan, V.; Sen Gupta, A. Synthetic Approaches to RBC Mimicry and Oxygen Carrier Systems. *Biomacromolecules* **2013**, *14*, 939-948, doi:10.1021/bm400074t.
226. Zhou, Z.; Song, J.; Nie, L.; Chen, X. Reactive oxygen species generating systems meeting challenges of photodynamic cancer therapy. *Chem Soc Rev* **2016**, *45*, 6597-6626, doi:10.1039/c6cs00271d.

227. Wan, G.; Chen, B.; Li, L.; Wang, D.; Shi, S.; Zhang, T.; Wang, Y.; Zhang, L.; Wang, Y. Nanoscaled red blood cells facilitate breast cancer treatment by combining photothermal/photodynamic therapy and chemotherapy. *Biomaterials* **2018**, *155*, 25-40, doi:10.1016/j.biomaterials.2017.11.002.
228. Vankayala, R.; Huang, Y.-K.; Kalluru, P.; Chiang, C.-S.; Hwang, K.C. First Demonstration of Gold Nanorods-Mediated Photodynamic Therapeutic Destruction of Tumors via Near Infra-Red Light Activation. *Small* **2014**, *10*, 1612-1622, doi:10.1002/smll.201302719.
229. Gunaydin, G.; Turan, I.; Yildiz, D.; Turksoy, A.; Akkaya, E. A novel approach for fractional photodynamic therapy utilizing a photosensitizer with an additional 2-pyridone module. *FEBS Open Bio* **2018**, *8*, 179.
230. Luo, G.-F.; Chen, W.-H.; Hong, S.; Cheng, Q.; Qiu, W.-X.; Zhang, X.-Z. A Self-Transformable pH-Driven Membrane-Anchoring Photosensitizer for Effective Photodynamic Therapy to Inhibit Tumor Growth and Metastasis. *Advanced Functional Materials* **2017**, *27*, 1702122, doi:10.1002/adfm.201702122.
231. Wyatt, L.C.; Moshnikova, A.; Crawford, T.; Engelman, D.M.; Andreev, O.A.; Reshetnyak, Y.K. Peptides of pHLIP family for targeted intracellular and extracellular delivery of cargo molecules to tumors. *Proceedings of the National Academy of Sciences* **2018**, *115*, E2811-E2818, doi:10.1073/pnas.1715350115.
232. Yu, M.; Guo, F.; Wang, J.; Tan, F.; Li, N. Photosensitizer-Loaded pH-Responsive Hollow Gold Nanospheres for Single Light-Induced Photothermal/Photodynamic Therapy. *ACS Applied Materials & Interfaces* **2015**, *7*, 17592-17597, doi:10.1021/acsami.5b05763.
233. Han, K.; Zhang, W.-Y.; Zhang, J.; Lei, Q.; Wang, S.-B.; Liu, J.-W.; Zhang, X.-Z.; Han, H.-Y. Acidity-Triggered Tumor-Targeted Chimeric Peptide for Enhanced Intra-Nuclear Photodynamic Therapy. *Advanced Functional Materials* **2016**, *26*, 4351-4361, doi:10.1002/adfm.201600170.
234. Gao, M.; Fan, F.; Li, D.; Yu, Y.; Mao, K.; Sun, T.; Qian, H.; Tao, W.; Yang, X. Tumor acidity-activatable TAT targeted nanomedicine for enlarged fluorescence/magnetic resonance imaging-guided photodynamic therapy. *Biomaterials* **2017**, *133*, 165-175, doi:10.1016/j.biomaterials.2017.04.013.
235. Copolovici, D.M.; Langel, K.; Eriste, E.; Langel, Ü. Cell-Penetrating Peptides: Design, Synthesis, and Applications. *ACS Nano* **2014**, *8*, 1972-1994, doi:10.1021/nn4057269.
236. Huang, H.-C.; Pigula, M.; Fang, Y.; Hasan, T. Immobilization of Photo-Immunoconjugates on Nanoparticles Leads to Enhanced Light-Activated Biological Effects. *Small* **2018**, *14*, 1-11, doi:10.1002/smll.201800236.
237. You, H.; Yoon, H.-E.; Jeong, P.-H.; Ko, H.; Yoon, J.-H.; Kim, Y.-C. Pheophorbide-a conjugates with cancer-targeting moieties for targeted photodynamic cancer therapy. *Bioorganic & Medicinal Chemistry* **2015**, *23*, 1453-1462, doi:10.1016/j.bmc.2015.02.014.
238. Zhang, Q.; Cai, Y.; Li, Q.-Y.; Hao, L.-N.; Ma, Z.; Wang, X.-J.; Yin, J. Targeted Delivery of a Mannose-Conjugated BODIPY Photosensitizer by

Nanomicelles for Photodynamic Breast Cancer Therapy. *Chemistry – A European Journal* **2017**, *23*, 14307-14315, doi:10.1002/chem.201702935.
239. García Calavia, P.; Chambrier, I.; Cook, M.J.; Haines, A.H.; Field, R.A.; Russell, D.A. Targeted photodynamic therapy of breast cancer cells using lactose-phthalocyanine functionalized gold nanoparticles. *Journal of Colloid and Interface Science* **2018**, *512*, 249-259, doi:10.1016/j.jcis.2017.10.030.
240. Hayashi, N.; Kataoka, H.; Yano, S.; Tanaka, M.; Moriwaki, K.; Akashi, H.; Suzuki, S.; Mori, Y.; Kubota, E.; Tanida, S., et al. A Novel Photodynamic Therapy Targeting Cancer Cells and Tumor-Associated Macrophages. *Molecular Cancer Therapeutics* **2015**, *14*, 452-460, doi:10.1158/1535-7163.Mct-14-0348.
241. Tran, T.H.; Nguyen, H.T.; Phuong Tran, T.T.; Ku, S.K.; Jeong, J.H.; Choi, H.G.; Yong, C.S.; Kim, J.O. Combined photothermal and photodynamic therapy by hyaluronic acid-decorated polypyrrole nanoparticles. *Nanomedicine (Lond)* **2017**, *12*, 1511-1523, doi:10.2217/nnm-2016-0438.
242. Obaid, G.; Chambrier, I.; Cook, M.J.; Russell, D.A. Cancer targeting with biomolecules: a comparative study of photodynamic therapy efficacy using antibody or lectin conjugated phthalocyanine-PEG gold nanoparticles. *Photochem Photobiol Sci* **2015**, *14*, 737-747, doi:10.1039/c4pp00312h.
243. Kato, T.; Jin, C.S.; Ujiie, H.; Lee, D.; Fujino, K.; Wada, H.; Hu, H.P.; Weersink, R.A.; Chen, J.; Kaji, M., et al. Nanoparticle targeted folate receptor 1-enhanced photodynamic therapy for lung cancer. *Lung Cancer* **2017**, *113*, 59-68, doi:10.1016/j.lungcan.2017.09.002.
244. Ma, X.; Qu, Q.; Zhao, Y. Targeted delivery of 5-aminolevulinic acid by multifunctional hollow mesoporous silica nanoparticles for photodynamic skin cancer therapy. *ACS Appl Mater Interfaces* **2015**, *7*, 10671-10676, doi:10.1021/acsami.5b03087.
245. Clement, S.; Chen, W.; Deng, W.; Goldys, E.M. X-ray radiation-induced and targeted photodynamic therapy with folic acid-conjugated biodegradable nanoconstructs. *Int J Nanomedicine* **2018**, *13*, 3553-3570, doi:10.2147/ijn.S164967.
246. Sebak, A.A.; Gomaa, I.E.O.; ElMeshad, A.N.; AbdelKader, M.H. Targeted photodynamic-induced singlet oxygen production by peptide-conjugated biodegradable nanoparticles for treatment of skin melanoma. *Photodiagnosis Photodyn Ther* **2018**, *23*, 181-189, doi:10.1016/j.pdpdt.2018.05.017.
247. Meyers, J.D.; Cheng, Y.; Broome, A.M.; Agnes, R.S.; Schluchter, M.D.; Margevicius, S.; Wang, X.; Kenney, M.E.; Burda, C.; Basilion, J.P. Peptide-Targeted Gold Nanoparticles for Photodynamic Therapy of Brain Cancer. *Part Part Syst Charact* **2015**, *32*, 448-457, doi:10.1002/ppsc.201400119.
248. Stuchinskaya, T.; Moreno, M.; Cook, M.J.; Edwards, D.R.; Russell, D.A. Targeted photodynamic therapy of breast cancer cells using antibody-phthalocyanine-gold nanoparticle conjugates. *Photochem Photobiol Sci* **2011**, *10*, 822-831, doi:10.1039/c1pp05014a.
249. Broekgaarden, M.; van Vught, R.; Oliveira, S.; Roovers, R.C.; van Bergen en Henegouwen, P.M.; Pieters, R.J.; Van Gulik, T.M.; Breukink, E.; Heger, M. Site-specific conjugation of single domain antibodies to liposomes enhances

photosensitizer uptake and photodynamic therapy efficacy. *Nanoscale* **2016**, *8*, 6490-6494, doi:10.1039/c6nr00014b.
250. Kalli, M.; Stylianopoulos, T. Defining the role of solid stress and matrix stiffness in Cancer cell proliferation and metastasis. Front Oncol 2018; 8: 55. 2018.
251. Komohara, Y.; Takeya, M. CAFs and TAMs: maestros of the tumour microenvironment. *J Pathol* **2017**, *241*, 313-315, doi:10.1002/path.4824.
252. Liu, F.-T.; Rabinovich, G.A. Galectins as modulators of tumour progression. *Nature Reviews Cancer* **2005**, *5*, 29-41, doi:10.1038/nrc1527.
253. Ghazarian, H.; Idoni, B.; Oppenheimer, S.B. A glycobiology review: Carbohydrates, lectins and implications in cancer therapeutics. *Acta Histochemica* **2011**, *113*, 236-247, doi:10.1016/j.acthis.2010.02.004.
254. Zwicke, G.L.; Mansoori, G.A.; Jeffery, C.J. Utilizing the folate receptor for active targeting of cancer nanotherapeutics. *Nano Rev* **2012**, *3*, doi:10.3402/nano.v3i0.18496.
255. Wang, F.; Li, Y.; Shen, Y.; Wang, A.; Wang, S.; Xie, T. The functions and applications of RGD in tumor therapy and tissue engineering. *Int J Mol Sci* **2013**, *14*, 13447-13462, doi:10.3390/ijms140713447.
256. Zhao, N.; Qin, Y.; Liu, H.; Cheng, Z. Tumor-Targeting Peptides: Ligands for Molecular Imaging and Therapy. *Anticancer Agents Med Chem* **2018**, *18*, 74-86, doi:10.2174/1871520617666170419143459.
257. Li, L.; Huh, K.M. Polymeric nanocarrier systems for photodynamic therapy. *Biomaterials Research* **2014**, *18*, 19, doi:10.1186/2055-7124-18-19.
258. Gao, L.; Zhang, C.; Gao, D.; Liu, H.; Yu, X.; Lai, J.; Wang, F.; Lin, J.; Liu, Z. Enhanced Anti-Tumor Efficacy through a Combination of Integrin αvβ6-Targeted Photodynamic Therapy and Immune Checkpoint Inhibition. *Theranostics* **2016**, *6*, 627-637, doi:10.7150/thno.14792.
259. Pacheco-Soares, C.; Maftou-Costa, M.; CG, D.A.C.M.C.; AC, D.E.S.S.; Moraes, K.C. Evaluation of photodynamic therapy in adhesion protein expression. *Oncol Lett* **2014**, *8*, 714-718, doi:10.3892/ol.2014.2149.
260. Noy, R.; Pollard, J.W. Tumor-associated macrophages: from mechanisms to therapy. *Immunity* **2014**, *41*, 49-61, doi:10.1016/j.immuni.2014.06.010.
261. Afik, R.; Zigmond, E.; Vugman, M.; Klepfish, M.; Shimshoni, E.; Pasmanik-Chor, M.; Shenoy, A.; Bassat, E.; Halpern, Z.; Geiger, T., et al. Tumor macrophages are pivotal constructors of tumor collagenous matrix. *J Exp Med* **2016**, *213*, 2315-2331, doi:10.1084/jem.20151193.
262. Wen, A.M.; Lee, K.L.; Cao, P.; Pangilinan, K.; Carpenter, B.L.; Lam, P.; Veliz, F.A.; Ghiladi, R.A.; Advincula, R.C.; Steinmetz, N.F. Utilizing Viral Nanoparticle/Dendron Hybrid Conjugates in Photodynamic Therapy for Dual Delivery to Macrophages and Cancer Cells. *Bioconjugate Chemistry* **2016**, *27*, 1227-1235, doi:10.1021/acs.bioconjchem.6b00075.
263. Satelli, A.; Li, S. Vimentin in cancer and its potential as a molecular target for cancer therapy. *Cell Mol Life Sci* **2011**, *68*, 3033-3046, doi:10.1007/s00018-011-0735-1.
264. Pereira, P.M.R.; Korsak, B.; Sarmento, B.; Schneider, R.J.; Fernandes, R.; Tomé, J.P.C. Antibodies armed with photosensitizers: from chemical

synthesis to photobiological applications. *Organic & Biomolecular Chemistry* **2015**, *13*, 2518-2529, doi:10.1039/C4OB02334J.
265. Chang, M.H.; Pai, C.L.; Chen, Y.C.; Yu, H.P.; Hsu, C.Y.; Lai, P.S. Enhanced Antitumor Effects of Epidermal Growth Factor Receptor Targetable Cetuximab-Conjugated Polymeric Micelles for Photodynamic Therapy. *Nanomaterials (Basel)* **2018**, *8*, doi:10.3390/nano8020121.
266. Fernandes, S.R.G.; Fernandes, R.; Sarmento, B.; Pereira, P.M.R.; Tome, J.P.C. Photoimmunoconjugates: novel synthetic strategies to target and treat cancer by photodynamic therapy. *Org Biomol Chem* **2019**, *17*, 2579-2593, doi:10.1039/c8ob02902d.
267. Zhen, Z.; Tang, W.; Wang, M.; Zhou, S.; Wang, H.; Wu, Z.; Hao, Z.; Li, Z.; Liu, L.; Xie, J. Protein Nanocage Mediated Fibroblast-Activation Protein Targeted Photoimmunotherapy To Enhance Cytotoxic T Cell Infiltration and Tumor Control. *Nano Letters* **2017**, *17*, 862-869, doi:10.1021/acs.nanolett.6b04150.
268. Li, L.; Zhou, S.; Lv, N.; Zhen, Z.; Liu, T.; Gao, S.; Xie, J.; Ma, Q. Photosensitizer-Encapsulated Ferritins Mediate Photodynamic Therapy against Cancer-Associated Fibroblasts and Improve Tumor Accumulation of Nanoparticles. *Mol Pharm* **2018**, *15*, 3595-3599, doi:10.1021/acs.molpharmaceut.8b00419.
269. Mew, D.; Wat, C.K.; Towers, G.H.; Levy, J.G. Photoimmunotherapy: treatment of animal tumors with tumor-specific monoclonal antibody-hematoporphyrin conjugates. *The Journal of Immunology* **1983**, *130*, 1473.
270. Carcenac, M.; Dorvillius, M.; Garambois, V.; Glaussel, F.; Larroque, C.; Langlois, R.; Hynes, N.E.; van Lier, J.E.; Pèlegrin, A. Internalisation enhances photo-induced cytotoxicity of monoclonal antibody-phthalocyanine conjugates. *Br J Cancer* **2001**, *85*, 1787-1793, doi:10.1054/bjoc.2001.2170.
271. Hamblin, M.R.; Miller, J.L.; Hasan, T. Effect of charge on the interaction of site-specific photoimmunoconjugates with human ovarian cancer cells. *Cancer Res* **1996**, *56*, 5205-5210.
272. Dikov, M.M.; Ohm, J.E.; Ray, N.; Tchekneva, E.E.; Burlison, J.; Moghanaki, D.; Nadaf, S.; Carbone, D.P. Differential Roles of Vascular Endothelial Growth Factor Receptors 1 and 2 in Dendritic Cell Differentiation1. *The Journal of Immunology* **2005**, *174*, 215-222, doi:10.4049/jimmunol.174.1.215.
273. Vrouenraets, M.B.; Visser, G.W.; Stewart, F.A.; Stigter, M.; Oppelaar, H.; Postmus, P.E.; Snow, G.B.; van Dongen, G.A. Development of meta-tetrahydroxyphenylchlorin-monoclonal antibody conjugates for photoimmunotherapy. *Cancer Res* **1999**, *59*, 1505-1513.
274. Walker, C.; Mojares, E.; Del Río Hernández, A. Role of Extracellular Matrix in Development and Cancer Progression. In *Int J Mol Sci*, 2018; Vol. 19.
275. Savellano, M.D.; Hasan, T. Targeting cells that overexpress the epidermal growth factor receptor with polyethylene glycolated BPD verteporfin photosensitizer immunoconjugates. *Photochem Photobiol* **2003**, *77*, 431-439, doi:10.1562/0031-8655(2003)077<0431:tctote>2.0.co;2.
276. Mitsunaga, M.; Ogawa, M.; Kosaka, N.; Rosenblum, L.T.; Choyke, P.L.; Kobayashi, H. Cancer cell-selective in vivo near infrared

photoimmunotherapy targeting specific membrane molecules. *Nat. Med.* **2011**, *17*, 1685-1691, doi:10.1038/nm.2554.
277. Spring, B.Q.; Abu-Yousif, A.O.; Palanisami, A.; Rizvi, I.; Zheng, X.; Mai, Z.; Anbil, S.; Sears, R.B.; Mensah, L.B.; Goldschmidt, R., et al. Selective treatment and monitoring of disseminated cancer micrometastases in vivo using dual-function, activatable immunoconjugates. *Proceedings of the National Academy of Sciences* **2014**, *111*, E933-E942, doi:10.1073/pnas.1319493111.
278. Ogawa, M.; Tomita, Y.; Nakamura, Y.; Lee, M.-J.; Lee, S.; Tomita, S.; Nagaya, T.; Sato, K.; Yamauchi, T.; Iwai, H., et al. Immunogenic cancer cell death selectively induced by near infrared photoimmunotherapy initiates host tumor immunity. *Oncotarget; Vol 8, No 6* **2017**, 10.18632/oncotarget.14425, doi:10.18632/oncotarget.14425.
279. Sato, K.; Ando, K.; Okuyama, S.; Moriguchi, S.; Ogura, T.; Totoki, S.; Hanaoka, H.; Nagaya, T.; Kokawa, R.; Takakura, H., et al. Photoinduced Ligand Release from a Silicon Phthalocyanine Dye Conjugated with Monoclonal Antibodies: A Mechanism of Cancer Cell Cytotoxicity after Near-Infrared Photoimmunotherapy. *ACS Central Science* **2018**, *4*, 1559-1569, doi:10.1021/acscentsci.8b00565.
280. Chen, X.; Song, E. Turning foes to friends: targeting cancer-associated fibroblasts. *Nature Reviews Drug Discovery* **2019**, *18*, 99-115, doi:10.1038/s41573-018-0004-1.
281. Miao, L.; Lin, C.M.; Huang, L. Stromal barriers and strategies for the delivery of nanomedicine to desmoplastic tumors. *J Control Release* **2015**, *219*, 192-204, doi:10.1016/j.jconrel.2015.08.017.
282. Reader, J.; Holt, D.; Fulton, A. Prostaglandin E2 EP receptors as therapeutic targets in breast cancer. *Cancer Metastasis Rev.* **2011**, *30*, 449-463, doi:10.1007/s10555-011-9303-2.
283. An, Y.; Yao, J.; Niu, X. The Signaling Pathway of PGE₂ and Its Regulatory Role in T Cell Differentiation. *Mediators of Inflammation* **2021**, *2021*, 9087816, doi:10.1155/2021/9087816.
284. Markovič, T.; Jakopin, Ž.; Dolenc, M.S.; Mlinarič-Raščan, I. Structural features of subtype-selective EP receptor modulators. *Drug Discovery Today* **2017**, *22*, 57-71, doi:10.1016/j.drudis.2016.08.003.
285. Yokoyama, U.; Iwatsubo, K.; Umemura, M.; Fujita, T.; Ishikawa, Y. The Prostanoid EP4 Receptor and Its Signaling Pathway. *Pharmacological Reviews* **2013**, *65*, 1010-1052, doi:10.1124/pr.112.007195.
286. Majumder, M.; Nandi, P.; Omar, A.; Ugwuagbo, K.C.; Lala, P.K. EP4 as a Therapeutic Target for Aggressive Human Breast Cancer. *Int J Mol Sci* **2018**, *19*, 1-20, doi:10.3390/ijms19041019.
287. De Paz Linares, G.A.; Opperman, R.M.; Majumder, M.; Lala, P.K. Prostaglandin E2 Receptor 4 (EP4) as a Therapeutic Target to Impede Breast Cancer-Associated Angiogenesis and Lymphangiogenesis. *Cancers (Basel)* **2021**, *13*, doi:10.3390/cancers13050942.
288. Jin, Y.; Smith, C.; Hu, L.; Coutant, D.E.; Whitehurst, K.; Phipps, K.; McNearney, T.A.; Yang, X.; Ackermann, B.; Pottanat, T., et al. LY3127760, a

Selective Prostaglandin E4 (EP4) Receptor Antagonist, and Celecoxib: A Comparison of Pharmacological Profiles. *Clin Transl Sci* **2018**, *11*, 46-53, doi:10.1111/cts.12497.
289. Hong, D.S.; Parikh, A.; Shapiro, G.I.; Varga, A.; Naing, A.; Meric-Bernstam, F.; Ataman, Ö.; Reyderman, L.; Binder, T.A.; Ren, M., et al. First-in-human phase I study of immunomodulatory E7046, an antagonist of PGE₂-receptor E-type 4 (EP4), in patients with advanced cancers. *Journal for ImmunoTherapy of Cancer* **2020**, *8*, e000222, doi:10.1136/jitc-2019-000222.
290. Morales, J.; Li, L.; Fattah, F.J.; Dong, Y.; Bey, E.A.; Patel, M.; Gao, J.; Boothman, D.A. Review of poly (ADP-ribose) polymerase (PARP) mechanisms of action and rationale for targeting in cancer and other diseases. *Crit Rev Eukaryot Gene Expr* **2014**, *24*, 15-28, doi:10.1615/critreveukaryotgeneexpr.2013006875.
291. Pascal, J.M. The comings and goings of PARP-1 in response to DNA damage. *DNA Repair (Amst)* **2018**, *71*, 177-182, doi:10.1016/j.dnarep.2018.08.022.
292. Schreiber, V.; Dantzer, F.; Ame, J.-C.; de Murcia, G. Poly(ADP-ribose): novel functions for an old molecule. *Nature Reviews Molecular Cell Biology* **2006**, *7*, 517-528, doi:10.1038/nrm1963.
293. Javle, M.; Curtin, N.J. The role of PARP in DNA repair and its therapeutic exploitation. *Br J Cancer* **2011**, *105*, 1114-1122, doi:10.1038/bjc.2011.382.
294. Ray Chaudhuri, A.; Nussenzweig, A. The multifaceted roles of PARP1 in DNA repair and chromatin remodelling. *Nat Rev Mol Cell Biol* **2017**, *18*, 610-621, doi:10.1038/nrm.2017.53.
295. Polo, L.M.; Xu, Y.; Hornyak, P.; Garces, F.; Zeng, Z.; Hailstone, R.; Matthews, S.J.; Caldecott, K.W.; Oliver, A.W.; Pearl, L.H. Efficient Single-Strand Break Repair Requires Binding to Both Poly(ADP-Ribose) and DNA by the Central BRCT Domain of XRCC1. *Cell Rep* **2019**, *26*, 573-581.e575, doi:10.1016/j.celrep.2018.12.082.
296. Rose, M.; Burgess, J.T.; O'Byrne, K.; Richard, D.J.; Bolderson, E. PARP Inhibitors: Clinical Relevance, Mechanisms of Action and Tumor Resistance. *Frontiers in Cell and Developmental Biology* **2020**, *8*, doi:10.3389/fcell.2020.564601.
297. Farmer, H.; McCabe, N.; Lord, C.J.; Tutt, A.N.J.; Johnson, D.A.; Richardson, T.B.; Santarosa, M.; Dillon, K.J.; Hickson, I.; Knights, C., et al. Targeting the DNA repair defect in BRCA mutant cells as a therapeutic strategy. *Nature* **2005**, *434*, 917-921, doi:10.1038/nature03445.
298. Bryant, H.E.; Schultz, N.; Thomas, H.D.; Parker, K.M.; Flower, D.; Lopez, E.; Kyle, S.; Meuth, M.; Curtin, N.J.; Helleday, T. Specific killing of BRCA2-deficient tumours with inhibitors of poly(ADP-ribose) polymerase. *Nature* **2005**, *434*, 913-917, doi:10.1038/nature03443.
299. Gottipati, P.; Vischioni, B.; Schultz, N.; Solomons, J.; Bryant, H.E.; Djureinovic, T.; Issaeva, N.; Sleeth, K.; Sharma, R.A.; Helleday, T. Poly(ADP-Ribose) Polymerase Is Hyperactivated in Homologous Recombination–Defective Cells. *Cancer Research* **2010**, *70*, 5389-5398, doi:10.1158/0008-5472.Can-09-4716.

300. Murai, J.; Huang, S.-y.N.; Das, B.B.; Renaud, A.; Zhang, Y.; Doroshow, J.H.; Ji, J.; Takeda, S.; Pommier, Y. Trapping of PARP1 and PARP2 by Clinical PARP Inhibitors. *Cancer Research* **2012**, *72*, 5588-5599, doi:10.1158/0008-5472.Can-12-2753.
301. Murai, J.; Huang, S.-Y.N.; Renaud, A.; Zhang, Y.; Ji, J.; Takeda, S.; Morris, J.; Teicher, B.; Doroshow, J.H.; Pommier, Y. Stereospecific PARP Trapping by BMN 673 and Comparison with Olaparib and Rucaparib. *Molecular Cancer Therapeutics* **2014**, *13*, 433-443, doi:10.1158/1535-7163.Mct-13-0803.
302. Lord, C.J.; Ashworth, A. PARP inhibitors: Synthetic lethality in the clinic. *Science* **2017**, *355*, 1152-1158, doi:10.1126/science.aam7344.
303. Anscher, M.S.; Chang, E.; Gao, X.; Gong, Y.; Weinstock, C.; Bloomquist, E.; Adeniyi, O.; Charlab, R.; Zimmerman, S.; Serlemitsos-Day, M., et al. FDA Approval Summary: Rucaparib for the Treatment of Patients with Deleterious BRCA-Mutated Metastatic Castrate-Resistant Prostate Cancer. *The Oncologist* **2021**, *26*, 139-146, doi:10.1002/onco.13585.
304. Benov, L. Photodynamic Therapy: Current Status and Future Directions. *Medical Principles and Practice* **2015**, *24(suppl 1)*, 14-28, doi:10.1159/000362416.
305. De Silva, P.; Saad, M.A.; Thomsen, H.C.; Bano, S.; Ashraf, S.; Hasan, T. Photodynamic therapy, priming and optical imaging: Potential co-conspirators in treatment design and optimization — a Thomas Dougherty Award for Excellence in PDT paper. *Journal of Porphyrins and Phthalocyanines* **2020**, *24*, 1320-1360, doi:10.1142/S1088424620300098.
306. Wang, Y.; Gonzalez, M.; Cheng, C.; Haouala, A.; Krueger, T.; Peters, S.; Decosterd, L.-A.; van den Bergh, H.; Perentes, J.Y.; Ris, H.-B., et al. Photodynamic induced uptake of liposomal doxorubicin to rat lung tumors parallels tumor vascular density. *Lasers in Surgery and Medicine* **2012**, *44*, 318-324, doi:10.1002/lsm.22013.
307. Wang, X.; Gronchi, F.; Bensimon, M.; Mercier, T.; Decosterd, L.A.; Wagnières, G.; Debefve, E.; Ris, H.-B.; Letovanec, I.; Peters, S., et al. Treatment of pleural malignancies by photo-induction combined to systemic chemotherapy: Proof of concept on rodent lung tumors and feasibility study on porcine chest cavities. *Lasers in Surgery and Medicine* **2015**, *47*, 807-816, doi:10.1002/lsm.22422.
308. Cheng, C.; Wang, Y.; Haouala, A.; Debefve, E.; Andrejevic Blant, S.; Krueger, T.; Gonzalez, M.; Ballini, J.P.; Peters, S.; Decosterd, L., et al. Photodynamic therapy enhances liposomal doxorubicin distribution in tumors during isolated perfusion of rodent lungs. *Eur Surg Res* **2011**, *47*, 196-204, doi:10.1159/000330744.
309. Debefve, E.; Pegaz, B.; Ballini, J.P.; Konan, Y.N.; van den Bergh, H. Combination therapy using aspirin-enhanced photodynamic selective drug delivery. *Vascular Pharmacology* **2007**, *46*, 171-180, doi:10.1016/j.vph.2006.09.006.
310. Debefve, E.; Pegaz, B.; Ballini, J.-P.; Van Den Bergh, H. Combination Therapy Using Verteporfin and Ranibizumab; Optimizing the Timing in the

CAM Model. *Photochemistry and Photobiology* **2009**, *85*, 1400-1408, doi:10.1111/j.1751-1097.2009.00604.x.
311. Debefve, E.; Mithieux, F.; Perentes, J.Y.; Wang, Y.; Cheng, C.; Schaefer, S.C.; Ruffieux, C.; Ballini, J.-P.; Gonzalez, M.; van den Bergh, H., et al. Leukocyte–endothelial cell interaction is necessary for photodynamic therapy induced vascular permeabilization. *Lasers in Surgery and Medicine* **2011**, *43*, 696-704, doi:10.1002/lsm.21115.
312. Overchuk, M.; Harmatys, K.M.; Sindhwani, S.; Rajora, M.A.; Koebel, A.; Charron, D.M.; Syed, A.M.; Chen, J.; Pomper, M.G.; Wilson, B.C., et al. Subtherapeutic Photodynamic Treatment Facilitates Tumor Nanomedicine Delivery and Overcomes Desmoplasia. *Nano Letters* **2021**, *21*, 344-352, doi:10.1021/acs.nanolett.0c03731.
313. Anbil, S.; Pigula, M.; Huang, H.-C.; Mallidi, S.; Broekgaarden, M.; Baglo, Y.; De Silva, P.; Simeone, D.M.; Mino-Kenudson, M.; Maytin, E.V., et al. Vitamin D Receptor Activation and Photodynamic Priming Enables Durable Low-dose Chemotherapy. *Molecular Cancer Therapeutics* **2020**, *19*, 1308-1319, doi:10.1158/1535-7163.MCT-19-0791.
314. Bulin, A.-L.; Broekgaarden, M.; Simeone, D.; Hasan, T. Low dose photodynamic therapy harmonizes with radiation therapy to induce beneficial effects on pancreatic heterocellular spheroids. *Oncotarget* **2019**, *10*, 2625-2643, doi:10.18632/oncotarget.26780.
315. Silva, P.D.; Bano, S.; Pogue, B.W.; Wang, K.K.; Maytin, E.V.; Hasan, T. Photodynamic priming with triple-receptor targeted nanoconjugates that trigger T cell-mediated immune responses in a 3D in vitro heterocellular model of pancreatic cancer. *Nanophotonics* **2021**, 10.1515/nanoph-2021-0304, 3199-3214, doi:10.1515/nanoph-2021-0304.
316. Inglut, C.T.; Gray, K.M.; Vig, S.; Jung, J.W.; Stabile, J.; Zhang, Y.; Stroka, K.M.; Huang, H.C. Photodynamic Priming Modulates Endothelial Cell–Cell Junction Phenotype for Light-Activated Remote Control of Drug Delivery. *IEEE Journal of Selected Topics in Quantum Electronics* **2021**, *27*, 1-11, doi:10.1109/JSTQE.2020.3024014.
317. Tonisen, F.; Perrin, L.; Bayarmagnai, B.; van den Dries, K.; Cambi, A.; Gligorijevic, B. EP4 receptor promotes invadopodia and invasion in human breast cancer. *Eur J Cell Biol* **2017**, *96*, 218-226, doi:10.1016/j.ejcb.2016.12.005.
318. Smith, P.G.; Roque, D.; Ching, M.M.; Fulton, A.; Rao, G.; Reader, J.C. The Role of Eicosanoids in Gynecological Malignancies. *Frontiers in Pharmacology* **2020**, *11*, 1-19, doi:10.3389/fphar.2020.01233.
319. Ching, M.M.; Reader, J.; Fulton, A.M. Eicosanoids in Cancer: Prostaglandin E(2) Receptor 4 in Cancer Therapeutics and Immunotherapy. *Frontiers in pharmacology* **2020**, *11*, 1-6, doi:10.3389/fphar.2020.00819.
320. Spinella, F.; Rosanò, L.; Di Castro, V.; Natali, P.G.; Bagnato, A. Endothelin-1-induced prostaglandin E2-EP2, EP4 signaling regulates vascular endothelial growth factor production and ovarian carcinoma cell invasion. *J. Biol. Chem.* **2004**, *279*, 46700-46705, doi:10.1074/jbc.M408584200.

321. Konya, V.; Marsche, G.; Schuligoi, R.; Heinemann, A. E-type prostanoid receptor 4 (EP4) in disease and therapy. *Pharmacol Ther* **2013**, *138*, 485-502, doi:10.1016/j.pharmthera.2013.03.006.
322. Gui, T.; Shen, K. The epidermal growth factor receptor as a therapeutic target in epithelial ovarian cancer. *Cancer Epidemiology* **2012**, *36*, 490-496, doi:10.1016/j.canep.2012.06.005.
323. Sigismund, S.; Avanzato, D.; Lanzetti, L. Emerging functions of the EGFR in cancer. *Mol Oncol* **2018**, *12*, 3-20, doi:10.1002/1878-0261.12155.
324. Parida, S.; Pal, I.; Parekh, A.; Thakur, B.; Bharti, R.; Das, S.; Mandal, M. GW627368X inhibits proliferation and induces apoptosis in cervical cancer by interfering with EP4/EGFR interactive signaling. *Cell Death & Disease* **2016**, *7*, 1-13, doi:10.1038/cddis.2016.61.
325. Ching, M.M.; Fan, C.; Roque, D.; Rao, G.; Staats, P.; Fulton, A.; Reader, J. Abstract A22: Functional analysis of PGE2 pathway members EP4 and MRP4 in ovarian cancer. *Clinical Cancer Research* **2018**, *24*, A22, doi:10.1158/1557-3265.OVCA17-A22.
326. Inglut, C.T.; Baglo, Y.; Liang, B.J.; Cheema, Y.; Stabile, J.; Woodworth, G.F.; Huang, H.C. Systematic Evaluation of Light-Activatable Biohybrids for Anti-Glioma Photodynamic Therapy. *J Clin Med* **2019**, *8*, 1-20, doi:10.3390/jcm8091269.
327. Liang, B.J.; Pigula, M.; Baglo, Y.; Najafali, D.; Hasan, T.; Huang, H.C. Breaking the selectivity-uptake trade-off of photoimmunoconjugates with nanoliposomal irinotecan for synergistic multi-tier cancer targeting. *J Nanobiotechnology* **2020**, *18*, 1-14, doi:10.1186/s12951-019-0560-5.
328. Kobayashi, H.; Choyke, P.L. Near-Infrared Photoimmunotherapy of Cancer. *Accounts of Chemical Research* **2019**, *52*, 2332-2339, doi:10.1021/acs.accounts.9b00273.
329. Kobayashi, H.; Furusawa, A.; Rosenberg, A.; Choyke, P.L. Near-infrared photoimmunotherapy of cancer: a new approach that kills cancer cells and enhances anti-cancer host immunity. *Int Immunol* **2021**, *33*, 7-15, doi:10.1093/intimm/dxaa037.
330. Coleman, R.L.; Spirtos, N.M.; Enserro, D.; Herzog, T.J.; Sabbatini, P.; Armstrong, D.K.; Kim, J.-W.; Park, S.-Y.; Kim, B.-G.; Nam, J.-H., et al. Secondary Surgical Cytoreduction for Recurrent Ovarian Cancer. *N. Engl. J. Med.* **2019**, *381*, 1929-1939, doi:10.1056/NEJMoa1902626.
331. Kim, S.; Han, Y.; Kim, S.I.; Kim, H.-S.; Kim, S.J.; Song, Y.S. Tumor evolution and chemoresistance in ovarian cancer. *npj Precision Oncology* **2018**, *2*, 1-9, doi:10.1038/s41698-018-0063-0.
332. Baglo, Y.; Sorrin, A.J.; Liang, B.J.; Huang, H.C. Harnessing the Potential Synergistic Interplay Between Photosensitizer Dark Toxicity and Chemotherapy. *Photochem Photobiol* **2019**, *96*, 636-645, doi:10.1111/php.13196.
333. Simmons, D.L.; Botting, R.M.; Hla, T. Cyclooxygenase Isozymes: The Biology of Prostaglandin Synthesis and Inhibition. *Pharmacological Reviews* **2004**, *56*, 387-437, doi:10.1124/pr.56.3.3.

334. Kochel, T.J.; Fulton, A.M. Multiple Drug Resistance-Associated Protein 4 (MRP4), Prostaglandin Transporter (PGT), and 15-Hydroxyprostaglandin Dehydrogenase (15-PGDH) as Determinants of PGE2 Levels in Cancer. *Prostaglandins & Other Lipid Mediators* **2015**, *116-117*, 99-103, doi:10.1016/j.prostaglandins.2014.11.003.
335. Zhang, H.; Kong, Q.; Wang, J.; Jiang, Y.; Hua, H. Complex roles of cAMP–PKA–CREB signaling in cancer. *Experimental Hematology & Oncology* **2020**, *9*, 1-13, doi:10.1186/s40164-020-00191-1.
336. Krysan, K.; Reckamp, K.L.; Dalwadi, H.; Sharma, S.; Rozengurt, E.; Dohadwala, M.; Dubinett, S.M. Prostaglandin E2 Activates Mitogen-Activated Protein Kinase/Erk Pathway Signaling and Cell Proliferation in Non–Small Cell Lung Cancer Cells in an Epidermal Growth Factor Receptor–Independent Manner. *Cancer Research* **2005**, *65*, 6275-6281, doi:10.1158/0008-5472.Can-05-0216.
337. Jiang, F.; Chopp, M.; Katakowski, M.; Cho, K.K.; Yang, X.; Hochbaum, N.; Tong, L.; Mikkelsen, T. Photodynamic Therapy with Photofrin Reduces Invasiveness of Malignant Human Glioma Cells. *Lasers in Medical Science* **2002**, *17*, 280-288, doi:10.1007/s101030200041.
338. Yang, T.-H.; Chen, C.-T.; Wang, C.-P.; Lou, P.-J. Photodynamic therapy suppresses the migration and invasion of head and neck cancer cells in vitro. *Oral Oncology* **2007**, *43*, 358-365, doi:10.1016/j.oraloncology.2006.04.007.
339. Coleman, R.A.; Grix, S.P.; Head, S.A.; Louttit, J.B.; Mallett, A.; Sheldrick, R.L. A novel inhibitory prostanoid receptor in piglet saphenous vein. *Prostaglandins* **1994**, *47*, 151-168, doi:10.1016/0090-6980(94)90084-1.
340. Xin, X.; Majumder, M.; Girish, G.V.; Mohindra, V.; Maruyama, T.; Lala, P.K. Targeting COX-2 and EP4 to control tumor growth, angiogenesis, lymphangiogenesis and metastasis to the lungs and lymph nodes in a breast cancer model. *Laboratory Investigation* **2012**, *92*, 1115-1128, doi:10.1038/labinvest.2012.90.
341. Majumder, M.; Xin, X.; Liu, L.; Girish, G.V.; Lala, P.K. Prostaglandin E2 receptor EP4 as the common target on cancer cells and macrophages to abolish angiogenesis, lymphangiogenesis, metastasis, and stem-like cell functions. *Cancer Sci* **2014**, *105*, 1142-1151, doi:10.1111/cas.12475.
342. Xu, S.; Zhou, W.; Ge, J.; Zhang, Z. Prostaglandin E2 receptor EP4 is involved in the cell growth and invasion of prostate cancer via the cAMP-PKA/PI3K-Akt signaling pathway. *Mol Med Rep* **2018**, *17*, 4702-4712, doi:10.3892/mmr.2018.8415.
343. Reader, J.; Harper, A.K.; Legesse, T.; Staats, P.N.; Goloubeva, O.; Rao, G.G.; Fulton, A.; Roque, D.M. EP4 and Class III β-Tubulin Expression in Uterine Smooth Muscle Tumors: Implications for Prognosis and Treatment. *Cancers (Basel)* **2019**, *11*, 1-17, doi:10.3390/cancers11101590.
344. Buchanan, F.G.; Gorden, D.L.; Matta, P.; Shi, Q.; Matrisian, L.M.; DuBois, R.N. Role of beta-arrestin 1 in the metastatic progression of colorectal cancer. *Proc Natl Acad Sci U S A* **2006**, *103*, 1492-1497, doi:10.1073/pnas.0510562103.

345. Abu-Yousif, A.O.; Moor, A.C.E.; Zheng, X.; Savellano, M.D.; Yu, W.; Selbo, P.K.; Hasan, T. Epidermal growth factor receptor-targeted photosensitizer selectively inhibits EGFR signaling and induces targeted phototoxicity in ovarian cancer cells. *Cancer letters* **2012**, *321*, 120-127, doi:10.1016/j.canlet.2012.01.014.
346. Cherukuri, D.P.; Chen, X.B.O.; Goulet, A.-C.; Young, R.N.; Han, Y.; Heimark, R.L.; Regan, J.W.; Meuillet, E.; Nelson, M.A. The EP4 receptor antagonist, L-161,982, blocks prostaglandin E2-induced signal transduction and cell proliferation in HCA-7 colon cancer cells. *Experimental Cell Research* **2007**, *313*, 2969-2979, doi:10.1016/j.yexcr.2007.06.004.
347. Swarthout, J.T.; Tyson, D.R.; Jefcoat JR., S.C.; Partridge, N.C. Induction of Transcriptional Activity of the Cyclic Adenosine Monophosphate Response Element Binding Protein by Parathyroid Hormone and Epidermal Growth Factor in Osteoblastic Cells. *Journal of Bone and Mineral Research* **2002**, *17*, 1401-1407, doi:10.1359/jbmr.2002.17.8.1401.
348. Barlow, C.A.; Kitiphongspattana, K.; Siddiqui, N.; Roe, M.W.; Mossman, B.T.; Lounsbury, K.M. Protein kinase A-mediated CREB phosphorylation is an oxidant-induced survival pathway in alveolar type II cells. *Apoptosis* **2008**, *13*, 681-692, doi:10.1007/s10495-008-0203-z.
349. Ferrario, A.; von Tiehl, K.; Wong, S.; Luna, M.; Gomer, C.J. Cyclooxygenase-2 Inhibitor Treatment Enhances Photodynamic Therapy-mediated Tumor Response. *Cancer Research* **2002**, *62*, 3956 –3961.
350. Makowski, M.; Grzela, T.; Niderla, J.; M, L.A.; Mroz, P.; Kopee, M.; Legat, M.; Strusinska, K.; Koziak, K.; Nowis, D., et al. Inhibition of cyclooxygenase-2 indirectly potentiates antitumor effects of photodynamic therapy in mice. *Clin Cancer Res* **2003**, *9*, 5417-5422.
351. Hendrickx, N.; Volanti, C.; Moens, U.; Seternes, O.M.; de Witte, P.; Vandenheede, J.R.; Piette, J.; Agostinis, P. Up-regulation of Cyclooxygenase-2 and Apoptosis Resistance by p38 MAPK in Hypericin-mediated Photodynamic Therapy of Human Cancer Cells. *J. Biol. Chem.* **2003**, *278*, 52231-52239, doi:10.1074/jbc.M307591200.
352. Vincent, P.; Maeder, M.E.; Hunt, B.; Linn, B.; Mangels-Dick, T.; Hasan, T.; Wang, K.K.; Pogue, B.W. CT radiomic features of photodynamic priming in clinical pancreatic adenocarcinoma treatment. *Physics in Medicine & Biology* **2021**, *66*, 1-10, doi:10.1088/1361-6560/ac1458.
353. Wang, Y.; Wang, X.; Le Bitoux, M.-A.; Wagnieres, G.; Vandenbergh, H.; Gonzalez, M.; Ris, H.-B.; Perentes, J.Y.; Krueger, T. Fluence plays a critical role on the subsequent distribution of chemotherapy and tumor growth delay in murine mesothelioma xenografts pre-treated by photodynamic therapy. *Lasers in Surgery and Medicine* **2015**, *47*, 323-330, doi:10.1002/lsm.22329.
354. Cormier, N.; Yeo, A.; Fiorentino, E.; Paxson, J. Optimization of the Wound Scratch Assay to Detect Changes in Murine Mesenchymal Stromal Cell Migration After Damage by Soluble Cigarette Smoke Extract. *J Vis Exp* **2015**, 10.3791/53414, 1-9, doi:10.3791/53414.

355. van Zijl, F.; Krupitza, G.; Mikulits, W. Initial steps of metastasis: cell invasion and endothelial transmigration. *Mutat Res* **2011**, *728*, 23-34, doi:10.1016/j.mrrev.2011.05.002.
356. Take, Y.; Koizumi, S.; Nagahisa, A. Prostaglandin E Receptor 4 Antagonist in Cancer Immunotherapy: Mechanisms of Action. *Front Immunol* **2020**, *11*, 324-324, doi:10.3389/fimmu.2020.00324.
357. Ma, X.; Holt, D.; Kundu, N.; Reader, J.; Goloubeva, O.; Take, Y.; Fulton, A.M. A prostaglandin E (PGE) receptor EP4 antagonist protects natural killer cells from PGE2-mediated immunosuppression and inhibits breast cancer metastasis. *Oncoimmunology* **2013**, *2*, 1-8, doi:10.4161/onci.22647.
358. Szender, J.B.; Emmons, T.; Belliotti, S.; Dickson, D.; Khan, A.; Morrell, K.; Khan, A.; Singel, K.L.; Mayor, P.C.; Moysich, K.B., et al. Impact of ascites volume on clinical outcomes in ovarian cancer: A cohort study. *Gynecol Oncol* **2017**, *146*, 491-497, doi:10.1016/j.ygyno.2017.06.008.
359. Shurbaji, S.; G. Anlar, G.; A. Hussein, E.; Elzatahry, A.; C. Yalcin, H. Effect of Flow-Induced Shear Stress in Nanomaterial Uptake by Cells: Focus on Targeted Anti-Cancer Therapy. *Cancers (Basel)* **2020**, *12*, 1916.
360. Hyler, A.R.; Baudoin, N.C.; Brown, M.S.; Stremler, M.A.; Cimini, D.; Davalos, R.V.; Schmelz, E.M. Fluid shear stress impacts ovarian cancer cell viability, subcellular organization, and promotes genomic instability. *PLoS One* **2018**, *13*, e0194170-e0194170, doi:10.1371/journal.pone.0194170.
361. Rizvi, I.; Gurkan, U.A.; Tasoglu, S.; Alagic, N.; Celli, J.P.; Mensah, L.B.; Mai, Z.; Demirci, U.; Hasan, T. Flow induces epithelial-mesenchymal transition, cellular heterogeneity and biomarker modulation in 3D ovarian cancer nodules. *Proceedings of the National Academy of Sciences* **2013**, *110*, E1974, doi:10.1073/pnas.1216989110.
362. Ip, C.K.M.; Li, S.-S.; Tang, M.Y.H.; Sy, S.K.H.; Ren, Y.; Shum, H.C.; Wong, A.S.T. Stemness and chemoresistance in epithelial ovarian carcinoma cells under shear stress. *Sci Rep* **2016**, *6*, 1-11, doi:10.1038/srep26788.
363. Han, J.; Zern, B.J.; Shuvaev, V.V.; Davies, P.F.; Muro, S.; Muzykantov, V. Acute and Chronic Shear Stress Differently Regulate Endothelial Internalization of Nanocarriers Targeted to Platelet-Endothelial Cell Adhesion Molecule-1. *ACS Nano* **2012**, *6*, 8824-8836, doi:10.1021/nn302687n.
364. Nath, S.; Pigula, M.; Khan, A.P.; Hanna, W.; Ruhi, M.K.; Dehkordy, F.M.; Pushpavanam, K.; Rege, K.; Moore, K.; Tsujita, Y., et al. Flow-induced Shear Stress Confers Resistance to Carboplatin in an Adherent Three-Dimensional Model for Ovarian Cancer: A Role for EGFR-Targeted Photoimmunotherapy Informed by Physical Stress. *J Clin Med* **2020**, *9*, 1-27, doi:10.3390/jcm9040924.
365. van Driel, W.J.; Koole, S.N.; Sikorska, K.; Schagen van Leeuwen, J.H.; Schreuder, H.W.R.; Hermans, R.H.M.; de Hingh, I.H.J.T.; van der Velden, J.; Arts, H.J.; Massuger, L.F.A.G., et al. Hyperthermic Intraperitoneal Chemotherapy in Ovarian Cancer. *New England Journal of Medicine* **2018**, *378*, 230-240, doi:10.1056/NEJMoa1708618.
366. Sorrin, A.J.; Kemal Ruhi, M.; Ferlic, N.A.; Karimnia, V.; Polacheck, W.J.; Celli, J.P.; Huang, H.-C.; Rizvi, I. Photodynamic Therapy and the Biophysics

of the Tumor Microenvironment. *Photochemistry and Photobiology* **2020**, *96*, 232-259, doi:10.1111/php.13209.
367. Nath, S.; Saad, M.A.; Pigula, M.; Swain, J.W.R.; Hasan, T. Photoimmunotherapy of Ovarian Cancer: A Unique Niche in the Management of Advanced Disease. *Cancers (Basel)* **2019**, *11*, 1-25, doi:10.3390/cancers11121887.
368. Ulfo, L.; Costantini, P.E.; Di Giosia, M.; Danielli, A.; Calvaresi, M. EGFR-Targeted Photodynamic Therapy. *Pharmaceutics* **2022**, *14*, 241.
369. Sorrin, A.J.; Liu, C.; Cicalo, J.; Reader, J.; Najafali, D.; Zhang, Y.; Roque, D.M.; Huang, H.-C. Photodynamic Priming Improves the Anti-Migratory Activity of Prostaglandin E Receptor 4 Antagonist in Cancer Cells In Vitro. *Cancers (Basel)* **2021**, *13*, 5259, doi:10.3390/cancers13215259.
370. Kessel, D.; Luo, Y.; Deng, Y.; Chang, C.K. The role of subcellular localization in initiation of apoptosis by photodynamic therapy. *Photochem Photobiol* **1997**, *65*, 422-426, doi:10.1111/j.1751-1097.1997.tb08581.x.
371. Mahalingam, S.M.; Ordaz, J.D.; Low, P.S. Targeting of a Photosensitizer to the Mitochondrion Enhances the Potency of Photodynamic Therapy. *ACS Omega* **2018**, *3*, 6066-6074, doi:10.1021/acsomega.8b00692.
372. Oliveira, C.S.; Turchiello, R.; Kowaltowski, A.J.; Indig, G.L.; Baptista, M.S. Major determinants of photoinduced cell death: Subcellular localization versus photosensitization efficiency. *Free Radical Biology and Medicine* **2011**, *51*, 824-833, doi:10.1016/j.freeradbiomed.2011.05.023.
373. Mo, J.; Mai Le, N.P.; Priefer, R. Evaluating the mechanisms of action and subcellular localization of ruthenium(II)-based photosensitizers. *European Journal of Medicinal Chemistry* **2021**, *225*, 113770, doi:10.1016/j.ejmech.2021.113770.
374. Liao, H.-J.; Carpenter, G. Cetuximab/C225-induced intracellular trafficking of epidermal growth factor receptor. *Cancer research* **2009**, *69*, 6179-6183, doi:10.1158/0008-5472.CAN-09-0049.
375. Okada, Y.; Kimura, T.; Nakagawa, T.; Okamoto, K.; Fukuya, A.; Goji, T.; Fujimoto, S.; Sogabe, M.; Miyamoto, H.; Muguruma, N., et al. EGFR Downregulation after Anti-EGFR Therapy Predicts the Antitumor Effect in Colorectal Cancer. *Molecular Cancer Research* **2017**, *15*, 1445, doi:10.1158/1541-7786.MCR-16-0383.
376. Patel, D.; Lahiji, A.; Patel, S.; Franklin, M.; Jimenez, X.; Hicklin, D.J.; Kang, X. Monoclonal Antibody Cetuximab Binds to and Down-regulates Constitutively Activated Epidermal Growth Factor Receptor vIII on the Cell Surface. *Anticancer Res.* **2007**, *27*, 3355.
377. Jaramillo, M.L.; Leon, Z.; Grothe, S.; Paul-Roc, B.; Abulrob, A.; O'Connor McCourt, M. Effect of the anti-receptor ligand-blocking 225 monoclonal antibody on EGF receptor endocytosis and sorting. *Experimental Cell Research* **2006**, *312*, 2778-2790, doi:10.1016/j.yexcr.2006.05.008.
378. Savellano, M.D.; Hasan, T. Photochemical Targeting of Epidermal Growth Factor Receptor: A Mechanistic Study. *Clinical Cancer Research* **2005**, *11*, 1658-1668, doi:10.1158/1078-0432.Ccr-04-1902.

379. Björnmalm, M.; Yan, Y.; Caruso, F. Engineering and evaluating drug delivery particles in microfluidic devices. *Journal of Controlled Release* **2014**, *190*, 139-149, doi:10.1016/j.jconrel.2014.04.030.
380. Vázquez-Medina, J.P.; Dodia, C.; Weng, L.; Mesaros, C.; Blair, I.A.; Feinstein, S.I.; Chatterjee, S.; Fisher, A.B. The phospholipase A2 activity of peroxiredoxin 6 modulates NADPH oxidase 2 activation via lysophosphatidic acid receptor signaling in the pulmonary endothelium and alveolar macrophages. *The FASEB Journal* **2016**, *30*, 2885-2898, doi:10.1096/fj.201500146R.
381. Kutluay, Sebla B.; Zang, T.; Blanco-Melo, D.; Powell, C.; Jannain, D.; Errando, M.; Bieniasz, Paul D. Global Changes in the RNA Binding Specificity of HIV-1 Gag Regulate Virion Genesis. *Cell* **2014**, *159*, 1096-1109, doi:10.1016/j.cell.2014.09.057.
382. Samuel, S.P.; Jain, N.; O'Dowd, F.; Paul, T.; Kashanin, D.; Gerard, V.A.; Gun'ko, Y.K.; Prina-Mello, A.; Volkov, Y. Multifactorial determinants that govern nanoparticle uptake by human endothelial cells under flow. *Int J Nanomedicine* **2012**, *7*, 2943-2956, doi:10.2147/ijn.S30624.
383. Hosta-Rigau, L.; Städler, B. Shear Stress and Its Effect on the Interaction of Myoblast Cells with Nanosized Drug Delivery Vehicles. *Mol Pharm* **2013**, *10*, 2707-2712, doi:10.1021/mp4001298.
384. Teo, B.M.; van der Westen, R.; Hosta-Rigau, L.; Städler, B. Cell response to PEGylated poly(dopamine) coated liposomes considering shear stress. *Biochimica et Biophysica Acta (BBA) - General Subjects* **2013**, *1830*, 4838-4847, doi:10.1016/j.bbagen.2013.06.022.
385. Godoy-Gallardo, M.; Ek, P.K.; Jansman, M.M.; Wohl, B.M.; Hosta-Rigau, L. Interaction between drug delivery vehicles and cells under the effect of shear stress. *Biomicrofluidics* **2015**, *9*, 052605, doi:10.1063/1.4923324.
386. Kang, T.; Park, C.; Choi, J.-S.; Cui, J.-H.; Lee, B.-J. Effects of shear stress on the cellular distribution of polystyrene nanoparticles in a biomimetic microfluidic system. *Journal of Drug Delivery Science and Technology* **2016**, *31*, 130-136, doi:10.1016/j.jddst.2015.12.001.
387. Kang, T.; Park, C.; Lee, B.-J. Investigation of biomimetic shear stress on cellular uptake and mechanism of polystyrene nanoparticles in various cancer cell lines. *Archives of Pharmacal Research* **2016**, *39*, 1663-1670, doi:10.1007/s12272-016-0847-0.
388. Charwat, V.; Olmos Calvo, I.; Rothbauer, M.; Kratz, S.R.A.; Jungreuthmayer, C.; Zanghellini, J.; Grillari, J.; Ertl, P. Combinatorial in Vitro and in Silico Approach To Describe Shear-Force Dependent Uptake of Nanoparticles in Microfluidic Vascular Models. *Analytical chemistry* **2018**, *90*, 3651-3655, doi:10.1021/acs.analchem.7b04788.
389. Nowak, M.; Brown, T.D.; Graham, A.; Helgeson, M.E.; Mitragotri, S. Size, shape, and flexibility influence nanoparticle transport across brain endothelium under flow. *Bioengineering & Translational Medicine* **2020**, *5*, e10153, doi:10.1002/btm2.10153.
390. Xu, Y.; Qin, S.; Niu, Y.; Gong, T.; Zhang, Z.; Fu, Y. Effect of fluid shear stress on the internalization of kidney-targeted delivery systems in renal

tubular epithelial cells. *Acta Pharmaceutica Sinica B* **2020**, *10*, 680-692, doi:10.1016/j.apsb.2019.11.012.
391. López-Hernández, T.; Haucke, V.; Maritzen, T. Endocytosis in the adaptation to cellular stress. *Cell Stress* **2020**, *4*, 230-247, doi:10.15698/cst2020.10.232.
392. He, Z.; Zhang, W.; Mao, S.; Li, N.; Li, H.; Lin, J.-M. Shear Stress-Enhanced Internalization of Cell Membrane Proteins Indicated by a Hairpin-Type DNA Probe. *Analytical chemistry* **2018**, *90*, 5540-5545, doi:10.1021/acs.analchem.8b00755.
393. Siwak, D.R.; Carey, M.; Hennessy, B.T.; Nguyen, C.T.; McGahren Murray, M.J.; Nolden, L.; Mills, G.B. Targeting the epidermal growth factor receptor in epithelial ovarian cancer: current knowledge and future challenges. *J Oncol* **2010**, *2010*, 568938-568938, doi:10.1155/2010/568938.
394. Teplinsky, E.; Muggia, F. EGFR and HER2: is there a role in ovarian cancer? *Translational Cancer Research* **2015**, *4*, 107-117, doi:10.3978/j.issn.2218-676X.2015.01.01.
395. Bhandari, C.; Guirguis, M.; Savan, N.A.; Shrivastava, N.; Oliveira, S.; Hasan, T.; Obaid, G. What NIR photodynamic activation offers molecular targeted nanomedicines: Perspectives into the conundrum of tumor specificity and selectivity. *Nano Today* **2021**, *36*, 101052, doi:10.1016/j.nantod.2020.101052.
396. Baglo, Y.; Sorrin, A.J.; Pu, X.; Liu, C.; Reader, J.; Roque, D.M.; Huang, H.-C. Evolutionary dynamics of cancer multidrug resistance in response to olaparib and photodynamic therapy. *Translational Oncology* **2021**, *14*, 101198, doi:10.1016/j.tranon.2021.101198.
397. Valabrega, G.; Scotto, G.; Tuninetti, V.; Pani, A.; Scaglione, F. Differences in PARP Inhibitors for the Treatment of Ovarian Cancer: Mechanisms of Action, Pharmacology, Safety, and Efficacy. *Int J Mol Sci* **2021**, *22*, doi:10.3390/ijms22084203.
398. Sandhu, D.; Antolin, A.A.; Cox, A.R.; Jones, A.M. Identification of different side effects between PARP inhibitors and their polypharmacological multi-target rationale. *British Journal of Clinical Pharmacology* **2022**, *88*, 742-752, doi:10.1111/bcp.15015.
399. Boussios, S.; Abson, C.; Moschetta, M.; Rassy, E.; Karathanasi, A.; Bhat, T.; Ghumman, F.; Sheriff, M.; Pavlidis, N. Poly (ADP-Ribose) Polymerase Inhibitors: Talazoparib in Ovarian Cancer and Beyond. *Drugs R D* **2020**, *20*, 55-73, doi:10.1007/s40268-020-00301-8.
400. Pommier, Y.; O'Connor, M.J.; de Bono, J. Laying a trap to kill cancer cells: PARP inhibitors and their mechanisms of action. *Science Translational Medicine* **2016**, *8*, 362ps317-362ps317, doi:doi:10.1126/scitranslmed.aaf9246.
401. Mokhtari, R.B.; Homayouni, T.S.; Baluch, N.; Morgatskaya, E.; Kumar, S.; Das, B.; Yeger, H. Combination therapy in combating cancer. *Oncotarget* **2017**, *8*, doi:10.18632/oncotarget.16723.
402. Tanaka, M.; Sasaki, M.; Suzuki, T.; Nishie, H.; Kataoka, H. Combination of talaporfin photodynamic therapy and Poly (ADP-Ribose) polymerase (PARP) inhibitor in gastric cancer. *Biochem. Biophys. Res. Commun.* **2021**, *539*, 1-7, doi:10.1016/j.bbrc.2020.12.073.

403. Lei, S.; Ge, F.; Lin, M.; Wang, X.; Shen, J.; Yang, Y.; Deng, J.; Wang, Z.; Wang, J.; Li, K. PARP inhibitors diminish DNA damage repair for the enhancement of tumor photodynamic therapy. *Photodiagnosis and Photodynamic Therapy* **2022**, *40*, 103058, doi:10.1016/j.pdpdt.2022.103058.
404. Magalhães, J.A.; Arruda, D.C.; Baptista, M.S.; Tada, D.B. Co-Encapsulation of Methylene Blue and PARP-Inhibitor into Poly(Lactic-Co-Glycolic Acid) Nanoparticles for Enhanced PDT of Cancer. *Nanomaterials* **2021**, *11*, 1514, doi:10.3390/nano11061514.
405. Rottenberg, S.; Jaspers, J.E.; Kersbergen, A.; van der Burg, E.; Nygren, A.O.; Zander, S.A.; Derksen, P.W.; de Bruin, M.; Zevenhoven, J.; Lau, A., et al. High sensitivity of BRCA1-deficient mammary tumors to the PARP inhibitor AZD2281 alone and in combination with platinum drugs. *Proc Natl Acad Sci U S A* **2008**, *105*, 17079-17084, doi:10.1073/pnas.0806092105.
406. Oplustilova, L.; Wolanin, K.; Mistrik, M.; Korinkova, G.; Simkova, D.; Bouchal, J.; Lenobel, R.; Bartkova, J.; Lau, A.; O'Connor, M.J., et al. Evaluation of candidate biomarkers to predict cancer cell sensitivity or resistance to PARP-1 inhibitor treatment. *Cell Cycle* **2012**, *11*, 3837-3850, doi:10.4161/cc.22026.
407. Singh, B.; Yang, S.; Krishna, A.; Sridhar, S. Nanoparticle Formulations of Poly (ADP-ribose) Polymerase Inhibitors for Cancer Therapy. *Front Chem* **2020**, *8*, 594619, doi:10.3389/fchem.2020.594619.
408. Sargazi, S.; Mukhtar, M.; Rahdar, A.; Barani, M.; Pandey, S.; Díez-Pascual, A.M. Active Targeted Nanoparticles for Delivery of Poly(ADP-ribose) Polymerase (PARP) Inhibitors: A Preliminary Review. *Int J Mol Sci* **2021**, *22*, doi:10.3390/ijms221910319.
409. Cai, L.; Xu, X.; Chen, W. The Current State of the Art in PARP Inhibitor-Based Delivery Nanosystems. In *Pharmaceutics*, 2022; Vol. 14.
410. Gomes-da-Silva, L.C.; Kepp, O.; Kroemer, G. Regulatory approval of photoimmunotherapy: photodynamic therapy that induces immunogenic cell death. *Oncoimmunology* **2020**, *9*, 1841393, doi:10.1080/2162402x.2020.1841393.
411. Wurz, G.T.; DeGregorio, M.W. Activating adaptive cellular mechanisms of resistance following sublethal cytotoxic chemotherapy: Implications for diagnostic microdosing. *International Journal of Cancer* **2015**, *136*, 1485-1493, doi:10.1002/ijc.28773.
412. Reginato, E.; Wolf, P.; Hamblin, M.R. Immune response after photodynamic therapy increases anti-cancer and anti-bacterial effects. *World J Immunol* **2014**, *4*, 1-11, doi:10.5411/wji.v4.i1.1.
413. Finetti, F.; Travelli, C.; Ercoli, J.; Colombo, G.; Buoso, E.; Trabalzini, L. Prostaglandin E2 and Cancer: Insight into Tumor Progression and Immunity. *Biology (Basel)* **2020**, *9*, doi:10.3390/biology9120434.
414. Chen, J.; Shen, P.; Zhang, X.C.; Zhao, M.D.; Zhang, X.G.; Yang, L. Efficacy and safety profile of celecoxib for treating advanced cancers: a meta-analysis of 11 randomized clinical trials. *Clin Ther* **2014**, *36*, 1253-1263, doi:10.1016/j.clinthera.2014.06.015.

415. Bresalier, R.S.; Sandler, R.S.; Quan, H.; Bolognese, J.A.; Oxenius, B.; Horgan, K.; Lines, C.; Riddell, R.; Morton, D.; Lanas, A., et al. Cardiovascular events associated with rofecoxib in a colorectal adenoma chemoprevention trial. *N Engl J Med* **2005**, *352*, 1092-1102, doi:10.1056/NEJMoa050493.
416. Dai, P.; Li, J.; Ma, X.-P.; Huang, J.; Meng, J.-J.; Gong, P. Efficacy and safety of COX-2 inhibitors for advanced non-small-cell lung cancer with chemotherapy: a meta-analysis. *Onco Targets Ther* **2018**, *11*, 721-730, doi:10.2147/OTT.S148670.
417. Helderman, R.; Löke, D.R.; Tanis, P.J.; Tuynman, J.B.; Ceelen, W.; de Hingh, I.H.; van der Speeten, K.; Franken, N.A.P.; Oei, A.L.; Kok, H.P., et al. Preclinical In Vivo-Models to Investigate HIPEC; Current Methodologies and Challenges. *Cancers (Basel)* **2021**, *13*, doi:10.3390/cancers13143430.
418. Yu, H.; Ai, L.; Rouhanizadeh, M.; Patel, D.; Kim, E.S.; Hsiai, T.K. Flexible Polymer Sensors for In Vivo Intravascular Shear Stress Analysis. *Journal of Microelectromechanical Systems* **2008**, *17*, 1178-1186, doi:10.1109/JMEMS.2008.927749.
419. Baldwin, A.; Yu, L.; Meng, E. An Electrochemical Impedance-Based Thermal Flow Sensor for Physiological Fluids. *Journal of Microelectromechanical Systems* **2016**, *25*, 1015-1024, doi:10.1109/JMEMS.2016.2614664.
420. Zhang, D.; Baldwin, P.; Leal, A.S.; Carapellucci, S.; Sridhar, S.; Liby, K.T. A nano-liposome formulation of the PARP inhibitor Talazoparib enhances treatment efficacy and modulates immune cell populations in mammary tumors of BRCA-deficient mice. *Theranostics* **2019**, *9*, 6224-6238, doi:10.7150/thno.36281.
421. Pathade, A.D.; Kommineni, N.; Bulbake, U.; Thummar, M.M.; Samanthula, G.; Khan, W. Preparation and Comparison of Oral Bioavailability for Different Nano-formulations of Olaparib. *AAPS PharmSciTech* **2019**, *20*, 276, doi:10.1208/s12249-019-1468-y.